Tailoring Surfaces in Porous Media for Catalysis and Separation Applications

Department of Chemical Engineering

University of Manchester

Luke Forster

A thesis submitted for the degree of Doctor of Philosophy

August 2021

Table of contents

Word count: 65107 words

Publications

1. "Tailoring pore structure and surface chemistry of microporous Alumina-Carbon Molecular Sieve Membranes (Al-CMSMs) by altering carbonization temperature for optimal gas separation performance: An investigation using low-field NMR relaxation measurements". **Luke Forster**, Carmine D'Agostino, Margot Anabell Llosa-Tanco, Vincenzo Spallina, Camilla Brencio, Fausto Gallucci, Matthew Lindley, Sarah J. Haigh, David Alfredo Pacheco-Tanaka, *Chemical Engineering Journal*, 2021, doi: https://doi.org/10.1016/j.cej.2021. (Thesis Chapter 8)

2. "Light-driven, heterogeneous organocatalysts for C-C bond formation toward valuable perfluoroalkylated intermediates". Giacomo Fillippini, Francesco Longobardo, **Luke Forster**, Alejandro Criado, Graziano Di Carmine, Lucia Nasi, Carmine D'Agostino, Michele Melchionna, Paolo Fornasiero and Maurizio Prato, *Science Advances*, 2020, **6**, eabc9923, Light-driven, heterogeneous organocatalysts for C–C bond formation toward valuable perfluoroalkylated intermediates | Science Advances (sciencemag.org), (Thesis Chapter 7).

3. "Tailoring morphology of hierarchical catalysts for tuning pore diffusion behaviour: a rational guideline exploiting bench-top pulsed-field gradient (PFG) nuclear magnetic resonance (NMR)". **Luke Forster**, Michal Lutecki, Henrik Fordsmand, Le Yu and Carmine D'Agostino, *Molecular Systems Design and Engineering*, 2020, 5, 1193-1204, Tailoring morphology of hierarchical catalysts for tuning pore diffusion behaviour: a rational guideline exploiting bench-top pulsed-field gradient (PFG) nuclear magnetic resonance (NMR) - Molecular Systems Design & Engineering (RSC Publishing) (Thesis Chapter 4).

4. "Self-diffusion of glycerol in γ-alumina nanopores. The neglected role of pore saturation in the dynamics of confined polyols". Gerardo Campos-Villalobos, Flor R. Siperstein, Carmine D'Agostino, **Luke Forster** and Alessandro Patti, *Applied Surface Science*, 2020, 516, 146089, Self-diffusion of glycerol in γ-alumina nanopores. The neglected role of pore saturation in the dynamics of confined polyalcohols - ScienceDirect (Not included in thesis)

5. "Creation of Al-Enriched Mesoporous ZSM-5 Nanoboxes with High Catalytic Activity: Converting Tetrahedral Extra-Framework Al into Framework Sites by Post Treatment".

Yilai Jiao, **Luke Forster**, Shaojun Xu, Huanhao Chen, Jingfeng Han, Xuqing Liu, Yangtao Zhou, Jinmin Liu, Jinsong Zhang, Jihong Yu, Carmine D'Agostino and Xiaolei Fan, *Angewandte Chemie*, 2020, 132, 2-11, Creation of Al-Enriched Mesoporous ZSM-5 Nanoboxes with High Catalytic Activity: Converting Tetrahedral Extra-Framework Al into Framework Sites by Post Treatment - Jiao - 2020 - Angewandte Chemie - Wiley Online Library (Thesis Chapter 5).

6. "Solvent Effects in the Homogeneous Catalytic Reduction of Propionaldehyde with Aluminium Isopropoxide Catalyst: New Insights from PFG NMR and NMR Relaxation Studies". Atika Muhammad, Graziano Di Carmine**, Luke Forster** and Carmine D'Agostino, *ChemPhysChem*, 2020, 21, 1-7, Solvent Effects in the Homogeneous Catalytic Reduction of Propionaldehyde with Aluminium Isopropoxide Catalyst: New Insights from PFG NMR and NMR Relaxation Studies - Muhammad - 2020 - ChemPhysChem - Wiley Online Library (Not included in thesis).

7. "Alkaline Pre-treatment of Walnut Shells Increases Pore Surface Hydrophilicity of Derived Biochars". Meredith Rose Barr, **Luke Forster**, Carmine D'Agostino and Roberto Volpe, *Applied Surface Science¸* 2022, 571, 151253, Alkaline pretreatment of walnut shells increases pore surface hydrophilicity of derived biochars | Elsevier Enhanced Reader (Not included in thesis).

Conference presentations

1. "Tailoring morphology of hierarchical catalysts for tuning pore diffusion behaviour: a rational guideline exploiting bench-top pulsed-field gradient (PFG) nuclear magnetic resonance (NMR)". **Luke Forster**, Michal Lutecki, Henrik Fordsmand, Le Yu and Carmine D'Agostino, *15th International Conference on Materials Chemistry (MC15)*, 2021.

2. "Tailoring morphology of hierarchical catalysts for tuning pore diffusion behaviour: a rational guideline exploiting bench-top pulsed-field gradient (PFG) nuclear magnetic resonance (NMR)". **Luke Forster**, Michal Lutecki, Henrik Fordsmand, Le Yu and Carmine D'Agostino, *Junior Moulton Medal Award Webinar*, 2021.

3. "Tailoring morphology of hierarchical catalysts for tuning pore diffusion behaviour: a rational guideline exploiting bench-top pulsed-field gradient (PFG) nuclear magnetic resonance (NMR)". **Luke Forster**, Michal Lutecki, Henrik Fordsmand, Le Yu and Carmine D'Agostino, *11th International Conference on Environmental Catalysis*, Manchester, UK, 2020.

4. "Studying Mass Transport and Surface Adsorption in Porous Catalytic Materials Using Low Field NMR Spectroscopy". *UK Catalysis Conference*, Loughborough, UK, 2020.

Abstract

Catalytic processes are important and widely studied chemical processes aimed at making chemical reactions as efficient and environmentally friendly as possible. Heterogeneous catalysis involves the use of a generally highly porous, solid catalytic material with liquid or gaseous reactant molecules. Two important factors determining the overall performance of a heterogeneous catalytic material are the interactions of any species present during the process with the catalyst surface and the mass transport of said species through the porous network of the catalytic materials. Therefore, it is desirable to tailor the surface chemistry and pore structures of catalytic materials to exploit these factors and give catalytic materials with increased performance. An overview of the impact of mass transport and reactant-catalyst surface interactions are given in Chapter 1.

In this thesis, Nuclear Magnetic Resonance (NMR) methods, amongst others, are used to quantitatively characterise mass transport through the pores of catalytic materials and also probe the strength of surface interactions between guest molecules and the solid surface. Pulsed-Field Gradient (PFG)-NMR and NMR relaxation are used to study diffusion and molecular dynamics of relevant molecules in the pores of porous materials with a particular focus on catalytic materials. As such an outline of such NMR methods are given in Chapter 2 as well as an evaluation and comparison of other methods used for the same purpose.

Declaration

No portion of the work referred to in the thesis has been submitted in support of an application for another degree or qualification of this or any other university or other institute of learning

Copyright Statement

- The author of this thesis (including any appendices and/or schedules to this thesis) owns certain copyright or related rights in it (the "Copyright") and he has given the University of Manchester certain rights to use such Copyright, including for administrative purposes.

- Copies of this thesis, either in full or in extracts and whether in hard or electronic copy, may be made only in accordance with the Copyright, Designs and Patents Act 1988 (as amended) and regulations issued under it or, where appropriate, in accordance with licensing agreements which the University has from time to time. This page must form part of any such copies made

- The ownership of certain Copyright, patents, designs, trademarks and other intellectual property (the "Intellectual Property") and any reproductions of copyright works in the thesis, for example graphs and tables ("Reproductions"), which may be described in this thesis, may not be owned by the author and may be owned by third parties. Such Intellectual Property and Reproductions cannot and must not be made available for use without the prior written permission of the owner(s) of the relevant Intellectual Property and/or Reproductions.

- **iv.** Further information on the conditions under which disclosure, publication and commercialisation of this thesis, the Copyright and any Intellectual Property and/or Reproductions described in it may take place is available in the University IP Policy (see http://documents.manchester.ac.uk/DocuInfo.aspx?DocID=2442 0), in any relevant Thesis restriction declarations deposited in the University Library, the University Library's regulations (see http://www.library.manchester.ac.uk/about/regulations/) and in the University's policy on Presentation of Theses.

Acknowledgements

First and foremost, I would like to thank my supervisors, Dr. Carmine D'Agostino and Prof. Chris Hardacre for providing me with the opportunity to join the Catalysis and Porous Materials Research Group which has truly been the perfect place to carry out my research. Particularly, I would like to thank Carmine for all of the invaluable guidance and advice he has given throughout the past 3 years and always in the friendliest manner. He has been the ideal supervisor and it is very much appreciated.

I would like to express my thanks to all of my colleagues in the Catalysis and Porous Materials Research Group for making my time spent in the group as happy and positive as can be during difficult times. Especially, I would like to thank Dr. Sarayute Chansai and Dr. Helen Daly for all of their help, guidance and patience in training me in the various techniques I have learned and aiding my development as an independent researcher.

I would like to thank all of the people with whom I have collaborated on the works that are presented in this thesis including colleagues at Haldor Topsøe, Tecnalia, The University of Trieste, Shenyang National Laboratory for Materials Science and The University of Sheffield. My thanks go out to all of these collaborators for providing samples for the analysis and other supporting data. Without you all there would be no thesis at all and for this I am very grateful.

Of course, I would like to thank my parents, who have always provided me with the utmost support and with endless amounts of love. Without them I would not be where I am and I am eternally grateful for all they have done for me. I would also like to thank my grandparents and the rest of my family who also have always been there for me with maximum support and care.

I would like to thank all of my friends for always being there to support me and especially for all the constant laughs and good times.

Last but definitely not least, I would like to thank Laura who has always been there to support me and cheer me up after a long day. Through some of the hardest times of our lives she has been a constant positive influence in my life and always knows how to make me smile again.

Summary

In Chapter 4, PFG-NMR measurements were used to study the diffusion of guest molecules through the pores of various alumina carriers prepared using different conditions to tailor the pore size and structure. These results show that it is possible to design alumina supports with clearly defined pore sizes and structures in order to tailor the mass transport properties for specific applications by changing simple preparation conditions (i.e. temperature and mixing time).

In Chapter 5, PFG-NMR methods were then used to study the diffusion of molecules of varying kinetic diameter through the hierarchical pore structure of novel zeolites with remarkable fluid catalytic cracking performance. It is shown that the hierarchical structure of the novel zeolites alleviates mass transport limitations and increases accessibility of reactive species to the strong acidic sites within the intra-crystalline pore space. In chapters 4 and 5, the use of PFG-NMR as a powerful tool to investigate materials with hierarchical porosity is highlighted.

In Chapter 6, NMR relaxation has been used to investigate the solvent effect seen during the isomerisation of glucose by novel metal-doped zeolites. Results show that reductions in reactivity seen upon changing the solvent used are due to adsorption of the solvent molecules to catalytically active sites on the zeolite surface thereby restricting isomerisation of glucose molecules. Chapters 5 and 6 serve to highlight the importance of low field NMR methodology to investigate catalytic systems using zeolite catalysts.

In Chapter 7, NMR relaxation has also been used to characterise surface interactions in the photocatalytic C-C bond formation using solid carbon nitride prepared using a range of pre-treatment protocols. Results show that the optimal catalysts are those that limit solvent adsorption and maximise the strength of halogen bonding between the reactive species and the carbon nitride surface. Chapters 6 and 7 show the effectiveness of NMR relaxation in investigating solvent effects in catalytic reactions.

In Chapter 8, NMR relaxation is extended to investigation of porous membranes and was used to unravel the effect of altering carbon membrane preparation temperature upon the surface chemistry and pore size and structure of the resultant materials. In turn, these factors were related to the membrane CH_4/H_2O separation performance and transport mechanism. It was found that the preparation temperature significantly impacts the pore size and pore wettability which both in turn,

act to alter the membrane separation performance dependent upon the dominant transport mechanism. Chapter 8 further highlights the importance of NMR relaxation to investigate surface interactions of molecules with the surface of porous materials such as catalysts. In addition to this, Chapter 8 also highlights how such measurements can be used to gain insight into mass transport processes taking place within the pores nicely tying together the contents of all the results chapters in the thesis.

Chapter 10 outlines the impact of this thesis work through discussion of future applications based on the findings of this work. In particular, the work presented in this thesis offers insights into the measurement of diffusion in hierarchical porous materials for the purpose of material design and characterisation of such materials as well as associated processes. This work also highlights the use of NMR relaxation to characterise adsorption processes and surface interactions occurring in porous catalysts presenting, for the first time, NMR relaxation used to measure halogen bonding with a catalyst surface. Finally, this work demonstrates new NMR relaxation methods for the characterisation of porosity and wettability in microporous materials and how these factors can impact the usefulness of such materials.

Chapter 1: Introduction: Porous materials as catalyst and separation media

Catalysis is a fundamental branch of chemistry contributing to modern life as we know it. Catalysis occurs all around us, from the industrial plants manufacturing the chemical products we need to live and thrive, to the exhausts of our vehicles preventing our cities from becoming severely polluted and even to plants and our own bodies in the form of enzymes allowing reactions that enable life itself. Catalysis truly is essential to all that we do.

In industry, heterogeneous catalysts are generally the favoured method of catalysing chemical reactions as they are easily removed from reaction mixtures and are typically more thermally stable than homogenous catalysts and therefore more suitable for continuous processes. However, active sites are often difficult to identify, meaning reaction mechanisms are generally difficult to unveil whilst reaction rates may be limited by diffusion in and out of pores found on the solid catalyst surface. It is these widespread applications and many advantages of heterogeneous catalysis that make research into the development and improvement of these systems of such great importance.

Most of the current work in the area however, is focused on the role of the active metal [1-3] and the effect of the catalyst support upon catalytic performance is much more poorly understood. The catalyst support is generally considered to be a relatively cheap, inert, high surface area, often highly porous material to accommodate catalytically active sites but its role in a catalyst's performance is generally neglected. Nevertheless, the support accounts for a significantly large proportion of the makeup of the whole catalyst and as such, it is vital that the role of the heterogeneous catalyst support is fully investigated and understood to allow for the optimal performance of catalytic systems. This work aims to investigate the influence of the support in catalytic systems to determine how the surface and structure of the support can be effectively altered to maximise catalyst performance.

1.1. Strong metal support interactions

The effect of the support in altering activity and selectivity in catalytic reactions is generally thought to be dominated by the presence of strong metal support interactions (SMSI). SMSIs generally arise from the use of metal nanoparticles supported on reducible metal oxide supports and favourable interactions between the active metal and the support can greatly enhance catalytic

activity. [4] This can occur through one of three effects: an electronic effect, a geometric effect or a bifunctional effect, where the metal and support provide separate but synergistic reaction sites. Electronic and geometric effects are typically quantified using X-ray photoelectron spectroscopy (XPS) to look for peak shifts indicating changes in charge or electron density (electronic effect) [5, 6] or the formation of new species, bonds and changes in bond lengths (geometric effect). [7] Temperature Programmed Desorption (TPD), Fourier Transform Infrared Spectroscopy (FTIR) and Raman spectroscopy have been used to quantify bifunctional effects by indicating the reduction of species or the formation of new species altogether. [8, 9]

An example of SMSI has been found to occur in the selective hydrogenation of furfural over supported Pd catalysts. It has been reported that furfural shows an increased selectivity to tetrahydrofurfuryl alcohol (THFA) when Pd is supported on TiO_2 or Al_2O_3 as opposed to other supports. [10] Further work has shown that a physical mixture of Pd/Al_2O_3 and Ru/ZrO_2 gives the total hydrogenation product, tetrahydrofurfuryl alcohol, in very high yield, with the Pd catalyst responsible for ring hydrogenation and the Ru catalyst responsible for carbonyl hydrogenation with a clear support dependent promotion effect present for both catalyst when compared to with other supports. [11] These works show a good example of SMSI and how this can be utilised to achieve high conversions and selectivities, however, the exact understanding of why or how the supports enhance these reactions is still unclear.

SMSIs can also be seen in the selective hydrogenation of various nitroaromatics over Au/TiO_2. In this reaction, 3-nitrostyrene adsorbs onto the TiO_2 surface preferentially through the nitro group to give the corresponding aniline with the alkene group being unaffected. With other supports complete hydrogenation of both groups occurred implying a large contribution to the reaction selectivity from the support. [12] Further studies upon the selective hydrogenation of 3-nitrostyrene found that for Pt supported catalysts, alumina and carbon supports resulted in reduction of both the alkene and nitro groups whereas when reducible supports were used only the nitro group was reduced with ZnO showing the highest selectivity to the aniline. [13] Nonetheless, Pt/C catalysts have recently found use in the selective hydrogenation of 3-nitrostyrene by utilising a variation in reduction temperature with a simple pre-treatment. At lower reduction temperatures, the vinyl group is preferentially reduced due to the presence of surface acidic groups next to the metal active sites which adsorb NO_2 strongly and thereby enhance reactivity of the alkene. At high

temperatures, P species introduced in the pre-treatment form and interact with Pt to form $Pt\text{-}PO_x$ species which can adsorb and reduce the NO_2 group selectively. [14]

Similar favourable metal support interactions are seen in the selective hydrogenation of cinnamaldehyde, [15] citral, [16] acetophenone, [17] 4-phenyl-2-butanone [18] and p-chloronitrobenzene. [19]

1.2. Influence of catalyst wettability

Catalyst supports can work to enhance and alter catalytic reactions in more ways than by just interacting with the metal active site by SMSIs. Catalyst supports are generally considered to be otherwise inert, however, it has been shown that certain properties, pre-treatments and modifications applied to catalyst supports can greatly affect reactions involving heterogeneous catalysts. One such support property that has been shown to be of great importance is the wettability of the surface and this is due to the interactions of water with catalyst surfaces seen in many common catalytic reactions. [20]

The surface wettability is thought to aid catalyst performance by many methods; enriching the concentration of reactants at the catalyst surface and thereby enhancing catalyst activity, inhibiting side reactions therefore giving only desirable products and by reducing poisoning of active sites to increase stability of the catalyst. [21] In addition to this, surface wettability can act to increase the fast diffusion of products to shift the reaction balance and even to form new reaction intermediates. [22]

The enrichment of reactants due to surface wettability is reported to occur in the oxidation of hexane, hexene and benzyl alcohol with H_2O_2 over the hydrophilic zeolite catalyst, H-TS-1. The catalytic activity is enhanced by the increased number of hydroxyl groups on the hydrophilic catalyst surface after being subject to a calcination treatment which enriches the concentration of H_2O_2 in the micropores and causes an increase in activity. [23]

Due to the effectiveness of altering surface wettability to enhance catalytic reactions many different methods have been developed to tune the hydrophilicity/hydrophobicity of supports. Methods to alter surface wettability that have been reported include, but are not limited to; physical mixtures of hydrophilic and hydrophobic catalyst particles, [24] encapsulating catalyst particles in zeolite sheaths with controllable wettabilities, [25] doping the support with zirconia causing a favourable interaction between ZnO crystals and Ru particles which increases catalytic activity [26]

and the chemical modification of surfaces by addition of groups with desirable functionalities. [27,] [28] It has been shown that the wettability can be finely tuned by varying the chain length and functionality of these added groups and silanes are usually the preferred choice for this type of surface modification. [29] Catalysts with modified wettability have been shown to be of use in a wide range of reactions such as; oxidations, [30] biofuel upgrading, [31] dehydrogenative organosilane coupling, [32] and dehydrogenation reactions. [33]

The fine tuning of surface wettability has presented some very interesting results in certain reactions. Indeed, it has been reported that for the oxidation of ethylbenzene over a hydrophilic Co/SiO_2 catalyst a low activity was seen with the major product being acetophenone. However, when the catalyst was designed to instead be hydrophobic, activity drastically increased with a high selectivity to acetophenone. [34]

More recently, the surface wettability has been shown to play a part in determining the reaction pathway during wet air oxidation over Pt and Ru nanoparticles. It is reported that Pt nanoparticles show increased activity when the support is hydrophobic yet Ru nanoparticles are more active when the support is hydrophilic [35] which is thought to be due to a change in the mass transfer properties of O_2 gas therefore overcoming the limitation of the realtively low solubility of O_2 in the condensed aqueous phase. This effect is theorised to be dependent on the metal active sites therefore explaining the difference in behaviour for Pt and Ru catalysts.

Particularly interesting results are seen in the hydrogenation of various nitroaromatics using Pd immobilized on a metal organic framework (MOF). A hydrophobic polydimethylsiloxane (PDMS) coating was applied and both coated and uncoated catalysts were tested for the hydrogenation of both hydrophobic nitrobenzene and hydrophilic 4-nitrophenol. It was reported that the uncoated catalyst showed a higher activity for the hydrogenation of 4-nitrophenol than for nitrobenzene. However, when the hydrophobic coated Pd/MOF was used, the reaction rate was much quicker for nitrobenzene and no hydrogenation occurred for the hydrophilic 4-nitrophenol. [36] Further to this work, Pd/MOF was coated in hydrophilic graphene oxide (GO) which can be selectively reduced to hydrophilic reduced graphene oxide (rGO) in order to alter the wettability of the catalyst to varying degrees. GO was found to enhance hydrogenation of hydrophilic reactants and rGO was found to enhance the hydrogenation of hydrophobic reactants by enhancing the adsorption and transfer of desirable reactants whilst still maintaining size selectivity. [37] The ability of this coating to impart tuneable wettability makes this a finding of great interest. Clearly, the surface wettability

of catalysts is essential to the efficient performance of catalytic systems and is essential to consider for the development of highly active and selective catalysts.

1.3. Catalyst surface modifications

The surface wettability of a catalyst has been identified as a key property in designing efficient catalysts. To utilise this property, different techniques to manipulate the surface chemistry and therefore influence the surface properties have been developed. One of the most common methods of modifying a catalyst surface is by silylation (Figure 1.1). Addition of silyl groups to a surface allows for the fine tuning of surface properties.

OH   **OH**   **OH**   **3 Si(OR)$_4$**   **OSiR$_3$**   **OSiR$_3$**   **OSiR$_3$**
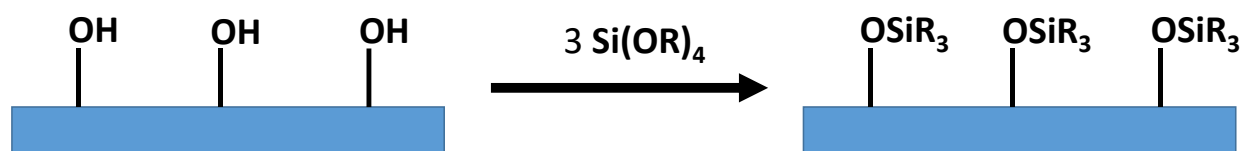
Figure 1.1. A standard silylation of a catalytic material by reaction of a silicate ester with hydroxyl groups present on the catalyst surface. The R groups can be varied accordingly to alter the chemical properties of the catalyst surface.

As previously discussed, silylation can be used to effectively alter the hydrophilicity of a catalyst thereby enhancing activity and selectivity due to changes in the adsorption interactions of reactants/products with the surface. [36-38] However, silylation has been shown to alter catalytic reactions in different ways. Indeed, it has been reported that large silyl groups can block the pores of some porous materials and reduce catalyst activity [39] and it has been shown in the methanation reaction over Ru/SiO$_2$ that silylation reduces CO adsorption affinity and therefore it increases methanation rate as CO acts as an inhibitor to this reaction. [40] Intriguingly, this steric blocking by silyl groups has recently been used to alter the selectivity of phenol hydrogenation by blocking coordinatively unsaturated sites on a Rh/SiO$_2$ catalyst. These sites, found on steps and kinks, are thought to be the active site for the direct conversion to cyclohexanol, therefore blocking these sites causes selectivity to cyclohexanone to increase. [41]

Functionalization of catalyst surfaces with amines is another attractive method to enhance catalyst performance. Recently, a bimetallic PdAg catalyst supported on a phenylamine functionalized mesoporous carbon was used to achieve the highly efficient conversion of carbon dioxide and hydrogen to give formic acid. The reaction was shown to be reversible depending on the reaction pH and rather interestingly, the phenylamine groups were found to promote both the backwards

and forwards reactions due to an increased dispersion of the metallic nanoparticles, increased stability of reaction intermediates and promotion of O-H bond dissociation in the reverse reaction. [42] A similar interaction between support and intermediates can be seen in the selective hydrogenation of furfural to tetrahydrofurfuryl alcohol by Pd nanoparticles supported on an amine functionalized MOF. The amine groups on the support hydrogen bond to the intermediate furfuryl alcohol allowing further reduction of the ring to produce the final product. [43]

Addition of amine functionality to catalyst surfaces can have additional benefits such as that seen in the reduction of bromate over amine functionalized Pt catalysts. In this reaction, the positive surface charge of the amine groups interact with the negative bromate ions and increase adsorption and subsequently catalyst activity. [44]

Coating a catalyst in a substance is seen as another effective way to change the surface properties and hence alter the reactivity of a catalyst. Subjecting a supported Pd catalyst to a pre-treatment of acetylene causes a hydrophobic trans-polyacetylene layer to form on the surface which protects Pd nanoparticles from sintering whilst boosting activity for the hydrogenation of hydrophobic substrates although a thick coating can reduce activity by blocking active sites. [45] Also, coating of a Ni catalyst in an ionic liquid has been shown to drastically increase the selectivity of the partial hydrogenation product butene in the hydrogenation of 1, 3-butadiene and this is thought to be due to a donation of electrons from the ionic liquid to the Ni sites as well as the solubility differences between reactants and products in the ionic liquid. [46] Similar work has shown that coating a variety of supports with polydopamine (PDA) or carboxylic acids layers prior to loading of Pd nanoparticles can greatly enhance activity by giving a greater dispersion of the metal. The PDA layer is thought to achieve this by introducing binding and adsorption sites for Pd whereas the carboxylic acid monolayer improves electrostatic interactions between Pd and the support. [47]

An interesting example of pre-treatments affecting the selectivity of a reaction can be seen in the selective hydrogenation of citral over Pt/TiO$_2$. It has been shown that subjecting the catalyst to a pre-treatment with H$_2$ gas greatly enhances the selectivity of the reaction to the alcohol as reduction of the titania support causes an SMSI to occur and oxygen vacancies form. These vacancies are thought to be the active site for reduction of the carbonyl bond therefore the alcohol is favoured after a pre-treatment with H$_2$. [48]

However, it is usually the case that although a change in catalyst activity is seen upon modifying the surface, the exact reason for this enhancement is poorly understood. [49] To gain a better

understanding of the interactions by which support modifications change reactivity is one of the main aims of this project.

1.4. Solvent effects in heterogeneous catalysis

A catalyst surface will not only interact with reactants and products during the reaction process, consequently, the interaction of the catalyst with the reaction solvent is important to consider. The nature of the solvent can have a profound effect upon both the activity and selectivity of certain reactions and is widely researched and developed in homogenous catalysis. [50] Indeed, it has been shown that solvent effects have a significant effect upon many heterogeneous catalytic reactions and solvent effects have been seen in hydrogenation reactions, [51-54] oxidations, [55-58] epoxidations [59] and dechlorinations [60] amongst others. However, the interactions between the solvent and surface are up to now, relatively poorly understood.

A clear solvent effect can be seen in the selective hydrogenation of acetophenone over silica supported catalysts and this solvent effect has been well studied. Carrying out this reaction over Cu/SiO_2 in different solvents gave differing initial rates of conversion in the order: Isopropyl alcohol (IPA) > cyclohexane > toluene > benzene. This is explained by the strong adsorption of toluene and benzene which strongly interact with and block Cu active sites thereby limiting the number of active sites available to dissociate hydrogen. IPA can dissociate on Cu active sites to give extra atomic hydrogen, therefore the rate is fastest when IPA is used as reaction solvent. [61]

Carrying out this reaction over a Ni/SiO_2 catalyst in a variety of protic, aprotic and apolar solvents gave similar interesting results with protic polar solvents giving the highest activity and apolar solvents the lowest. Activity in aprotic and apolar solvents was explained by considering the solvent-catalyst interactions and rate decreased with increased adsorption of solvent on the surface whilst in protic solvents the activity decreased with solvent H-bond ability which reduces adsorption of acetophenone. [62] Further studies into these two systems as well as the same reaction using Co/SiO_2 revealed that, for this reaction, the solvent effect is support dependent although the magnitude of the effect is dependent upon the nature of the metal. [63]

A study of this reaction using Rh/C and Rh/Al_2O_3, showed that both catalysts showed opposite solvent effects in terms of initial reaction rate and this is thought to be due to the respective hydrophobicity and hydrophilicity of the catalyst surfaces. [64] Further studies on this reaction using analogous Pd catalysts proved that these effects are also support dependent. The carbon support

conversion values correlate well with the solvents hydrogen bond donor ability due to the reactant-solvent interaction with the carbonyl bond whereas the alumina support conversion values correlate well with the solvents hydrogen acceptor ability and this is thought to be due to solvent-catalyst interactions resulting in blocking of the catalyst active sites. [65] Similar solvent effects have been seen in the selective hydrogenation of acetophenone over Raney nickel, [66] molecular sieve supported silver catalysts [67] and the hydrogenation of p-chloronitrobenzene. [68]

An interesting combination of both support modifications and solvent effects has been reported in the hydrogenation of acetophenone over Ru supported on an amine functionalized polymer in a biphasic isooctane/water solvent system. In this system, isooctane solvates the phenyl ring and promotes interaction of the carbonyl bond with the active site whilst water makes the surface hydrophilic to further enhance the reaction with hydrophilic acetophenone. In addition to this, steric effects of the polymer chains cause the reactant to orientate favourably for carbonyl reduction. [69]

It has also been shown how a change in solvent can completely change the selectivity of a given reaction. The hydrogenation of furfural over a bimetallic CuNi catalyst in ethanol has been shown to produce tetrahydrofurfuryl alcohol at a high selectivity. However, by simply switching the reaction solvent to methanol, the reaction will produce furfuryl alcohol at a high selectivity and this thought to be due to methanol adsorbing to and blocking the active sites for ring hydrogenation. [70] Similarly, the selective hydrogenation of cinnamaldehyde over Pd/C in all of the solvents tested except pyridine and 4-methylpyridine produced hydrocinnamaldehyde as the main product at a high rate which increases with solvent polarity whereas in pyridine and 4-methylpyridine the main product is cinnamyl alcohol produced at a much slower rate and this is again thought to be due to these solvents blocking the active sites for ring hydrogenation. [71]

1.5. Altering catalyst morphology and pore structures

Heterogeneous catalysts and associated catalytic processes are, of course, defined not only by the interactions of the respective species involved with the catalytic active sites on the catalyst surface. The ability of desired molecules to access these active sites on the catalyst surface and indeed, the ability to restrict access of undesired molecules is vitally important to the design of effective catalytic materials. That is, it is not enough to only tailor the surface of the catalysts appropriately

for a given system but also the pore structure must be designed in a way to maximise the transfer of species to the catalyst surface and optimise the efficiency of catalytic processes occurring.
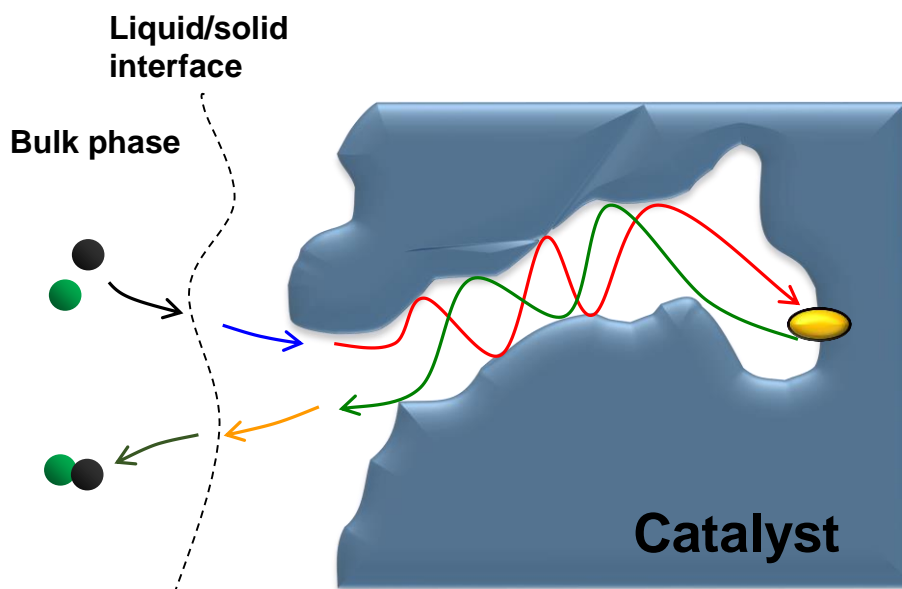
Figure 1.2. Mass transport process taking place in a porous catalyst. The reactants diffuse from the bulk phase into the catalyst pores where the catalytically active sites can be found. The pore structure and surface chemistry must be appropriately tailored to maximise catalytic activity.

Previous works have shown that alterations of the catalyst pore structures is an effective method of altering both the catalytic activity and selectivity. [72] Indeed, catalytic activity has been shown to vary significantly for a range of Ni/CeO_2 catalysts used for CO_2 methanation dependent upon the CeO_2 morphology. [73] A similar morphology dependant catalytic activity is seen in a range of TiO_2-Al_2O_3 composite support NiMo desulfurization catalysts. [74]

The addition of secondary pore networks to catalytic materials is a common method of altering a catalysts activity by changing its pore structure. The activity of a Ni-CaO_2-ZrO_2 catalyst for CO_2 reforming of CH_4 was shown to vary greatly dependent upon the pore structure of the catalyst. Ni-CaO_2-ZrO_2 with a mesoporous framework showed the greatest activity and stability and also was not deactivated after use. [75] This was due to a "confine effect" preventing Ni sintering and giving an improved resistance to coking. [75] Furthermore, mesoporous channels of varying size and uniformity were formed in a series of Ce-Co catalysts by altering the molar amount of Ce and Co to form lattice defects and expose surface active sites. [76] These catalysts were then tested for mercury oxidation processes. It was found that those catalysts with unequal molar amounts of Ce and Co were less active due to low mass transfer owing to non-uniform mesopores and low surface

areas. [76] The addition of a secondary mesoporous pore structure has also been shown to increase the performance of metal organic framework (MOF) based catalysts used for the hydrogenation of nitro compounds. [77]

Although less reported than changes in activity, it is possible for an alteration of the catalyst structure to result in changes in the reaction selectivity. The shape dependence of selective H_2S oxidation over ceria nanocrystals was investigated and it was found that the hierarchical porous structure, that is the pore structure consists of types of pores of two or more sizes, hindered SO_2 and sulfate formation thereby giving an increased selectivity to sulphur, the desired product. [78] Hollow multishelled structures (HoMSs), namely Au/CeO_2 HoMSs, have also been reported to show a pore structure dependent selectivity for the catalysed reduction of nitrophenol. [79, 80]

This method of introducing a hierarchical porous network into the structure of a catalytic material is one that finds much use in the field of zeolite catalysis. A relatively large, secondary series of pores is introduced into the zeolite structure that is highly interconnected with the existing pores in the zeolite crystal. This highly interconnected porosity acts to enhance diffusion of species within the zeolite pores and reduce pore blocking by coking thereby increasing catalytic performance and longevity respectively. [81] However, the catalytic mechanisms associated with hierarchical zeolite catalysts are not yet fully understood and remain the subject of much interest. Recent work from Zhou et al stresses the importance of mesopore surface diffusion acting to limit mass transfer in hierarchical zeolites and theorises that, for optimal catalytic performance, the zeolite surface should be modified to reduce surface interactions and therefore limit surface diffusion. [82] Nonetheless, the use of hierarchical porous structures has enabled the creation of many different zeolite catalysts capable of increased catalytic activity and selectivity for many processes. [83-87] This approach has also been applied to other catalytic materials with similar results. [88-91]

1.6. Porous materials as separation media

Porous materials are also widely used in separation processes to allow the separation of one species from another. For example, porous materials are commonly used for the separation of different gases [92, 93] and the separation of oil/water emulsions [94] although they also find use in other separation processes.

Similarly to catalysis, as previously described, the separation performance can be greatly impacted by the morphology and pore structure of the porous medium used and the surface

interactions between the different species present during the separation process. [95] For example, the wettability, and therefore the interaction between the surface and water present, is essential to determining optimal separation performance in oil/water emulsion separation. [96]

1.7. Studying surface interactions in catalysis using NMR

NMR spectroscopy, in particular (PFG)-NMR, continues to be incredibly useful to the design of heterogeneous catalysts, [97, 98] their characterisation [99] and studying their deactivation. [100, 101] Using NMR to study catalytic materials can provide valuable information to aid the design of more active and efficient catalytic systems.

The molecular dynamics of reactants and solvents interacting with the catalyst surface continue to be of great importance to the design of heterogeneous catalytic systems and these interactions are something that can be simply and effectively studied by NMR techniques. Indeed, it has been shown that NMR relaxation time measurements can be used to characterise the adsorption strengths of reactants with the catalyst surface. [102] By comparison of these adsorption strengths for both the reactant and solvents, the solvent effects seen in the liquid phase oxidations of both 1,4-butanediol [55, 56] and various 1,3-propanediols [57] have been explained using NMR relaxation measurements and therefore the optimal solvent in which to carry out these reactions can be identified. Recently, NMR relaxation measurements have also shown that oxygenated heterocyclic compounds form Lewis acid-base pairs with sites on the surface of TiO_2 and therefore inhibit catalyst activity [103] showing that non oxygenated solvents such as cyclohexane are preferable for reactions using this support.

NMR relaxation measurements are not limited to investigating only the effects of solvents. It has been shown that in the oxidation of glycerol over Au/TiO_2, the reaction products inhibit the reaction thereby limiting the catalytic activity. [104]

Finally, and crucial to this project, (PFG)-NMR and NMR relaxation measurements can be used to characterise and probe the effects of modifications upon a surface upon the adsorption of reactants. Recent work has shown that use of a polymer modified with sulfonic acid groups enhanced the adsorption of pyridine from aqueous solutions [105] and determination of the self-diffusivity coefficient of pyridine over both the modified and unmodified surface allows the effect of the surface modification to be fully quantified. This technique can be applied to reactions involving heterogeneous catalysts. Indeed, work from Robinson et al, [106] has shown that coating

various catalyst supports with a layer of silanes can significantly increase the motional freedom of adsorbed liquid methanol by replacing hydroxyl groups on the surface preventing interactions of the surface with the hydroxyl group of methanol as well as detailing a general method to use NMR to study more general cases of surface functionalisation.

References

1. L. Liu, F. Gao, P. Concepcion and A. Corma, *J. Catal.*, 2017, **350**, 218-225.

2. Z. L. Zhang, Y. H. Zhu, H. Asakura, B. Zhang, J. G. Zhang, M. X. Zhou, Y. Han, T. Tanaka, A. Q. Wang, T. Zhang and N. Yan, *Nat. Commun.*, 2017, **8**, 10.

3. L. C. Liu and A. Corma, *Chem. Rev.*, 2018, **118**, 4981-5079.

4. C. Pan, M. Tsai, W. Su, J. Rick, N. Akalework, A. Agegnehu, S. Cheng and B. Hwang, *J. Taiwan Inst. Chem. Eng.*, 2017, **74**, 154-186.

5. J. Ohyama, A. Yamamoto, K. Teramura, T. Shishido and T. Tanaka, *ACS Catal.*, 2011, **1 (3)**, 187-192.

6. J-H. Kim, S. Chang and Y-T. Kim, *Appl. Catal. B*, 2014, **158-159**, 112-118.

7. Q. Fu, T. Wagner, S. Olliges and H-D. Carstanjen, *J. Phys. Chem. B*, 2004, **109 (2)**, 944-951.

8. P. Panagiotopoulou, A. Christodoukalis, D. I. Kondarides and S. Boghosian, *J. Catal.*, 2006, **240 (2)**, 114-125.

9. P. Panagiotopoulou and D. I. Kondarides, *Appl. Catal. B, 2011*, **101 (3-4)**, 738-746.

10. R. Albilali, M. Douthwaite, Q. He and S. Taylor, *Catal. Sci. Technol.*, 2018, **8**, 252-267.

11. R. J. Huang, Q. Q. Cui, Q. Q. Yuan, H. H. Wu, Y. J. Guan and P. Wu, *ACS Sustain. Chem. Eng.*, 2018, **6**, 6957-6964.

12. M. Boronat, P. Concepcion, A. Corma, S. Gonzalez, F. Illas and P. Serna, *J. Am. Chem. Soc.*, 2007, **129**, 16230-16237.

13. C. Berguerand, A. Yarulin, F. Cardenas-Lizana, J. Warna, E. Sulman, D. Murzin and L. Kiwi-Minsker, *Ind. Eng. Chem. Res.*, 2015, **54**, 8659-8669.

14. Q. Wu, B. Zhang, C. Zhang, X. Meng, X. Su, S. Jiang, R. Shi, Y. Li, W. Lin, M. Arai, H. Cheng and F. Zhao, *J. Catal.*, 2018, **364**, 297-307.

15. C. M. Piqueras, V. Gutierrez, D. A. Vega and M. A. Volpe, *Appl. Catal. A*, 2013, **467**, 253-260.

16. P. Reyes, H. Rojas, G. Pecchi and J. Fierro, *J. Mol. Catal. A Chem.*, 2002, **179**, 293-299.

17. Y. Z. Xiang, Y. A. Lv, T. Y. Xu, X. N. Li and J. G. Wang, *J. Mol. Catal. A Chem.*, 2011, **351**, 70-75.

18.   S. Wilkinson, I. McManus, H. Daly, J. Thompson, C. Hardacre, N. Bonab, J. ten Dam, M. Simmons, C. D'Agostino, J. McGregor, L. Gladden and E. Stitt, *J. Catal.*, 2015, **330**, 362-373.

19.   Y. T. Tsu and Y. W. Chen, *J. Nanosci. Nanotechnol.*, 2018, **18**, 301-308.

20.   P. Davies, *Top. Catal.*, 2016, **59**, 671-677.

21.   L. Wang and F. Xiao, *ChemCatChem*, 2014, **6**, 3048-3052.

22.   L. Wang and F. Xiao, *Sci. China Mater.*, 2018, **61**, 1137-1142.

23.   L. Wang, J. Sun, X. Meng, W. Zhang, J. Zhang, S. Pan, Z. Shen and F. Xiao, *ChemComm*, 2014, **50**, 2012-2014.

24.   C. Franch, R. Lammertink and L. Lefferts, *Appl. Catal. B*, 2014, **156**, 166-172.

25.   Z. Jin, L. Wang, Q. Hu, L. Zhang, S. Xu, X. Dong, X. Gao, R. Ma, X. Meng and F. Xiao, *ACS Catal.*, 2018, **8**, 5250-5254.

26.   H. G. Liao, D. H. Ouyang, J. Zhang, Y. J. Xiao, P. L. Liu, F. Hao, K. Y. You and H. Luo, *Chem. Eng. J.*, 2014, **243**, 207-216.

27.   F. Liu, K. Huang, A. Zheng, F. Xiao and S. Dai, *ACS Catal.*, 2018, **8**, 372-391.

28.   L. Vanyorek, E. Sikora, A. Kiss, A. Sike, Z. G. Hutkai, P. Pekker, B. Viskolcz and B. Fiser, *React. Kinet. Mech. Catal.*, 2018, **125**, 37-46.

29.   L. Fu, S. Li, Z. Han, H. Liu and H. Yang, *ChemComm*, 2014, **50**, 10045-10048.

30.   Q. Wang, W. Hou, S. Li, J. Xie, J. Li, Y. Zhou and J. Wang, *Green Chem.*, 2017, **19**, 3820-3830.

31.   Q. Sun, M. Chen, B. Aguila, N. Nguyen and S. Ma, *Faraday Discuss.*, 2017, **201**, 317-326.

32.   J. Lin, Q. Bi, L. Tao, T. Jiang, Y. Liu, H. He, Y. Cao and Y. Wang, *ACS Catal.*, 2017, **7**, 1720-1727.

33.   C. Wang, Z. Liu, L. Wang, X. Dong, J. Zhang, G. Wang, S. Han, X. Meng, A. Zheng and F. Xiao, *ACS Catal.*, 2018, **8**, 474-481.

34.   C. Chen, J. Xu, Q. Zhang, Y. Ma, L. Zhou and M. Wang, *ChemComm*, 2011, **47**, 1336-1338.

35.   D. Davies, S. Golunski, P. Johnston, G. Lalev and S. Taylor, *ACS Catal.*, 2018, **8**, 2730-2734.63

36.   G. Huang, Q. Yang, Q. Xu, S. Yu and H. Jiang, *Angew. Chem. Int. Ed. Engl.*, 2016, **55**, 7379-7383.

37. X. Chen, P. Qian, T. Zhang, Z. Xu, C. Fang, X. Xu, W. Chen, P. Wu, Y. Shen, S. Li, J. Wu, B. Zheng, W. Zhang and F. Huo, *ChemComm*, 2018, **54**, 3936-3939.

38. A. Quintanilla, J. Bakker, M. Kreutzer, J. Moulijn and F. Kapteijn, *J. Catal.*, 2008, **257**, 55-63.

39. A. Zola, L. da Silva, A. Moretti, A. Fraga, E. Sousa-Aguiar and P. Arroyo, *Top. Catal.*, 2016, **59**, 219-229.

40. K. Furman, D. Baudouin, T. Margossian, K. D. Sabnis, Y. R. Cui, F. H. Ribeiro and C. Coperet, *J. Catal.*, 2015, **324**, 9-13.

41. H. W. Zhang, A. Han, K. Okumura, L. X. Zhong, S. Z. Li, S. Jaenicke and G. K. Chuah, *J. Catal.*, 2018, **364**, 354-365.

42. S. Masuda, K. Mori, Y. Futamura and H. Yamashita, *ACS Catal.*, 2018, **8**, 2277-2285.

43. D. Yin, H. Ren, C. Li, J. Liu and C. Liang, *Chinese J. Catal.*, 2018, **39**, 319-326.

44. Z. Zhang, J. Cheng, Y. Luo, W. Shi, W. Wang, B. Zhang, R. Zhang, X. Bao, Y. Guo and F. Cui, *Catal. Commun.*, 2018, **105**, 11-15.

45. Y. Dai, S. J. Liu and N. F. Zheng, *J. Am. Chem. Soc.*, 2014, **136**, 5583-5586.

46. A. Jalal and A. Uzun, *Appl. Catal. A*, 2018, **562**, 321-326.

47. P. Fu, Z. Xiao, Y. Liu, L. Wang, X. Zhang and G. Li, *ChemistrySelect*, 2018, **3**, 3351-3361.

48. E. Bailon-Garcia, F. Carrasco-Marin, A. Perez-Cadenas and F. Maldonado-Hodar, *J. Catal.*, 2015, **327**, 86-95.

49. Z. B. Tian, C. Liu, Q. Y. Li, J. Y. Hou, Y. Li and S. Y. Ai, *Appl. Catal. A*, 2015, **506**, 134-142.

50. P. J. Dyson and P. G. Jessop, *Catal. Sci. Technol.*, 2016, **6**, 3302-3316.

51. H. Rojas, J. L. G. Fierro and P. Reyes, *J. Chil. Chem. Soc.*, 2007, **52**, 1155-1159.

52. P. Reyes, M. Aguirre, G. Pecchi and J. Fierro, *J. Mol. Catal. A Chem.*, 2000, **164**, 245-251.

53. B. Akpa, C. D'Agostino, L. Gladden, K. Hindle, H. Manyar, J. McGregor, R. Li, M. Neurock, N. Sinha, E. Stitt, D. Weber, J. Zeitler and D. Rooney, *J. Catal.*, 2012, **289**, 30-41.

54. L. Nikoshvili, E. Shimanskaya, A. Bykov, I. Yuranov, L. Kiwi-Minsker and E. Sulman, *Catal. Today*, 2015, **241**, 179-188.

55. C. D'Agostino, G. Brett, P. Miedziak, D. Knight, G. Hutchings, L. Gladden and M. Mantle, *Chem. -Eur. J.*, 2012, **18**, 14426-14433.

56.   C. D'Agostino, M. Feaviour, G. Brett, J. Mitchell, A. York, G. Hutchings, M. Mantle and L. Gladden, *Catal. Sci. Technol.*, 2016, **6**, 7896-7901.

57.   C. D'Agostino, T. Kotionova, J. Mitchell, P. Miedziak, D. Knight, S. Taylor, G. Hutchings, L. Gladden and M. Mantle, *Chem. -Eur. J.*, 2013, **19**, 11725-11732.

58.   S. Schunemann, F. Schuth and H. Tuysuz, *Catal. Sci. Technol.*, 2017, **7**, 5614-5624.

59.   P. Lignier, S. Mangematin, F. Morfin, J. L. Rousset and V. Caps, *Catal. Today*, 2008, **138**, 50-54.

60.   X. Z. Li, F. Qin, Q. Q. Dai, S. J. Shao and X. Y. Wang, *Res. Chem. Intermed.*, 2018, **44**, 6087-6104.

61.   N. Bertero, C. Apesteguia and A. Marchi, *Appl. Catal. A*, 2008, **349**, 100-109.

62.   N. Bertero, A. Trasarti, C. Apesteguia and A. Marchi, *Appl. Catal. A*, 2011, **394**, 228-238.

63.   A. Trasarti, N. Bertero, C. Apesteguia and A. Marchi, *Appl. Catal. A*, 2014, **475**, 282-291.

64.   H. Yoshida, Y. Onodera, S. Fujita, H. Kawamori and M. Arai, *Green Chem.*, 2015, **17**, 1877-1883.

65.   S. Fujita, Y. Onodera, H. Yoshida and M. Arai, *Green Chem.*, 2016, **18**, 4934-4940.

66.   J. Masson, P. Cividino and J. Court, *Appl. Catal. A*, 1997, **161**, 191-197.

67.   G. D. Yadav and R. K. Mewada, *Catal. Today*, 2012., **198**, 330-337.

68.   Z. Hu, S. Q. Tan, R. L. Mi, X. Li, D. Li and B. L. Yang, *Catal. Lett.*, 2018, **148**, 1490-1498.

69.   D. Duraczynska, A. Drelinkiewicz, E. Bielanska, E. M. Serwicka and L. Litynska-Dobrzynska, *Catal. Lett.*, 2011, **141**, 83-94.

70.   J. Wu, G. Gao, J. L. Li, P. Sun, X. D. Long and F. W. Li, *Appl. Catal. B*, 2017, **203**, 227-236.

71.   Y. Li, H. Cheng, W. Lin, C. Zhang, Q. Wu, F. Zhao and M. Arai, *Catal. Sci. Technol.*, 2018, **8**, 3580-3589.

72.   P. Sudarsanam, E. Peeters, E. V. Makashina, V. I. Parvulescu and B. F. Sels, *Chem. Soc. Rev.*, 2019, **48**, 2366.

73.   T. Jomjaree, P. Sintuya, A. Srifa, W. Koo-amornpattana, S. Kiatphuengporn, S. Assabumrungrat, M. Sudoh, R. Watanabe, C. Fukuhara and S. Ratchahat, *Catal. Today*, 2020, https://doi.org/10.1016/j.cattod.2020.08.010.

74. W. Zhou, L. Yang, L. Liu, Z. Chen, A. Zhou, Y. Zhang, X. He, F. Shi and Z. Zhao, *Appl. Catal. B*, 2020, **268**, 118428.

75. N. Sun, X. Wen, F. Wang, W. Wei and Y. Sun, *Energy Environ. Sci.*, 2010, **3**, 366-369.

76. X. Zhang, J. Wang, B. Tan, N. Zhang, J. Bao, and G. He, *Fuel*, 2018, **226**, 18-26.

77. F. Tang, L. Wang, G. Zhang, M. Zhang and Y. Liu, *Ind. Eng. Chem. Res.*, 2019, **58**, 5543-5551.

78. X. Zheng, Y. Li, L. Zhang, L. Shen, Y. Xiao, Y. Zhang, C. Au and L. Jiang, *Appl. Catal. B*, 2019, **252**, 98-110.

79. P. Xu, R. Yu, H. Ren, L. Zong, J. Chen and X. Xing, *Chem. Sci.*, 2014, **5**, 4221-4226.

80. J. Wang, J. Wan and D. Wang, *Acc. Chem. Res.*, 2019, **52**, 2169-2178.

81. R. Bai, Y. Song, Y. Li and J. Yu, *Trends Chem.*, 2019, **1 (6)**, 601-611.

82. J. Zhou, W. Fan, Y. Wang and Z. Xie, *Natl. Sci. Rev.*, 2020, **7 (11)**, 1630-1632.

83. J. Zhou, Y. Wang, W. Zou, C. Wang, L. Li, Z. Liu, A. Zheng, D. Kong, W. Yang and Z. Xie, *Ind. Eng. Chem. Res.*, 2017, **56**, 9310-9321.

84. D. Kerstens, B. Smeyers, J. Van Waeyenberg, Q. Zhang, J. Yu and B. F. Sels, *Adv. Mater.*, 2020, **32**, 2004690.

85. A. Chang, T. Yang, M. Chen, H. Hsiao and C. Yang, *J. Hazard. Mater.*, 2020, **400**, 123241.

86. B. Velaga and N. R. Peela, *Adv. Sustain. Syst.*, 2021, **5**, 2000205.

87. C. Zhu, D. P. Gamliel, J. A. Valla and G. M. Bollas, *Appl. Catal. B*, 2021, **284**, 119719.

88. L. Chen, Q. Wang, X. Wang, Q. Cong, H. Ma, T. Guo, S. Li and W. Li, *Chem. Eng. J.¸* 2020, **390**, 124451.

89. M. Wu, M. Cui, L. Wu, S. Hwang, C. Yang, Q. Xia, G. Zhong, H. Qiao, W. Gan, X. Wang, D. Kline, M. R. Zachariah, D. Su, T. Li and L. Hu, *Adv. Energy. Mater.*, 2020, **10**, 2001119.

90. X. Zhao, X. Yang, M. Wang, S. Hwang, S. Karakalos, M. Chen, Z. Qiao, L. Wang, B. Liu, Q. Ma, D. A. Cullen, D. Su, H. Yang, H. Zang, Z. Feng and G. Wu, *Appl. Catal. B*, 2020, **279**, 119400.

91. Y. Li, X. Zhang, Z. Peng, P. Liu and X. Cheng, *ACS Sustain. Chem. Eng.¸* 2020, **8**, 8458-8468.

92. M. Zeeshan, K. Yalcin, F. E. S. Oztuna, U. Unal, S. Keskin and A. Uzun, *Carbon*, 2021, **171,** 79-87.

93. R-B. Lin, S. Xiang, W. Zhou, B. Chen, *Chem.*, 2020, **6 (2)**, 337-363.

94.   W. Zhang, N. Liu, Y. Cao, X. Lin, Y. Liu and L. Feng, *Adv. Mater.*, 2017, **4**, 1700029.

95.   J. Fonseca and S. Choi, *Microporous Mesoporous Mater.*, 2021, **310**, 110600.

96.   C-F. Wang and L-T. Chen, *Langmuir*, 2-17, **33 (8)**, 1969-1973.

97.   K. Ralphs, C. D'Agostino, R. Burch, S. Chansai, L. Gladden, C. Hardacre, S. James, J. Mitchell and S. Taylor, *Catal. Sci. Technol.*, 2014, **4**, 531-539.

98.   J. Wang, L. Xiao, G. Liao, Y. Zhang, L. Guo, C. Arns and Z. Sun, *Sci. Rep.*, 2018, **8**.

99.   C. D'Agostino, G. Brett, G. Divitini, C. Ducati, G. Hutchings, M. Mantle and L. Gladden, *ACS Catal.*, 2017, **7**, 4235-4241.

100.   B. Zhou, Z. Liao, C. Mattea, S. Stapf, H. Jiao, L. Wang, Z. Zhuang, B. Jiang, J. Wang and Y. Yang, *Ind. Eng. Chem. Res.*, 2018, **57**, 6647-6653.

101.   C. D'Agostino, Y. Ryabenkova, P. Miedziak, S. Taylor, G. Hutchings, L. Gladden and M. Mantle, *Catal. Sci. Technol.*, 2014, **4**, 1313-1322.

102.   C. D'Agostino, J. Mitchell, M. Mantle and L. Gladden, *Chem. -Eur. J.*, 2014, **20**, 13009-13015.

103.   C. D'Agostino, R. Armstrong, G. Hutchings and L. Gladden, *ACS Catal.*, 2018, **8**, 7334-7339.

104.   Q. Zhu, G. Moggridge, M. Ainte, M. Mantle, L. Gladden and C. D'Agostino, *Chem. Eng. J.*, 2016, **306**, 67-76.

105.   N. Robinson, L. Gladden and C. D'Agostino, *Faraday Discuss.*, 2017, **204**, 439-452.

106.   L. Liu, F. Gao, P. Concepcion and A. Corma, *J. Catal.*, 2017, **350**, 218-225.

Chapter 2: Theory of NMR

In this project, nuclear magnetic resonance (NMR) will be of central importance in order to probe the interactions of liquids inside the respective materials pores. NMR will be used to obtain a greater understanding of the way reactants, products and solvents are affected by the catalyst surface composition and characteristics and how activity and selectivity to desired products can be maximized by modifications of catalyst surfaces. Therefore, a brief overview of basic NMR theory is given below.

2.1. Basic principles of NMR

2.1.1. Nuclear spins and bulk magnetisation

Nuclear magnetic resonance is a phenomenon that arises due to the quantum mechanical property known as "nuclear spin". [1] Nuclear spin is a fundamental property intrinsic to all elementary particles. Atomic nuclei act as if they are spinning about their axis resulting in a property known as nuclear spin angular momentum; **P**. Nuclear spin angular momentum generates a magnetic field and an associated magnetic moment, **μ**, in which nuclei act as magnetic bars with north and south poles. The values of the nuclear spin angular momentum, P, is quantised according to quantum mechanics and its magnitude is defined as follows:

$$P = \frac{h}{2\pi}[I(I+1)]^2 \tag{2.1}$$

Where h is the Plank constant ($h = 6.626 \times 10^{-34}$ J s) and the quantity I is the nuclear spin quantum number which describes the spin of an atomic nucleus. Every nucleus has a characteristic value of I and the nuclear spin of each nucleus will have $2I + 1$ possible orientations, denoted by the magnetic quantum number, m, which may take the values $–I, -I + 1, …, I – 1, I$. Nuclei are only NMR active if they have a non-zero value of the nuclear spin quantum number, I. The value of I is dependent upon the number of protons and neutrons that the atomic nucleus is composed of, more specifically, it depends upon the number of unpaired protons and neutrons. The rules for determining the net spin of an atomic nucleus are given below:

1) Number of protons **and** neutrons are both even $\rightarrow I = 0$
2) Number of protons **plus** number of neutrons is odd $\rightarrow I = (2n + 1)/2$
3) Number of protons **and** number of neutrons are both odd $\rightarrow I = (2n)/2$

where n is a positive integer. For example, ^{4}He, ^{12}C and ^{16}O will all be NMR inactive as they have no net spin whereas nuclei such as ^{1}H, ^{13}C and ^{19}F have $I = \frac{1}{2}$ and ^{2}H and ^{14}N have integer values of $I = 1$.

The nuclear spin angular momentum, **P**, of nuclei with a non-zero spin number is related to the associated magnetic moment as follows:

$$\mathbf{\mu} = \gamma\mathbf{P} \tag{2.2}$$

The parameter γ is known as the gyromagnetic ratio of a given nucleus. In the absence of an external magnetic field, all possible magnetic quantum states are equal in energy. When an external magnetic field of strength B_0 is applied, the magnetic moment of the nucleus acquires an energy, E, defined by:

$$E = -\mathbf{\mu} \cdot \mathbf{B}_0 = -\gamma \frac{h}{2\pi} m B_0 \tag{2.3}$$

In the presence of an external magnetic field, the nucleus will develop $2I + 1$ energy levels corresponding to the different values taken by m. Energy level transitions are quantised and as such, these transitions are governed by selection rules. The NMR selection rule governing such transitions is $\Delta m = \pm 1$. That is, the magnetic quantum number, m, must decrease or increase by 1 only. The most commonly studied NMR nuclei ^{1}H and ^{13}C have $I = \frac{1}{2}$ and therefore adopt two spin energy states with $m = -\frac{1}{2}$ and $m = \frac{1}{2}$ respectively. These two states are described as being parallel and anti-parallel and are often referred to as α-state and β-state, respectively. The α-state, or parallel orientation, is the lower energy state. The energy required to induce a transition between the two energy levels is given by:

$$\Delta E = h\nu = \left| \gamma \frac{h}{2\pi} \Delta m B_0 \right| = \gamma \frac{h}{2\pi} B_0 \tag{2.4}$$

The last equation defines the Larmor frequency of the nucleus. This is also known as the precessional frequency and refers to the rate of precession of the magnetic moment of the nucleus around the external magnetic field. The Larmor frequency is written as:

$$\nu_0 = \frac{\gamma B_0}{2\pi} \text{ [Hz] } or \ \omega_0 = \gamma B_0 \text{ [rad s}^{-1}] \tag{2.5}$$

At thermal equilibrium and in a static magnetic field, the population of the α-state and β-state obeys the Boltzmann distribution:

$$\frac{N_\beta}{N_\alpha} = e^{-\frac{\Delta E}{k_B T}} \tag{2.6}$$

Where k_B is the Boltzmann constant ($k_B = 1.380649 \, J \, K^{-1}$) and T is the temperature of the spin system. As the α-state is lower in energy, an excess of nuclear spins in the spin system will exist in the α-state. This excess can be visualised as a number of magnetic moments distributed randomly around a precessional cone, as shown in Figure 2.1.
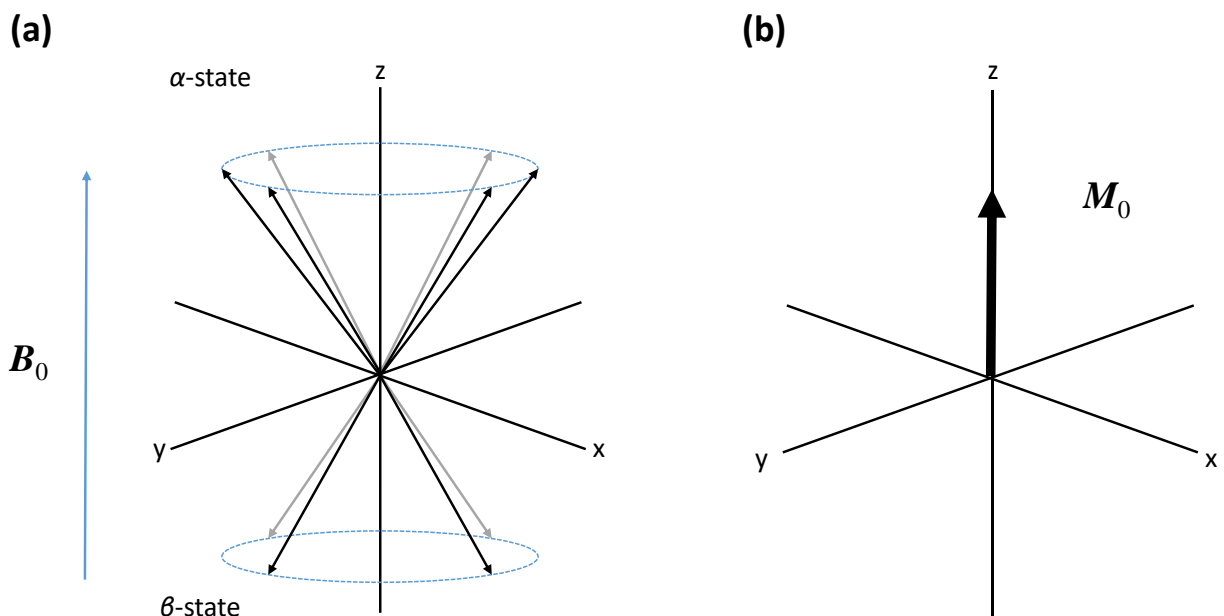
Figure 2.1. (a) Representation of the Bloch vector model showing the spins in both α and β states precessing around an external magnetic field, B_0, at the Larmor frequency, ω_0, and (b) the resultant bulk magnetisation vector.

The excess of spins in the α-state results in a net magnetisation parallel to the external magnetic field, along the z-direction. As the spins are randomly distributed about the z-axis, the net magnetisation in the transverse plane is zero. Thus, the entire spin system can be considered as a bulk magnetisation vector, M_0, aligned along the z-axis with the external magnetic field. This way of visualising spin magnetisation is known as the Bloch vector model.

2.1.2. Spin excitation and the rotating frame of reference

The earliest examples of NMR spectrometers were based on continuous-wave (CW) NMR spectroscopy. In CW NMR spectroscopy, the sample can be analysed in two different ways. Firstly, the sample can be held in a strong magnetic field whilst the frequency of the source is slowly scanned. Alternatively, the source frequency can be held constant whilst the field is

scanned. Modern day NMR spectrometers operate using Fourier Transform (FT) NMR spectroscopy where the static magnetic field, $\mathbf{B_0}$, is usually produced using a superconducting magnet cooled to cryogenic temperatures. A time-dependant magnetic field, $\mathbf{B_1}$, oscillating at the Larmor frequency is then applied to produce the quantum energy required to instigate magnetic resonance. $\mathbf{B_1}$ is generated using a transmission coil to induce a radio-frequency (RF) signal which is then applied perpendicular to $\mathbf{B_0}$ to tilt the bulk magnetisation from its equilibrium position (i.e. along the z-axis). The bulk magnetisation then relaxes back to the equilibrium position by a precessional motion thereby inducing a current in a detection coil placed around the sample. The oscillating signal produced is known as Free Induction Decay (FID). The FID, typically an exponential decay, is then Fourier transformed to give the NMR spectrum. The process can be seen in Figure 2.2.
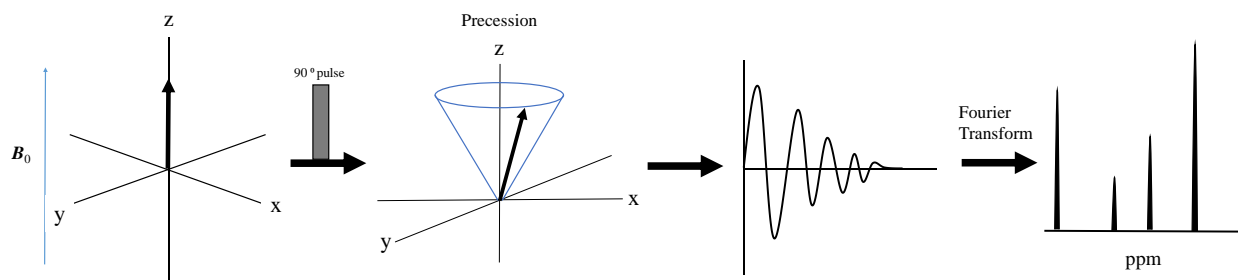
Figure 2.2. Representation of the basic NMR experiment. Spins aligned with the external magnetic field are titled into the transverse plane using a radiofrequency pulse where their precession frequencies are detected and an FID is acquired. The FID is then Fourier transformed to give the NMR spectrum.

To understand the complex interactions between the ensemble of spins within the sample immersed in the static magnetic field vector, $\mathbf{B_0}$, and experiencing an oscillating field, $\mathbf{B_1}$, it is more convenient to consider the concept of a rotating frame of reference and use a classical mechanical description to explain the behaviour of NMR active systems in an external magnetic field. As such, the magnetic moment, $\boldsymbol{\mu}$, can be defined as a vector relating the aligning torque, $\boldsymbol{\Gamma}$, to the external magnetic field, $\mathbf{B_0}$. The relationship is given by:

$$\boldsymbol{\Gamma} = \frac{d\mathbf{P}}{dt} = \boldsymbol{\mu} \times \mathbf{B_0} \qquad (2.7)$$

Where the symbol $\times$ represents the cross products of two vectors. Combining this with Equation 2.2, it follows that:

$$\frac{d\boldsymbol{\mu}}{dt} = \boldsymbol{\mu} \times \gamma \, \mathbf{B}_0 \tag{2.8}$$

The general behaviour of the bulk magnetisation vector, $\mathbf{M}_0$, can be obtained using Equation 2.8 and replacing the magnetic moment, $\boldsymbol{\mu}$, with $\mathbf{M}_0$, giving the Bloch equation:

$$\frac{d\mathbf{M}_0}{dt} = \mathbf{M}_0 \times \gamma \, \mathbf{B}_0 \tag{2.9}$$

As the RF pulse is applied, the magnetisation precesses about the static field, $\mathbf{B}_0$, and the RF field, $\mathbf{B}_1$. The field $\mathbf{B}_1$ can be viewed as two identical magnetic field vectors, rotating in opposite senses that, when summed, give a vector that mimics the oscillating field. The rotating frame of reference is when the x, y and z-axis are said to rotate at the same rate, ω_1, and in the same sense as one of the two $\mathbf{B}_1$ vectors. In a frame such as this, one $\mathbf{B}_1$ vector appears frozen with respect to the rotating coordinate axes, whilst the second appears to rotate in the opposite sense at a rate of $2\omega_1$, which is twice the rate observed in the stationary frame. This means that the angular frequency of this second component is too high to interact with the magnetisation and is not considered further. Equation 2.9 can now be transformed using the rotating frame of reference as follows:

$$\frac{d\mathbf{M}_0'}{dt} = \frac{d\mathbf{M}_0}{dt} - (\omega \times \mathbf{M}_0) \tag{2.10}$$

Where the prime symbol indicates that the quantity is in the rotating frame and ω is the angular velocity of the rotating frame. Combining Equations (2.9) and (2.10) gives the following expression:

$$\frac{d\mathbf{M}_0'}{dt} = \mathbf{M}_0 \times \gamma \left(\mathbf{B}_0 - \frac{\boldsymbol{\omega}}{\gamma} \right) = \mathbf{M}_0 \times \gamma \, \mathbf{B}_{eff} \tag{2.11}$$

Where $\mathbf{B}_{eff}$ is the field experienced by the nuclear spins as observed in the rotating frame. If the irradiation field, $\mathbf{B}_1$, is applied in the plane perpendicular to the static field, $\mathbf{B}_0$. Hence, the effective magnetic field, $\mathbf{B}_{eff}$, is given by:

$$\mathbf{B}_{eff} = \left[\left(B_0 - \frac{\omega_1}{\gamma} \right) \mathbf{k} \right] + (B_1 \, \mathbf{i}) \tag{2.12}$$

It is important to note that if ω_1 is equal to ω_0 (the Larmor frequency) then $\mathbf{M}_0$ will precess around $\mathbf{B}_1$ only. Therefore, when the situation is viewed using the rotating frame of reference rotating at the Larmor frequency, only the motion caused by the RF pulse is required to be considered.
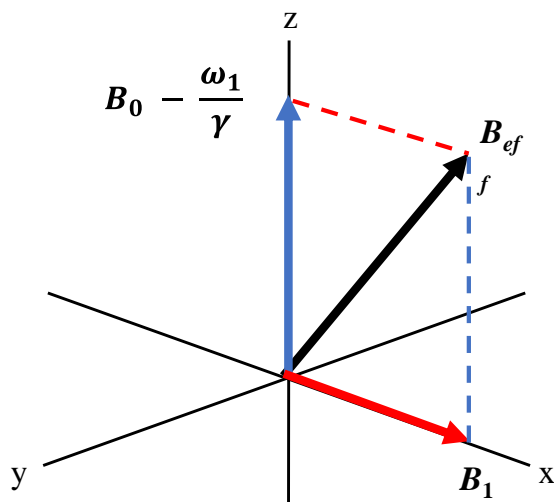
Figure 2.3. The effective magnetic field in the rotating frame of reference. At resonance, i.e., $\omega_1 = \omega_0$, the effective longitudinal field is zero.

2.1.3. Radiofrequency pulses

Pulse NMR experiments use a short radiofrequency (RF) pulse to provide the oscillating field in the laboratory frame, $\mathbf{B}_1$. The field produced by the RF pulse may be chose to lie along the x-axis of the rotating frame. The nuclear spins of this system respond to the pulse in such a way as to move the equilibrium magnetisation vector, $\mathbf{M}_0$, away from the z-axis and into the transverse (x-y) plane (as viewed in the rotating frame). The resultant angle of rotation depends on the length of time the field $\mathbf{B}_1$ is applied, t_1, and its magnitude, B_1, according to:

$$\theta = \omega_1 t_1 = \gamma B_1 t_1 \tag{2.13}$$

NMR pulse sequences generally make use of 90º $\left(\frac{\pi}{2}\right)$ and 180º (π) which are demonstrated in Figure 2.4. A 90º pulse (shown in Figure 2.4a) rotates the magnetisation into the transverse plane where it can be detected by the receiver coil. After such a pulse, referred to as an excitation pulse, the spin population of α and β states are equivalent and there is no net magnetisation along the

longitudinal (z) direction. Net polarisation now exists on the transverse plane. A 180⁰ pulse (shown in Figure 2.4b) will invert the spin population of α and β states. Net magnetisation will now be negative along the z-axis due to a surplus of spins in the β states.
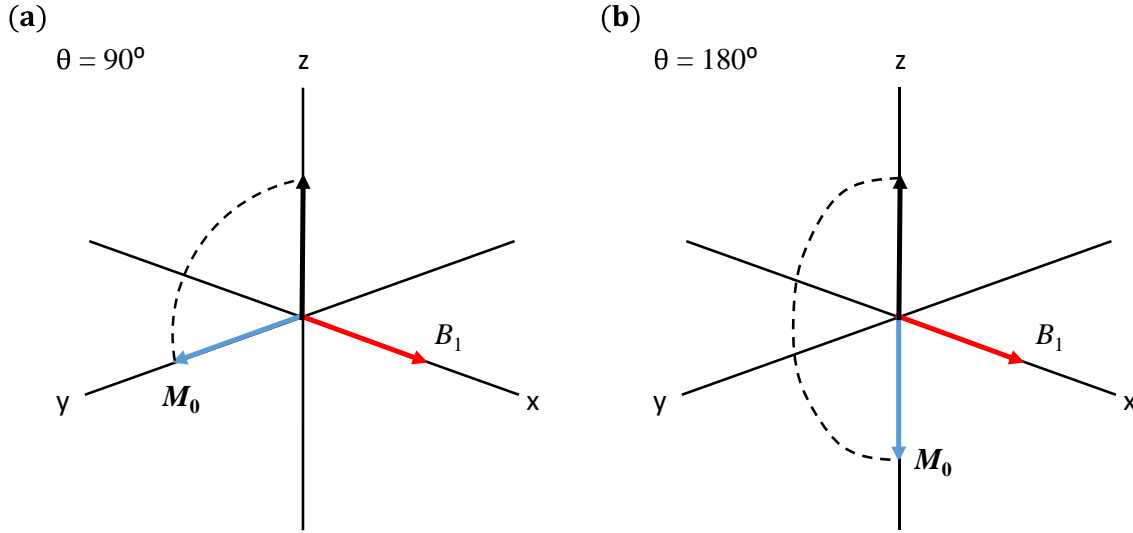
Figure 2.4. The effect of the RF field B_1 on the magnetisation vector, M_0, viewed in the rotating frame. The diagrams show: (a) a 90° pulse and (b) a 180° pulse.

2.1.4. Spin-lattice relaxation

Following an RF pulse, the non-equilibrium distribution of spins will give rise to two components of magnetisation relative to the equilibrium vector; a transverse component and a longitudinal component. The recovery of the longitudinal component of the magnetisation, M_z, back to its equilibrium positon is known as spin-lattice relaxation. It is known as spin-lattice relaxation as energy is lost to the surroundings (the "lattice") as the magnetisation relaxes back from its higher energy state. Bloch theory assumes the equilibrium is restored according to:

$$\frac{dM_z}{dt} = -\frac{(M_z - M_0)}{T_1} \tag{2.14}$$

where T_1 is the spin-lattice (or longitudinal) relaxation time constant. T_1 is the characteristic relaxation time taken for the longitudinal component of the magnetisation, M_z, to relax back to its equilibrium positon. Solving Equation 2.14 gives:

$$M_z(t) = M_z(0) e^{\left(-\frac{t}{T_1}\right)} + M_0 \left[1 - e^{-\left(\frac{t}{T_1}\right)}\right] \tag{2.15}$$

40

where $M_z(0)$ is the longitudinal magnetisation at $t = 0$. Generally, the equilibrium magnetisation is restored after a time $t = 5 \times T_1$. The spin-lattice relaxation time constant, T_1, is typically measured with the inversion recovery pulse sequence,[2] that can be seen in Figure 2.5.
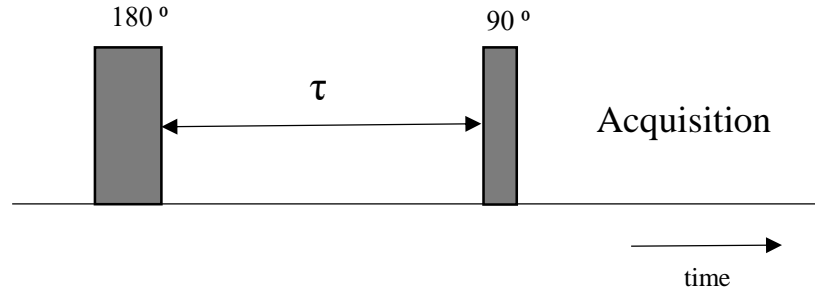
Figure 2.5. The inversion recovery experiment: (a) Inversion recovery pulse sequence. During the time delay τ the magnetisation recovers. The experiment is repeated for a list of time delays.

Magnetisation along the z-axis cannot be detected; therefore, the relaxation process is monitored by applying a 90^0 pulse after a time, τ, to place the magnetisation into the transverse plane where it can be detected. The recovery of magnetisation proceeds according to $M_z(0) = -M_0$. T_1 is measured by performing many inversion recovery experiments with τ ranging from 0 to $t > 5 \times T_1$ and fitting the measured signal intensities to the following equation:

$$M_z(t) = M_0 \left[1 - 2\, e^{\left(-\frac{t}{T_1} \right)} \right] \tag{2.16}$$

Alternatively, the saturation recovery pulse sequence [2] can be used to determine the spin-lattice relaxation time constant. In a saturation recovery pulse sequence, the magnetisation is disturbed from thermal equilibrium by complete saturation of nuclear polarisation. The system is then allowed to recover by spin-lattice processes. Similarly to the inversion recovery experiment, a 90^0 pulse is used to monitor the relaxation process at a time τ after saturation. The measured signal intensities are fitted to Equation 2.15 with the condition $M_z(0) = 0$ to give the following:

$$M_z(t) = M_0 \left[1 - e^{-\left(\frac{t}{T_1} \right)} \right] \tag{2.17}$$

The saturation recovery method finds use due to its decreased experimental times as short repetition times can be used. However, it can prove very difficult to achieve the complete removal of magnetisation in the transverse plane.

2.1.5. Spin-spin relaxation

Spin-spin relaxation (also known as transverse relaxation) is a relaxation process by which spins with magnetisation in the transverse plane come to equilibrium with each other. Excitation pulses of certain lengths may result in a transverse net magnetisation. The precession frequency of each spin will be slightly different due to variations in the local field across the whole spin ensemble. As such, the nuclear spins will lose phase coherence as magnetisation in the transverse plane evolves. This causes the NMR signal to decay as the precession of the spins become incoherent. The process is represented in Figure 2.6.
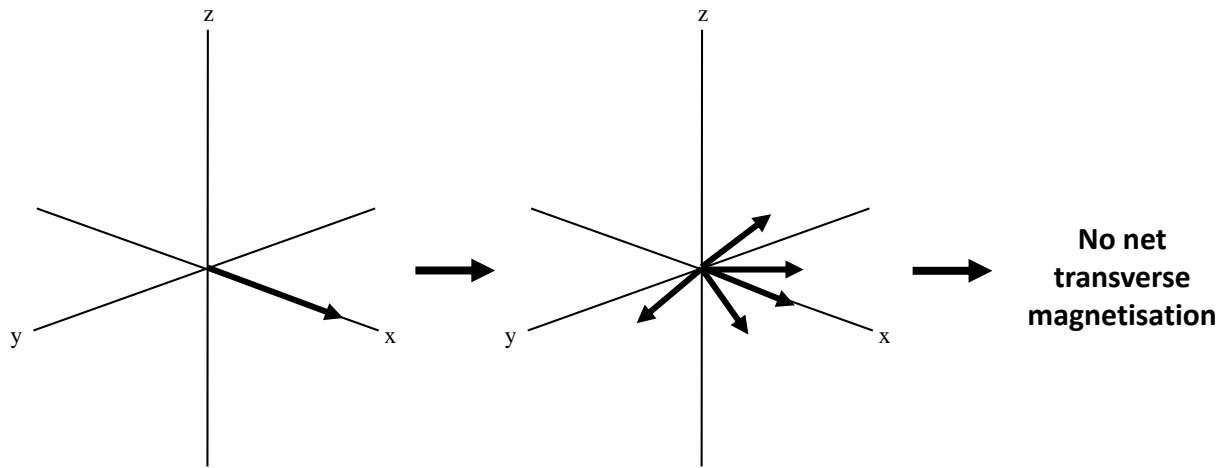
Figure 2.6. The process of spin-spin relaxation showing the spreading out of the net transverse magnetisation. Initially, the spins are aligned with the external magnetic field along the z-axis and are tilted into the transverse plane using a 90º RF pulse.

The evolution of spin-spin relaxation in the transverse plane is given by:

$$\frac{dM_{x,y}(t)}{dt} = -\frac{M_{x,y}(t)}{T_2} \tag{2.18}$$

$$M_{x,y} = M_{x,y}(0)e^{\left(-\frac{t}{T_2}\right)} \tag{2.19}$$

It should be noted that as thermal equilibrium is restored, spin-lattice relaxation will destroy the transverse magnetisation and therefore $T_1 \geq T_2$. Loss of spin phase coherence will not only occur due to local magnetic field differences. Indeed, phase coherence will also be lost due to inhomogeneities in the static magnetic field, $\mathbf{B}_0$, and this will also contribute to the dephasing of

42

transverse magnetisation Therefore, the loss of signal in the transverse plane is determined by the contribution of each of these processes.

It is important to note that whilst the loss of signal due to variations of the local magnetic field is an *irreversible* process (due to the nature of the system), the loss of signal caused by inhomogeneities of the static magnetic field, $\mathbf{B}_0$, is a *reversible* process. Therefore, an apparent transverse relaxation constant, T_2, and reversible, $T_2(\Delta B_0)$ components of spin-spin relaxation are related by the expression:

$$\frac{1}{T_2^*} = \frac{1}{T_2} + \frac{1}{T_2(\Delta B_0)} \tag{2.20}$$

The decay time constant, T_2^*, is seen not only in the decay of the FID but also in the width of the NMR resonances line shape. For liquids associated with a single resonance frequency. The spectrum is approximately Lorentzian in shape and has a width, Δv, at half its maximum height, known as the full width at half maximum (FWHM) given by:

$$\Delta v = \frac{1}{\pi T_2^*} \tag{2.21}$$

Δv is typically in the order of a few hertz. When a solid or a liquid is interacting with a solid surface, the relaxation rate will be much faster and consequently the line widths seen will range from $10^2 - 10^4$ Hz. Two methods, based on what is called a spin echo, are used to measure the transverse relaxation time constant, T_2. [3] The first technique, the Hahn echo sequence, involves the application of a 90⁰ pulse followed by the application of a 180⁰ pulse, after a delay time, τ. However, if molecular diffusion in the sample being studied is significant, then there will be incomplete spin refocusing leading to further signal loss and an underestimation of the transverse relaxation constant. When liquids imbibed within porous media are studied, local magnetic field gradients may exist due to changes in the magnetic susceptibility of the porous material. Hence, signal loss from diffusion can result in significant signal loss when investigating liquids imbibed within porous media.

To prevent loss of signal due to internal field gradients, the Carr-Purcell-Meiboom-Gill (CPMG) [4] pulse sequence was developed. The CPMG pulse sequence consists of a series of 180⁰ refocusing pulses and short τ delays. By using sufficiently short τ delay values, the contribution of molecular

diffusion to the signal loss is reduced substantially. The Hahn and CPMG pulse sequences are depicted in Figure 2.7.
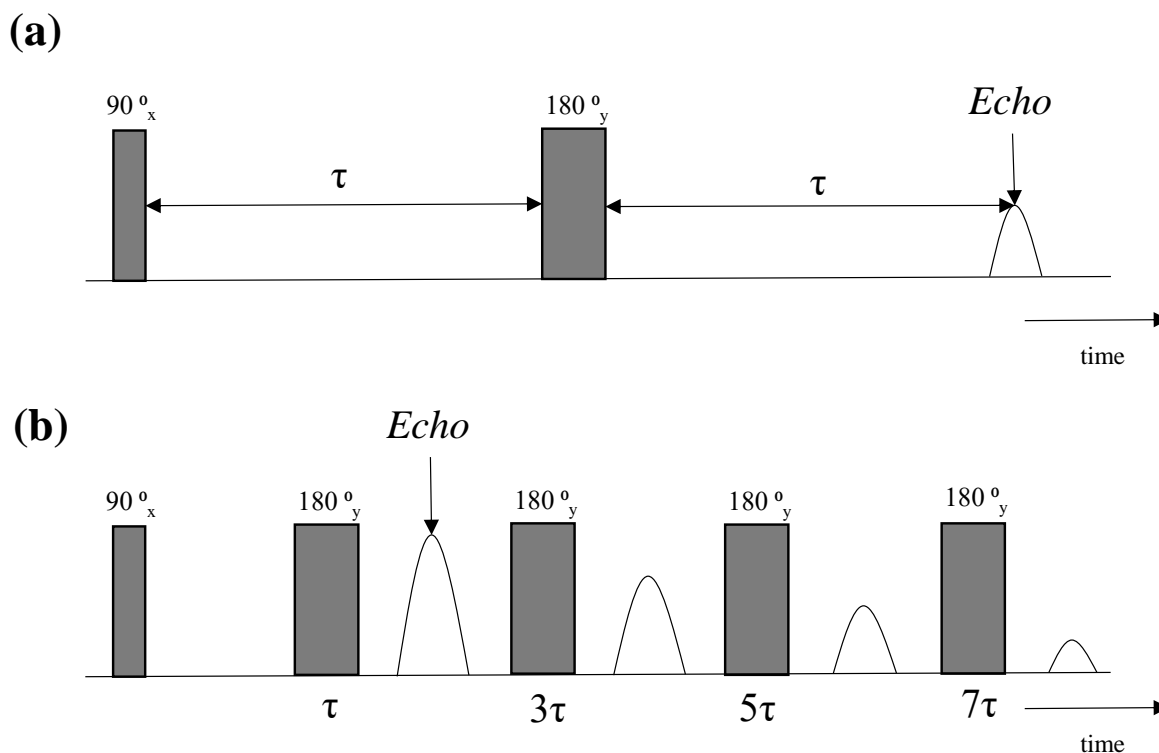
Figure 2.7. (a) The Hahn echo pulse sequence and (b) CPMG pulse sequence. The application of frequent 180° pulses in the CPMG sequence minimises the influence of molecular diffusion on signal decay.

2.1.6. Relaxation time constants and correlation time

The spin-lattice and spin-spin relaxation times are caused by fluctuating local fields, which induce nuclei to flip amongst their available spin states. The spin-lattice relaxation, T_1, process is dependent upon the probability that the local fields have a component oscillating at the appropriate frequency, that is, the resonance (or Larmor) frequency $\omega_0 = \gamma B_0$. The transverse relaxation rate also depends upon the variation of the local magnetic field.

The local field varies from spin to spin, so the precession frequency will differ slightly for each spin. Consequently, the precession frequencies of the individual moments will become out of step with one another over time. This decay could be reversed by the use of a spin echo were the local fields not to change over time. However, local fields are not time independent and will change rapidly over time. The rotational motion of a molecule, known as molecular tumbling motion, is

the main cause of fluctuations in local magnetic fields at a nucleus. A characteristic time for the molecular tumbling motion can be defined and this is known as the rotational correlation time, τ_c. The rotational correlation time is, roughly, the taken for a molecule to end up with a rotation of one radian ($\approx 57^o$) from its starting position. According to Bloembergen-Purcell-Pound (BPP) theory of relaxation [5] both T_1 and T_2 relaxation constants will be dependent on τ_c in the following way:

$$\frac{1}{T_1} = K \left[\frac{\tau_c}{1 + \omega_0^2 \tau_c^2} + \frac{4\tau_c}{1 + 4\omega_0^2 \tau_c^2} \right] \tag{2.22}$$

$$\frac{1}{T_2} = \frac{K}{2} \left[3\tau_C + \frac{5\tau_c}{1 + \omega_0^2 \tau_c^2} + \frac{2\tau_c}{1 + 4\omega_0^2 \tau_c^2} \right] \tag{2.23}$$

Where K is a constant, ω_0 is the Larmor frequency and τ_c is the rotational correlation time. The dependence of the spin-lattice relaxation time constant, T_1, and the spin-spin relaxation time constant, T_2, is shown in Figure 2.8.
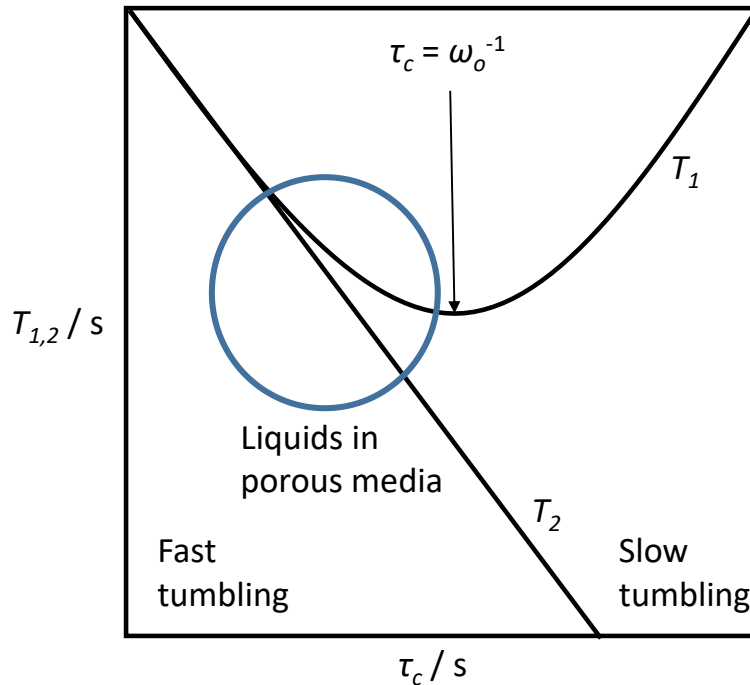

Figure 2.8. Qualitative behaviour of T_1 and T_2 relaxation times as function of correlation time, τ_c.

The dependence of spin-lattice relaxation time, T_1, on the rotational correlation time shows a minimum at $\tau_c = \omega_0^{-1}$ due to an exchange of energy between the magnetic energy of the spins

and the energy of thermal motion of the surrounding environment. This energy exchange is the most efficient when $\tau_c = \omega_0^{-1}$. This minimum separates the slow and fast tumbling regions. The spin-spin relaxation time, T_2, will decrease as τ_c increases, as dipolar interactions will act to enhance the overall transverse relaxation rate. It is clear from Figure 2.8 that in the fast tumbling region, T_1 and T_2 will be approximately the same and have a similar dependence on τ_c (characteristic of small, non-viscous molecules). In the slow tumbling region (characteristic of large, viscous molecules or molecules interacting strongly with a solid surface), the values of T_1 and T_2 will diverge and T_1 may become much larger than T_2. [6]

2.1.7. NMR signal detection

As discussed in the previous section, the NMR signal is detected by a coil placed around the sample with its axis of symmetry transverse to the static field, **B₀**. As the transverse magnetisation precesses, an electro-motive-force (emf) is induced in the coil with a frequency equal to the Larmor frequency of precession. This manifests itself as a radiofrequency (RF) signal, typically of μV amplitude. The NMR signal is then mixed with an output signal from an oscillator in a process known as heterodyning or quadrature detection. In this process, the NMR signal is mixed with two reference signals, one 90⁰ out of phase with the other, producing two output signals that represents the real (M_x) and imaginary (M_y) components of the magnetisation in the transverse plane. If the reference signal used matches the Larmor frequency of the nucleus being studied, heterodyning will detect a DC signal. If not, the signal detected will oscillate at a frequency $\Delta\omega$ equal to the difference between the precession frequency, ω_0, and the receiver reference frequency, ω_R. Note that although NMR precession frequencies are typically tens or hundreds of MHz, this process of mixing with a reference signal gives an output oscillating with frequency ~ 1- 10 kHz. Consequently, the frequency range that must be digitised is substantially reduced. In complex notation, the evolution of the magnetisation in the transverse plane following a 90⁰ pulse can be written as:

$$M(t) = M_0 e^{(i\omega_0 t)} e^{\left(-\frac{t}{T_2}\right)} \tag{2.24}$$

After heterodyning the signal at a frequency offset $\Delta\omega$, the detected signal will be:

$$S(t) = S_0 e^{(i\emptyset t)} e^{(i\Delta\omega t)} e^{\left(-\frac{t}{T_2}\right)} \tag{2.25}$$

where ϕ is the receiver phase and S_0 is the signal amplitude immediately following the RF pulse. The signal is measured in the time domain and the two conditions can occur:

$$\omega_R = \omega_0 \rightarrow \Delta\omega = 0 \rightarrow \text{DC signal with exponential decay} \quad (on-resonance \text{ condition})$$

$$\omega_R \neq \omega_0 \rightarrow \Delta\omega \neq 0 \rightarrow \text{signal oscillating at } \Delta\omega \quad (off-resonance \text{ condition})$$

Fourier transform, according to Equation 2.26 where **k** and **r** represent reciprocal variables, of such a time domain signal yields a Lorentzian absorption line shape (Figure 2.9a) and a dispersion line shape (Figure 2.9b) in the real part and imaginary part of the frequency domain, respectively.

$$F(\mathbf{k}) = \int_{-\infty}^{+\infty} f(\mathbf{r}) e^{-(i2\pi\mathbf{k}\mathbf{r})} \, d\mathbf{r} \tag{2.26}$$

(a) **(b)**
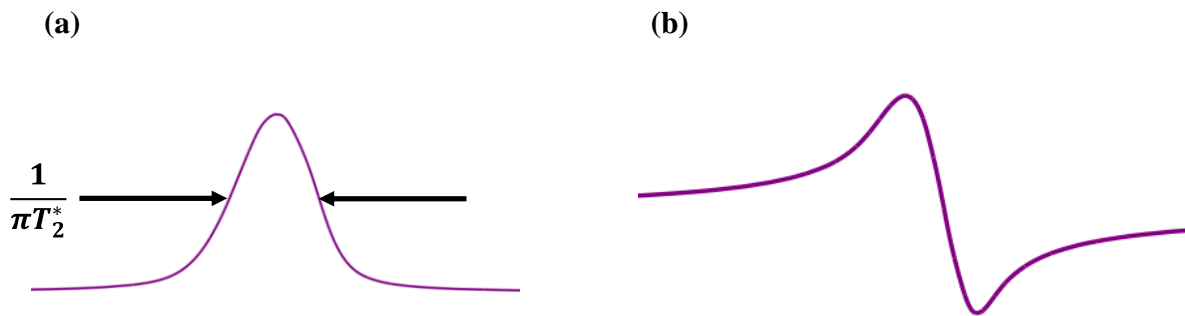
Figure 2.9. Fourier transform of (a) real and (b) imaginary part of the free induction decay.

The RF signal induced in the detection coil is sampled discretely. To determine NMR frequencies, the digitization of the NMR signal must be carried out at a minimum rate. According to the Nyquist theorem, at least two points per wavelength are required to characterise a regularly oscillating signal. Consequently, a signal must be sampled at a rate of at least twice its oscillating frequency. The highest frequency that must be sampled will hence provide a constraint on the minimum sampling rate. This frequency is commonly known as sweep width (SW). Sampling at twice the sweep width gives a dwell time (DW) between sample points of:

$$DW = \frac{1}{2 \times SW} \tag{2.27}$$

Any signal with frequency greater than the sweep width will be sampled incorrectly and will in fact appear in the NMR spectrum at a frequency lower than its true value.

2.2. NMR Spectroscopy

2.2.1. Chemical shift and NMR spectrum

NMR spectra are plots of radiofrequencies (x-axis) against absorption signal intensities along the y-axis. Generally speaking, NMR resonances occur at different frequencies, depending on the molecular structure of the compound under investigation. These differences in resonance frequencies are called chemical shift (δ) and are measured in parts per million (ppm). Chemical shift is a consequence of shielding of the nucleus by neighbouring electrons as this alters the local magnetic field experienced by the nucleus. This changes the resonance frequency of the nucleus and thus, chemical shifts are seen. The chemical shift is usually defined relative to the reference molecule tetramethyl silane (TMS) according to the following relationship:

$$\delta = \frac{\nu - \nu_{TMS}}{\nu_{TMS}} \times 10^6 \qquad\qquad (2.28)$$

where ν is the absolute frequency of the nucleus of interest and ν_{TMS} is the absolute frequency of TMS, which usually coincide with the operating frequency of the spectrometer, ν_{Ref}.

Conventionally, NMR spectra are plotted with δ increasing from the right to left. Trends in chemical shift are explained based on the degree of shielding or deshielding. More heavily shielded nuclei experience a lower magnetic field and hence appear towards the right hand-side of the spectrum or 'upfield'. Conversely, less shielded nuclei appear on the left hand-side of the spectrum and are said to be 'downfield'. Contributions to nuclear shielding include electronegativity and induced magnetic fields of neighbouring groups, local diamagnetic and paramagnetic shifts and hydrogen bonding. Electron-donating alkyl groups for example, lead to an increased shielding while electron-withdrawing substituents, such as nitro-groups, lead to the deshielding of the nucleus. In terms of electronegativity, a nucleus in the vicinity of an electronegative atom experiences reduced electron density and the nucleus is therefore deshielded. More details on shielding mechanisms are reported elsewhere. [7]

2.2.2. Scalar coupling

Scalar coupling, also known as *J*-coupling, is a through bond interaction where the spin of one nucleus perturbs (polarises) the spins of the intervening electrons, and the energy levels of neighbouring magnetic nuclei are in turn perturbed by the polarised electrons. This leads to a

decrease of the energy of the neighbouring nucleus when the perturbing nucleus has one spin and an increase of the energy when the neighbour has the other spin. The effective resonance of the nucleus is therefore split in $m = n + 1$ multiplets with n being the number of nearby coupled nuclei (i.e. ^{1}H nuclei). J-coupling (always reported in Hz) is field-independent (i.e. J is constant at different external magnetic field strength) and is mutual (i.e. $J_{AB} = J_{BA}$). As this effect is transmitted through bonding electrons, the magnitude of J falls off rapidly as the number of intervening bonds increases.

2.2.3. Proton NMR

The most exploited nucleus in NMR spectroscopy is the ^{1}H nucleus with a nuclear spin $I = \frac{1}{2}$. This is due to the high natural abundance of the ^{1}H isotope (99.99%) and its inherent NMR sensitivity. Both qualitative and quantitative information can be easily deduced by a proto NMR spectrum. The number of resonances, representative of different chemical groups or environments, can deduce qualitative information. Quantitative information can be obtained by the NMR signal intensity of different NMR resonances. The integration of such peaks is directly related to the number of protons making up a particular chemical group.

2.2.4. Carbon NMR

The power and usefulness of ^{1}H NMR should be evident from the previous discussion. However, there are certain cases where ^{1}H NMR spectroscopy is difficult to perform. For example, when significant portions of a molecule lack C-H bonds, little or no information will be obtained from the ^{1}H NMR spectrum. Furthermore, the use of ^{1}H NMR may become prohibitive when studying liquid phase reactions in porous catalysts as the relatively narrow chemical shift range of the ^{1}H nucleus together with the line broadening of ^{1}H resonances give rise to a large number of overlapping resonances, making the resulting NMR spectrum almost featureless and further analysis difficult, if not impossible. In such cases, ^{13}C NMR is typically the next best approach. When ^{13}C is used as the nucleus of choice, the chemical shift range is much wider than when ^{1}H is used, therefore, peak overlap typical of liquid species imbibed within porous materials. The major limitation of ^{13}C NMR lies in its much lower signal-to-noise ratio when compared to that of ^{1}H NMR. The natural abundance of the ^{13}C isotope is very low (1.1%), therefore, samples enriched with ^{13}C nuclei are often required and such samples can be very costly. Furthermore, the sensitivity

of the ^{13}C nucleus is only 1.6×10^{-2} relative to the reference value of 1, which is given to the ^{1}H nucleus.

A ^{13}C NMR spectrum is usually acquired with a broadband heteronuclear decoupling. In such a way, all the C-H couplings are removed by saturating the ^{1}H spin population, which no longer influences neighbouring ^{13}C nuclei. A spectrum acquired in this manner displays a single sharp signal for each structurally distinct carbon atom in a molecule, since the proton coupling is totally removed. It has to be pointed out that in order to obtain a quantitative ^{13}C NMR spectrum a very long recycle delay may be needed with the proton decoupling to be applied only in the acquisition time to minimise the effect of Nuclear Overhauser Effect (NOE). [8]

2.3. Pulsed-field gradient NMR

2.3.1. Magnetic field gradient NMR techniques

Using phase encoding methods, NMR can be used to measure both coherent (i.e. flow) and incoherent (i.e. diffusion) motion. A magnetic field gradient, $\mathbf{g}$, is applied to cause the Larmor frequency to vary with position, $\mathbf{r}$, according to:

$$\omega(r) = \gamma(B_0 + \mathbf{g} \cdot \mathbf{r}) \tag{2.29}$$

When the signal is heterodyned at the Larmor frequency, the dependence upon on the Larmor base frequency is removed and the phase of the precessing spins varies according to:

$$\phi(r) = \gamma \delta \mathbf{g} \cdot \mathbf{r} \tag{2.30}$$

Where δ is the duration of the gradient pulse, $\mathbf{r}$ is the position of the nuclear spins and $\mathbf{g}$ is the pulsed field gradient. Once the magnetic field gradient is applied and heterodyning has occurred, the nuclear spins are effectively labelled with regards to their positions. By applying a second pulse to reverse the effect of the first after a time, Δ, after the first pulse then it is possible to detect a change in the position of the spins. That is, any motion during the time, Δ, (known as the observation time) can be detected. If the nuclear spins have not changed position then second pulse will rewind the spin phases. Spins that have changed position will have a net phase given by:

$$\phi(r) = \gamma \delta \mathbf{g} \cdot (\mathbf{r} - \mathbf{r}') \tag{2.31}$$

This shift in net phase gives access to the displacement of nuclear spins due to coherent or incoherent motion.

The effect of field gradients and the process of diffusion can be explained by the random walk analogy. [3] Diffusive motion of a nucleus can be regarded as a random walk process in which the nucleus jumps a distance ξ in a time τ_s. The distance travelled after n jumps in the direction of the field gradient can be written as:

$$Z(n\tau_s) = \sum_{i=1}^{n} \xi a_i \tag{2.32}$$

where a_i is a random number equal to ± 1. For one dimensional motion the self-diffusion coefficient, D, is defined by:

$$\xi^2 = 2D\tau_s \tag{2.33}$$

Therefore, the mean square displacement, $\overline{Z^2}$, after a time $t = n\tau_s$, can be written as:

$$\overline{Z^2(t)} = \overline{Z^2(n\tau_s)} = \sum_{i=1}^{n} \xi^2 \overline{a_i^2} = \xi^2 \sum_{i=1}^{n} 1 = n\xi^2 = 2Dt \tag{2.34}$$

when the sample is subject to a magnetic field gradient, the phase acquired during the random walk after a time $t = n\tau_s$ is given by:

$$\phi(t) = \gamma B_0 n\tau_s + \sum_{m=1}^{n} \gamma g\tau_s \sum_{i=1}^{m} \xi a_i \tag{2.35}$$

The first term of Equation 2.35 represents the constant Larmor frequency precession and can be disregarded. The second term describes the dephasing $\Delta\phi$ due to the field gradient. Assuming a Gaussian distribution for $\Delta\phi$, the mean phase shift $\overline{e^{(i\Delta\phi)}}$, which represents the NMR signal attenuation at time t, can be written in terms of t and D as follows:

$$\overline{e^{(i\Delta\phi)}} = e^{\left(-\frac{\overline{\Delta\phi^2}}{2}\right)} = e^{\left(-\frac{\gamma^2 g^2 D t^3}{3}\right)} \tag{2.36}$$

where:

$$\overline{\Delta\phi^2} = \frac{\gamma^2 g^2 \tau_s^2 \xi^2 n^3}{3} \tag{2.37}$$

During a pulsed-field gradient (PFG)-NMR experiment, RF pulses are followed by gradient pulses and the signal attenuation, that is, the ratio of the echo amplitude in presence of a gradient, $E(g)$, and the echo amplitude of in absence of gradient, E_0, has the following expression: [9]

$$\frac{E(g)}{E_0} = e^{\left[-\gamma^2 g^2 \delta^2 D\left(\Delta - \frac{\delta}{3}\right)\right]} \tag{2.38}$$

When $\gamma^2 g^2 \delta^2 (\Delta - \delta/3)$, which is commonly known as the *b*-factor, is plotted against $E(g)/E_0$ on a logarithmic scale the self-diffusion coefficient, D, can be calculated. This is known as a Stejskal-Tanner plot and is acquired from PFG-NMR experiments.

2.3.2. PGSE

The most basic PFG-NMR experiment is the pulsed-gradient spin echo (PGSE) pulse sequence. The PGSE pulse sequence was developed by Stejskal and Tanner [9] and is shown in Figure 2.10.
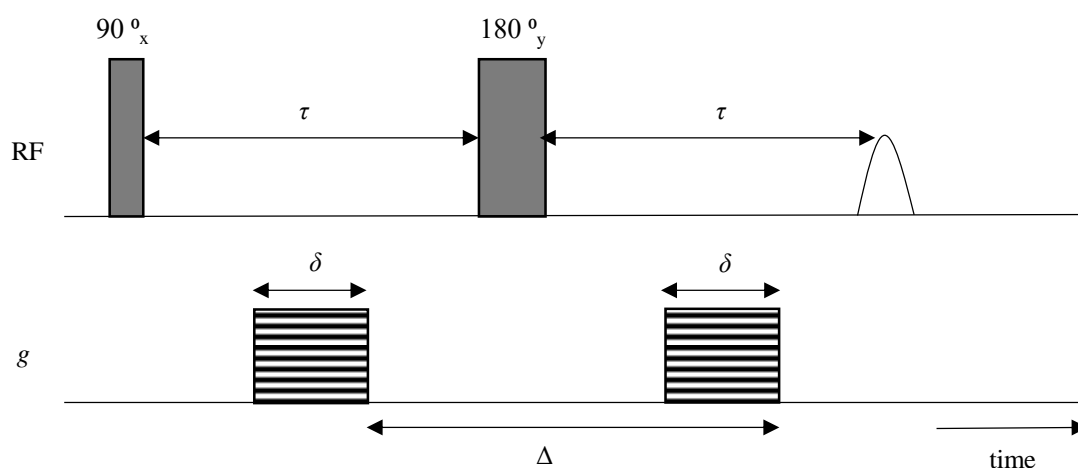
Figure 2.10. Pulsed-gradient spin echo (PGSE) NMR pulse sequence

During the PGSE pulse sequence, the pulsed magnetic field gradient is applied for a time δ either side of the 180º RF pulse and it is switched off during the RF pulse and acquisition. If motion occurs during the observation time, Δ, nuclear spins will exhibit a net phase offset and their contribution to the spin echo will be reduced, as there will be no complete refocusing of the phase-encoded spins along the direction of motion. The diffusion coefficient is then found by using Equation 2.38 and plotting a Stejskal-Tanner plot as described previously.

2.3.3. PGSTE

When a sample has short T_2, significant signal loss of the spin echo can occur during the PGSE pulse sequence. To combat this, the pulsed-field gradient stimulated echo (PGSTE) pulse sequence was developed (Figure 2.11). When the PGSTE pulse sequence is used, the system undergoes T_1 relaxation enabling longer observation times, Δ, to be used. [10]
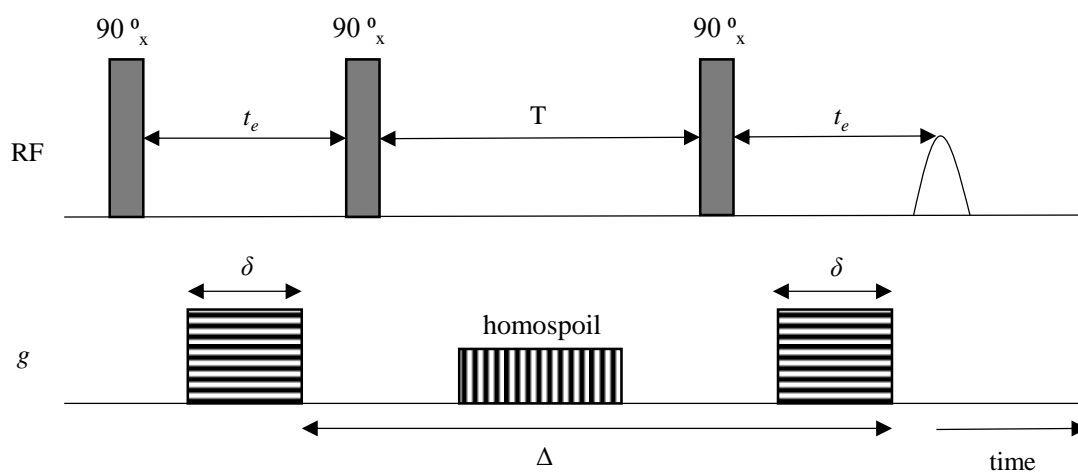
Figure 2.11. The pulsed-gradient stimulated echo (PGSTE) pulse sequence.

The homospoil gradient destroys any residual magnetisation in the transverse plane, which could otherwise result in unwanted signal.

2.3.4. APGSTE

For maximum accuracy in the PFG-NMR measurements, the external magnetic field, $\mathbf{B}_0$, must be as homogeneous as possible. If $\mathbf{B}_0$ is highly heterogeneous, local magnetic field gradients arising from the magnetic susceptibility of the sample will become significant. The alternating pulsed-field gradient stimulated echo (APGSTE) pulse sequence (Figure 2.12) was developed by Cotts et al [11] to combat this issue. The 180º and 90º pulses in the APGSTE sequence are applied in the *y*-axis and *x*-axis respectively.
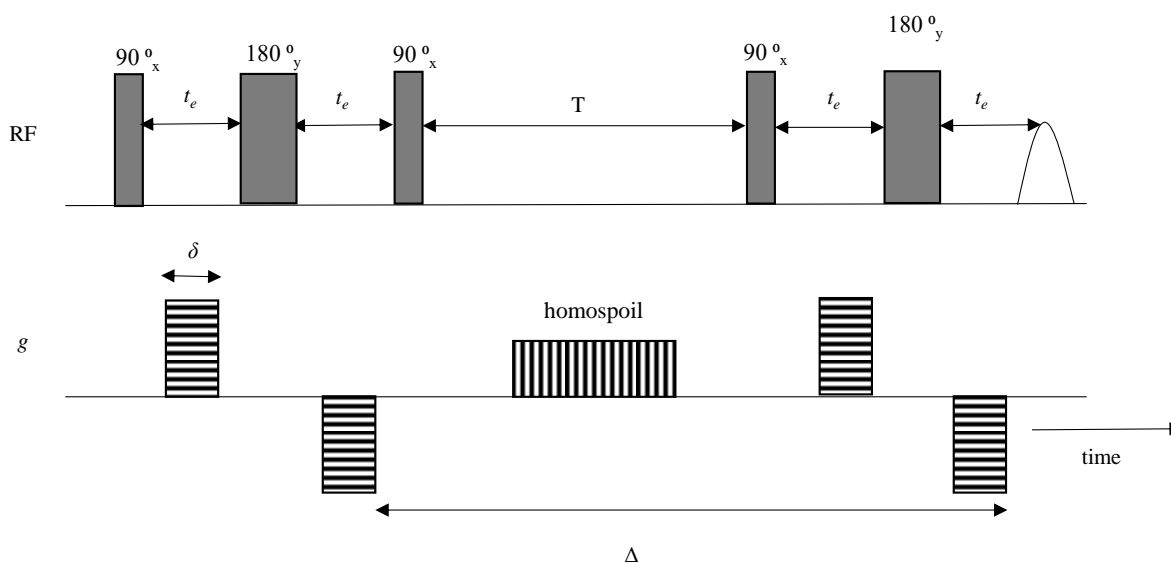
Figure 2.12. The 13-interval alternating pulsed-gradient stimulated echo (APGSTE) pulse sequence.

When this technique, referred to as a 13-interval sequence, is used, the effect of the background gradient g_0 is substantially reduced. The signal strength is correspondingly increased and the systematic errors in D measurements are reduced.

References

1.   I. Rabi, J. R. Zacharias, S. Millman and P. Kusch, *Phys. Rev.*, 1938, **53**, 318-318.

2.   E. Fukushima and S. W. Roeder, *Experimental pulse NMR: A Nuts and Bolts Approach¸* Addison-Wesley, Boston, U.S.A., 1981.

3.   P. T. Callaghan, *Principles of Nuclear Magnetic Resonance Microscopy*, Oxford University Press, Oxford, United Kingdom, 1993.

4.   H.Y. Carr and E. M. Purcell, *Phys. Rev.*, 1954, **94**, 630-638.

5.   N. Bloembergen, E. M. Purcell and R. V. Pound, *Phys. Rev.*, 1948, **73**, 679-746.

6.   M. Levitt, *Spin Dynamics: Basics of Nuclear Magnetic Resonance*, Wiley, New Jersey, U.S.A., 2001.

7.   P. J. Hore, S. G. Davies, R. G. Compton, J. Evans and L. F. Gladden, *Nuclear Magnetic Resonance*, Oxford Science Publications, Oxford, United Kingdom.

8.   J. Keeler, *Understanding NMR Spectroscopy*, Wiley, Chichester, England, 2005.

9.   E. O. Stejskal and J. E. Tanner, *J. Chem. Phys.*, 1965, **42**, 288-292.

10.   J. .E. Tanner, *J. Chem. Phys.*, 1970, **52**, 2523-2526.

11.   R. M. Cotts, M. J. R. Hoch, T. Sun and J. T. Markert, *J. Magn. Reson.*, 1989, **83**, 252-266.

Chapter 3: Theory of diffusion

3.1. Basic concept of molecular diffusion

Diffusion refers to the movement of molecules from a region of high concentration to a region of low concentration and is commonly known as "mutual diffusion". However, diffusion will also occur in the absence of a concentration gradient. This diffusion process in the absence of a concentration gradient is commonly referred to as "self-diffusion". However, it is questionable if the term "self-diffusion" is appropriate to fully describe the diffusion process in the absence of a concentration gradient.

Molecular diffusion, commonly referred to as simply diffusion, refers to the thermal motion of all particles at temperatures above absolute zero in the absence of mechanical or convective mixing. The rate of diffusion is a function of the temperature, fluid viscosity and particle size. In 1905, Einstein demonstrated that diffusion is the direct result of thermal molecular motion according to the molecular kinetic theory of heat. [1]

As discussed previously, mass transport by diffusion is vitally important to the design of catalytic materials and is the subject of much study. It is often the rate determining step in catalytic reactions and separation processes and as such it is important that the diffusivity of species involved in these processes is appropriately investigated. The diffusion processes occurring within porous materials are one of the main topics of this thesis work and, as such, the following chapter is devoted to providing an overview of different diffusion processes and clarifying the terminology involved in mass transport by diffusion.

3.2. Types of diffusion

3.2.1. Mutual diffusion

As discussed previously, mutual diffusion refers to the movement of molecules across a concentration gradient or, more specifically, a chemical potential gradient. [2] Fick's law [3] states that the net transport rate in a binary system of species i and j, is related to the concentration gradient by the equation:

$$J_{ij} = -D_{ij}^{mutual} \frac{dc_i}{dz}$$
(3.1)

Where J_{ij} is the molar flux, D_{ij}^{mutual} is the mutual diffusivity, c is the concentration and z is the spatial coordinate of the concentration gradient. As mutual diffusion is a net transport, the flux J_{ij} and the flux J_{ji} will be both equal and opposite. D_{ij}^{mutual} will therefore be equal to D_{ji}^{mutual} and the overall diffusion process will be described by a single diffusion coefficient. Generally speaking, concentration profiles fitted with a specific solution of the Fick's second law equation (Equation 3.2) are the basis for experimental techniques used to measure mutual diffusivity.

$$\frac{\partial c_i}{\partial t} = D_{ij}^{mutual} \frac{\partial^2 c_i}{\partial x^2} \tag{3.2}$$

where t indicates the time. The boundary and initial conditions used to solve Equation 3.2 and determine D_{ji}^{mutual} depends on the experimental conditions used.

3.2.2. Self-diffusion

Self-diffusion refers to the movement of molecules in the absence of a chemical potential gradient, $\nabla\mu$. As discussed previously, mutual diffusion returns a system to an equilibrium concentration by molecular motion in the presence of a chemical potential gradient, $\nabla\mu$. When the equilibrium concentration is reached, intermolecular collisions (Brownian motion) will cause a spontaneous mixing of molecules. This process is known as self-diffusion. Brownian motion is responsible for the root mean square displacement ($RMSD$) of molecules after a time t. The self-diffusion coefficient can then be defined using the Einstein relation. For a given spatial direction, this relation is given by:

$$RMSD = \sqrt{2D^{self}t} \tag{3.3}$$

Whereas mutual diffusivity is related to a net flux of mass, self-diffusivity is not. In a binary mixture of two components, i and j, both components will have their own diffusion coefficients, D_i^{self} and D_j^{self}. Generally, $D_i^{self} \neq D_j^{self}$ although it is possible for both diffusion coefficients to be equal. Self-diffusion coefficients can be measured with high accuracy and precision using PFG-NMR as discussed in Chapter 2. The self-diffusion coefficient, D^{self}, is related to the viscosity of the solution and the size of the diffusing species according to the Stokes-Einstein relationship:

$$D^{self} = \frac{k_B T}{c\eta r}$$

(3.4)

where k_B is the Boltzmann constant, T the absolute temperature, η the shear viscosity, r the hydrodynamic radius of the molecule and c is a constant equal to 6π for no-slip and 4π for slip boundary conditions. The Stokes-Einstein relation was derived at infinite dilution for large particles immersed in a bath of much smaller and lighter particles. This allows the solvent medium to be considered as a structureless continuum. [1]

3.3. Measurements of diffusion coefficients

3.3.1. Diaphragm cell

The diaphragm cell method of determining diffusion coefficients is one of the earliest developed methods. [4] The diaphragm cell consists of two compartments separated by a diaphragm (usually a glass frit or porous membrane). The two compartments are then filled with solutions of different concentrations of solute, c_1^0 and c_2^0. A typical diaphragm cell setup can be seen in Figure 3.1.
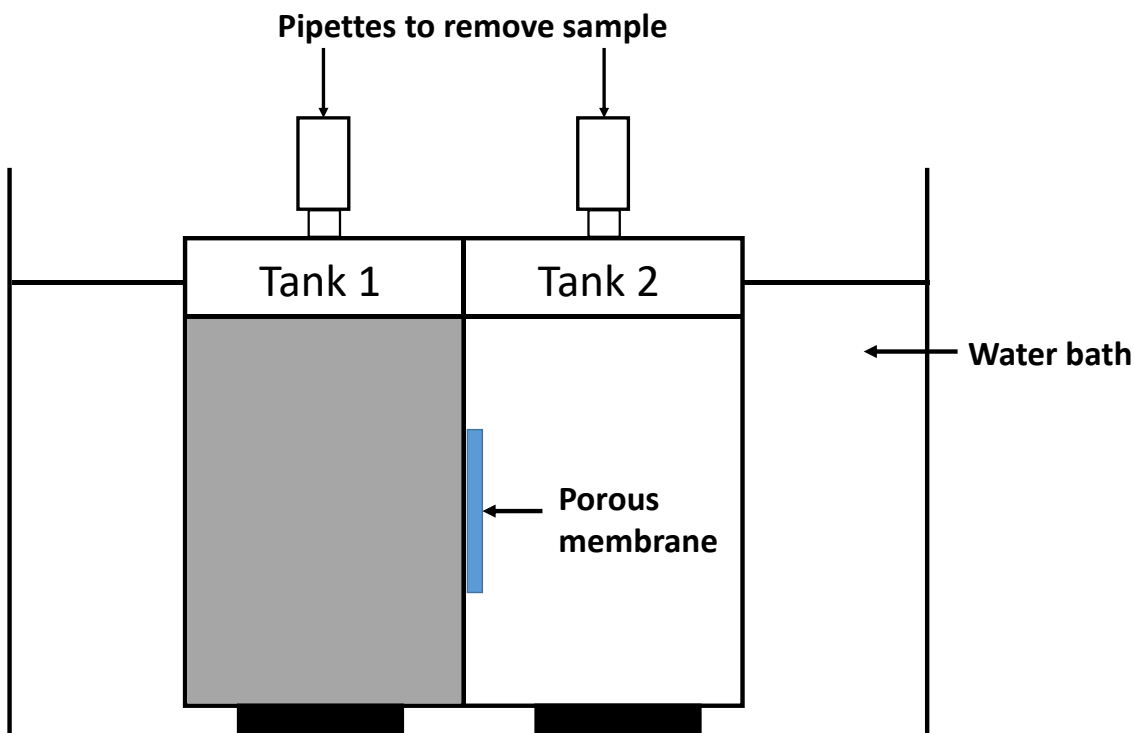

Figure 3.1. Typical setup of a diaphragm cell used to measure diffusivity through a porous membrane. Other materials can be used in place of the porous membrane i.e. a hydrogel or glass frit.

The concentrations of solute in the two chambers at any time, t, can be used to obtain the diffusion coefficient, D, using the following equation.

$$D = \frac{1}{\beta t} \ln \left[\frac{c_1^0 - c_2^0}{c_1(t) - c_2(t)} \right] \tag{3.5}$$

where the constant β depends on the geometry of the system and can be calculated from:

$$\beta = \frac{A}{L} \left[\frac{1}{V_1} + \frac{1}{V_2} \right] \tag{3.6}$$

where A is the effective cross-sectional area available for diffusion, L is the thickness of the diaphragm and V_1 and V_2 are the volumes of the two components.

The nature of the diaphragm will significantly impact the time required for the diaphragm cell measurement. Glass frits are one of the best options for use as a diaphragm in order to achieve accurate results but their use can result in experimental times of several days. An interesting application of this method is performed by replacing the diaphragm with a porous material of interest (i.e. a membrane or hydrogel) to measure the rate of diffusion of a solute through a specific porous material. [5] It is important to note that the diaphragm cell method can produce unreliable results due to the small concentration differences involved.

3.3.2. Pressure decay method

An indirect experimental method of determining diffusion coefficients of gas molecules is known as the pressure decay method. [6] In this method, the gas to be studied and an oil are both injected into a cell (Figure 3.2) and initially, they are at a non-equilibrium state.
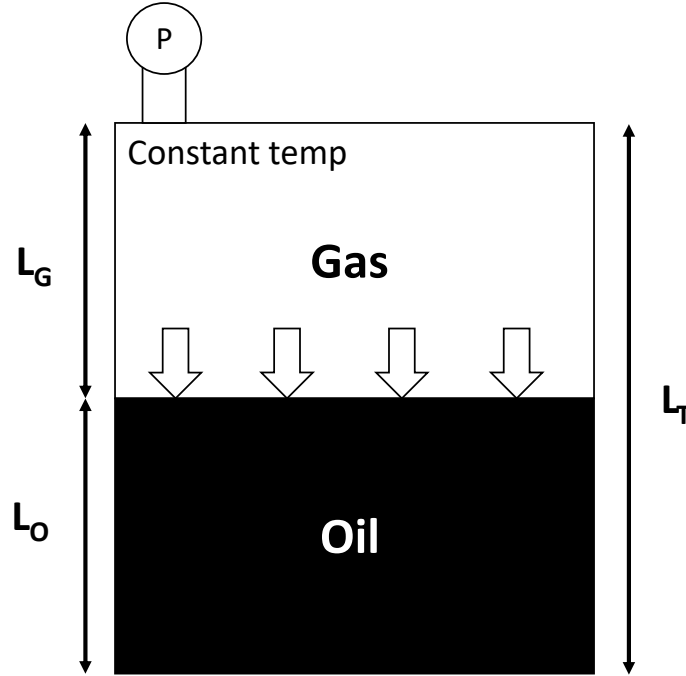
Figure 3.2. A pressure decay test cell setup for the determination of the diffusivity of a gas into an oil. L_T represents the total length of the cell whereas L_G and L_O represent the length of the oil and gas compartments respectively.

Over time, the gas will begin to diffuse into the oil resulting in a decrease in the overall cell pressure and a change in the position of the gas liquid interface. The cell pressure and the liquid level is recorded at various time intervals until the final state is reached, that is, the system is at thermal equilibrium. The rate of pressure change or the interface position can be used to determine the amount of gas transferred. The amount of gas transferred is dependent upon the rate of diffusion which allows for a determination of the diffusion coefficient for the system.

The accuracy of this method has been questioned as small changes to the assumptions used can result in massive differences in acquired diffusivity values [7] however, recent work has attempted to rectify this issue by using improved models in their calculations. [8]

3.3.3. Refractive index method

The refractive index of a substance can be defined as in Equation 3.7:

$$\eta = \frac{c}{v} \tag{3.7}$$

where η is the refractive index, c is the velocity of light in a vacuum and v is the velocity of light in the relevant phase. As light moves from one medium to another it may change its propagation direction in proportion to the change in refractive index (Figure 3.3).
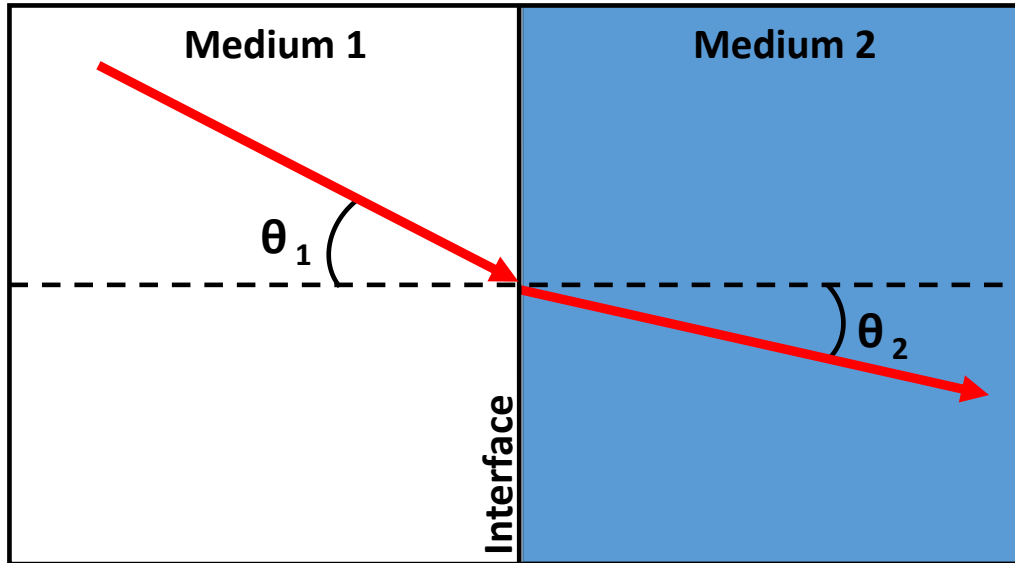
Figure 3.3. The refraction of light at the interface of two media. The refraction angle, θ, changes as the light passes from one medium to the other.

When light is shone through a solution, differences in concentration will result in changes of refractive index, η. The relationship between refraction angles, θ, and the refractive indexes is given by Snells Law:

$$\frac{sin\theta_1}{sin\theta_2} = \frac{v_1}{v_2} = \frac{\eta_2}{\eta_1} \tag{3.8}$$

In a typical diffusion study using the refractive index method, laser light is shone through a diffusion cell at many different elevations and the refractive angle is determined at each elevation point. [9] The point at which the laser beam is captured represents the concentration at each respective elevation point and these concentration values can be used to determine the diffusivity by using Ficks' second law.

The refractive index method is an appropriate indirect method to determine the diffusivity of transparent fluids, however, it cannot be used for opaque systems as the laser light is required to pass through the system.

3.3.4. Computer assisted tomography

Computer assisted tomography (CAT) scanning involves the use of an X-ray source revolving around the object of study while attenuated X-rays are captured by a detector on the other side of the object. As X-rays pass through a medium, they will lose energy dependent upon the substance density and the path length through the substance. These projections are collected and then used to form a two dimensional image of the object. [10]

For a narrow, mono-energetic beam of X-ray photons passing through a homogeneous medium, the inlet intensity, I_0, and outlet intensity, I, of the X-rays used for CAT scanning are given by:

$$\frac{I}{I_0} = e^{-\mu L} \tag{3.9}$$

where L is the path length through the substance and μ is the linear attenuation coefficient. If the medium is heterogeneous, the above equation must be modified:

$$\ln\left(\frac{I}{I_0}\right) = \int_s^d \mu(x,y)dL \tag{3.10}$$

where s represents the X-ray source, d the X-ray detector and $\mu(x,y)$ is a distribution perpendicular to the X-ray beam. The linear attenuation coefficient, μ, is related to the number stored in the computer (known as CT number or CTn) and the substance density, ρ, respectively by the following equations:

$$CTn = \frac{1000 \times (\mu_i - \mu_w)}{\mu_w} \tag{3.11}$$

$$\mu = \rho\left(\frac{a + bZ^{3.8}}{E^{3.2}}\right) \tag{3.12}$$

μ_i is the linear attenuation coefficient of the scanned object, μ_w is the linear attenuation coefficient of water, a is the Klein-Nishina coefficient, b is a constant, Z is the effective atomic number of the sample and E is the mean photon energy.

From the X-rays acquired, density and CTn values can be obtained. This is done for many different samples and solutions to form a density vs. CTn calibration curve. These calibration curves can then be used to find density values for any CAT scanned systems.

In a CAT diffusion study, a fixed vertical-sectional position of the diffusion cell is scanned at fixed frequency during the diffusion process. The diffusion process is considered as a one dimensional vertical process. [11] An average CT number is calculated for the horizontal direction and CT numbers are determined for each point along the region of interest in the vertical direction. Changes in the CT number profile along the vertical direction are then used to determine changes in the density of the system. [11] Normalised concentration profiles can then be obtained from the determined densities according to Equation 3.13 and using a modified version of Ficks' second law the diffusivity can be calculated.

$$\frac{C}{C_0} = \frac{\rho - \rho_x}{\rho_0 - \rho_x} \tag{3.13}$$

Where $\frac{C}{C_0}$ is the normalised concentration, ρ is the bulk substance density, ρ_x is the initial substance density and ρ_0 is the substance density close to the interface.

This method of determining diffusivities has been applied to solvent/heavy oil mixtures and liquid/solid systems.

3.3.5. PFG-NMR Diffusometry

This technique has been discussed in detail in the previous chapter and forms the basis of work to be discussed later in the thesis where its applications will be discussed in detail. It can be applied to a vast array of challenging systems including the diffusion of complex bulk liquids and liquids in porous media amongst many others. It is relatively fast, non-destructive and non-invasive whilst low-field, benchtop NMR spectrometers, as used in this work, have made these measurements simple and relatively cheap to perform.

3.3.6. Laser Raman spectroscopy

Laser Raman spectroscopy finds great use in the measurement of mutual diffusion coefficients for liquids imbibed within solid catalysts. [12] An experimental setup is shown in Figure 3.4.
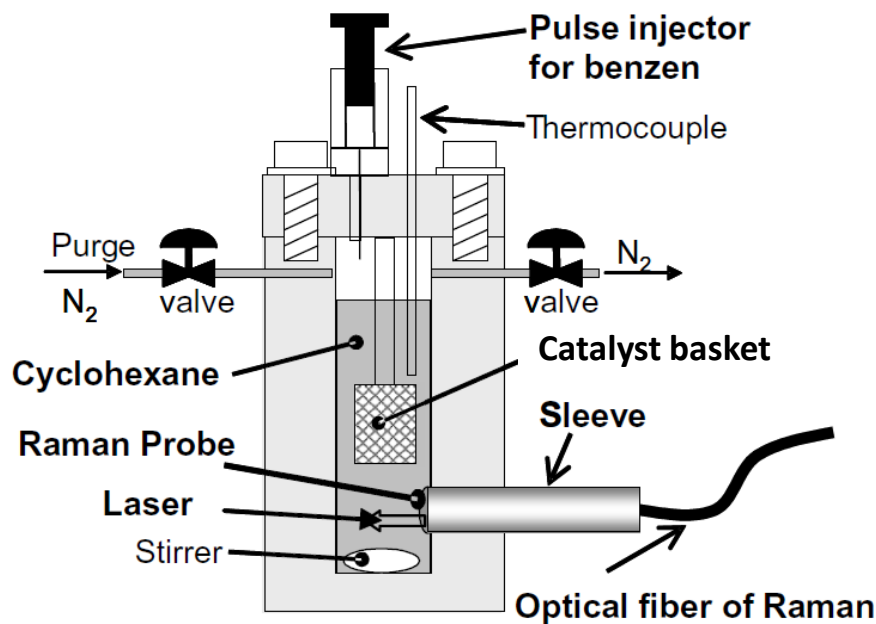
Figure 3.4. Apparatus for measuring the mutual diffusivity in zeolite crystals using Raman spectroscopy. [12]

In a laser Raman spectroscopy diffusion experiment, a catalyst basket is immersed in solution, magnetically stirred and heated to the required temperature. A small amount of solute is then added and the change of solute concentration with time is monitored using laser Raman spectroscopy. The solute concentration and the solute to solvent Raman peak intensity are directly proportional allowing for the change in solute concentration with time to be monitored effectively. The concentration profile determined is then fitted to theoretical equations to determine the diffusion coefficient, D, of the liquid within the porous catalyst.

The theoretical equations used for the fitting are derived under the assumption that mass transfer resistances through macropores and across the laminar films can be ignored. Additionally, the laser Raman method is based on geometric assumptions about the solid crystal shape. Whilst these assumptions generally hold true for silicates and zeolites [12] but does not necessarily apply to all porous materials.

3.3.7. Other techniques for measuring diffusion coefficients

There are many other methods that have been developed for the determination of diffusion coefficients. One of the simplest methods developed is known as the infinite couple method which

is used to measure diffusion in solids. [13] Two solids bars with differing compositions are joined together and the composition is measured at a known time. From this, the variation of the composition with time is determined and therefore the diffusivity can be obtained. The composition can be measured in a variety of different ways such as by using chemical tests or an electron microprobe. The Taylor dispersion method is used to determine mutual diffusion coefficients in diluted solutions to great effect [14] whilst the capillary method is a tracer method suitable for measurements with radioactive tracers [15] which can yield either mutual diffusion or self-diffusion coefficients depending on the experimental conditions. Cyclic voltammetry and chronoamperometry has been shown to be able to measure diffusivity in electrolyte systems [16] whereas diffusion of gases in solids can be measured using the constant volume method. [17] Additional methods used to measure diffusivities include those using interferometers, [18] tapered element oscillating microbalance (TEOM) method [19] and the zero length column. [20]

Table 3.1. A summary of the advantages and disadvantages of the diffusion measurement techniques discussed in Chapter 3.

Technique	Advantages	Disadvantages
Diaphragm cell	Detects diffusion of a solution through a porous medium.	Results can be unreliable due to small concentration differences involved. Experimental times can be relatively long.
Pressure decay	Able to measure diffusion of gases into oils which can be relevant to real life petrochemical applications.	Accuracy of results has been questioned due to inaccuracy of the models generally used.
Refractive index	Allows for measurement of transparent fluids systems.	Not applicable to opaque fluids.
Computer assisted tomography	Applicable to many systems (i.e. opaque solutions, liquid/solid systems).	Requires many calibrations and complex calculations.
PFG-NMR	Fast. non-destructive and non-invasive. Benchtop NMR is relatively cheap and simple.	Requires more complicated setups to measure non-liquids.
Laser raman spectroscopy	Widely used to measure the diffusion of liquids imbibed within solids.	The assumptions used are not applicable to all systems of liquids diffusing within solids.

3.4. Diffusion in porous materials

When a catalyst support is formed, a network of pores will be created. These pores will range in size from micropores (< 2 nm pore diameter) to mesopores (2 – 50 nm in pore diameter) to macropores (> 50 nm pore diameter). Amongst many other things (i.e. the porosity and tortuosity of the material) the mechanism of diffusion of molecules through the porous network of the catalytic materials will be determined by the size of the diameter of the pores. More precisely, the diffusion mechanism will be determined by the mean free path length of the diffusing molecule relative to the pore diameter. It is important to note that porous media will generally contain a distribution of pore diameters throughout the interconnected porous network. Therefore, it is possible for many different diffusion mechanisms to be occurring in the same porous material. Diffusion in porous materials can occur through a number of different diffusion processes such as molecular diffusion, Knudsen diffusion, configurational diffusion and surface diffusion. An overview of these different mechanisms is given below.

Molecular diffusion: Molecular diffusion occurs in porous materials when the pore diameter is significantly larger than the mean free path length of the diffusing species. As such, the diffusion process will be dominated by molecule-molecule collisions as opposed to molecule-pore wall collisions (Figure 3.5).

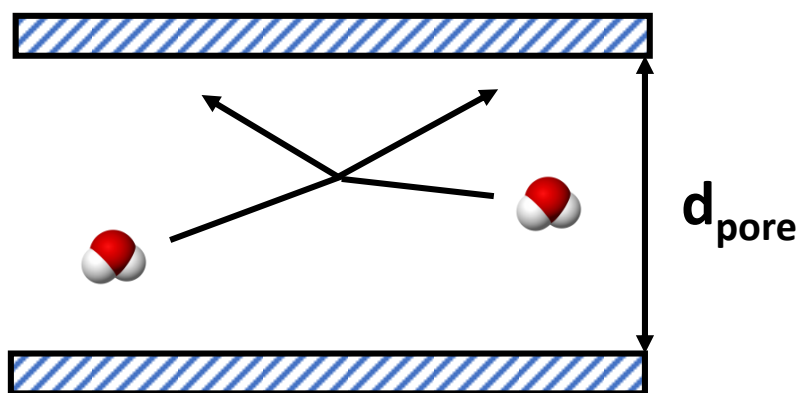
Figure 3.5. Molecular diffusion occurring within the pores of a porous medium. The mean free path length of the diffusing species is smaller than the pore diameter, d_{pore}. The diffusion process will therefore by dominated by molecule-molecule collisions.

This results in a diffusivity defined by Ficks laws as discussed previously. Molecular diffusion in porous materials is defined by:

$$D_M = \frac{2}{3}\left(\frac{kT}{\pi m}\right)^{\frac{1}{2}} \frac{kT}{\pi d^2 p} \tag{3.14}$$

Knudsen diffusion: Knudsen diffusion in porous materials occurs when the mean free path length of the diffusing species is significantly larger than the pore diameter. Consequently, the diffusion process will consist of the diffusing species colliding many times with the pore wall when compared to collisions with other molecules (Figure 3.6).
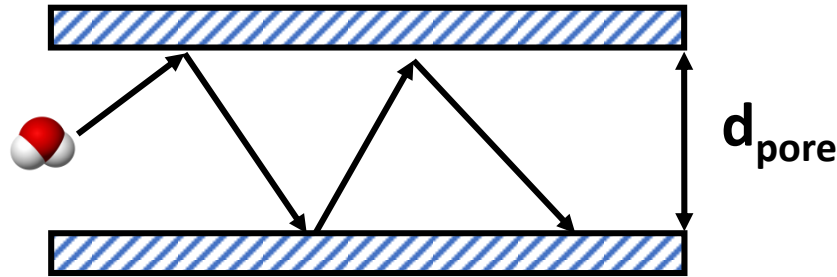
Figure 3.6. Knudsen diffusion occurring within the pores of a porous medium. The mean free path length of the diffusing species is greater than the pore diameter, d_{pore}. The diffusion process will therefore by dominated by molecule-pore wall collisions.

Knudsen diffusion in porous materials is defined by Equation 3.15.

$$D_K = \frac{1}{3} d_p \left(\frac{8kT}{\pi M}\right)^{\frac{1}{2}} \tag{3.15}$$

It is important to note that as the mean free path length of the diffusing species becomes approximately equal to the pore diameter, the overall diffusion process occurring within the porous media will be a result of contributions from both molecular diffusion and Knudsen diffusion as shown in Equation 3.16.

$$\frac{1}{D^*} = \frac{1}{D_M} + \frac{1}{D_K} \tag{3.16}$$

In catalytic materials, porous networks will be highly heterogeneous and consist of irregular porous structures. Therefore, an effective diffusion coefficient, D_{eff} must be defined which accounts for both the porosity, ε, and the tortuosity, τ, of the catalyst as seen in Equation 3.17.

$$D_{eff} = \frac{\varepsilon}{\tau} D_0 \tag{3.17}$$

where D_0 is the bulk diffusion coefficient.

The porosity of a porous medium is defined as the ratio of the total pore volume to the apparent volume and is essentially a measure of the void spaces in the porous medium. The tortuosity of a porous medium is a measure of the 'windiness' of a porous network and is defined as the ratio of the winding path length to the actual path length. A representation of the tortuosity of a porous medium can be seen in Figure 3.7.
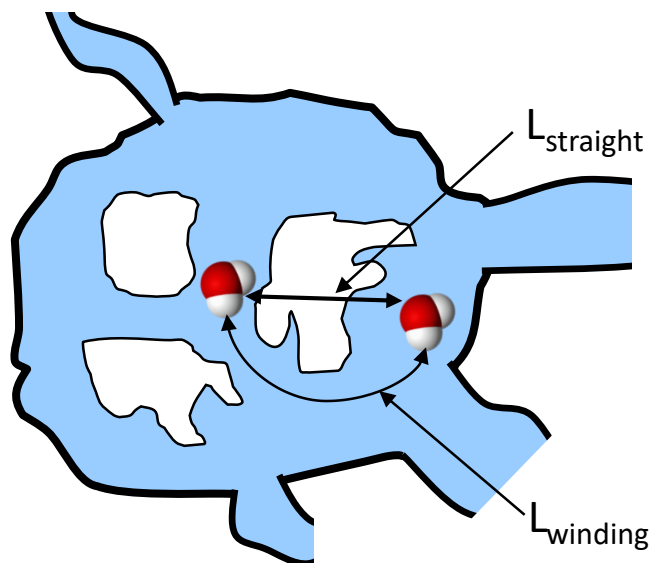
Figure 3.7. A visual representation of the tortuosity of a porous network.

Surface diffusion: In a porous medium, diffusing species will diffuse by a bulk diffusion process driven by a concentration gradient with little or no interaction with the pore walls other than collisions. However, it is also possible for diffusing particles to adsorb to the pore surface and migrate along the porous medium along the pore surface. For porous catalysts, surface diffusion has been shown to contribute significantly to the total mass transfer rate in gas-solid and liquid-solid systems. Surface diffusion is highly dependent upon the composition, structure, physical and chemical properties of the bare pore surface (known as the stationary phase). Additionally, surface diffusion is highly dependent upon the identity of the diffusing substrate as this will influence the strength of interaction between the pore surface and diffusing molecule. Whilst difficult to measure, surface diffusion in certain systems has been determined using certain techniques, both experimental [21] and modelling based. [22]

Configurational diffusion: Configurational diffusion (also known as hindered diffusion or restricted diffusion) occurs when the diffusing species is larger than the pore diameter (Figure 3.8), typically in microporous substrates such as zeolites.

Figure 3.8. Configurational diffusion occurring within the pores of a porous medium. The pore diameter, d_{pore}, is approximately equal to the size of the diffusing species. The diffusion process will therefore by dominated by friction between the diffusing species and the pore wall.

As a result of this, the diffusion process will be dominated by 'drag' on the pore walls and the diffusivity will be drastically reduced due to the steric implications. Configurational diffusion has been shown to result in diffusivity decreases of a few orders of magnitude when compared to other diffusion regimes resulting in severe mass transfer limitations when using catalysts such as microporous zeolites. Changes in the diffusion regime as a function of the pore diameter has been previously reported [23] and can be seen in Figure 3.9. It is important to note that this diagram is valid for gases diffusing within the pores of zeolites. The diagram and values listed are also highly dependent on other factors which may result in variations of the measured diffusivity values and subsequent diffusion regimes. For example, the temperature of the system will greatly impact the determined value. Also, for PFG-NMR, the field of the spectrometer will significantly impact the diffusivity values measured.

More information on diffusion mechanisms and definitions of general terms are given by Cussler. [24]
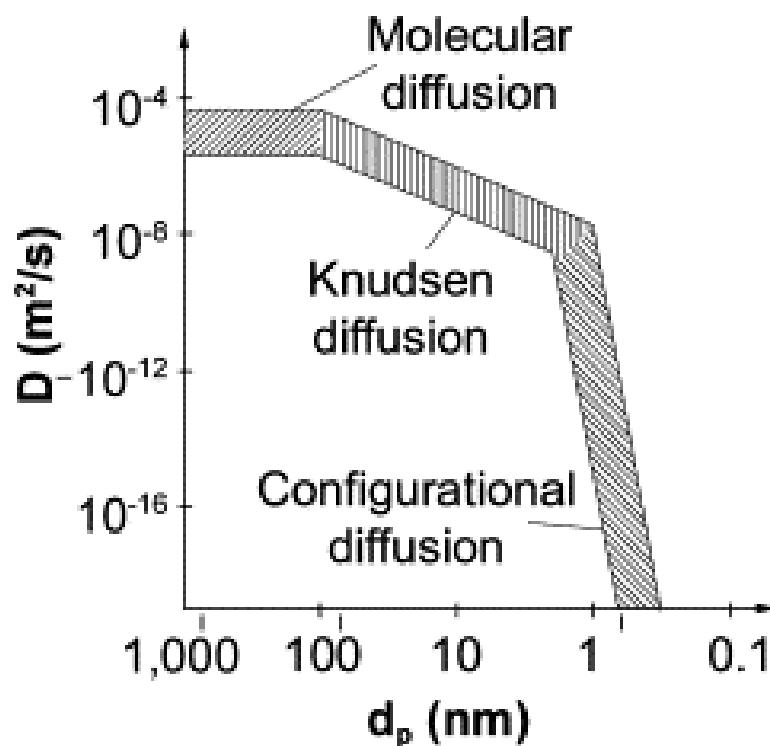
Figure 3.9. The change in diffusion regime as a function of the pore diameter. Figure taken from [23].

References

1. A. Einstein, *Investigations on the theory of the Brownian movement¸* Dover, New York, USA, 1956.

2. R. C. J. Turner, *Chem. Eng. Sci.*, 1975, **30**, 1304-1305.

3. A. E. Fick, *Ann. Phys.*, 1855, **94**, 59-86.

4. E. Wicke and R. Kallenbach, *Kolloid Z.*, 1941, **97**, 135-151.

5. B. Falk, S. Garramone and S. Shivkumar, *Mater. Lett.*, 2004, **58**, 3261-3265.

6. E. Behzadfar and S. G. Hatzikiriakos, *Energy Fuels*, 2014, **28 (2)**, 1304-1311.

7. P. Luo and Y. Gu, *Fluid Ph. Equilibria*, 2009, **277 (1)**, 1-8.

8. S. R. Upreti, A. Lohi, R. A. Kapadia and R. El-Haj, *Energy Fuels*, 2007, **21 (3)**, 1562-1574.

9. C. Gaffney and C. Chau, *Am. J. Phys.*, 2001, **69,** 821-825**.**

10. L. Song, A. Kantzas and J. Bryan, *Experimental measure of diffusion coefficient of CO_2 in heavy oil using X-ray computed-assisted tomography under reservoir conditions*, Canadian Unconventional Resources and International Petroleum Conference, Calgary, Alberta, Canada, 2010.

11. D. Salama and A. Kantzas, *Monitoring of diffusion of heavy oils with hydrocarbon solvents in the presence of sand*, SPE International Thermal Operations and Heavy Oil Symposium, Calgary, Alberta, Canada, 2005.

12. Y. Nakasaka, T. Tago, K. Odate and T. Masuda, *Microporous Mesoporous Mater.*, 2008, **112**, 162-169.

13. J. E. Mungall, D. B. Dingwell and M. Chaussidon, *Geochim. Cosmochim. Acta.*, 1999, **63 (17)**, 2599-2610.

14. H. Cottet, M. Martin, A. Papillaud, E. Souaïd and A. Commeyras, *Biomacromolecules*, 2007, **8 (10)**¸ 3235-3243.

15. P. Passiniemi, S. Liukkonen and Z. Noszticzius, *J. Chem. Soc. Faraday Trans. 1*, 1977, **73**, 1834-1839.

16. A. W. Taylor, P. Licence and A. P. Abbott, *Phys. Chem. Chem. Phys.*, 2011, **13**, 10147-10154.

17. T. Masuda, Y. Fujikata, T. Nishida and K. Hashimoto, *Microporous Mesoporous Mater.*, 1998, **23 (3-4)**, 157-167.

18. A. Anand, V. K. Chhaniwal and C. S. Narayanamurthy, *Appl. Opt.*, 2006, **45 (5)**, 904-909.

19. K. Gong, B. Subramaniam, P. A. Ramachandran and K. W. Hutchenson, *AIChE J.*, 2010, **56 (5)**, 1285-1296.

20. L. Hu, Z. Chen, W. Sun, T. Cheng, Y. Wei, C. Xu and S. Zhao, *Ind. Eng. Chem. Res.*, 2020, **59 (17)**, 8426-8435.

21. D. Weber, A. J. Sederman, M. D. Mantle, J. Mitchell and L. F. Gladden, *Phys. Chem. Chem. Phys.*, 2010, **12**, 2619-2624.

22. D. D. Do and R. G. Rice, *Chem. Eng. Sci.*, 1987, **42 (10)**, 2269-2284.

23. S. Sommer, T. Melin, J. L. Falconer and R. D. Noble, *J. Membr. Sci.*, 2003, **224(1-2)**, 51-67.

24. E. L. Cussler, *Diffusion: Mass Transfer in Fluid Systems*, Cambridge University Press, Cambridge, 1997.

Chapter 4: Tailoring textural properties for tuning diffusion behaviour of alumina catalytic materials: A rational guideline exploiting bench-top Pulsed-Field Gradient (PFG) Nuclear Magnetic Resonance (NMR)

This chapter has been published as a full article in the journal *Molecular Systems Design and Engineering.* [1] [Tailoring morphology of hierarchical catalysts for tuning pore diffusion behaviour: a rational guideline exploiting bench-top pulsed-field gradient (PFG) nuclear magnetic resonance (NMR) - Molecular Systems Design & Engineering (RSC Publishing)](#)

Author contributions are as follows; Luke Forster conceived the research ideas, performed the NMR measurements, data processing and analysis and wrote the full article. Henrik Fordsmand and Michal Lutecki performed the carrier preparation, porosimetry and XRD measurements. Carmine D'Agostino managed the research work, wrote and revised the article.

Luke Forster was awarded the IChemE Junior Moulton Medal 2021 awarded to the early career author, or authors, of the most meritorious paper published by IChemE during the last year for this paper.

Abstract

Alumina catalyst carriers were prepared from boehmite using varying preparation conditions to produce carriers with different pore sizes and macropore content. Pore size and macropore content decreased with boehmite mixing time and increased with calcination temperature due to alumina phase transformations occurring. Mass transport within the different materials was studied by pulsed-field gradient (PFG) NMR diffusion techniques, with a low-field, bench-top NMR instrument, using *n*-octane as the probe molecule. The diffusion results revealed that mass transport occurs more readily in carriers with greater pore size and macropore content, by providing a comprehensive and quantitative description of this behaviour. In particular, up to a pore size of 17.0 nm diffusion increases very rapidly with pore size; at pore sizes greater than 17.0 nm and macropore content greater than 27 % the major geometrical restrictions imposed by the pore structure on the probe molecule were removed and the diffusivity of guest molecules reaches a constant plateau, suggesting that above such values of pore size and macropore content, no

further improvements in mass transport are obtained. Diffusion studies using water, methanol and ethanol, as probe molecules with functional hydroxyl groups able to interact with the surface, showed that in samples with small pores and no amount of macropores, surface interactions of these guest molecules with the pore surface have a significant effect on determining the diffusive motion, in addition to the effect of the physical pore structure. For larger pores and larger macropore content, the surface chemistry of the pore walls has a much smaller impact on the diffusive motion inside the porous matrix. This work gives a comprehensive and quantitative overview on how to tailor carrier preparation procedures in order to tune mass transport, providing a rational guideline with important implications in preparation, applications and physical chemistry of porous materials

4.1. Introduction

The development of catalytic materials with suitable textural properties is essential to achieving high activity, [2] selectivity [3] and reusability [4] in catalytic processes. One example of where control of the textural properties of the catalyst is required can be seen in hydrotreating desulfurization processes, that is, the removal of sulphur from natural gas or refined petroleum products. [5] For example, in upstream hydrotreating of diesel, when alumina is used as a substrate a high surface area and relatively small pores (ca. 4 nm) are desired for high activity [6] whereas for downstream processes, such as heavy vacuum gas oil or resid hydrotreating, larger pores (ca. 7 –13 nm) [7, 8] are required to allow diffusion and access of larger molecules to the catalyst active sites. Conversely, certain highly selective processes such as the partial epoxidation of ethylene to ethylene oxide [9, 10] and the selective oxidation or selective hydrogenation of acetylene [11] require catalysts with large pores and low surface areas to limit the residence time of substrate on the catalyst thereby boosting selectivity to the desired products by limiting further reactions on the catalyst surface. [12, 13] The importance of controlling the textural properties of a catalyst can also be seen in the design of hierarchical zeolites, where an additional pore system is introduced to the zeolite crystal, aiming at alleviating mass transport limitations imposed by the zeolite micropores. [14] Many studies have investigated the tuning of textural properties of both catalysts and catalyst supports, including carbon materials, [15-17] zeolites, [18, 19] silicas, [20, 21] titanias [22] and aluminas [23-25] which are all commonly used as supports for catalytic materials.

Mass transport and textural properties are widely known to be highly inter-related; in particular, tailoring pore structures in order to modify diffusion properties is an aspect of high relevance in the field of heterogeneous catalysis. For example, the importance of such a relationship has been reported to play a role in zeolite catalysis during acetalization reactions, whereby the observed increase in catalytic activity of hierarchically structured Y zeolites with introduced mesoporosity was attributed to the enhanced diffusion of guest molecules within the pore matrix relative to the purely microporous parent Y zeolite. [26] Such a conclusion was solely based on observations on catalytic conversion measurements as no attempt to quantify diffusion rate inside the pore matrix was made. It is indeed the case that whilst the relationship between textural properties and mass transport is often discussed on qualitative basis, relatively little work has been carried out to systematically investigate the effect of tailoring textural properties of porous catalytic particles on intra-particle diffusion. Previous work has detailed the relationship between pore structure and the overall diffusivity of molecules throughout the respective porous space and how this can then, in turn, affect the catalytic activity of reactions using such catalytic materials. [27–29] Therefore, it is clear that a rational overview aimed towards the design of materials with tailored textural properties, and therefore molecular diffusivity through their porous network, is desirable.

A powerful tool to probe diffusion inside porous materials is the Pulsed-Field Gradient (PFG) NMR techniques. [30-36] Amongst notable work done in the area of zeolites, Kortunov et al. [37] have investigated the effect of introducing mesopores in microporous zeolites showing that if the introduced pores form as isolated cavities, little or no increase in diffusion coefficient is observed. Conversely, the formation of a newly formed interconnected pore network is expected to lead to significant changes in diffusion coefficients. Indeed, in a recent work on hierarchical macroporous–mesoporous SBA-15 sulfonic acid catalysts with interconnected macropores of tuneable diameter, used for esterification reactions of bio-derived feedstock, it was shown that pore size and connectivity are not mutually exclusive and that enhanced mass transport can be achieved through tailoring the macropore size to the reactant size. [38]

Whilst this previous work suggests that the introduction of macropores to mesoporous structures enhances mass transport by diffusion, a systematic study looking at the effect of catalyst manufacturing procedures for tailoring textural properties, by introducing macropores, and tuning diffusion properties, has not yet been reported; yet, a comprehensive analysis of this would lead to

a more rational and guided design of pore structures with certain transport properties. In this work, we carried out a comprehensive and systematic study on how tailoring textural properties of industrial catalytic materials, through various preparation procedures, affects mass transport by diffusion. In particular, we assess the effect of operating conditions in the preparation of hierarchical alumina carriers on the final textural properties of the materials and how this, in turn, affect mass transport by diffusion, the latter quantified using low-field, bench-top PFG NMR experiments with different guest probe molecules.

4.2. Experimental

4.2.1. Materials and chemicals

Methanol (anhydrous, 99.9 %, 25 mL) and ethanol (>99.7 %, 25 mL) were supplied by Alfa Aesar, *n*-octane (>99 %, 25 mL) was supplied by Merck. All chemicals were used as received. Deionised water was obtained from a laboratory water purification system.

4.2.2. Carrier preparation

The alumina carriers were supplied by Haldor Topsøe. A number of 8 different samples were investigated denoted as Al_2O_3 (1) – Al_2O_3 (8). Carriers were prepared by mixing boehmite powder with water in the presence of nitric acid to obtain 600 g of uniform paste. The amount of nitric acid was set to 10 mmol per 1 mol of alumina on calcined basis for all samples. The amount of water expressed as water-to-boehmite ratio (g/g) varied between samples and was set to 1 for Al_2O_3 (1) – Al_2O_3 (4) and 1.18 for Al_2O_3 (5) – Al_2O_3 (8). Additionally, Al_2O_3 (1) – Al_2O_3 (4) were mixed for 25 minutes, while samples Al_2O_3 (5) – Al_2O_3 (8) were only mixed for 6 minutes (Table 4.1). Subsequently, the resulting paste was extruded into trilobe pellets (4 mm length, 1 mm diameter), dried and calcined at various temperatures and conditions (Table 4.1). The structural properties of all carriers were studied by Haldor Topsøe using mercury (Hg)- intrusion porosimetry. Samples were dried at 250 °C prior to analysis. Hg-intrusion measurements were performed on an Autopore IV instrument from Micromeritics.

4.2.3. X-Ray diffraction (XRD) measurements

The materials were analyzed by X-ray diffraction using a Panalytical XPert Pro instrument system in Bragg-Brentano geometry working in reflectance mode using CuK_α radiation (λ = 1.541 Å).

The instrument is equipped with a monochromator, soller-, divergence- and anti-scatter slits with a scan range of 5-70 degrees. Rietveld analysis was carried out using the Topas Software.

4.2.4. PFG NMR diffusion measurements

The samples for PFG NMR measurements were prepared by soaking the porous solid under investigation in the liquid of choice (~2 mL) for over 24 h prior to the measurements in order to ensure full saturation of the intra-particle pore space; different guest molecules (*n*-octane, water, methanol or ethanol) were used for the study. The liquid-saturated solid samples were then dried on a pre-soaked filter paper to remove any excess liquid from the external surface and transferred to 5 mm NMR tubes. To ensure a saturated atmosphere in the NMR tube, hence minimising errors due to evaporation of volatile liquids, a small amount of the respective pure liquid was absorbed onto filter paper, which was then placed under the cap of the NMR tube. The tube sample was finally placed into the magnet and left for approximately 15 min before starting the measurements, in order to achieve thermal equilibrium. NMR experiments were performed in a Magritek SpinSolve benchtop NMR spectrometer operating at a ^{1}H frequency of 43 MHz. The PFG NMR experiments were carried out using a diffusion probe capable of producing magnetic field gradient pulses up to 163 mT m^{-1}. Diffusion measurements were performed using the pulsed-field gradient stimulated echo sequence (PGSTE sequence). [39] The sequence is made by combining a series of radiofrequency pulses (RF) with magnetic field gradients (g), according to Figure 2.11.

The NMR signal attenuation of a PFG NMR experiment as a function of the gradient strength, *E(g)*, is related to the experimental variables and the diffusion coefficient (*D*) by Equation 2.38.

Equation 2.38 assumes a Gaussian distribution of the diffusing spins and it generally applies to free diffusion, such as the case of bulk liquids. [40] However, this equation can also be applied for diffusion in porous materials with a quasi-homogeneous behaviour, that is, with a macroscopically homogeneous pore structure, [41] which shows a linear behaviour of the PFG log plot of the signal attenuation.

The measurements were performed by fixing Δ = 50 ms and using values of δ = 4 - 12 ms depending on the sample. The magnitude of g was varied linearly with sixteen spaced increments. In order to achieve full signal attenuation, maximum values of g of up to 163 mT m^{-1} were

necessary. All the measurements were performed at atmospheric pressure and 25 °C. The diffusion coefficients D were calculated by fitting Equation 1 to the experimental data.

4.3. Results and discussion

4.3.1. Effect of alumina preparation conditions upon the carrier textural properties

The alumina samples were prepared as detailed in the experimental section using varying preparation conditions and their impact upon the porous structure of the final alumina sample was determined. The parameters varied in the preparation of the alumina samples can be seen in Table 4.1.

Table 4.1. Preparation conditions used in the preparation of each alumina sample. All calcinations were carried out using a temperature ramp of 5 °C min^{-1} and a hold time of 2 hours. The mixing speed used for preparation was 5000 rpm. *calcined in the furnace on the net (1 cm layer), **calcined in the furnace in the closed container (5cm layer)

Sample	Water to boehmite ratio (-)	Mass of nitric acid (g)	Mixing time (min)	Calcination temperature (°C)
Al_2O_3 (1)	1.00	2.40	25	550 (dry*)
Al_2O_3 (2)	1.00	2.40	25	550 (wet**)
Al_2O_3 (3)	1.00	2.40	25	700 (dry)
Al_2O_3 (4)	1.00	2.40	25	700 (wet)
Al_2O_3 (5)	1.18	1.00	6	700 (wet)
Al_2O_3 (6)	1.18	1.00	6	900
Al_2O_3 (7)	1.18	1.00	6	1100
Al_2O_3 (8)	1.18	1.00	6	1200

The alumina carriers prepared according to the conditions reported in Table 4.1 were characterized by mercury porosimetry. The mean pore diameter (d_{pore}), percentage of macropores of varying size within the carrier studied and surface area-to-volume ratio (S/V) were determined and are listed in Table 4.2.

Table 4.2. Mercury porosimetry characterisation of the alumina carriers used in this study.

Sample	d_{pore} (nm)	Macropores > 50 nm (%)	Macropores > 200 nm (%)	Surface area (m^2g^{-1})
Al$_2$O$_3$ (1)	8.0 ± 0.2	2	1	367.7
Al$_2$O$_3$ (2)	9.2 ± 0.3	2	1	345.9
Al$_2$O$_3$ (3)	10.4 ± 0.3	2	1	293.8
Al$_2$O$_3$ (4)	11.8 ± 0.4	2	1	280.4
Al$_2$O$_3$ (5)	17.0 ± 0.5	25	21	225.1
Al$_2$O$_3$ (6)	22.4 ± 0.7	27	23	178.3
Al$_2$O$_3$ (7)	53.6 ± 1.6	67	32	49.6
Al$_2$O$_3$ (8)	201.6 ± 6.0	99	62	12.0

From the mercury porosimetry analysis, it can be seen that the samples studied contain a wide variety of average pore sizes, degrees of macroporosity and surface areas. From the results obtained, it is clear to see that there are 2 main factors which significantly influence the pore structure of the alumina produced: the mixing time, t_{mix}, and the calcination temperature. It can be seen that those samples with a significantly longer t_{mix} contain no macropores within their pore structures, for example, Al$_2$O$_3$ (4) and Al$_2$O$_3$ (5) are both calcined at 700 °C but mixed for differing lengths of time. Al$_2$O$_3$ (4) is mixed for 25 minutes and contains only 2 % of macropores with a mean pore diameter > 50 nm whereas Al$_2$O$_3$ (5) is mixed for only 6 minutes resulting in a final alumina carrier containing 25 % macropores with a mean pore diameter > 50 nm. In general, the average pore size increases as macroporosity increases and in turn, these factors reduce the overall surface area-to-volume ratio, as shown in Figure 4.2. It should be noted that the acid/boehmite and water/boehmite ratio also have an influence on the final pore volume of the alumina carrier. By increasing water/boehmite ratio, dry matter content decreases which acts to increase pore volume (at the same mixing time and rate). The acid it is needed to peptitize alumina, therefore, the more acid added will result in more peptitization. This means that the more acid added the lower the pore volume of the final carrier (at the same mixing time and rate as well as the same dry matter content).
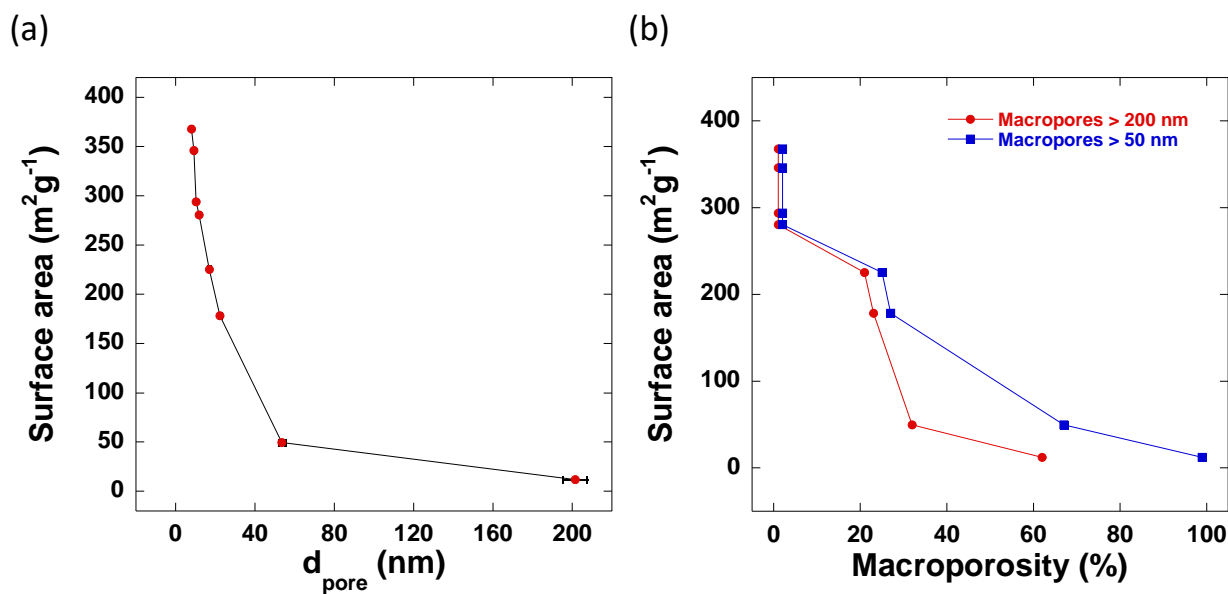
(a)

(b)

Figure 4.2. (a) The dependence of the surface area-to-volume ratio upon the average pore size of the alumina carriers and (b) the dependence of the degree of carrier macroporosity upon the surface area-to-volume ratio. The lines are a guide to the eye.

It must be considered that the surface area-to-volume ratio (*S/V*) of a porous particle is complex in nature and is dependent upon many factors including the porosity, shape, size and roughness of a specific particle in addition to the pore size distribution. However, the results of the mercury porosimetry analysis show that, for the samples being studied, *S/V* is significantly influenced by both the presence of macroporosity and the average pore size. In particular, both a low average pore size and degree of macroporosity is essential for preparing high surface area-to-volume ratio alumina carriers.

The calcination temperature is also seen to significantly affect the final pore structure of the alumina carriers. Al_2O_3 (5) - Al_2O_3 (8) were all prepared by mixing for a relatively short mixing time of 6 minutes resulting in the formation of macropores. Each of these alumina carriers containing macroporosity were then subject to calcination at varying temperatures. The effect of varying calcination temperature upon the final macropore content within the aluminas mixed for 6 minutes only can be seen in Figure 4.3.
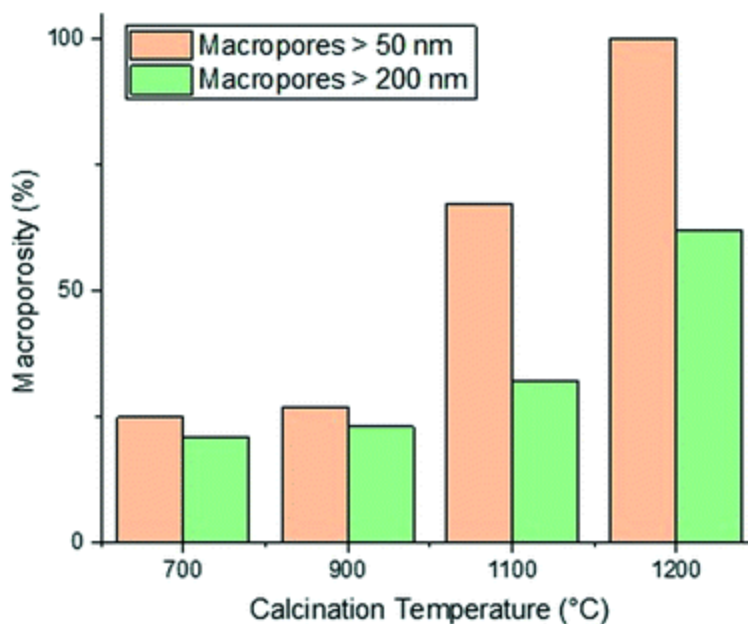
Figure 4.3. The dependence of the preparation calcination temperature of the carriers Al_2O_3 (5) – Al_2O_3 (8) upon the percentage of macropores with diameter > 50 nm and the percentage of macropores with diameter > 200 nm within the carrier produced.

As the calcination temperature is increased, the alumina particles will begin to sinter, forming bigger alumina particles and eventually inducing phase transformations causing the collapse of small pores and resulting in the formation of large mesopores and macropores. [42] At temperatures below 900 °C, phase transformations do not occur and the carriers are composed of γ-Al_2O_3 only. At 900 °C, γ-Al_2O_3 particles begin to sinter and transition partly to θ-Al_2O_3 and above 900 °C, the carriers are composed solely of θ-Al_2O_3 and α-Al_2O_3. The phase transformations that occur result in changes to the textural properties of the resultant carriers, specifically d_{pore} and the percentage of macropores within the samples increases whilst the surface area decreases. As such, the samples prepared using a calcination temperature less than 900 °C (Al_2O_3 (1) - Al_2O_3 (5)) will be composed of γ-Al_2O_3 only. This is confirmed from the XRD analysis of Al_2O_3 (5) (Figure 4.4a) showing peaks characteristic of γ-Al_2O_3. [43, 44]
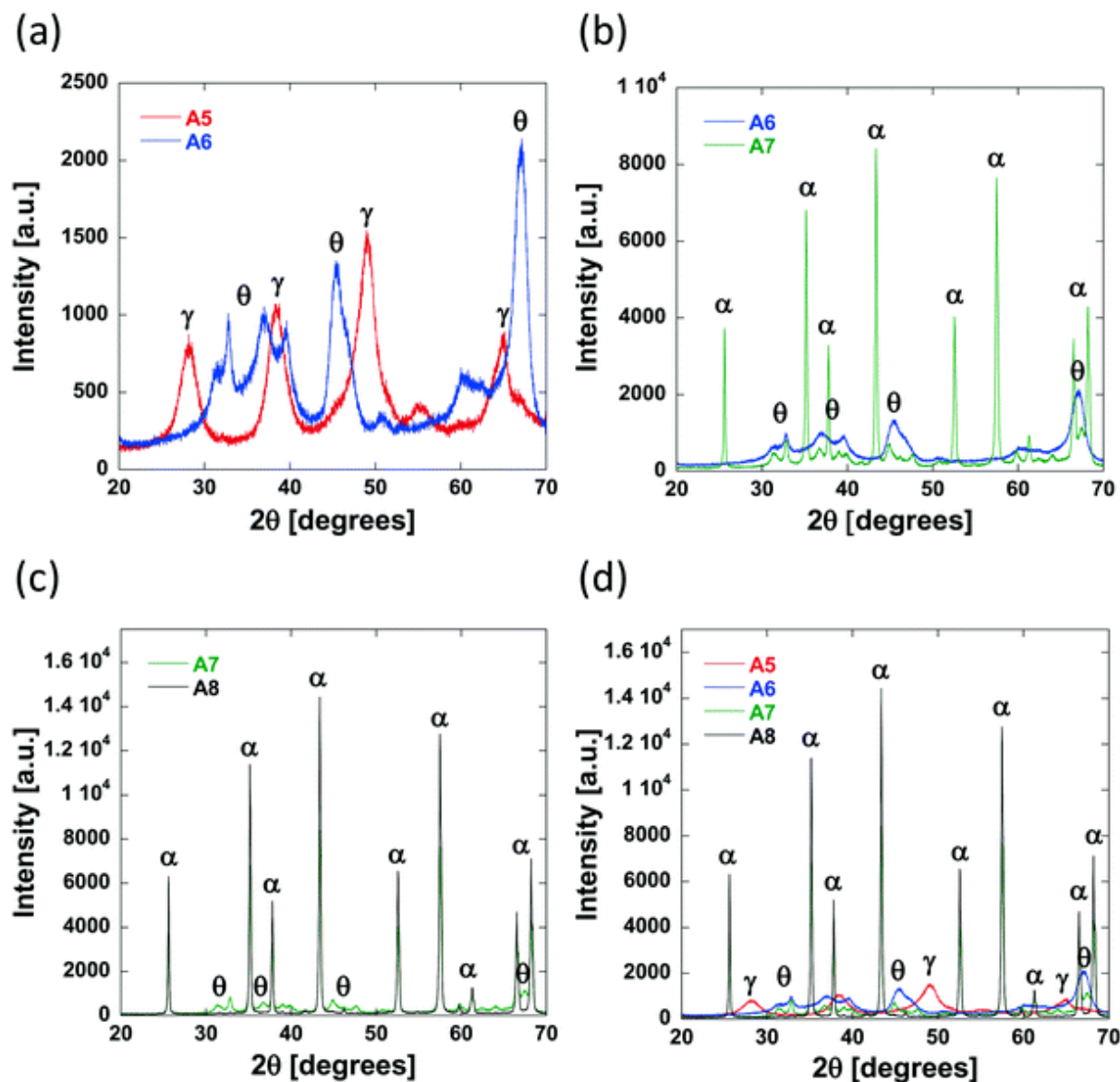
Figure 4.4. XRD patterns of (a) Al_2O_3 (5) and Al_2O_3 (6), (b) Al_2O_3 (6) and Al_2O_3 (7), (c) Al_2O_3 (7) and Al_2O_3 (8), and (d) Al_2O_3 (5) - Al_2O_3 (8) to show the different alumina phases present in each sample and the transformations that occur when the preparation conditions are altered. The symbols γ, θ and α indicate peaks representative of γ, θ and α-Al_2O_3 respectively.

As the preparation calcination temperature is increased from 800 ºC to 900 ºC (Al_2O_3 (5) to Al_2O_3 (6), Figure 4.4a) peaks indicative of the presence of θ-Al_2O_3 [45] appear confirming that phase transformations are taking place and are therefore responsible for the change in textural properties seen. As the calcination temperature is increased further, from 900 ºC for Al_2O_3 (5) to 1100 ºC and 1200 ºC in Al_2O_3 (7) and Al_2O_3 (8) respectively, it can be seen that the θ-Al_2O_3 peaks disappear

and sharper more intense peaks appear in their place, which are indicative of the presence of α-Al_2O_3, [46] the most thermally stable of the alumina phases.

4.3.2. PFG NMR studies: Effect of pore network connectivity on self-diffusion

We now turn our attention to how the textural properties of the final carrier, determined by the different operating conditions in the preparation methods, influence mass transport within the pore structure. One important parameter to assess is the tortuosity, which is a structural property of the porous matrix defining the pore connectivity; knowledge of this parameter is important as values of tortuosity are highly desirable as input parameters for modelling and molecular simulations of mass transport within porous materials. [47] The tortuosity is, in theory, a function of the pore structure only and can be calculated using PFG NMR. Taking the ratio of the free bulk liquid diffusivity, D_0, to the effective diffusivity of the liquid within the porous material, D_{eff}, gives a dimensionless "PFG interaction parameter", ξ. [48] This relation is shown in Equation 4.1:

$$\xi = \frac{D_0}{D_{eff}} \tag{4.1}$$

This ratio has commonly been inaccurately referred to as the tortuosity, τ, of a porous material. [49] PFG NMR allows the calculation of the tortuosity of a porous medium defined in Equation 3:

$$\tau = \frac{D_0}{D_{eff}} \tag{4.2}$$

The important distinction between the parameters defined in Equations (4.1) and (4.2) is that for Equation (4.2), D_{eff} represents the effective self-diffusivity of a weakly-interacting molecule only. Clearly then, the selection of an appropriate guest molecule for PFG NMR experiments is essential to determine the actual tortuosity of a porous medium. Liquid alkanes have been shown to be the most suitable guest molecules for determining tortuosity by PFG NMR experiments [50] due to their distinct lack of chemical functionalities which can interact with the porous medium or indeed, with any other molecules present with the porous medium under study. Effectively, the use of liquid alkanes ensures that the tortuosity calculated is dependant solely on the pore connectivity and is unaffected by any other interactions that could otherwise alter the self-diffusivity of the guest molecule. Previous work by D'Agostino et al. [50] has proven that a good estimate of tortuosity is therefore given by:

$$\tau \equiv \xi_{Alkanes} \qquad (4.3)$$

To probe the tortuosity of the samples studied here we have used *n*-octane. Previous studies have demonstrated that short chain liquid alkanes, namely *n*-octane, *n*-decane and cyclohexane, give reliable values of τ regardless of molecular dimension size. [41] A typical PFG NMR decay plot using *n*-octane imbibed within an alumina pellet used in this study can be seen below in Figure 4.5.
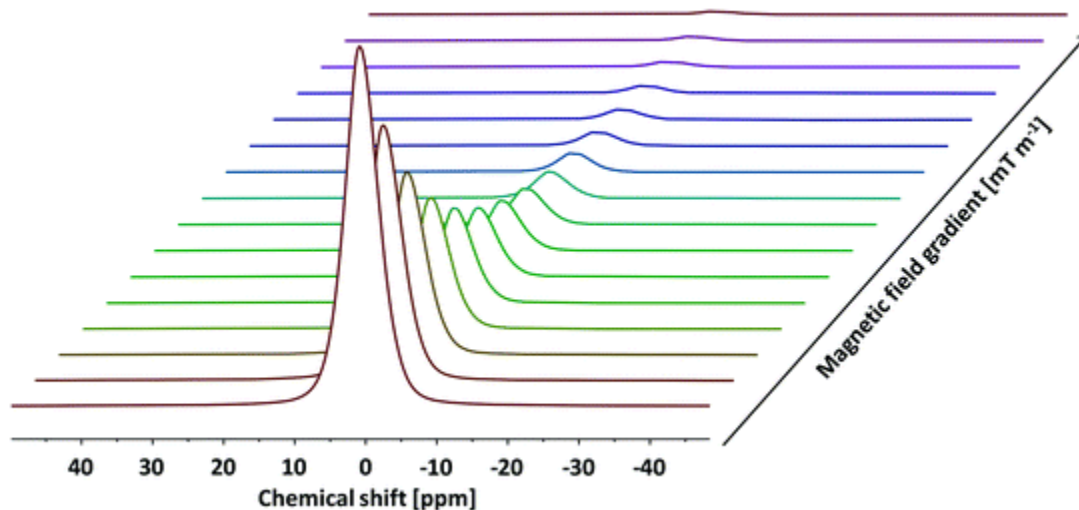

Figure 4.5. A typical PFG NMR decay plot of *n*-octane imbibed within Al_2O_3 (1) obtained using the PGSTE pulse sequence. Self-diffusion coefficients were obtained by fitting the log attenuations to Equation 1. Data collected at atmospheric pressure and 25 °C.

The log attenuation plots of n-octane imbibed within pellets of the alumina carriers under study can be seen in Figure 4.6. The experimental data were fitted using Equation 1, giving a straight line when plotted on a logarithmic scale. Diffusion coefficients were determined by taking the negative value of the respective slopes.
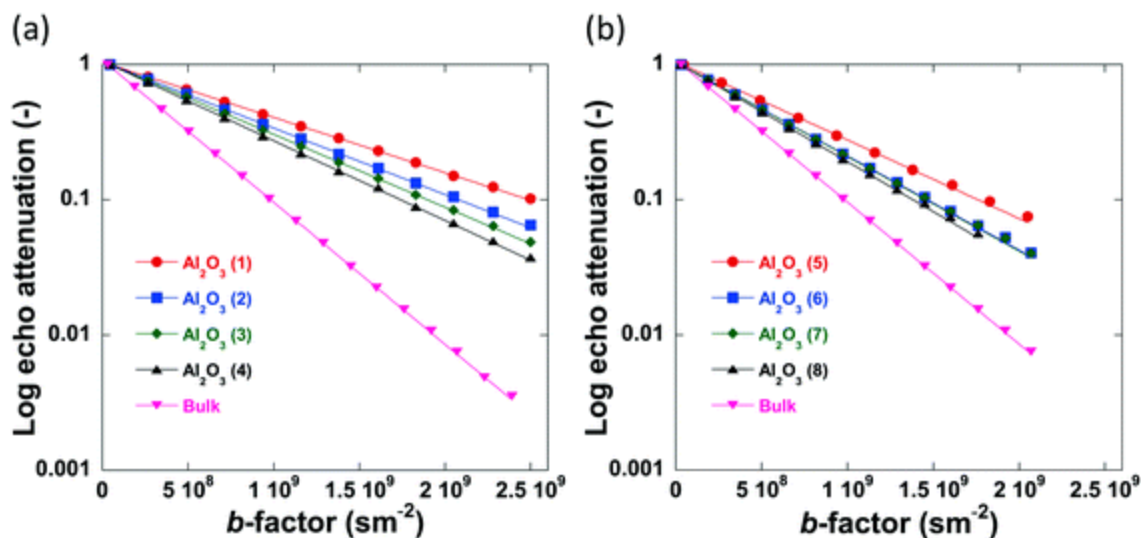
Figure 4.6. Log attenuation plots of *n*-octane imbibed within (a) Al_2O_3 (1) – Al_2O_3 (4) and (b) Al_2O_3 (5) – Al_2O_3 (8). Solid lines are fitting to Equation 1.

No evident curvature is seen in the log attenuation plots indicating that the behaviour is *quasi-homogeneous*. [51] This behaviour is usually observed for porous materials with a macroscopically homogeneous pore structure when the root mean squared displacement (*RMSD*) of the diffusing species is much larger than the average pore size of the sample, i.e., the probe molecule will collide with the pore walls many times. As a result, D_{eff} will be representative of the liquid confined within the porous medium and reduced by the tortuosity factor relative to the free bulk liquid. [51] The *RMSD* is defined by:

$$RMSD = \sqrt{2 \cdot D_{eff} \cdot t} \qquad (4.4)$$

The smallest *RMSD* used for the measurements with *n*-octane (Table S4.1) was used when investigating the tortuosity of Al_2O_3 (1) and this was equal to 9.7 μm, much larger than the largest average pore size of the samples studied (201.6 nm). The *quasi-homogeneous* diffusion behaviour reported for our samples have important implications in terms of industrial scale-up of carrier preparation as it indicates that the preparation method reported here gives carrier particles with a uniform pore structure. *RMSD* is far greater than the average pore size in each sample which implies that each measurement is representative of the entire pore space in each sample.

The numerical values of the self-diffusivity coefficients obtained from the PFG NMR measurements shown in Figure 4.6 are shown in Table 4.3. It should be noted that the reference *n-*

octane measurements in this thesis will likely differ from those in the literature due to factors such as the field of the spectrometers used and the temperature of the system

Table 4.3. Self-diffusivity coefficients and calculated tortuosity values of the alumina carriers determined using PFG NMR diffusometry of imbibed *n*-octane (free bulk self-diffusivity also reported). The relative error on all measurements is approximately 3 %. The error was determined from the standard deviation of many previous measurements on the spectrometer and this error value is used throughout the thesis for all NMR measurements.

Sample	D_{eff} (m^{2}s^{-1}·10^{10})	τ (-)
Al$_2$O$_3$ (1)	9.41 ± 0.28	2.57 ± 0.08
Al$_2$O$_3$ (2)	11.13 ± 0.33	2.17 ± 0.07
Al$_2$O$_3$ (3)	12.42 ± 0.37	1.95 ± 0.06
Al$_2$O$_3$ (4)	13.56 ± 0.41	1.78 ± 0.05
Al$_2$O$_3$ (5)	13.40 ± 0.40	1.81 ± 0.05
Al$_2$O$_3$ (6)	16.03 ± 0.48	1.51 ± 0.05
Al$_2$O$_3$ (7)	16.13 ± 0.48	1.50 ± 0.05
Al$_2$O$_3$ (8)	17.00 ± 0.51	1.42 ± 0.04
Bulk	24.14 ± 0.72	-

As the tortuosity is a measure of the pore connectivity and is therefore a function of the pore structure of the porous materials under study, it seems appropriate to evaluate this parameter as a function of the average pore size of the alumina carriers; despite tortuosity, which measures pore connectivity, and pore size are in theory independent of each other, previous work has reported that these two parameters can be inter-related [52] and that larger pores tend to enhance pore network connectivity, hence enhance the rate of diffusion of the probe molecule within the porous structure.

Figure 4.7 reports the values of self-diffusivity of *n*-octane and corresponding tortuosity values in the alumina samples studied here as a function of the average pore diameter.
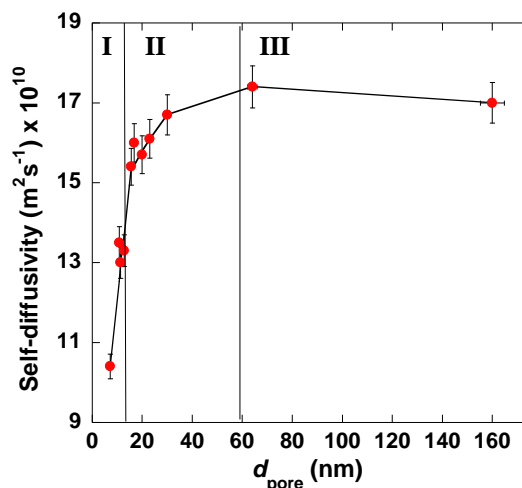
Figure 4.7. The pore size dependence of the self-diffusivity of *n*-octane imbibed within the pores of the alumina carriers.

The values of tortuosity reported in this work were found to be of a similar value to those reported in the literature for the same guest molecules within similar porous materials. [53, 54] Both the self-diffusivity and tortuosity values show a strong dependence upon the average pore diameter at low values of pore size. The self-diffusivity of *n*-octane increases drastically upon increasing the pore size from 8.0 nm to 17.0 nm. At average pore sizes higher than 17.0 nm the self-diffusivity no longer increases with increasing pore size and becomes constant, within error, at roughly $1.65 \times 10^{-9}\,\text{m}^2\text{s}^{-1}$ when pore sizes are greater than 17.0 nm. Clearly, it is reasonable to group the samples studied in this work into 2 groups based on these results. Those with small (up to 17.0 nm) average pore sizes and those with relatively 'large' pore sizes, that is, those with pore sizes greater than 17.0 nm. These groupings are indicated in Figure 4.7 by the regions I and II representing the small and relatively large pore size samples, respectively. These results can be explained as a molecular confinement effect due to the small size of the pores. At the low pore size of 8.0 nm, the *n*-octane molecules are highly confined and will be subject to many collisions with the pore walls. As the pore size is increased, some of this restriction is lifted; hence, molecules are relatively freer to move and as such collide with the pore walls less and therefore exhibiting a larger *RMSD*, hence faster diffusion. When the pore size is large ($d_{pore} > 17.0$ nm), the level of confinement is further decreased, which further increases the *RMSD* and hence the average self-diffusivity. As the tortuosity is effectively proportional to the inverse of the self-diffusivity the same trend is seen but with the tortuosity decreasing as pore size increases, as would be expected. In summary, the results

reported in Figure 4.7 clearly demonstrate that larger pores ensure a better pore network connectivity, hence a lower tortuosity.

Due to the pore size dependence of both the diffusivity and tortuosity of the samples studied in this work, it is important to consider also the contribution of the relative proportions of macropores present within the samples in determining the average pore size. Figure 4.8 reports the values of self-diffusivity as a function of the macropore percentage. It can be seen that in general, a greater percentage of macropores present within a sample aids mass transport and decrease tortuosity, hence improving pore network connectivity, possibly by providing wider, less restricted pathways through which molecules can diffuse. Wider pores will inevitably result in less collisions with the pore walls and therefore molecules will diffuse faster within the porous structure.
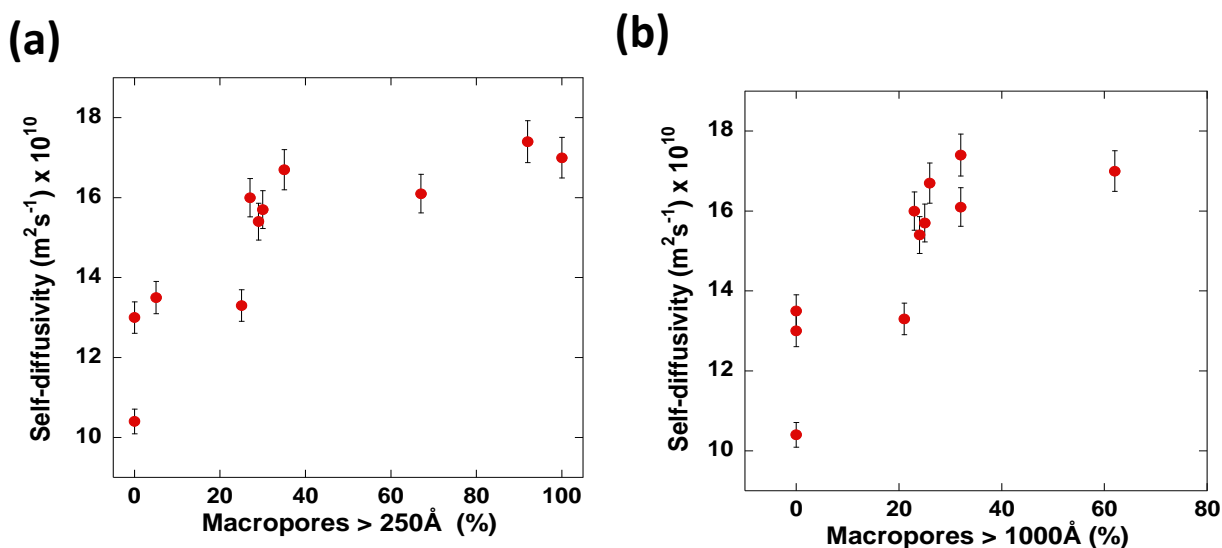

Figure 4.8. The effect of the percentage of macropores with a radius greater than 50 nm on (a) the self-diffusivity of *n*-octane imbibed within the alumina carriers and ((b) the effect of the percentage of macropores with a radius greater than 200 nm on the self-diffusivity of imbibed *n*-octane and the calculated tortuosities, respectively.

The samples possessing no macropores with a radius greater than 50 nm, show differing values of diffusivity and tortuosity. As there are little to no macropores present in these samples, the value of diffusivity measured is influenced solely by the average pore sizes. Indeed, this is evidenced as, of the samples containing no macropores, the slowest self-diffusivity value of 9.41×10^{-10} m^2s^{-1} is observed in Al_2O_3 (1) with an average pore size of 8.0 nm. Al_2O_3 (2) – Al_2O_3 (4) also possess no macropores but show faster self-diffusivity values owing to their larger pore sizes. Therefore, it is

reasonable to conclude that, for samples containing a similar macropore content, the diffusivity is determined by the restrictions imposed upon the guest molecules due to the average size of the pores.

When the carriers contain between 0 – 27 % of macropores with a radius greater than 50 nm, the diffusivity increases/tortuosity decreases as the contribution of the macropore diffusivity to the overall mass transport processes taking place becomes significant. Carrier samples containing more than 27 % of macropores with a radius greater than 50 nm show no significant increase in diffusivity indicating that at 27 % macroporosity the main transport route is through the macropores.

When the percentage of macropores with a radius greater than 200 nm are considered, a similar trend is observed. Therefore, it is reasonable to conclude that, for the samples studied here, a macropore radius of 50 nm is sufficient to alleviate any restriction upon guest molecules, allowing *n*-octane to diffuse faster with less geometrical restrictions imposed by the porous network. It can also be concluded that the pore connectivity of the alumina carriers is enhanced up to a maximum path length of 1 μm as determined from the RMSD values. Despite the obvious interlinked relationship between the percentage of large macropores and the average pore diameter seen within the samples, it is important to consider how both factors impact the mass transport of guest molecules throughout the entire porous network.

4.3.3. PFG NMR studies: Effect of pore surface chemistry on self-diffusion

The previously discussed 'PFG interaction parameter' ξ, can be used to determine the effect of the surface chemistry and subsequent surface interactions upon the self-diffusivity of guest molecules imbibed within the pores of a given porous material. [48, 50] The PFG interaction parameters determined using water, methanol and ethanol are shown in Table 4.4 and the variation in these values with increasing pore size can be seen in Figure 4.9. The log attenuation plots of water, methanol and ethanol imbibed within pellets of the alumina carriers under study can be seen in Figures S4.1 – S4.3. Hydrogen bonding between molecules with appropriate functional groups and surface hydroxyl groups on a catalyst surface are thought to be significant interactions in adsorption and desorption in catalytic processes [55] and can contribute to solvent effects [56, 57] resulting in changes in catalytic activity.

Table 4.4. PFG interaction parameter values, ξ, of water, methanol and ethanol imbibed within the alumina carriers. The tortuosity, τ, of the carriers measured using weakly-interacting n-octane is reported as a benchmark.

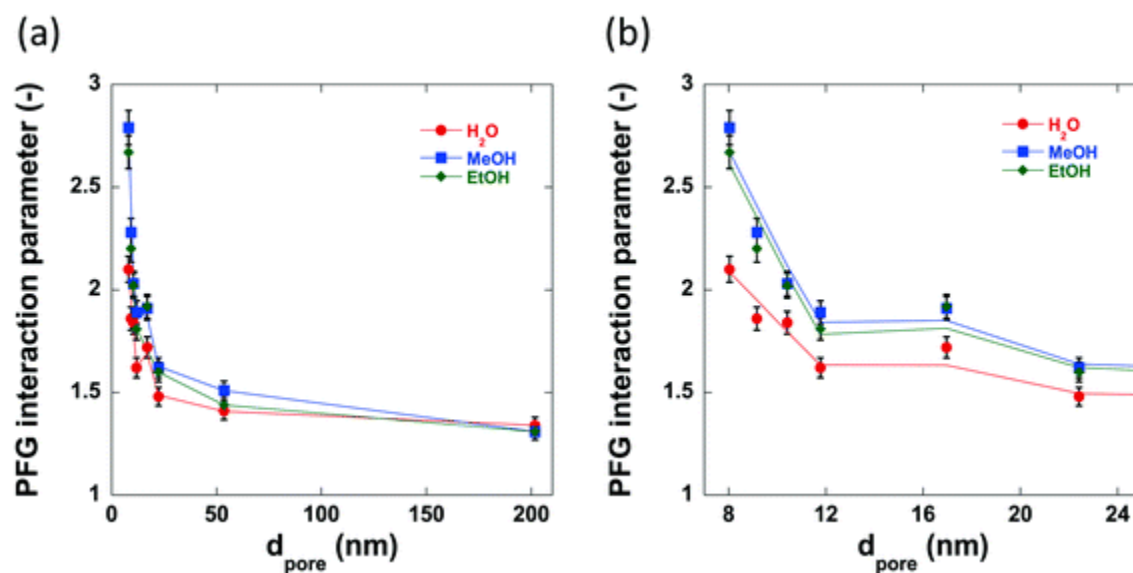| Sample	ξ_{Water} (-)	$\xi_{Methanol}$ (-)	$\xi_{Ethanol}$ (-)	τ (-)
Al_2O_3 (1)	2.10 ± 0.06	2.79 ± 0.08	2.67 ± 0.08	2.57 ± 0.08
Al_2O_3 (2)	1.86 ± 0.06	2.28 ± 0.07	2.20 ± 0.07	2.17 ± 0.07
Al_2O_3 (3)	1.84 ± 0.06	2.03 ± 0.06	2.02 ± 0.06	1.95 ± 0.06
Al_2O_3 (4)	1.62 ± 0.05	1.89 ± 0.06	1.81 ± 0.05	1.78 ± 0.05
Al_2O_3 (5)	1.72 ± 0.05	1.91 ± 0.06	1.92 ± 0.06	1.81 ± 0.05
Al_2O_3 (6)	1.48 ± 0.04	1.62 ± 0.05	1.60 ± 0.05	1.51 ± 0.05
Al_2O_3 (7)	1.41 ± 0.04	1.51 ± 0.05	1.44 ± 0.04	1.50 ± 0.05
Al_2O_3 (8)	1.34 ± 0.04	1.31 ± 0.04	1.31 ± 0.04	1.42 ± 0.04

Figure 4.9. The pore size dependence of ξ for water, methanol and ethanol imbibed within (a) the alumina carriers and (b) the alumina carriers with Al_2O_3 (8) omitted to aid comparison of the smaller pore size samples.

The PFG interaction parameter, ξ, generally decreases for all three molecules imbibed within the alumina carriers. This effect can be attributed to changes in structural properties, in particular it is due to the reduced restriction of the guest molecules within the carrier pores resulting in less collisions with the pore walls and therefore a faster diffusivity. However, there are significant

differences between the values of ξ for water, methanol and ethanol diffusing within the small pore size samples; conversely, the medium to large pore size samples (d_{pore} > 17.0 nm) show very similar values of ξ (between 1.3 – 1.6) regardless of probe molecule used. Within the structure of the small pore size samples there is a relatively high concentration of the guest molecule close to the pore wall and thereby the diffusivity will be significantly affected by interactions of the guest molecules with the pore surface, meaning that those molecules interacting more strongly with the surface will diffuse more slowly. This is consistent with recently reported results on alcohol diffusion in mesoporous silica. [58] In the larger pore size samples, there is a much higher concentration of bulk liquid diffusing in the pore volume as opposed to at the surface, and therefore, surface interactions will have a lower impact on the diffusivity. Intriguingly, water confined within the pores of Al_2O_3 (1)-Al_2O_3 (7) show lower values of interaction parameter than the respective tortuosity values obtained using *n*-octane indicating an 'enhanced' diffusivity of water relative to *n*-octane confined within the same network of pores, a property that has been previously detailed for various polyols confined within TiO_2, SiO_2 and γ-Al_2O_3 carriers. [50, 59] This property is attributed to the disruption of the extensive hydrogen bonding networks between polyol molecules by the porous medium and recent work has confirmed this as well as demonstrating the importance of pore saturation to measuring accurate values of diffusivity in similar systems. [59] However, further discussion of this phenomenon is beyond the scope of this work.

4.4. Conclusions

In this paper, alumina carriers with differing textural properties were prepared under different operating conditions. Among the conditions varied during the preparation, two main parameters, specifically, mixing time and calcination temperature, were changed. Mercury porosimetry analysis confirmed that longer mixing times resulted in smaller average pore sizes and a lower percentage of macropores present in the aluminas produced. Higher calcination temperatures were found to trigger phase transitions of the alumina thereby resulting in the alumina samples produced to have larger average pore sizes and to contain a higher percentage of macropores. It is clear that the textural properties of the alumina carriers can be easily controlled and effectively tailored to form structures with optimal pore characteristics required for specific applications by simply varying the preparation conditions.

A comprehensive set of PFG NMR studies using *n*-octane to probe the effect of textural properties of the prepared carriers confirmed that, up to an average pore size of 17.0 nm, the diffusivity of *n*-octane increases rapidly with the average pore. When alumina samples with larger pore sizes were analysed, diffusivity was only slightly higher, reaching a plateau with increasing pore size suggesting that a pore size greater than 17.0 nm is sufficient to alleviate the major restrictions on the probe molecules motion. When alumina samples containing no macroporosity were analysed, the probe molecule diffusivity was determined only by the average pore size of the sample. However, probe molecule diffusivity was found to increase as the percentage of macropores within the sample increased. When the samples contained approximately 27 % macroporosity or above, the probe molecule diffusivity remained constant suggesting that 27 % macroporosity is sufficient to alleviate any mass transport limitations due to geometrical restriction of the probe molecule within the pore structure of the carriers.

In order to study the effect of the pore surface chemistry on diffusion, PFG NMR using water, methanol and ethanol were conducted. The results revealed that, for the samples with low average pore size and low macropore content, surface interactions between the probe molecules and the pore surface are significant in determining the diffusivity through the pore structure; conversely, for samples with much larger pore size and macropore content, surface interactions have little effect on determining the diffusive motion of guest molecules.

In summary, the study reported here highlights in a very comprehensive and quantitative manner the role of pore size and macropore content on mass transport by diffusion in macroporous–mesoporous catalytic materials. The reported methodology and results, obtained with a bench-top NMR instrument, which is recently increasing accessibility to NMR techniques for the wider scientific academic and industrial communities, may serve as a guideline for tailoring textural properties of porous materials through adopting suitable operating condition of the preparation procedure, which can lead to pore structure with tuned diffusion properties. We believe the work will be a useful tool for those working in the area of catalyst preparation, physical chemistry of porous materials and their applications.

References

1.   L. Forster, M. Lutecki, H. Fordsmand, L. Yu and C. D'Agostino, *Mol. Syst. Des. Eng.*, 2020, **5**, 1193.

2.   J. Aguado, D. P. Serrano , J. M. Escola and A. Peral, *J. Anal. Appl. Pyrolysis*, 2009, **85**, 352-358.

3.   E. Ghedini, F. Menegazzo, M. Signoretto, M. Manzoli, F. Pinna and G. Strukul, *J. Catal.*, 2010, **273**, 266-273.

4.   D. P. Serrano, J. Aguado, J. M. Rodriguez and A. Peral, *J. Anal. Appl. Pyrolysis*, 2007, **79**, 456-464.

5.   I. V. Babich and J. A. Moulijn, *Fuel*, 2003, **82**, 607-631.

6.   H. Wang, Q. Fan, Z. D. Yang, S. Y. Tang, J. Y. Chen and Y. Wu, *Mol. Catal.*, 2019, **468**, 1-8.

7.   S. Badoga, A. Ganesan, A. K. Dalai and S. Chand, *Catal. Today*, 2017, **291**, 160-171.

8.   P. P. Minaev, M. S. Nikulshina, L. A. Gulyaeva, O. L. Ovsienko, V. A. Khavkin, O. I. Shmel'kova and P. A. Nikulshin, *Pet. Chem.*, 2017, **57**, 1161-1164.

9.   D. M. Minahan, G. B. Hoflund, W. S. Epling and D. W. Schoenfeld, *J. Catal.*, 1997, **168**, 393-399.

10.   S. Adhami , M. N. Esfahany , K. Eranen , M. Peurla , E. Makila , D. Y. Murzin and T. Salmi , *J. Chem. Technol. Biotechnol.*, 2019, **94** , 3839 —3849.

11.   M. T. Ravanchi, S. Fadaeerayeni and M. R. Fard, *Res. Chem. Intermed.*, 2016, **42**, 4797-4811.

12.   C. F. Mao and M. A. Vannice, *Appl. Catal., A*, 1995, **122**, 61-76.

13.   H. Kanoh, T. Nishimura and A. Ayame, *J. Catal.*, 1979, **57**, 372-379.

14.   L. H. Chen, X. Y. Li, J. C. Rooke, Y. H. Zhang, X. Y. Yang, Y. Tang, F. S. Xiao and B. L. Su, *J. Mater. Chem.*, 2012, **22**, 17381-17403.

15.   S. Mezzavilla, C. Baldizzone, K. J. J. Mayrhofer and F. Schuth, *ACS Appl. Mater. Interfaces*, 2015, **7**, 12914-12922.

16.   Y. W. Shi, X. W. Zhang and G. Z. Liu, *Fuel*, 2015, **158**, 565-571.

17.   J. Du, L. Liu, B. B. Liu, Y. F. Yu, H. J. Lv and A. B. Chen, *Carbon*, 2019, **143**, 467-474.

18. S. S. Zhuang, Z. J. Hu, L. Huang, F. Qin, Z. Huang, C. Sun, W. Shen and H. L. Xu, *Catal. Commun.*, 2018, **114**, 28-32.

19. Q. Gao, Y. Zhang, K. D. Zhou, H. D. Wu, J. Guo, L. F. Zhang, A. J. Duan, Z. Zhao, F. Q. Zhang and Y. X. Zhou, *RSC Adv.*, 2018, **8**, 28879-28890.

20. R. P. Liu and C. A. Wang, *Ceram. Int.*, 2015, **41**, 1101-1106.

21. L. Y. Jaramillo, K. Arango-Benitez, W. Henao, E. Vargas, G. Recio-Sanchez and M. Romero-Saez, *Mater. Lett.*, 2019, **257**, 126749.

22. R. P. Liu, F. Ren, W. M. Su, P. He, C. Shen, L. Zhang and C. A. Wang, *Ceram. Int.*, 2015, **41**, 14615-14620.

23. R. Feng, X. Y. Hu, X. L. Yan, Z. F. Yan and M. J. Rood, *Microporous Mesoporous Mater.*, 2017, **241**, 89-97.

24. B. Gu, S. B. He, X. Rong, Y. Shi and C. L. Sun, *Catal. Lett.*, 2016, **146**, 1415-1422.

25. Y. F. Li , J. J. Su , J. H. Ma , F. Yu and R. F. Li , *Mater. Lett.*, 2015, **153** , 165 —167.

26. W. Q. Jiao, W. H. Fu, X. M. Liang, Y. M. Wang and M.-Y. He, *RSC Adv.*, 2014, **4**, 58596-58607.

27. Z. Liu, X. Yi, G. Wang, X. Tang, G. Li, L. Huang and A. Zheng, *J. Catal.*, 2019, **369**, 335-344.

28. S. Gao, Z. Liu, S. Xu, A. Zheng, P. Wu, B. Li, X. Yuan, Y. Wei and Z. Liu, *J. Catal.*, 2019, **377**, 51-62.

29. Z. Liu, Y. Chu, X. Tang, L. Huang, G. Li, X. Yi and A. Zheng, *J. Phys. Chem. C*, 2017, **121**, 22872-22882.

30. S. Kolitcheff, E. Jolimaitre, A. Hugon, J. Verstraete, M. Rivallan, P. L. Carrette, F. Couenne and M. Tayakout-Fayolle, *Catal. Sci. Technol.*, 2018, **8**, 4537-4549.

31. A. Galarneau, F. Guenneau, A. Gedeon, D. Mereib, J. Rodriguez, F. Fajula and B. Coasne, *J. Phys. Chem. C*, 2016, **120**, 1562-1569.

32. J. Kärger, R. Valiullin, D. Enke and R. Glaser, *Mesoporous Zeolites*, 2015, 385-423.

33. M. Goepel, H. Kabir, C. Kuster, E. Saraci, P. Zeigermann, R. Valiullin, C. Chmelik, D. Enke, J. Kärger and R. Glaser, *Catal. Sci. Technol.*, 2015, **5**, 3137-3146.

34. D. H. Tang, C. Kern and A. Jess, *Appl. Catal., A*, 2004, **272**, 187-199.

35. G. Di Carmine, D. Ragno, A. Massi and C. D'Agostino, *Org. Lett.*, 2020, **22**, 4927-4931.

36.   Y. Jiao, L. Forster, S. Xu, H. Chen, J. Han, X. Liu, Y. Zhou, J. Liu, J. Zhang, J. Yu, C. D'Agostino and X. Fan, *Angew. Chem., Int. Ed.*, 2020, **132**, 19646–19654.

37.   P. Kortunov, S. Vasenkov, J. Kärger, R. Valiullin, P. Gottschalk, M. F. Elia, M. Perez, M. Stocker, B. Drescher, G. McElhiney, C. Berger, R. Glaser and J. Weitkamp, *J. Am. Chem. Soc.*, 2005, **127**, 13055-13059.

38.   M. A. Isaacs, N. Robinson, B. Barbero, L. J. Durndell, J. C. Manayil, C. M. A. Parlett, C. D'Agostino, K. Wilson and A. F. Lee, *J. Mater. Chem. A*, 2019, **7**, 11814-11825.

39.   E. O. Stejskal and J. E. Tanner, *J. Chem. Phys.*, 1965, **42**, 288-292.

40.   E. O. Stejskal, *J. Chem. Phys.*, 1965, **43**, 3597-3606.

41.   C. D'Agostino, J. Mitchell, L. F. Gladden and M. D. Mantle, *J. Phys. Chem. C*, 2012, **116**, 8975-8982.

42.   H. Schaper, E. B. M. Doesburg, P. H. M. Dekorte and L. L. Vanreijen, *Solid State Ionics*, 1985, **16**, 261-265.

43.   M. S. Djosic, V. B. Miskovic-Stankovic, D. T. Janackovic, Z. M. Kacarevic-Popovic and R. D. Petrovic, *Colloids Surf., A*, 2006, **274**, 185-191.

44.   X. Krokidis, P. Raybaud, A. E. Gobichon, B. Rebours, P. Euzen and H. Toulhoat, *J. Phys. Chem. B*, 2001, **105**, 5121-5130.

45.   J. S. Lee, H. S. Kim, N. K. Park, T. J. Lee and M. Kang, *Chem. Eng. J.*, 2013, **230**, 351-360.

46.   A. Boumaza, L. Favaro, J. Ledion, G. Sattonnay, J. B. Brubach, P. Berthet, A. M. Huntz, P. Roy and R. Tetot, *J. Solid State Chem.*, 2009, **182**, 1171-1176.

47.   S. Ferreira, J. J. Verstraete, E. Jolimaitre, D. Leinekugel-le-Cocq and C. Jallut, *Comput.-Aided Chem. Eng.*, 2017, **40a**, 91-96.

48.   M. D. Mantle, D. I. Enache, E. Nowicka, S. P. Davies, J. K. Edwards, C. D'Agostino, D. P. Mascarenhas, L. Durham, M. Sankar, D. W. Knight, L. F. Gladden, S. H. Taylor and G. J. Hutchings, *J. Phys. Chem. C*, 2011, **115**, 1073-1079.

49.   P. J. Barrie, *Annu. Rep. NMR Spectrosc.*, 2000, **41**, 265-316.

50.   C. D'Agostino, J. Mitchell, L. F. Gladden and M. D. Mantle, *J. Phys. Chem. C*, 2012, **116**, 8975-8982.

51.   M. Dvoyashkin, R. Valiullin and J. Kärger, *Phys. Rev. E: Stat., Nonlinear, Soft Matter Phys.*, 2007, **75**, 041202.

52.   C. D'Agostino, J. Mitchell, M. D. Mantle and L. F. Gladden, *Chem. – Eur. J.*, 2014, **20**, 13009-13015.

53.   J. Wood and L. F. Gladden, *Appl. Catal., A*, 2003, **249**, 241-253.

54.   S. Kolitcheff, E. Jolimaitre, A. Hugon, J. Verstraete, P. L. Carrette and M. Tayakout-Fayolle, *Microporous Mesoporous Mater.*, 2017, **248**, 91-98.

55.   S. Fujita, H. Kawamori, D. Honda, H. Yoshida and M. Arai, *Appl. Catal., B*, 2016, **181**, 818-824.

56.   C. D'Agostino, G. L. Brett, P. J. Miedziak, D. W. Knight, G. J. Hutchings, L. F. Gladden and M. D. Mantle, *Chem. – Eur. J.*, 2012, **18**, 14426-14433.

57.   C. D'Agostino, T. Kotionova, J. Mitchell, P. J. Miedziak, D. W. Knight, S. H. Taylor, G. J. Hutchings, L. F. Gladden and M. D. Mantle, *Chem. – Eur. J.*, 2013, **19**, 11725-11732.

58.   N. Robinson and C. D'Agostino, *Top. Catal.*, 2019, **19**, 11725-11732.

59.   G. Campos-Villalobos, F. R. Siperstein, C. D'Agostino, L. Forster and A. Patti, *Appl. Surf. Sci.*, 2020, **516**, 146089.

Supporting information

Table S1. Root mean squared displacements (*RMSD*) used to investigate the self-diffusivity of the guest molecules; *n*-octane, water, methanol and ethanol within the alumina carriers Al_2O_3 (1) - Al_2O_3 (8) during PFG-NMR diffusometry experiments.

Sample	$RMSD_{OCT}$ (µm)	$RMSD_{H2O}$ (µm)	$RMSD_{MeOH}$ (µm)	$RMSD_{EtOH}$ (µm)
Al_2O_3 (1)	9.70	10.63	9.31	6.39
Al_2O_3 (2)	10.55	11.29	10.30	7.04
Al_2O_3 (3)	11.14	11.34	10.93	7.35
Al_2O_3 (4)	11.64	12.09	11.30	7.75
Al_2O_3 (5)	11.58	11.74	11.26	7.52
Al_2O_3 (6)	12.66	12.65	12.24	8.26
Al_2O_3 (7)	12.70	12.94	12.66	8.69
Al_2O_3 (8)	13.04	13.29	13.61	9.12
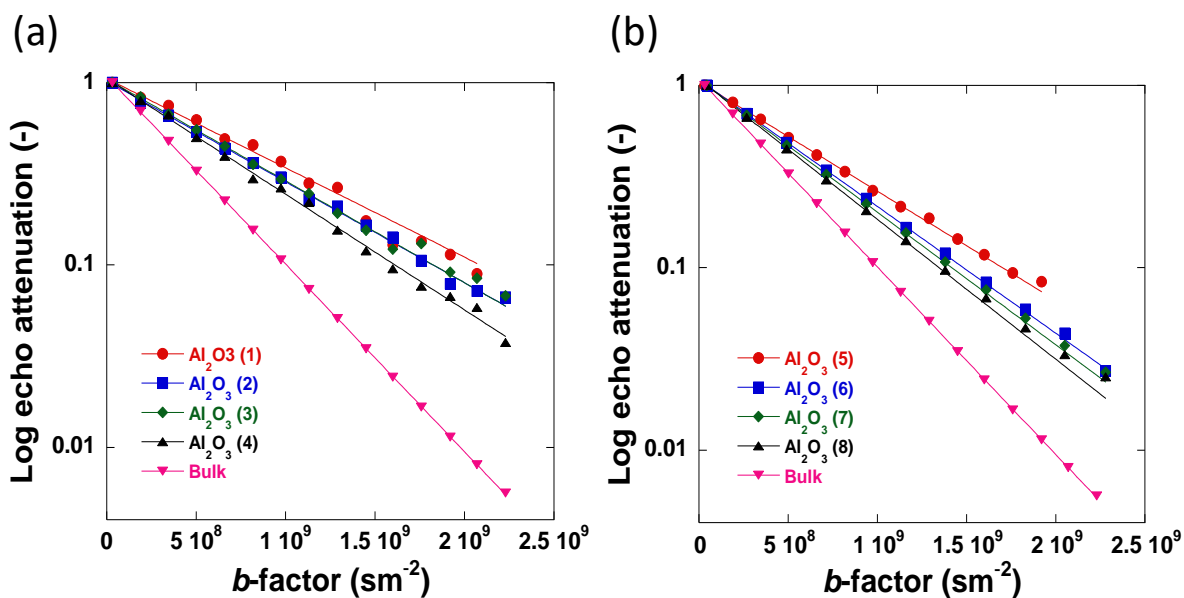
Figure S1. Log attenuation plots of water imbibed within (a) Al_2O_3 (1) – Al_2O_3 (4) and (b) Al_2O_3 (5) – Al_2O_3 (8). Solid lines are fitting to Equation (1).
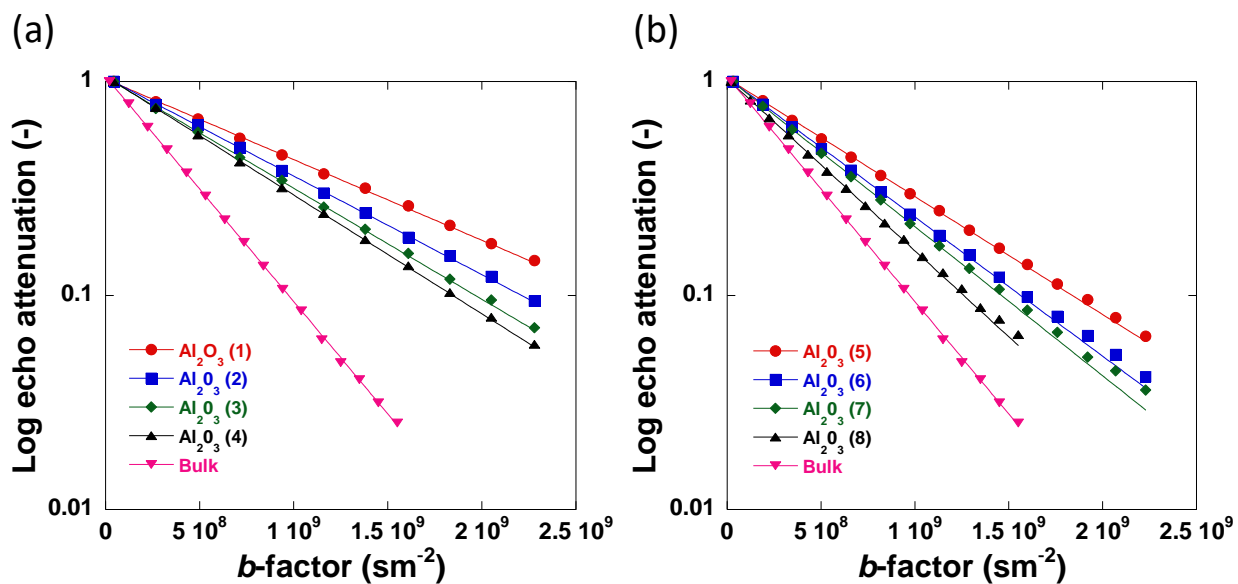
Figure S2. Log attenuation plots of methanol imbibed within (a) Al_2O_3 (1) – Al_2O_3 (4) and (b) Al_2O_3 (5) – Al_2O_3 (8). Solid lines are fitting to Equation (1).
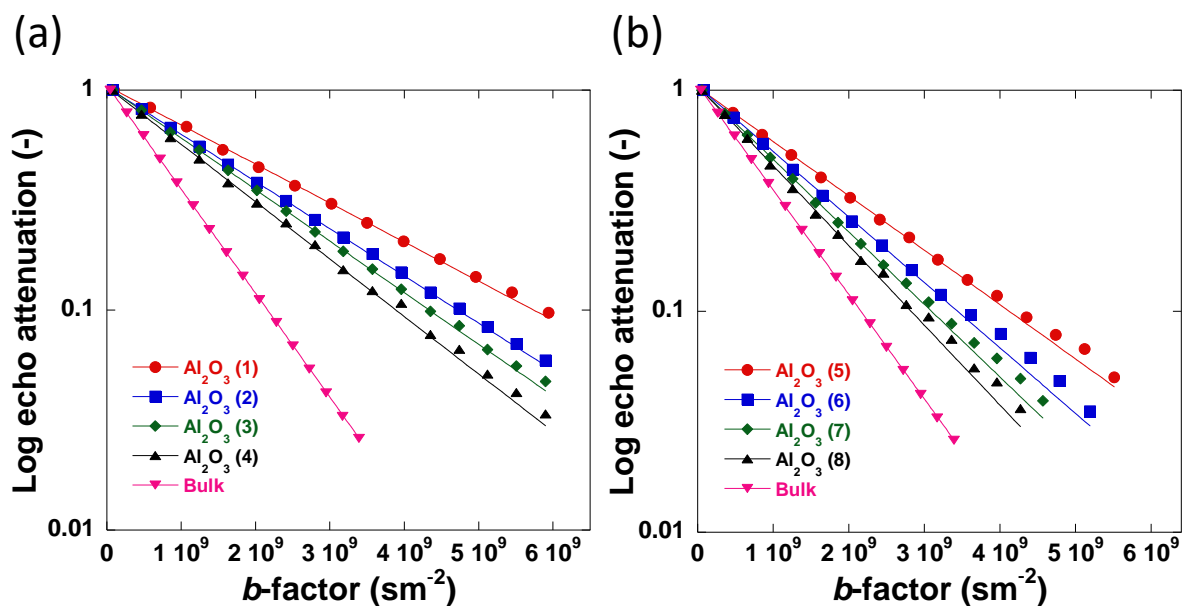
Figure S3. Log attenuation plots of ethanol imbibed within (a) Al_2O_3 (1) – Al_2O_3 (4) and (b) Al_2O_3 (5) – Al_2O_3 (8). Solid lines are fitting to Equation (1).

Chapter 5: Creation of Al-enriched mesoporous ZSM-5 nanoboxes with high catalytic activity: converting tetrahedral extra-framework Al into framework sites by post treatment

This chapter has been published as a full article in the journal *Angewandte Chemie*. [1] [Creation of Al-Enriched Mesoporous ZSM-5 Nanoboxes with High Catalytic Activity: Converting Tetrahedral Extra-Framework Al into Framework Sites by Post Treatment - Jiao - 2020 - Angewandte Chemie - Wiley Online Library](#)

Author contributions are as follows; Luke Forster conceived part of the main ideas related to diffusion, performed the NMR measurements and subsequent data processing and analysis, as well as interpretation and discussion of the data, and contributed to the preparation of the article. Yilai Jiao, Xiaolei Fan and Carmine D'Agostino prepared the article. All other authors contributed to the testing and characterisation of the catalytic materials studied (i.e. SS-NMR, TEM, SEM, NH_3-TPD, BET, XRD, pyridine-FTIR and TGA).

Abstract

ZSM-5 zeolite nanoboxes with accessible meso-micro-pore architecture and strong acid sites are important to heterogeneous catalysis suffering from mass transfer limitations and weak acidities. Rational design of parent zeolites with concentrated and non-protective coordination of Al species can facilitate the post-synthetic treatments to produce mesoporous ZSM-5 nanoboxes. In this work, a simple and effective method was developed to prepare and convert parent MFI zeolites with tetrahedral extra-framework aluminium (EFAL) into Al-enriched mesoporous ZSM-5 nanoboxes with low silicon-to-aluminium ratios (SARs) of ~16. The parent MFI zeolite was prepared by a strategy of rapid ageing of the zeolite sol gel synthesis mixture. The accessibility to the well-developed meso-micro-porous intra-crystalline network was probed systematically by comparative pulsed field gradient nuclear magnetic resonance (PFG-NMR) diffusion measurements, which, in synergy with the high concentration of strong acidity of nanoboxes, provided superb catalytic activity and catalyst longevity in hydrocarbon cracking for producing propylene.

5.1. Introduction

Hierarchical zeolites with mesoporous features are a class of materials with high industrial relevance, particularly heterogeneous catalysis for both conventional petrochemical and the emerging biomass conversions, due to the improved diffusion properties of reactants and/or products within their crystalline domains. [2] MFI-type zeolites (with a nearly circular cross section of ~0.54 nm diameter), particularly ZSM-5, are one of the most important active components (along with FAU-type Y zeolites) in petroleum refining and petrochemical catalysts, and have seen significant growth in recent years for developing propylene-selective processes such as catalytic cracking and methanol-to-olefins (MTO). [3] The limited accessibility of guest molecules to intrinsic micropores of ZSM-5 is still very problematic for realising its full catalytic potential. ZSM-5 normally has medium to high silicon-to-aluminium ratios (SAR $\geq$~12) with heterogeneous Al distribution across its framework, [4,5] and the post-synthetic alkaline treatments (*via* selective desilication) using sodium hydroxide (NaOH) [5-8] and sodium carbonate (Na_2CO_3) [9-13] are generally effective to create mesoporous structures in ZSM-5, such as mesopores and hollow crystals. Notice that SAR values of parent ZSM-5 zeolites are the critical parameter in the controlled dissolution of Si species from the framework of the parent zeolites to form accessible meso-micro-porosity.

Previous research has confirmed the protective role of the tetrahedral framework Al for the Si extraction in alkaline media. For parent ZSM-5 zeolites with low SAR values of <20 (*i.e.* Al-rich), post-synthetic alkaline treatments are not effective for the formation of mesoporous features, and sequential fluorination-desilication and steaming-desilication for creating mesoporous structures in the ZSM-5 zeolites (*via* tandem dealumination and desilication treatments) are necessary. [14] However, the use of corrosive chemicals and steam makes the sequential treatment processes dangerous and energy-intensive, and thus industrially unfavourable. Conversely, for highly siliceous ZSM-5 with SAR values >50, excessive desilication occurs during post-synthetic alkaline treatments, leading to the uncontrollable mesopores formation.[4] Accordingly, the optimal framework SAR of 25–50 was identified for forming mesoporous structures effectively and controllably. [5-8, 14, 15]

The use of structural directing agents (SDAs), especially tetrapropylammonium hydroxide (TPAOH), in the modification of MFI zeolites (such as TS-1, [16] silicalite-1 [17-20] and ZSM-5) [21, 22] under alkaline conditions can facilitate the recrystallisation of leached species from dissolution

(*i.e.* the dissolution-recrystallisation mechanism), [16] and hence enabling the controlled formation of hollow yet mesoporous zeolite crystals (*i.e.* nanoboxes). Such zeolite nanoboxes are important for catalysis, not only being able to allow percolation diffusion through short paths but also providing the opportunity for functionalisation (*e.g.* encapsulation of metal nanoparticles). [21, 22] Since recrystallisation on the outer surface of parent zeolite crystals occurs only with the pre-selective dissolution of unprotected Si species, the dissolution-recrystallisation route is again limited by the precise location of Al in the framework of the parent zeolite; this is critical to the success of post-synthetic desilication methods aiming to improve molecular transport through the zeolite crystals. Currently, to enable the post-synthetic modification using SDAs for making mesoporous ZSM-5 nanoboxes, the use of parent zeolites such as siliceous silicalite-1 (in presence of Al sources) [17-20] or ZSM-5 with SAR values >40 [19, 21-23] (ideally 40–74) [22] is the essential prerequisite. Therefore, although ZSM-5 nanoboxes with a low framework SAR of <25 (and hence high Brønsted acidity) are significantly beneficial to zeolite catalysis (especially diffusion-limited reactions), one-step post-synthetic alkaline treatments of the homologous parent zeolites to obtain such materials is challenging, regardless with or without SDAs or additional Al sources. Therefore, rational design of the parent zeolite with high concentration yet non-protective coordination of Al species (which facilitates dissolution of Si and recrystallisation of Si and Al to crystallographic T-sites during the post-synthetic treatment) can be the solution to develop novel mesoporous ZSM-5 nanoboxes with the combination of meso-micro-pore architecture and concentrated Brønsted acidity.

Herein, we report a simple yet effective method to synthesise mesoporous ZSM-5 nanoboxes with the low SAR value of ~16. The method involves (i) the synthesis of a parent zeolite with tetrahedral extra-framework Al (EFAL) and (ii) post-synthetic treatment of the parent zeolite with TPAOH solution. The novel feature of the method lies in the rapid ageing of zeolite sol gel synthesis mixture at 40 °C (*i.e.* 30 min), which enables the synthesis of the parent zeolite with tetrahedral EFAL. The subsequent treatment using TPAOH solution allows the recrystallisation and redistribution of dissolved Si and EFAL to occur, forming highly crystalline hollow ZSM-5 zeolites with Al-rich shell (SAR = *ca.* 16, shell thickness = *ca.* 20 nm), and hence affording both improved acidity and diffusivity for catalysis. The mechanism of the new method is elaborated based on the comprehensive characterisation of materials using X-ray powder diffraction (XRD), nitrogen (N_2) physisorption, solid-state nuclear magnetic resonance (NMR) spectroscopy and

ammonia temperature programmed desorption (NH$_3$-TPD) analysis at different stages of the synthesis. Notably, the obtained ZSM-5 nanoboxes possess significantly high Al concentration (SAR of ~16) in the shell (~20 nm) and mesoporous features (*e.g.* specific mesopore volume = ~0.26 cm^3 g^{-1}). The percolation diffusion of probing molecules within the materials was assessed by pulsed-field gradient NMR (PFG-NMR) measurements. Previous research has shown that PFG-NMR is a powerful tool of investigating the mass transport in zeolites with mesoporous features [24-26] and cracking catalysts, [27] such as intracrystalline diffusivity. However, the interpretation of the diffusion data in relation to the relevant catalytic data has not yet been reported. Benefits of the mesoporous ZSM-5 nanoboxes to catalytic cracking (of model naphtha and aromatic compounds) is demonstrated, showing excellent activity and selectivity to propylene due to the unique combination of pore structural features and chemical properties (*i.e.* the low SRA and percolating porous network). The simple and effective strategy solves the challenge of preparing mesoporous ZSM-5 zeolites with low SAR values.
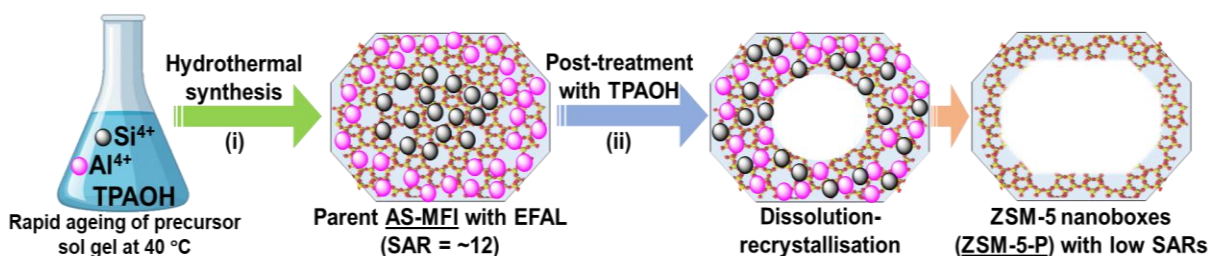

Figure 5.1. Schematic illustration of the preparation of the mesoporous ZSM-5-P nanoboxes *via* the rapid ageing (of the precursor sol gel mixture) and post-synthetic TPAOH treatment.

5.2. Experimental

5.2.1. Synthesis of materials

5.2.1.1. Synthesis of mesoporous ZSM-5 nanoboxes

All chemicals were obtained from Sinopharm Chemical Reagent Co., Ltd and used as received. The procedure to prepare the parent zeolite is described as: aluminium chloride (AlCl$_3$) was added to a mixture of tetrapropylammonium hydroxide (TPAOH) and deionised (DI) water and continually stirred for 1 h at room temperature (RT), then the mixture was heated to 40 °C. Subsequently, tetraethylorthosilicate (TEOS) was added rapidly into the mixture under vigorous stirring and continuously stirred for 30 min until the synthesis gel become clear. The molar

composition of the sol gel mixture is $SiO_2:0.04Al_2O_3:0.3TPAOH:19H_2O$. After rapid aging of the sol gel synthesis mixture, it was transferred into a Teflon-lined stainless-steel (SS) autoclave (500 ml capacity) for crystallisation at 160 °C (for different h). The resulting product was recovered by centrifugation and washed with DI water (100 mL for each wash, 3 times), then dried at 110 °C (overnight) and calcined in static air at 550 °C for 6 h (heating rate = 1 °C min^{-1}). The as-synthesised parent zeolite is denoted as AS-MFI. For comparison, conventional ZSM-5 (denoted as C-ZSM-5) was also prepared using the conventional aging method (*i.e.* precursor aging at RT for 24 h), then followed by the same hydrothermal synthesis and work-up.

ZSM-5 nanoboxes are synthesised using a post-synthetic treatment method. Post-synthetic hydrothermal treatment of AS-MFI using TPAOH aqueous solution was carried by mixing the sample (4 g) with TPAOH solution (0.1 M, 40 mL, pH ≈ 13) at 400 rpm (for 20 min to form a slurry). Then the slurry was transferred to a Teflon-lined SS autoclave (100 ml) and left at autogenous pressure and 160 °C under hydrostatric condition for various h (specifically, 6, 12, 24, 48 and 96 h). Finally, the mixture was filtered, washed with DI water, dried at 120 °C for 12 h, and calcined at 550 °C for 6 h. The post-treated sample was denoted as ZSM-5-P-*x-y*, in which P represents *via* post-synthetic treatment, *x* represents the TPAOH concentration using in the post-treatment (in M) and *y* represents post-treatment time (in h), respectively.

5.2.1.2. Post-synthetic treatment of AS-MFI using concentrated TPAOH solutions (0.3 and 0.5 M)

Post-synthetic treatment of AS-MFI using 0.3 and 0.5 M TPAOH aqueous solutions was carried by mixing AS-MFI (4 g) with TPAOH solution (0.3 M and 0.5 M, 40 mL) at 400 rpm (for 20 min to form a slurry). Then the slurry was transferred to a Teflon-lined SS autoclave (100 ml) and left at autogenous pressure and 160 °C for 24 h. Finally, the mixture was filtered, washed with DI water, dried at 120 °C for 12 h, and calcined at 550 °C for 6 h. The treated sample was denoted as ZSM-5-P-0.3-24 and ZSM-5-P-0.5-24. Relevant pH values of the systems are ~14.

5.2.1.3. Synthesis and post-synthetic treatment of conventional ZSM-5

Standard procedure was used to synthesise the conventional ZSM-5 zeolite (denoted as C-ZSM-5), and it is described as: AlCl$_3$ was added to a mixture of TPAOH and DI water and continually stirred for 1 hour at RT. Subsequently, TEOS was added dropwise into the mixture under vigorous stirring at ice bath temperature (~12 h) and continuously stirred for 12 h at the same temperature.

The molar composition of the sol gel mixture is $SiO_2:0.04Al_2O_3:0.3TPAOH:19H_2O$. After the 24 h aging of the sol gel synthesis mixture at RT, it was transferred into a Teflon-lined SS autoclave (500 ml capacity) for crystallisation at 160 °C for 48 h. The resulting product was recovered by centrifugation and washed with DI water (100 mL for each wash, 3 times, then dried at 110 °C (overnight) and calcined in static air at 550 °C (with a ramp rate of 1 °C min^{-1} for 6 h) to obtain C-ZSM-5.

The post-synthetic treatment of C-ZSM-5 using 0.1 M TPAOH aqueous solution was carried by mixing the C-ZSM-5 (4 g) with TPAOH solution (0.1 M, 40 mL) at 400 rpm (for 20 min to form a slurry). Then the slurry was transferred to a Teflon-lined SS autoclave (100 ml) and left at autogenous pressure and 160 °C for 6 h. Finally, the mixture was filtered, washed with DI water, dried at 120 °C for 12 h, and calcined at 550 °C for 6 h. The resulting sample of the post-treated C-ZSM-5 was denoted as C-ZSM-5-P-0.1-6 (6).

5.2.1.4. Synthesis of conventional hollow ZSM-5 with a SAR of ~45 (C-HO-ZSM-5)

The procedure to prepare the relevant parent ZSM-5 is described as: $AlCl_3$ was added to a mixture of TPAOH and DI water and continually stirred for 1 h at RT. Subsequently, TEOS was added into the mixture under vigorous stirring and continuously stirred for 24 h. The molar composition of the precursor sol is $SiO_2:0.0125Al_2O_3:0.3TPAOH:19H_2O$. After the 24 h aging of the precursor sol at RT, it was transferred into a Teflon-lined SS autoclave (500 ml capacity) for crystallisation at 160 °C for 48 h. The resulting product was recovered by centrifugation and washed with DI water (100 mL for each wash, 3 times, then dried at 110 °C (overnight) and calcined in static air at 550 °C with a ramp rate of 1 °C min^{-1} for 6 h.

The post-synthetic treatment of the parent zeolite using 0.7 M TPAOH aqueous solution was carried by mixing the sample (4 g) with TPAOH aqueous solution (0.7 M, 40 mL) at 400 rpm (for 20 min to form a slurry). Then the slurry was transferred to a Teflon-lined SS autoclave (100 ml) and left at autogenous pressure and 160 °C for 24 h. Finally, the mixture was filtered, washed with DI water, dried at 120 °C for 12 h, and calcined at 550 °C for 6 h. The treated sample was denoted as C-HO-ZSM-5.

5.2.2. Characterisation of materials

5.2.2.1. Powder X-ray diffraction (XRD)

XRD patterns of materials were recorded using a Panalytical X'Pert Pro system fitted with CuKα_1 X-ray source ($\lambda = 0.15406$ nm) operated at 40 kV and 40 mA. The measurement was performed over a 2θ range of 5°–35° in 0.02 step size at a scanning rate of 1° min^{-1}. The relative crystallinity (RC) of zeolites was determined by using a standard Integrated Peak Area Method, which involves a comparison of the integrated peak areas in the range of 22.5 to 25.0° 2θ. Details of the method has been described elsewhere. [28] The sample with the strongest peak at 23.1° 2θ was selected as the reference, which was ZSM-5-P-0.1-12 in this study. It is worth mentioning that, in this work, the parent zeolite, *i.e.* AS-MFI, was not perfectly crystallised with the non-coordinated tetrahedral Al and Si species, and hence the crystallinity of AS-MFI is comparatively poor. The subsequent post-treatment with the aqueous TPAOH solution (at 0.1 M) under hydrothermal conditions can facilitate the re-crystallisation of the parent AS-MFI zeolite during the post-treatment, and hence producing the relevant ZSM-5-P zeolites with the improved crystallinity.

5.2.2.2. Nitrogen (N_2) adsorption-desorption

N_2 physisorption measurements at the liquid nitrogen temperature (-196.15 °C) using a Micromeritics 3Flex surface area and pore size analyser. Prior to the measurement, the sample (~100 mg) was degassed at 350 °C under vacuum overnight. The micropore size distribution was calculated by the Horvath-Kawazoe (HK) method, [29] and mesopore size distribution was determined from the adsorption branch of the isotherms by the Barrett-Joyner-Halenda (BJH) method. [30]

5.2.2.3. Solid-state nuclear magnetic resonance (NMR)

Solid-state NMR spectra were recorded on an Agilent 600 DD2 spectrometer operating at a Larmor frequency of 600 MHz for 1H. ^{29}Si magic angle spinning (MAS) NMR spectra were recorded at 119.15 MHz (with the proton decoupling (TPPM) during acquisition) at a spinning rate of 8 kHz using a 3.6 μs pulse with a 30 s recycle delay and 1024 scans (tetramethylsilane as the reference). ^{27}Al MAS NMR spectra were recorded at 156.25 MHz (with the proton decoupling (TPPM) during acquisition) at a spinning rate of 12 kHz using a 3.6 μs pulse with a 5 s recycle delay and 512 scans (aluminium chloride as the reference).

5.2.2.4. Scanning electron microscopy (SEM) and energy dispersive X-ray spectroscopy (EDX)

SEM-EDX analysis was performed on a JEOL 7401 high-resolution field emission scanning electron microscope with an Oxford INCA 350 EDX system.

5.2.2.5. High resolution transmission electron microscopy (HRTEM)

HRTEM analysis of the microstructure of zeolites was performed using a Fei Tecnai F20 field emission gun transmission electron microscope at 200 kV. Before TEM analysis, the sample was dispersed in ethanol (which was sonicated for 5 min in an ultrasonic bath), and a droplet of the solution was casted on a carbon-coated mesh grid.

5.2.2.6. Inductively coupled plasma-atomic emission spectroscopy (ICP-AES)

ICP-AES analysis of various zeolites for the elemental analysis of their Al and Si contents was performed on a Varian Vista AX ICP-AES spectrometer. To prepare the solutions for ICP-AES analysis, the zeolite sample (0.1 g) was dissolved using hydrofluoric acid (HF) solution (10 wt.% HF in water, 5 ml) at RT, then diluted using DI water to 100 ml.

5.2.2.7. X-ray photoelectron spectroscopy (XPS)

XPS analysis was carried out using ThermoScientific ESCALAB 250 spectrometer equipped with monochromated AlKα X-ray source (1486.6 eV, 150W, spot size = 500 μm), a charge neutraliser and a hemispherical electron energy analyser. During data acquisition, the chamber pressure was kept below 10^{-9} mbar. The spectra were analysed using the CasaXPS software pack and corrected for charging using C1s binding energy (BE) as the reference at 284.8 eV.

5.2.2.8. Ammonia temperature-programmed desorption (NH₃-TPD)

NH_3-TPD measurements were performed using a Micromeritics AutoChem II 2920 chemisorption analyser (Micromeritics, USA) to determine the acidic property of the zeolites. ~100 mg zeolite was pre-treated at 823 K for 1 h and then cooled down to 323 K under Helium (He). A gas mixture of NH_3 in He (10%:90%, 30 cm^3 min^{-1}) was then introduced to saturate the catalyst followed by the purge of pure He (60 cm^3 min^{-1}) at 373 K for 2 h to remove the physically adsorbed NH_3. Finally, NH_3-TPD was performed by heating the catalyst from 373 K to 873 K with a heating rate of 10 K min^{-1} under He flow (30 cm^3 min^{-1}) and the desorbed NH_3 was monitored by a gas chromatography (GC) equipped with a thermal conductivity detector (TCD).

5.2.2.9. Pyridine fourier transform infrared (py-FTIR)

py-FTIR analysis was performed using a nexus Model Infrared Spectrophotometer (Thermo Nicolet Co, USA) operating at 2 cm^{-1} full width at half maximum (FWHM) equipped with an *in situ* cell containing CaF_2 windows. Adsorption of pyridine was performed at RT and then evacuated at 200 °C measuring pyridine adsorbed at all acid sites. After that, the sample was evacuated *in situ* at 350 °C corresponding to the pyridine adsorption at the strong acid sites.

5.2.2.10. Thermogravimetric analysis (TGA)

TGA of the used zeolites from the cracking reaction was performed using a TG analyser (Q600 TGA-DSC, TA Instruments, Germany) under air (flow rate = 100 ml min^{-1}). The temperature ramp was from RT to 800 °C with the heating rate of 10 °C min^{-1}.

5.2.3. Pulsed-Field Gradient Nuclear Magnetic Resonance (PFG-NMR) diffusion experiments

Zeolites were pelletised with particle sizes of 1.6–1.8 mm for PFG-NMR measurements. The zeolite particles were dried at 60 °C in a vacuum oven overnight and calcined at 550 °C for 12 h. To prepare samples for PFG-NMR experiments, the zeolite particles were soaked in *n*-octane (Merck, ≥99%, ~2 mL), cumene (Sigma, 99%, ~2 mL) or 1,3,5-triisopropylbenzene (TIPB) (Sigma, 95%, ~2 mL) for 2 days to ensure full saturation of the porous matrix of the zeolite samples with the respective probe molecule. The saturated samples were then dried on a filter paper to remove any excess liquid from the external surface of the particles and transferred to 5 mm NMR tubes. To minimise relevant errors due to evaporation of the volatile liquid, a small amount of pure liquid was dropped onto a filter paper, which was placed under the cap of the NMR tube. The tube was then placed into the magnet and left for approximately 15 min to achieve thermal equilibrium before measurements started. NMR experiments were performed on a Magritek SpinSolve benchtop NMR spectrometer operating at a ^{1}H frequency of 43 MHz. PFG-NMR experiments were carried out using a diffusion probe capable of producing magnetic field gradient pulses up to 163 mT m^{-1}. Diffusion measurements were performed using the pulsed-field gradient stimulated echo sequence (PGSTE sequence). [31] The sequence is made by combining a series of radiofrequency pulses (RF) with magnetic field gradients (*g*, Figure 2.11). The NMR signal attenuation of PFG-NMR experiments as a function of the gradient strength, $E(g)$, is related to the experimental variables and the diffusion coefficient (D) by Equation 2.38.

The measurements using cumene and octane were performed by fixing $\Delta = 200$ ms and $\delta = 3$ ms, and measurements with TIPB were performed by fixing $\Delta = 500$ ms and $\delta = 5$ ms. The magnitude of g was varied linearly with 16 spaced increments. To achieve full signal attenuation, maximum values of g of up to 163 mT m^{-1} were necessary. All the measurements were performed at atmospheric pressure and 25 °C. The diffusion coefficients D were calculated by fitting Equation 2.38 to the experimental data.

Root-mean-square displacement (RMSD) values of the probing molecules are determined using Equation 4.4.

To understand the diffusion process occurring within the pore structures under investigation, the PFG interaction parameter is calculated, [32] which in the case of using hydrocarbons as probe species, can be approximated to the tortuosity of the pore network, τ, defined as in Equation 4.2. [33]

5.2.4. Catalysis, stability and regeneration

5.2.4.1. Cracking reactions

Cracking of *n*-octane and cumene over the catalyst was carried out in a fixed bed reactor (I.D. = 10mm). The packed bed consists of 1 g pelletised zeolite catalysts (particle size = 1.6–1.8 mm) with glass beads as dilution. For catalytic cracking, the catalyst bed was preheated at the reaction temperature for 2 h, then *n*-octane (0.1 ml min^{-1} with N$_2$ as the carrier gas at 240 ml min^{-1}) or cumene (0.1 ml min^{-1} with N$_2$ as the carrier gas at 150 ml min^{-1}) was introduced to start the reaction at the same temperature (*i.e.* 540 °C for *n*-octane and 320 °C for cumene). The gaseous products of the reactions were analysed using an in-line gas chromatograph (GC, Agilent 7890B) equipped with a flame ionisation detector (FID) and Agilent PoraPLOT Q column. The carbon balance is above 95%.

5.2.4.2. Hydrothermal steam aging of zeolite

Hydrothermal aging of ZSM-5 nanoboxes (~100 mg) using steam was carried out in a tube furnace (Carbolite Gero Ltd., UK) at 500 °C. N$_2$ (at 200 mL min^{-1}) was used as the carrier gas which was passed through a bubbler containing DI water (at 50 °C) to generate steam. The samples were treated by steaming for 10 h prior to XRD and N$_2$ physisorption analysis.

5.2.4.3. Catalyst regeneration

Regeneration of the used ZSM-5-P-0.1-6 zeolite catalyst (the used catalyst is denoted as ZSM-5-P-0.1-6-U, the ZSM-5-P-0.1-6-U catalyst was recovered from of *n*-octane cracking) was performed by calcining ZSM-5-P-0.1-6-U at 550 °C in O_2 (10 vol.%) in N_2 (at 200 mL min^{-1}) for 6 h. The regenerated ZSM-5-P-0.1-6-U was assessed in catalytic cracking of *n*-octane and characterised by N_2 physisorption, NH_3-TPD and MAS NMR.

5.3. Results and Discussion

For the first time, the rapid ageing of the sol gel synthesis mixture (at 40 °C for 30 min, thereby increasing the rate of hydrolysis of the silica source, *i.e.* tetraethylorthosilicate, TEOS) was explored to produce the as-synthesised parent MFI zeolite (AS-MFI) with tetrahedral EFAL (Supporting Information). Comparison of X-ray powder diffraction (XRD) patterns of AS-MFI and conventional ZSM-5 (C-ZSM-5) is shown in Figure 5.2a, showing the distinct difference at 2θ of ~24.4°. AS-MFI shows the characteristic of monoclinic phase for MFI zeolites, [34] *i.e.* the split twin peaks, proving the presence of tetrahedral EFAL. Conversely, C-ZSM-5 (prepared *via* conventional ageing at ice bath temperature for 24 h) shows the sole peak at *ca.* 24.4° which is assigned to the typical orthorhombic crystal symmetry of ZSM-5. [35]
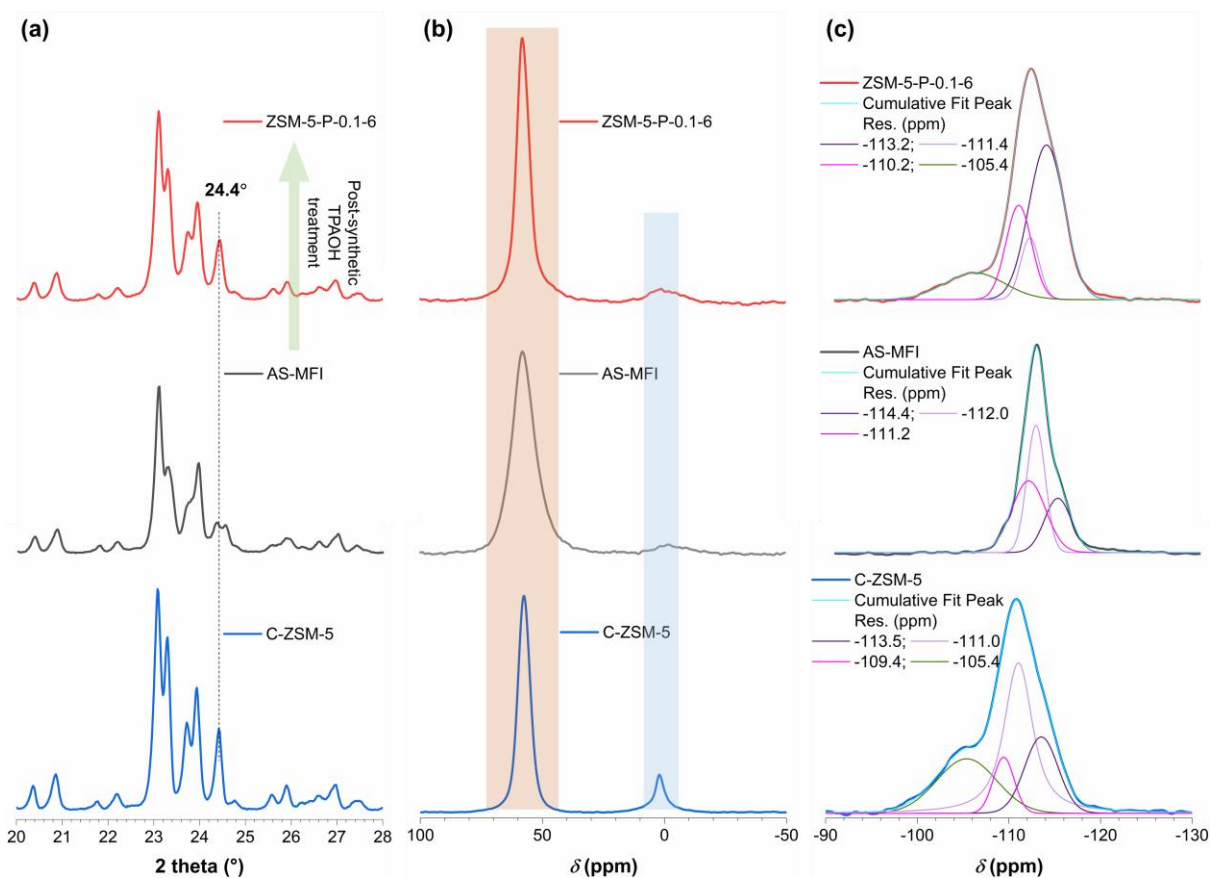
Figure 5.2. (a) XRD patterns, (b) ^{27}Al MAS NMR spectra and (c) ^{29}Si MAS NMR spectra of ZSM-5-P-0.1-6 (top), AS-MFI (middle) and C-ZSM-5 zeolites (bottom). SS-NMR spectra were deconvoluted using a Gaussian function.

Comparably, after TPAOH treatment of AS-MFI (pH ≈ 13, at 160 °C under static conditions), the resulting zeolites (denoted as ZSM-5-P-x-y, where P represents *via* post-treatment, x represents the TPAOH concentration in M and y represents post-treatment time in h, respectively) show the single peak at about 24.4° as well (Figures 5.2a and S5.1a), suggesting the re-insertion of the tetrahedral EFAL in AS-MFI into the newly formed framework (due to dissolution and recrystallisation mechanism) [16] during the post-treatment. We found that a 6 h post-treatment of AS-MFI with 0.1 M TPAOH was sufficient to produce ZSM-5 nanoboxes with excellent crystallinity (relative crystallinity, RC, >98%, Figure S5.1b) and mesoporous features (Figure S5.2 and Table S5.1). By extending the treatment time beyond 12 h, excessive dissolution occurred, damaging the intactness of the hollow structure to certain extents (as evidenced by the transmission electron, TEM, and scanning electron microscopy, SEM, analysis, Figures S5.3 and S5.4) and variation in mesoporosity of ZSM-5-P zeolites (Table S5.1). The excessive dissolution due to the

prolonged treatment time (>12 h) was also reflected by the reduced RC values of the relevant ZSM-5-P zeolites (at ~81%, Figure S5.1b).

Solid-state ^{27}Al magic angle spinning (MAS) NMR analysis (Figure 5.2b) shows the presence of tetrahedral (chemical shift centres at ~58 ppm) and octahedral Al species (at ~0 ppm) for all zeolites. However, one-dimensional ^{27}Al MAS NMR is not possible to elucidate the local symmetry and coordination state of Al species in zeolites. [36] Previous research has confirmed that the change of peak width at ~58 ppm indicates the variation of local Al coordination after post-treatments of MFI zeolites. [18, 19, 37, 38] In this work, it was measured that the peak width of the tetrahedral ^{27}Al in AS-MFI is the broadest among the samples under investigation (as the shaded orange area in Figure 5.2b), suggesting the presence of EFAL in AS-MFI. The post-treatment using TPAOH changed the local Al coordination substantially, and the peak width of the resulting ZSM-5-P-0.1-6 was narrowed noticeably, being comparable to that of the highly crystallised C-ZSM-5. Such variation of the NMR signal of tetrahedral Al may be attributed to the reintegration of EFAL in the recrystallised framework. [18, 19, 37, 38] Comparison of ^{29}Si MAS NMR spectra of AS-MFI, ZSM-5-P-0.1-6 and C-ZSM-5 is shown in Figure 5.2c. Only the resonances above -110 ppm were measured for AS-MFI, which are assigned to Si(4Si) sites, [39] proving the insignificant presence of the framework Al in AS-MFI. Conversely, for C-ZSM-5, the chemical shifts of lower intensities at $-103 - -108$ ppm (corresponding to Si(1Al)) and <-100 ppm (corresponding to Si(2Al)) [39] were identified. After the TPAOH treatment, the band at -105.4 ppm was measured for ZSM-5-P-0.1-6, evidencing the conversion of EFAL into framework T-sites.

Post-treatments using SDAs, especially TPAOH, are known to be effective to recover the dissolved species to a certain extent (reducing the loss of materials) and to form hollow MFI zeolites with controlled properties such as wall thickness. [4, 16-22] However, for ZSM-5, SAR value of the parent zeolite is the most important parameter to ensure the successful dissolution-recrystallisation process. Accordingly, the formation of ZSM-5 with regular hollow structures is only likely with the parent ZSM-5 having the SAR value >40, [21-23] leading to hollow materials with the Si-rich shell. According to the energy dispersive X-ray spectrometry (EDX) and inductively coupled plasma-atomic emission spectrometry (ICP-AES), the parent AS-MFI has a bulk SAR of ~12 (Table S5.1). A conventional ZSM-5 with the low SAR of about 12 is not appropriate as the parent zeolite for preparing ZSM-5 with mesoporous hollow structures *via* the controlled dissolution and

recrystallisation approach. However, as discussed above, AS-MFI inherently possesses tetrahedral EFAL which does not interfere with the Si dissolution during the post-treatment. More importantly, the co-recrystallisation of dissolved Si and EFAL facilitated by TPAOH (0.1 M at 160 °C) on the external surface during the post-treatment (6 h to 96 h) produced zeolite nanoboxes with Al-rich walls (SARs of ~16, Table S5.1). X-ray photoelectron spectroscopy (XPS) also shows that the surface SARs of ZSM-5-P zeolites are lower than the according bulk ones by EDX and ICP (Table S5.1), suggesting the occurrence of Al redistribution during the TPAOH treatment.

AS-MFI is primarily microporous (specific external surface area, $S_{BET} = 375$ m^2 g^{-1}) with uniform sizes of about 300–500 nm (as shown by the High resolution TEM (HRTEM) and scanning transmission electron microscopy (STEM) analysis, Figures 5.3a1, b1 and c).
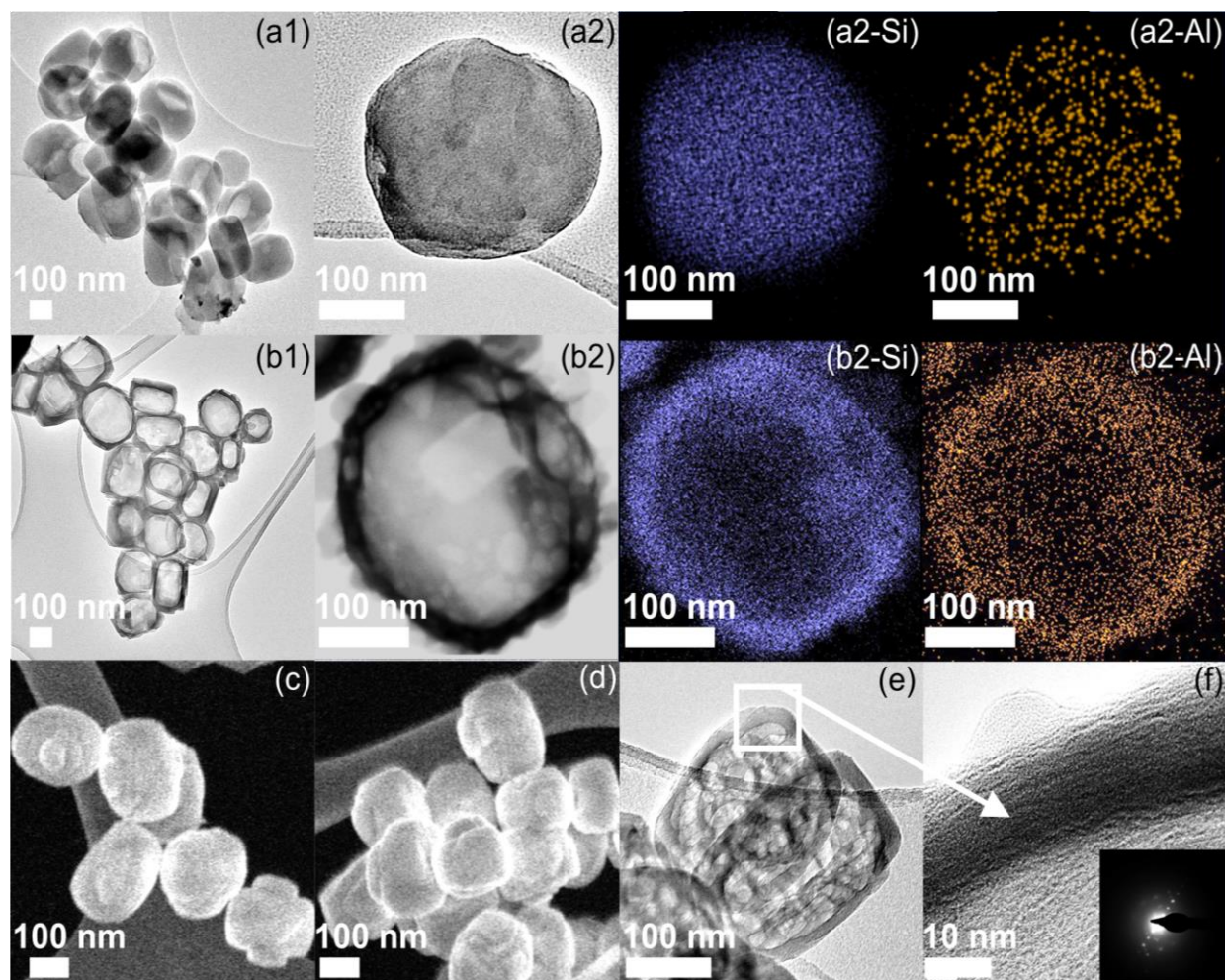
Figure 5.3. HRTEM micrographs of (a1-a2) AS-MFI and (b1-b2) ZSM-5-P-0.1-6 zeolites; STEM micrographs of (c) AS-MFI and (d) ZSM-5-O-0.1-6 zeolites; (e-f) HRTEM micrograph of ZSM-5-P-0.1-6 zeolite (Inset: the corresponding fast Fourier transform (FFT) of HRTEM).

After the post-treatment, zeolite nanoboxes were formed with comparable crystal sizes (Figures 5.3a1, b1, c, d and S5.3). The post-treatment condition used (*i.e.* 0.1 M TPAOH, at 160 °C for <12 h) was appropriate to produce the regular ZSM-5 nanoboxes with uniform cavities, which can be attributed to the preferential desilication of siliceous part of AS-MFI and recrystallisation of dissolved Si and EFAL. The shell thickness of ZSM-5-P zeolites is about 20 nm (Figures 5.3e, f and S5.3). The shell of ZSM-5-P-0.1-6 is well crystallised, as evidenced by the fast Fourier transform (FFT) of HRTEM (inset in Figure 5.3f) and XRD analysis (Figure S5.1). The Al-rich walls of ZSM-5 nanoboxes are also confirmed by EDX, as shown in Figure 5.3. ZSM-5-P nanoboxes show the significant mesoporous features as revealed by the nitrogen (N_2) adsorption-

desorption analysis (Figures 5.4a and S5.2, Table S5.1) with specific external surface areas ($S_{ext.}$) = 113–149 m^2 g^{-1} and mesopores volumes ($V_{meso.}$) = 0.16–0.26 cm^3 g^{-1}. Using concentrated SDA (*i.e.* 0.3 M or 0.5 M TPAOH, Supporting Information) in the post-treatment (24 h) was not beneficial to the formation of mesoporous hollow structures (*e.g.* $S_{ext.}$ <86 m^2 g^{-1}), as well as reducing the crystallinity of the resulting zeolites (*i.e.* ZSM-5-P-0.3-24 and ZSM-5-P-0.5-24, RC <56%), which is evidenced by various characterisation data of the materials (Figures S5.5–S5.8 and Table S5.2). This is again due to the fast and excessive dissolution, which suppresses the recrystallisation rate, making the formation of mesoporous hollow structures challenging. RC value of ZSM-5-P-0.5-24 from the treatment using 0.5 M TPAOH aqueous solution was only ~51% (Table S5.2), suggesting the significant loss of crystallinity due to the fast dissolution. N$_2$ physisorption analysis also shows that the hysteresis loops of ZSM-5-P-0.3-24 and ZSM-5-P-0.5-24 zeolites are less significant (Figure S5.7) in comparison to that of ZSM-5-P zeolites (Figure S5.2). In summary, the post-treatment with TPAOH solution is effective to revive EFAL in the parent AS-MFI, converting it into framework Al in ZSM-5-P zeolites. However, the balance of dissolution and recrystallisation needs to be regulated (by varying the treatment time and the concentration of aqueous TPAOH solution) in order to obtain well-defined crystalline nanoboxes. C-ZSM-5 shows the typical features of conventional ZSM-5 zeolites which were characterised as presented in Table S5.2. Comparably, as discussed above, the post-synthetic treatment of C-ZSM-5 (with 0.1 M TPAOH for 6 h, Supporting Information) was not able to develop mesoporous structures (*e.g.* $S_{ext.}$ = ~76 m^2 g^{-1}, Figures S5.9–S5.11, Table S5.2) due to the presence of abundant framework Al in its framework (Figures 5.2b and S5.12), inhibiting the effective dissolution of Si, and resulting in the post-treated ZSM-5 zeolite (*i.e.* P-C-ZSM-5-0.1 (6)) with limited and irregular mesopores (by SEM and TEM, Figure S5.10).

Al-rich ZSM-5-P nanoboxes (*i.e.* with low SARs) show the improved acidity, especially strong acidity corresponding to Brønsted acidity (concentration of strong acid sites, as determined by NH$_3$-TPD for NH$_3$ desorption at 300–500 °C, Figure S5.13 and Table S5.3), which is beneficial to catalysis. Due to the absence of Al-O-Si sites in AS-MFI, its strong acidity is insignificant at 24.1 µmol g^{-1}, as shown in Figure 5.4b and Table S5.33 and infrared (IR) study of pyridine adsorption on zeolites (Figure S5.14). It should be noted that the lack of strong acidity in AS-MFI also serves as the evidence of the absence of framework tetrahedral Al in it.
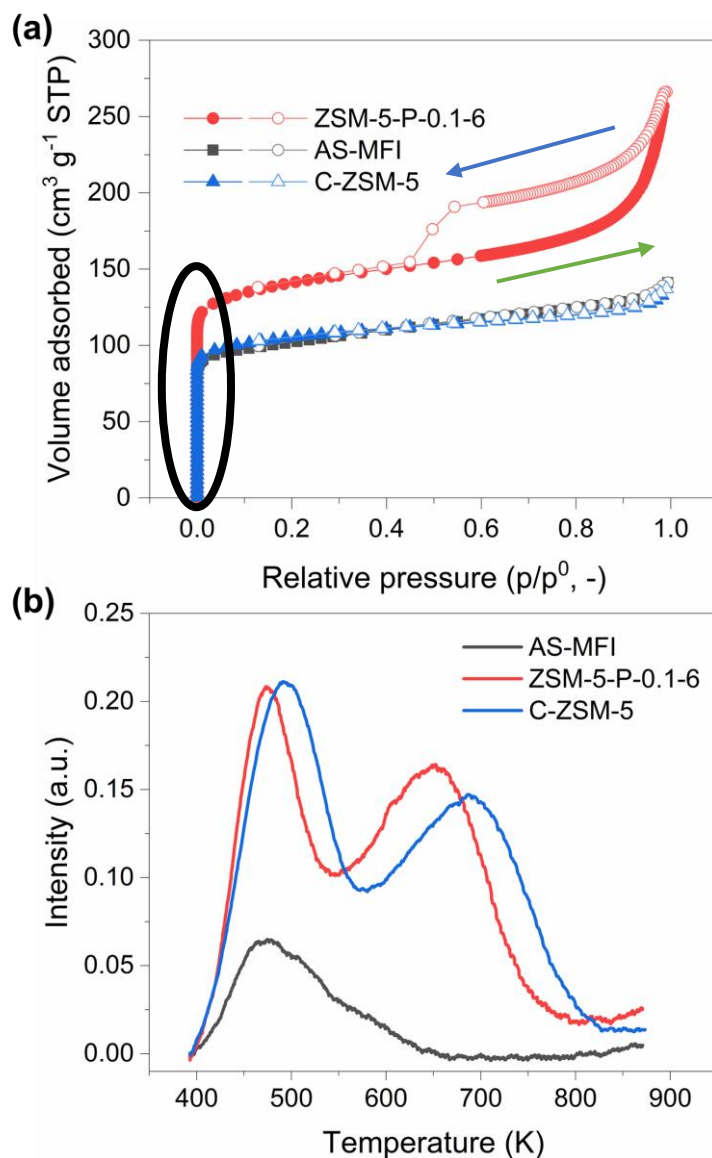
Figure 5.4. (a) N_2 adsorption (solid symbols)/desorption (open symbols) isotherms and (b) NH_3-TPD curves of AS-MFI, C-ZSM-5 and ZSM-5-P-0.1-6. The steep initial increase in volume of N_2 adsorbed (circled) is within the micropore region and is due to filling of the micropores. Increases in volume adsorbed after this point are due to filling of the mesopores. Hysteresis at high relative pressure (indicated by the arrows) are due to differences in filling and emptying of the pore space, indicated by the green and blue arrows respectively.

Conversely, ZSM-5-P nanoboxes show a significantly enhanced acidity (with an average strong acidity of 404.9±33.4 µmol g^{-1}), reflecting the reconstruction of EFAL to the tetra-coordinated framework Al during the post-treatment using TPAOH. Regarding the acidity of C-ZSM-5, it is

116

comparable to that of ZSM-5-P nanoboxes (Figure S5.13c and Table S5.3). However, the post-treatment of C-ZSM-5 (to P-C-ZSM-5-0.1 (6)) reduced the strong acidity by *ca.* 28% (from 393.6 to 282.3 µmol g^{-1}).

ZSM-5-P nanoboxes combine the mesoporous structure with the low SAR value (~16, corresponding to a high concentration of framework Al) favour the relevant zeolite catalysis such as propylene-selective catalytic cracking. ZSM-5 is the widely used additives in cracking catalysts for improving propylene selectivity, [10] due to its pore diameter which can provide size/shape selectivity. However, the conventional microporous ZSM-5 zeolite is prone to deactivate due to carbon deposition which is mainly the results of long diffusion pathway, as well as the redundant strong acid sites. [40] Although strong acid sites are crucial for catalytic reactions, especially for hydrocarbon cracking, the reactants could over-react on the acid sites and convert to aromatic hydrocarbons or carbon deposition, resulting in the deactivation of catalyst. Therefore, the development of zeolite catalysts combing the strong acidity with improved accessibility to active sites will be highly beneficial to address the challenge.

Comparative catalytic evaluation of ZSM-5-P-0.1-6 along with the control catalysts, *i.e.* AS-MFI, C-ZSM-5 and a conventional hollow ZSM-5 nanoboxes with a SAR value of ~45 (*i.e.* C-HO-ZSM-5, Figures S5.15 and S5.16, Table S5.4, Supporting Information) was performed using cracking reactions with *n*-octane (kinetic diameter, KD, = 0.43 nm) [41] and cumene (KD = 0.68 nm) [42] as the model naphtha and aromatic compounds (Figures 5.5 and S5.17, Tables S5.5 and S5.6). Catalysis was carried out in a fixed bed reactor (I.D = 10 mm) with 1 g pelletised zeolite catalysts (particle size = 1.6–1.8 mm). Figure 5.6 presents the conversion of *n*-octane over different zeolites at 540 °C as a function of time-on-stream (ToS).
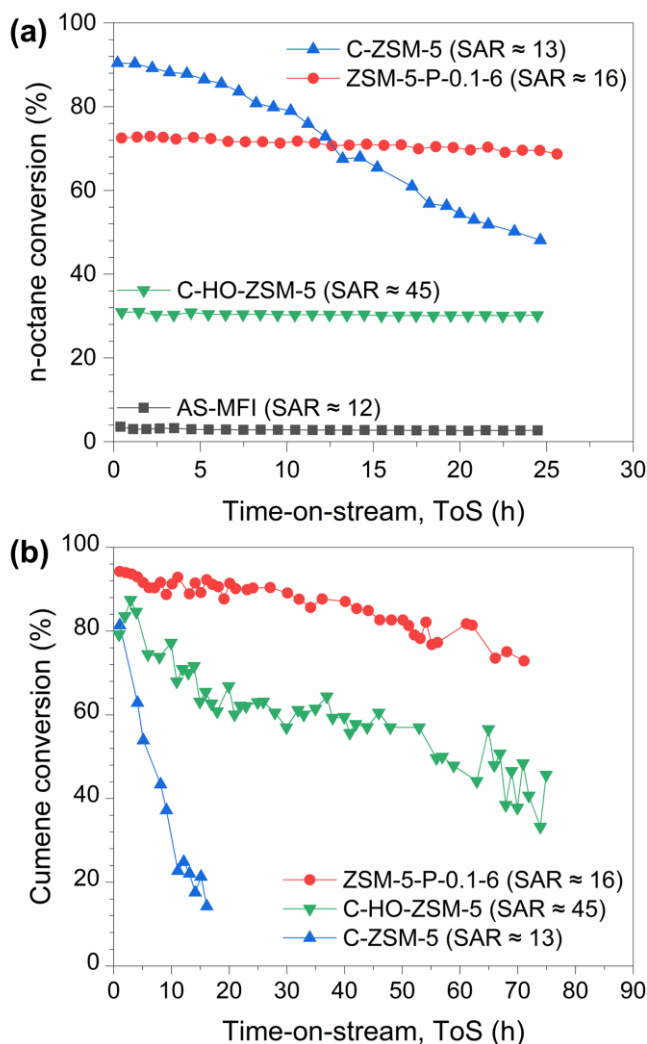
Figure 5.5. Conversion profiles of different zeolite catalysts as a function of time-on-stream (ToS) in (a) catalytic *n*-octane cracking and (b) catalytic cumene cracking.

AS-MFI shows insignificant activity compared to other catalysts due to the lack of framework Al, and thus Brønsted acidity (Figures S5.13a and S5.14). Although the microporous C-ZSM-5 presented the highest initial activity (with an initial *n*-octane conversion of ~90%), it deactivated gradually and significantly over time (the final *n*-octane conversion and dropped to ~48% after 25 h on stream). The deactivation of C-ZSM-5 was due to the coke formation on the external surface of the crystals, which was the result of the diffusion resistance caused by the pure microporous framework of C-ZSM-5, leading to the loss of accessibility and acidity (*i.e.* S_{BET} and strong acidity dropped by about 73% and 57%, respectively, according to the post-reaction characterisation of the used catalysts using N_2 physisorption and NH_3-TPD analyses, Tables S5.7 and S5.8).

Conversely, the ZSM-5-P-0.1-6 nanoboxes promoted the diffusion of *n*-octane through their newly formed percolating pore network, being highly stable regarding both *n*-octane conversion (at *ca.* 73%) and selectivity to propylene (at ~30%, as shown in Figure S5.17). C-HO-ZSM-5 with the mesoporous hollow structure (Figures S5.15 and S5.16) showed a stable catalytic performance in cracking *n*-octane as well. However, due to the low concentration of strong acidity in C-HO-ZSM-5 (at 214.4 µmol g^{-1}), it was outperformed by ZSM-5-P-0.1-6 nanoboxes by ~130% regarding *n*-octane conversion. The used ZSM-5-P-0.1-6 (denoted as ZSM-5-P-0.1-6-U) can be regenerated (by calcination at 550 °C under 10 vol.% O$_2$ in N$_2$), and the regenerated ZSM-5-P-0.1-6 showed the comparable chemical, physical and catalytic properties, as shown in Figures S5.18–S5.20 and Tables S5.7–S5.8).

The accessibility issue was substantial when relatively bulky cumene (KD = 0.68 nm) [42] was cracked (at 320 °C), the advantages of Al-rich ZSM-5-P-0.1-6 nanoboxes over the conventional microporous C-ZSM-5 and conventional C-HO-ZSM-5 (SAR = ~45) are highly recognisable. Severe deactivation (*i.e.* cumene conversion dropped by ~88% within 10 h) was measured for C-ZSM-5 due to coke deposition (as shown by the thermogravimetric, N$_2$ physisorption and NH$_3$-TPD analysis of the used zeolite catalysts, Figure S5.21, Tables S5.9–S5.10). By comparing the two ZSM-5 nanoboxes under study, ZSM-5-P-0.1-6 showed remarkably better activity than C-HO-ZSM-5 on stream of 70 h (*e.g.* deactivation rate regarding the cumene conversion: −0.31% h^{-1} for ZSM-5-P nanoboxes vs. −0.48% h^{-1} for C-HO-ZSM-5). More importantly, although with a low SAR value of ~16, ZSM-5 nanoboxes remained stable as well, as evidenced by the comparable XRD and N$_2$ physisorption analysis of the used ZSM-5-P-0.1-6 before and after steam ageing (at 500 °C for 10 h with 50% water in N$_2$, Figure S5.22 and Table S5.11). The specific micropore surface area (S_{micro}) of the used ZSM-5-P-0.1-6 after steam ageing dropped by *ca.* 6% (from 415 m^2 g^{-1} to 391 m^2 g^{-1}), while the RC values remained comparable at ~85%.

As previously mentioned, it is likely that the creation of an intra-crystalline accessible meso-microporous structure of ZSM-5-P nanoboxes contributes to the measured catalytic activity; this was experimentally confirmed by PFG-NMR measurements carried out at a ^{1}H frequency of 43 MHz, with a diffusion probe capable of producing magnetic field gradient pulses up to 163 mT m^{-1}, at atmospheric pressure and 25 °C. The mass transport properties of the zeolites under study measured by PFG-NMR (using probing molecules of *n*-octane, cumene and 1,3,5-

triisopropylbenzene, TIPB) are shown in Figure 5.6, together with PFG-NMR plots of the bulk liquid of probing molecules (*i.e.* purple inverted triangle symbols in Figures 5.6a–5.6c) as a reference. Diffusion measurements were performed using the pulsed-field gradient stimulated echo sequence (PGSTE sequence). [31] The sequence is made by combining a series of radiofrequency pulses (RF) with magnetic field gradients (*g*, Figure 2.11). According to Equation 2.38, the NMR signal attenuation of PFG-NMR experiments as a function of the gradient strength, $E(g)$, is related to the experimental variables and the diffusion coefficient (*D*, calculated by fitting Equation 2.38 to the experimental data). PFG-NMR plots, *i.e.* log-attenuation plots as shown in Figures 5.6a–5.6c, provide a visual representation of the diffusion properties of the guest molecules within the porous media being studied.
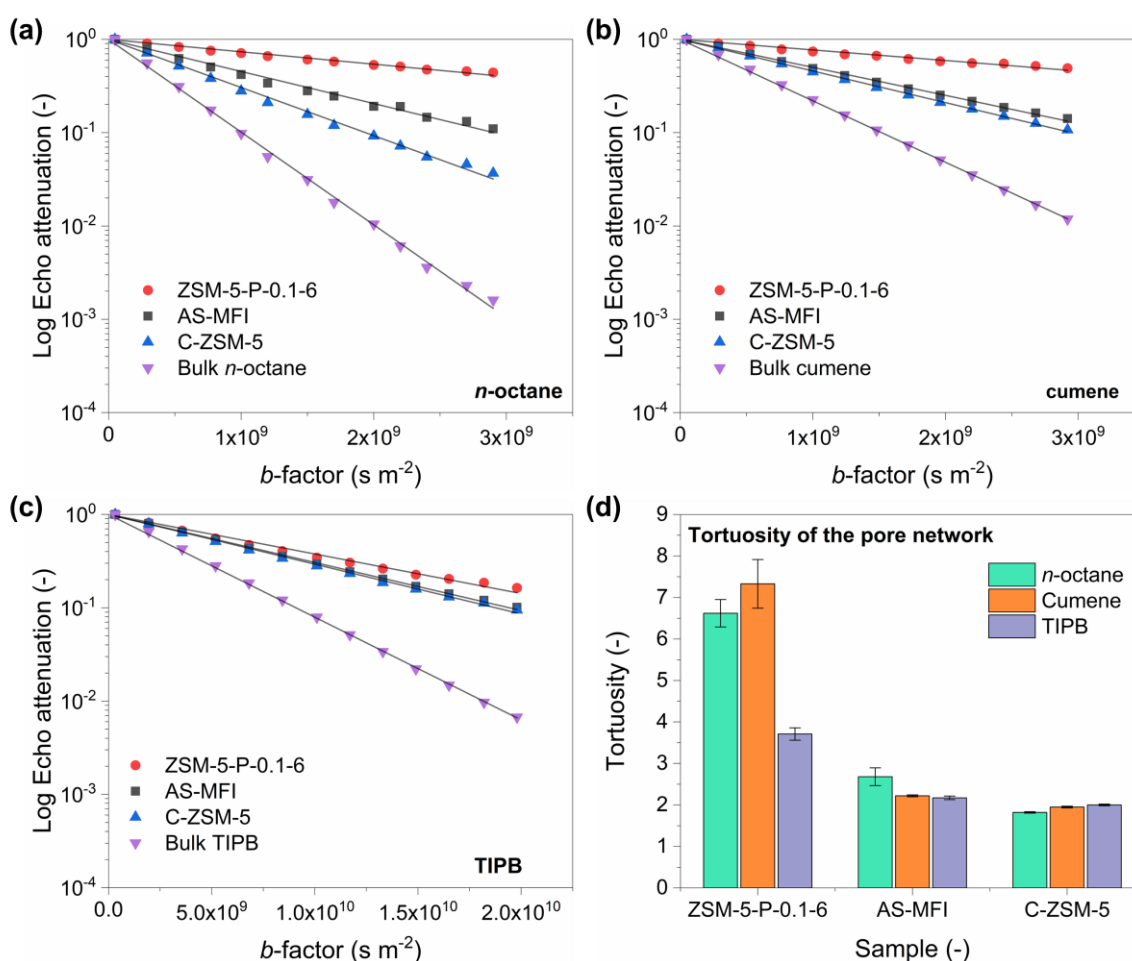
Figure 5.6. PFG-NMR log attenuation plots for (a) *n*-octane, (b) cumene and (c) TIPB within different zeolite samples under investigation (solid lines represent the fittings using Equation 2.38); (d) values of tortuosity of the probe molecules of *n*-octane, cumene and TIPB in different zeolite samples.

The lack of any evident curvature for PFG-NMR plots, as well as the relatively large root-mean-square displacement (RMSD) values (Table 5.1), [43] which are much greater than the average crystal size of the zeolite particles, indicates that the guest molecules have the time to explore the overall pore structure of the solid samples (both inter- and intra-crystalline space) during the observation times used for the experiments (*i.e.* 200 ms for *n*-octane/cumene and 500 ms for TIPB).

Table 5.1. Root mean squared displacements (RMSD) of *n*-octane, cumene and 1,3,5-triisopropylbenzene (TIPB) imbibed within the ZSM-5-P-0.1-6, AS-MFI and C-ZSM-5 zeolite catalysts.

Sample	$RMSD_{OCT}$ [μm]	$RMSD_{CUM}$ [μm]	$RMSD_{TIPB}$ [μm]
C-ZSM-5	23.0	18.6	11.4
AS-MFI	18.9	17.7	11.1
ZSM-5-P-0.1-6	12.1	11.6	8.2

Therefore, the calculated diffusion coefficients (D) represent the averaged molecular diffusivity across the whole zeolite particle. [44] Consequently, the diffusion measured is not solely intracrystalline diffusion but rather, an effective diffusivity comprised of diffusion within the intracrystalline pore space and the pore space between crystallites, commonly referred to as long-range diffusion. By fitting PFG-NMR plots using Equation 2.38, the relevant diffusion coefficient of the systems under investigation was obtained (the negative value of the slope is equivalent to the numerical value of D of the guest molecules being studied), as shown in Table 5.2.

Table 5.2. Self-diffusivity and diffusivity values of bulk *n*-octane, cumene and TIPB, and *n*-octane and cumene imbibed within the C-ZSM-5, AS-MFI and ZSM-5-P-0.1-6 samples, and the calculated tortuosity values of the samples.

Sample	D_{OCT} [m^2 s^{-1}] × 10^9	τ_{OCT}	D_{CUM} [m^2 s^{-1}] × 10^9	τ_{CUM}	D_{TIPB} [m^2 s^{-1}] × 10^9	τ_{TIPB}
C-ZSM-5	1.29±1 %	1.82±1 %	0.80±1 %	1.95±1 %	0.13±1 %	2.00±1 %
AS-MFI	0.76±8 %	2.68±8 %	0.70±1 %	2.22±1 %	0.14±1 %	1.86±1 %
ZSM-5-P-0.1-6	0.30±5 %	6.62±5 %	0.22±8 %	7.33±8 %	0.07±2 %	3.71±2 %
Bulk liquid	2.30±1 %	-	1.56±1 %	-	0.26±4 %	-

Interestingly, PFG-NMR measurements showed that D values of the probing molecules in ZSM-5-P-0.1-6 were the smallest in comparison with the microporous AS-MFI and C-ZSM-5. As a consequence, the pore network tortuosity, defined as the ratio of the bulk diffusivity of the guest molecule and that of the same molecule within the pore space, (τ, Figure 5.6d, calculated using Equation 4.2) of the ZSM-5-P-0.1-6 sample is the largest. Considering the kinetic diameter n-octane (0.43 nm) and cumene (0.68 nm), for ZSM-5-P-0.1-6, the comparatively small value of D and large value of τ, suggest that the developed method created a new percolating network within ZSM-5-P-0.1-6 zeolite crystals. As a result, the probing molecules gain access to the newly formed percolating network in the intra-crystalline pores, which is more tortuous than the inter-crystalline space, hence leading to lower values of the averaged measured diffusion coefficient due to increased collisions with the intra-crystalline pore walls. It is also possible that the measured diffusivities are impacted by a change in diffusion mechanism. Within the purely microporous crystal, molecules will not be able to enter the small pore space so will diffuse through the relatively large intercrystalline pore space, most likely by the molecular diffusion mechanism, as discussed in Chapter 3, where diffusion is dominated by molecule-molecule interactions and is relatively fast. Within the intracrystalline pores, the diffusion is more likely to be Knudsen type diffusion, also discussed in Chapter 3, where molecule-pore wall interactions dominate and the diffusivity is relatively slow. This slowing of diffusivity due to change in diffusion mechanism can also be responsible for the higher tortuosity values observed.

For the microporous AS-MFI and C-ZSM-5, the probing molecules diffuse primarily within the inter-crystalline pore space (since the intra-crystalline space is less accessible due to the much smaller pore size of 0.54 nm). To prove this further, PFG-NMR experiments were carried out using a bulky molecule, TIPB (kinetic diameter = 0.94 nm), [45] which is not able to enter the micropores of the intra-crystalline space (*i.e.* the intrinsic micropores of ZSM-5 zeolites). It was found that, when bulky TIPB was used as the probing species, (*i*) unlike n-octane and cumene, PFG-NMR plots of the materials are comparable for all the zeolite samples (Figure 5.6c) and (*ii*) the rate of diffusion within the ZSM-5-P-0.1-6 sample measured across the whole zeolite particle increases, leading to a significant decrease in τ values, which becomes comparable with values measured for the parent and conventional zeolites (Table 5.2). Such findings can be clearly explained by considering the larger size of TIPB (in comparison with n-octane and cumene) hinders the access to newly formed percolating network inside the crystalline space of ZSM-5-P-0.1-6 zeolites, hence

the probe molecules experience a faster diffusion, lower tortuosity, within the inter-crystalline space only. This is also confirmed by the comparable D and τ values of the zeolites under investigation when TIPB was used as the probing molecules in PFG-NMR measurements (Table 5.2). In comparison with the state-of-the-art post-synthetic alkaline treatments (with or without SDA, Tables S5.12 and S5.13), the method produced ZSM-5 nanoboxes with (*i*) a well-developed percolating meso-micro-porous network and (*ii*) high concentration of strong acid sites (*i.e.* low SAR) in zeolite crystals.

5.4. Conclusions

ZSM-5 zeolites are important catalysts for many catalytic conversions such as catalytic cracking (to increase propylene selectivity by cracking gasoline range molecules selectively), MTO, alkylation and ethanol dehydration. Accessibility issues and mass transfer limitations in ZSM-5's microporous framework commonly affect the outcome of the catalysis to a great extent. Post-synthetic desilication treatment of ZSM-5 is the practical way to introduce mesoporosity to ZSM-5 zeolites but is limited by SAR of the parent zeolites. This work presents a simple and novel strategy *via* rapid ageing of the sol gel mixture to prepare the parent zeolite with the tetrahedral EFAL and low SAR of about 12, which can be subsequently reconstructed (during the post-synthetic treatment using SDA, *i.e.* TPAOH) to give mesoporous hollow ZSM-5 nanoboxes with low SAR of ~16. The developed protocol removed the constraint of SAR of the parent zeolite on properties of the post-treated ZSM-5. The unique combination of the hierarchical meso-micro-porous thin shell and low SAR of such ZSM-5 nanoboxes led to (*i*) the significantly improved accessibility of guest molecules to the active sites (evidenced by PFG-NMR measurements) and (*ii*) comparably high yet stable catalytic performance in cracking reactions, which is significantly important for the development of specific propylene-selective catalysts aiming to improve the current on-purpose propylene production technologies.

References

1. Y. Jiao, L. Forster, S. Xu, H. Chen, J. Han, X. Liu, Y. Zhou, J. Liu, J. Zhang, J. Yu, C. D'Agostino and X. Fan, *Angew. Chem., Int. Ed.*, 2020, **132**, 19646–19654.

2. D. Zhang, C. Jin, M. Zou and S. Huang, *Chem. Eur. J.*, 2019, **25**, 2675 – 2683.

3.   J. C. Groen, J. C. Jansen, J. A. Moulijn and J. Pérez-Ramírez, *J. Phys. Chem. B*, 2004, **108**, 13062–13065.

4. J. C. Groen, T. Bach, U. Ziese, A. M. Paulaime-van Donk, K. P. de Jong, J. A. Moulijn and J. Pérez-Ramírez, *J. Am. Chem. Soc.*, 2005, **127**, 10792–10793.

5. J. C. Groen, J. A. Moulijn and J. Pérez-Ramírez, *Ind. Eng. Chem. Res.*, 2007, **46**, 4193–4201.

6. R. Chal, C. Grardin, M. Bulut and S. van Donk, *ChemCatChem*, 2011, **3**, 67–81.

7. Y. Li, L. Li and J. Yu, *Chem*, 2017, **3**, 928–949.

8. R. Bai, Y. Song, Y. Li and J. Yu, *Trends Chem.*, 2019, **1**, 601–611.

9. A. V. Lavrenov, L. F. Saifulina, E. A. Buluchevskii and E. N. Bogdanets, *Catal. Ind.*, 2015, **7**, 175–187.

10. E. T. C. Vogt and B. M. Weckhuysen, *Chem. Soc. Rev.*, 2015, **44**, 7342–7370.

11. Y. Jiao, X. Fan, M. Perdjon, Z. Yang and J. Zhang, *Appl. Catal. A*, 2017, **545**, 104–112.

12. J. Li, M. Liu, X. Guo, S. Zeng, S. Xu, Y. Wei, Z. Liu and C. Song, *Ind. Eng. Chem. Res.*, 2018, **57**, 15375–15384.

13. Y. Jiao, X. Ou, J. Zhang and X. Fan, *React. Chem. Eng.*, 2019, **4**, 427–435.

14. C. Pagis, A. R. Morgado Prates, D. Farrusseng, N. Bats and A. Tuel, *Chem. Mater.*, 2016, **28**, 5205–5223.

15. C. Mei, Z. Liu, P. Wen, Z. Xie, W. Hua and Z. Gao, *J. Mater. Chem.*, 2008, **18**, 3496–3500.

16. Y. Wang, M. Lin and A. Tuel, *Microporous Mesoporous Mater.*, 2007, **102**, 80–85.

17. Y. Wang and A. Tuel, *Microporous Mesoporous Mater.*, 2008, **113**, 286–295.

18. J. Shao, T. Fu, Z. Ma, C. Zhang, H. Li, L. Cui, Z. Li, *Catal. Sci. Technol.*, 2019, **9**, 6647–6658.

19. D. Verboekend and J. Pérez-Ramírez, *Chem. Eur. J.*, 2011, **17**, 1137–1147.

20. Z. Ma, T. Fu, Y. Wang, J. Shao, Q. Ma, C. Zhang, L. Cui and Z. Li, *Ind. Eng. Chem. Res.*, 2019, **58**, 2146–2158.

21.   S. Li, A. Tuel, D. Laprune, F. Meunier and D. Farrusseng, *Chem. Mater.*, 2015, **27**, 276–282.

22.   C. Dai, A. Zhang, M. Liu, X. Guo and C. Song, *Adv. Funct. Mater.*, 2015, **25**, 7479–7487.

23.   Z. Hong, Z. Wang, D. Chen, Q. Sun and X. Li, *Appl. Surf. Sci.*, 2018, **440**, 1037–1046.

24.   P. Kortunov, S. Vasenkov, J. Kärger, R. Valiullin, P. Gottschalk, M. Fé Elía, M. Perez, M. Stöcker, B. Drescher, G. McElhiney, C. Berger, R. Gläser and J. Weitkamp, *J. Am. Chem. Soc.*, 2005, **127**, 13055–13059.

25.   R. Valiullin, J. Kärger, K. Cho, M. Choi and R. Ryoo, *Microporous Mesoporous Mater.*, 2011, **142**, 236–244.

26.   D. Mehlhorn, R. Valiullin, J. Kärger, K. Cho and R. Ryoo, *Microporous Mesoporous Mater.*, 2012, **164**, 273–279.

27.   P. Kortunov, S. Vasenkov, J. Kärger, M. Fé Elía, M. Perez, M. Stöcker, G. K. Papadopoulos, D. Theodorou, B. Drescher, G. McElhiney, B. Bernauer, V. Krystl, M. Kočiřík, A. Zikánová, H. Jirglová, C. Berger, R. Gläser, J. Weitkamp and E. W. Hansen, *Chem. Mater.*, 2005, **17**, 2466–2474.

28.   X. Ou, S. Xu, J. M. Warnett, S. M. Holmes, A. Zaheer, A. A. Garforth, M. A. Williams, Y. Jiao and X. Fan, *Chem. Eng. J.*, 2017, **312**, 1-9.

29.   G. Horvath, K. Kawazoe, *J. Chem. Eng. Jpn.*, 1983, **16** , 470-475.

30.   E. P. Barrett, L. G. Joyner, P. P. Halenda, *J. Am. Chem. Soc.*, 1951, 73, 373-380.

31.   E. O. Stejskal and J. E. Tanner, *J. Chem. Phys.*, 1965, **42**, 288-292.

32.   C. D'Agostino, J. Mitchell, L. F. Gladden and M. D. Mantle, *J. Phys. Chem. C¸* 2012, **116**, 8975-8982.

33.   E. L. Perkins, J. P. Lowe, K. J. Edler, N. Tanko and S. P. Rigby, *Chem. Eng. Sci.¸* 2008, **63**, 1929-1940.

34.   E. Duprey, P. Beaunier, M. A. Springuel-Huet, F. BozonVerduraz, J. Fraissard, J. M. Manoli and J. M. Brgeault, *J. Catal.*, 1997, **165**, 22–32.

35.   M. Ardit, A. Martucci and G. Cruciani, *J. Phys. Chem. C*, 2015, **119**, 7351–7359.

36.   Z. Yu, A. Zheng, Q. Wang, L. Chen, J. Xu, J.-P. Amoureux and F. Deng, *Angew. Chem. Int. Ed.*, 2010, **49**, 8657–8661; *Angew. Chem.*, 2010, **122**, 8839–8843.

37.   D. Verboekend, S. Mitchell, M. Milina, J. C. Groen and J. Pérez-Ramírez, *J. Phys. Chem. C*, 2011, **115**, 14193–14203.

38. A. Erigoni, S. H. Newland, G. Paul, L. Marchese, R. Raja and E. Gianotti, *ChemCatChem*, 2016, **8**, 3161–3169.

39. S. Sklenak, J. Dĕdeček, C. Li, B. Wichterlová, V. Gábová, M. Sierka and J. Sauer, *Phys. Chem. Chem. Phys.*, 2009, **11**, 1237–1247.

40. Y. Ji, H. Yang and W. Yan, *Catalysts*, 2017, **7**, 367.

41. H. H. Funke, A. M. Argo, J. L. Falconer and R. D. Noble, *Ind. Eng. Chem. Res.*, 1997, **36**, 137 – 143.

42. M. Jahandar Lashaki, M. Fayaz, S. Niknaddaf and Z. Hashisho, *J. Hazard. Mater.*, 2012, **241–242**, 154–163.

43. M. Dvoyashkin, R. Valiullin and J. Kärger, *Phys. Rev. E*, 2007, **75**, 041202.

44. Q. Zhu, G. D. Moggridge, M. Ainte, M. D. Mantle, L. F. Gladden and C. D'Agostino, *Chem. Eng. J.*, 2016, **306**, 67–76.

45. N. Hosseinpour, Y. Mortazavi, A. Bazyari, A. A. Khodadadi, *Fuel Process. Technol.*, 2009, **90**, 171–179.

Supporting information
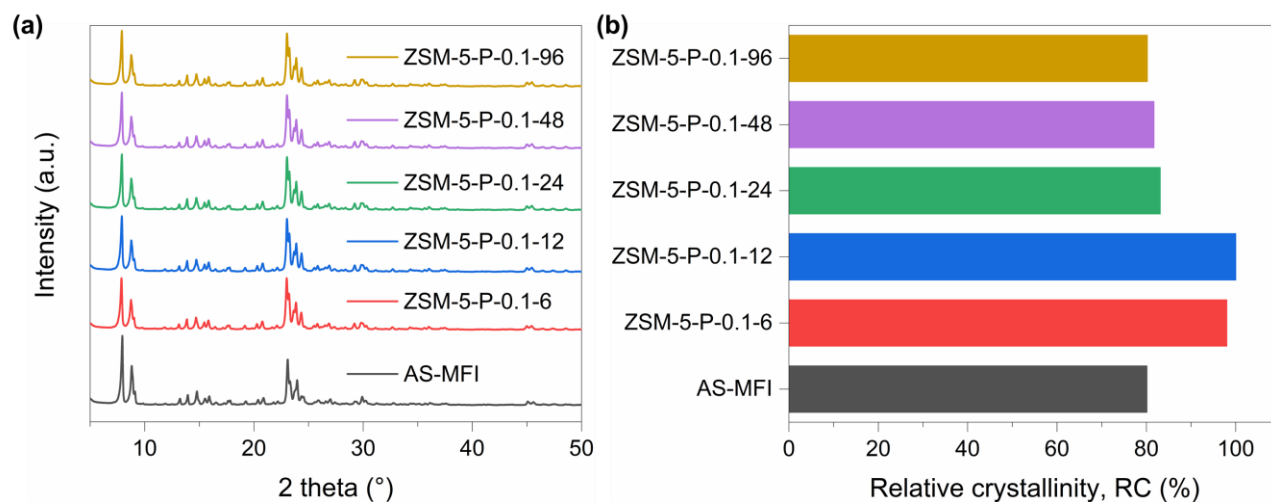
Figure S5.1. (a) XRD patterns and (b) relative crystallinity (RC) of AS-MFI and mesoporous ZSM-5 nanoboxes (*i.e.* ZSM-5-P zeolites) from the post-synthetic TPAOH (0.1 M) treatment of AS-MFI with different treatment times (6–96 h, ZSM-5-P-0.1-12 as the reference with 100% RC).
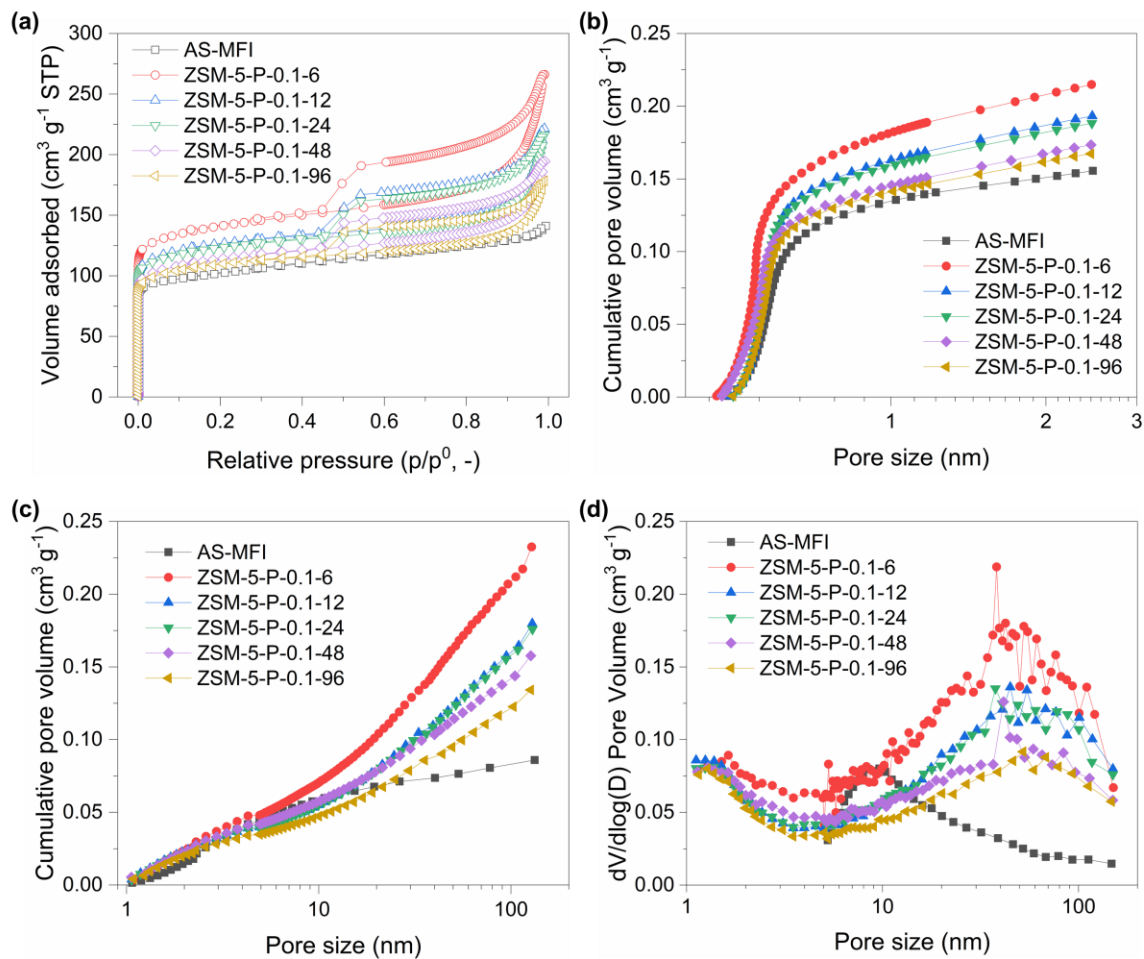
Figure S5.2. (a) Nitrogen (N_2) adsorption/desorption isotherms, (b) micropore cumulative pore volume, (c) mesopore cumulative pore volume and (d) differential pore size distribution of AS-MFI and mesoporous ZSM-5 nanoboxes (*i.e.* ZSM-5-P zeolites) from the post-synthetic TPAOH (0.1 M) treatment of AS-MFI with different treatment times (6–96 h).

Table S5.1. Textural properties and molar SARs of AS-MFI and mesoporous ZSM-5 nanoboxes (*i.e.* ZSM-5-P zeolites) from the post-synthetic TPAOH (0.1 M) treatment of AS-MFI with different treatment times (6–96 h).

Sample	S_{BET} $[m^2\,g^{-1}]$	S_{micro} $[m^2\,g^{-1}]$	$S_{ext.}$ $[m^2\,g^{-1}]$	V_{micro} $[cm^3\,g^{-1}]$	V_{total} $[cm^3\,g^{-1}]$	V_{meso} $[cm^3\,g^{-1}]$	Molar SAR [-] by XPS	by EDX	by ICP
AS-MFI	375	275	100	0.12	0.22	0.10	5.9	12.1	12.3
ZSM-5-P-0.1-6	521	372	149	0.15	0.41	0.26	10.9	16.3	15.6
ZSM-5-P-0.1-12	468	339	129	0.14	0.34	0.20	9.1	16.6	16.3
ZSM-5-P-0.1-24	456	331	125	0.14	0.34	0.20	10.2	17.6	17.1
ZSM-5-P-0.1-48	420	295	125	0.12	0.30	0.18	12.5	15.2	16.4
ZSM-5-P-0.1-96	406	293	113	0.12	0.28	0.16	12.6	14.7	15.2
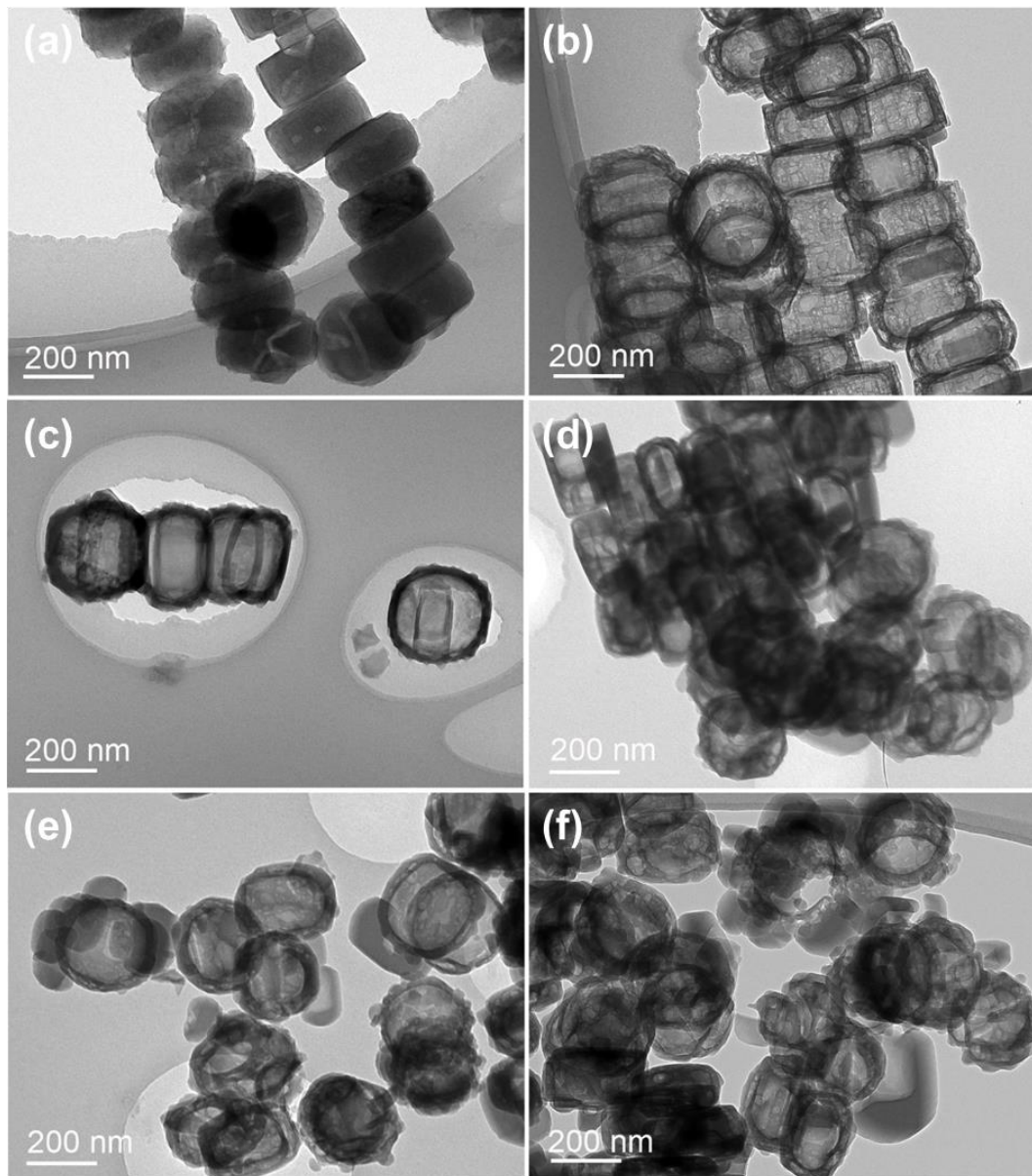
Figure S5.3. TEM micrographs of (a) AS-MFI, (b) ZSM-5-P-0.1-6, (c) ZSM-5-P-0.1-12, (d) ZSM-5-P-0.1-24, (e) ZSM-5-P-0.1-48 and (f) ZSM-5-P-0.1-96 zeolites.
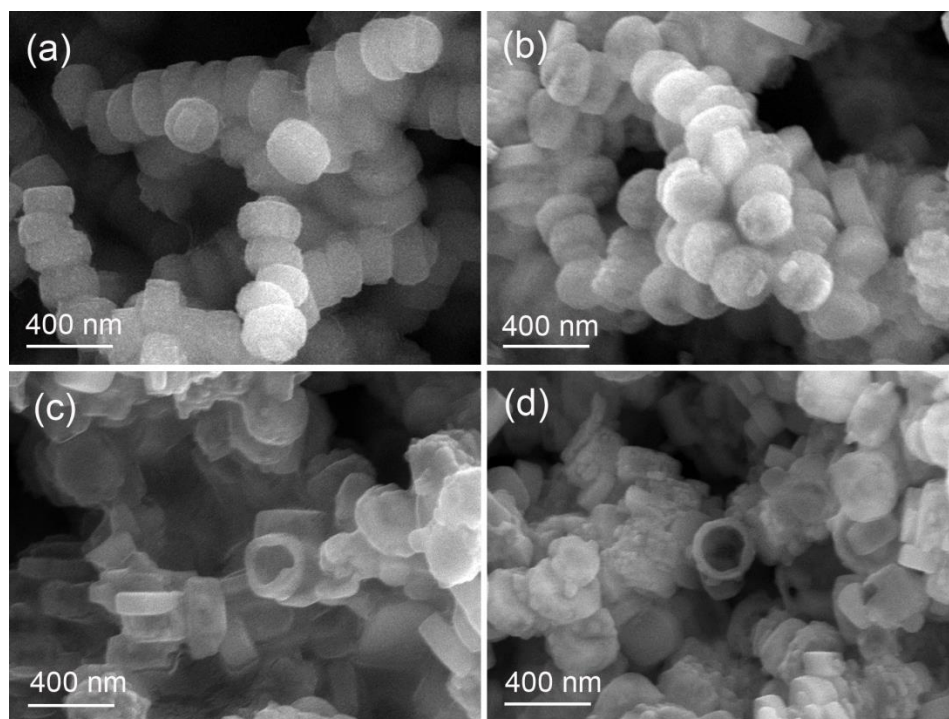
Figure S5.4. SEM micrographs of (a) ZSM-5-P-0.1-12, (b) ZSM-5-P-0.1-24, (c) ZSM-5-P-0.1-48 and (d) ZSM-5-P-0.1-96 zeolites.
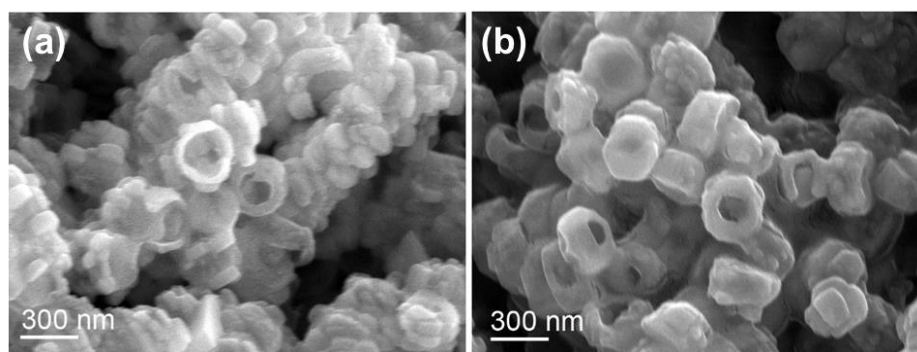

Figure S5.5. SEM micrographs of (a) ZSM-5-P-0.3-24 and (b) ZSM-5-P -0.5-24 zeolites (the samples were obtained by treating AS-MFI using 0.3 M and 0.5 M TPAOH solutions for 24 h).
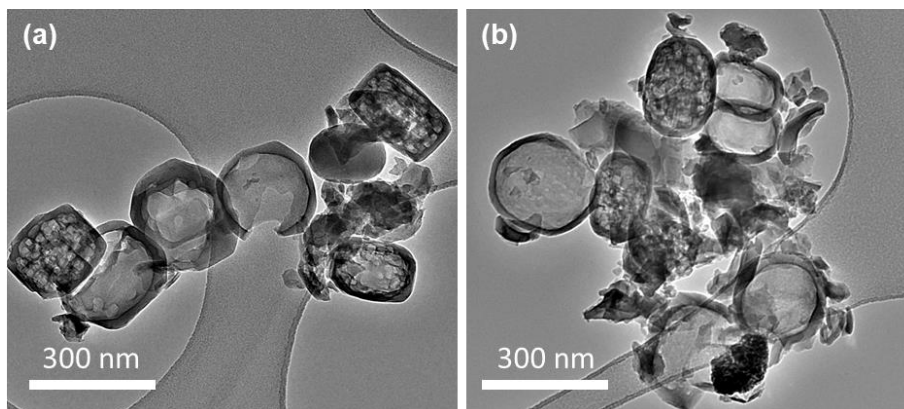
Figure S5.6. TEM micrographs of (a) ZSM-5-0.3-P-24 and (b) ZSM-5-P-0.5-24 zeolites.
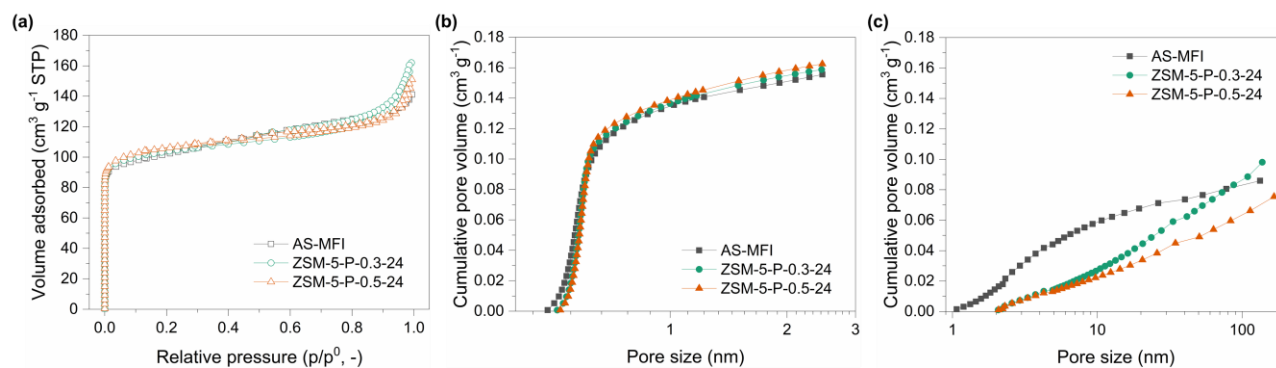
Figure S5.7. (a) N_2 adsorption/desorption isotherms, (b) micropore cumulative pore volume, (c) mesopore cumulative pore volume of AS-MFI, ZSM-5-P-0.3-24 and ZSM-5-P-0.5-24 zeolites.
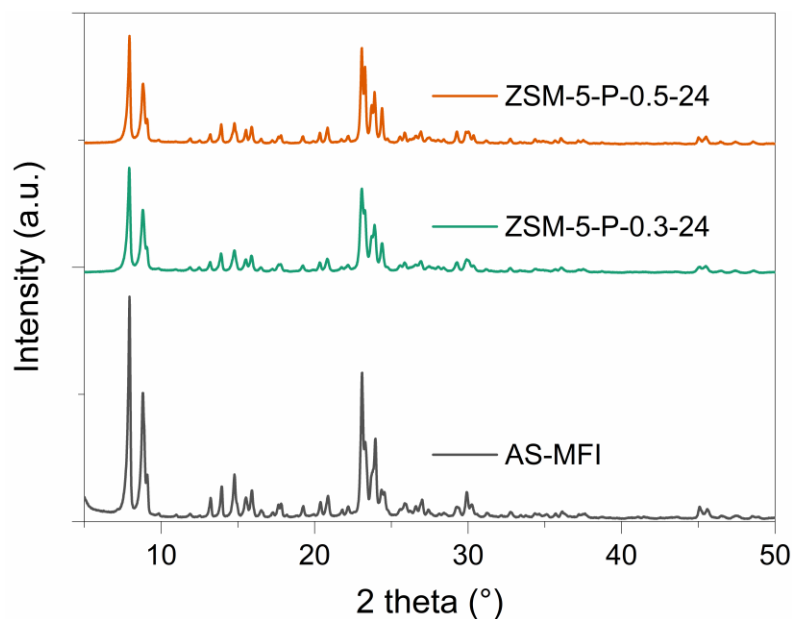
Figure S5.8. XRD patterns of AS-MFI, ZSM-5-P-0.3-24 and ZSM-5-P-0.5-24 zeolites.

Table S5.2. Textural properties, molar SARs and relative crystallinities (RC) of AS-MFI, P-ZSM-5-0.3-24 and P-ZSM-5-0.5-24 zeolites.

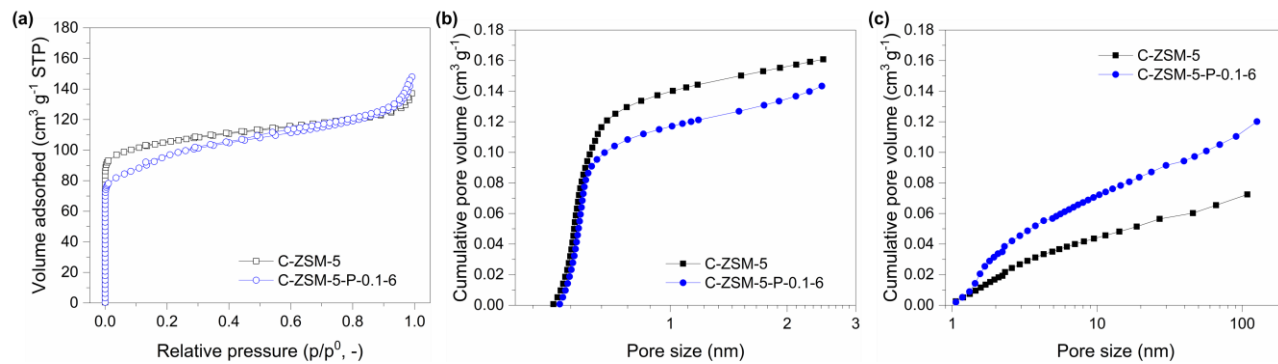| Sample	S_{BET} [$m^2\,g^{-1}$]	S_{micro} [$m^2\,g^{-1}$]	$S_{ext.}$ [$m^2\,g^{-1}$]	V_{micro} [$cm^3\,g^{-1}$]	V_{total} [$cm^3\,g^{-1}$]	Molar SAR [-] by XPS	by EDX	by ICP	RC [%]
AS-MFI	375	275	100	0.12	0.22	5.9	12.1	12.3	80.1
ZSM-5-P-0.3-24	392	317	75	0.13	0.25	15.4	15.6	14.9	55.9
ZSM-5-P-0.5-24	388	302	86	0.13	0.23	13.9	13.7	14.3	51.0
C-ZSM-5	341	285	56	0.14	0.21	9.7	13	13.4	-
C-ZSM-5-0.1-6	337	261	76	0.12	0.23	12.0	16.5	16.1	77.3
C-HO-ZSM-5	379	234	145	0.10	0.28	42.0	45.1	44.9	-

Figure S5.9. (a) N_2 adsorption/desorption isotherms, (b) micropore cumulative pore volume, (c) mesopore cumulative pore volume of C-ZSM-5 and C-ZSM-5-P-0.1-6 zeolites (C-ZSM-5-P-0.1-6 was obtained from the post-synthetic TPAOH (0.1 M) treatment of C-ZSM-5 for 6 h).
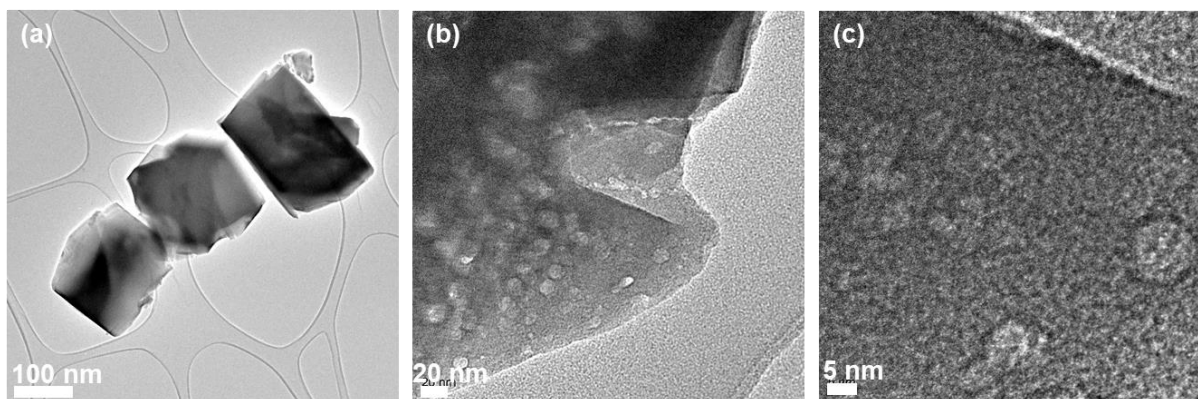

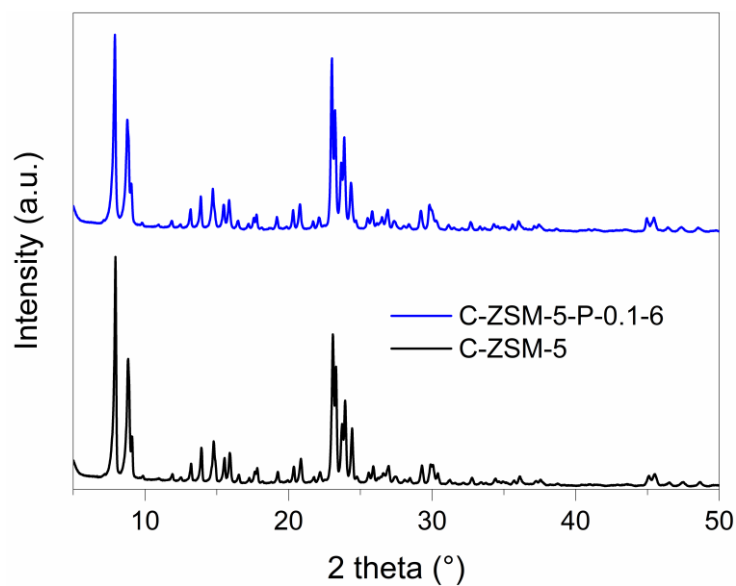**Figure S5.10**. TEM micrographs of (a) C-ZSM-5 and (b–c) C-ZSM-5-P-0.1-6 zeolites.

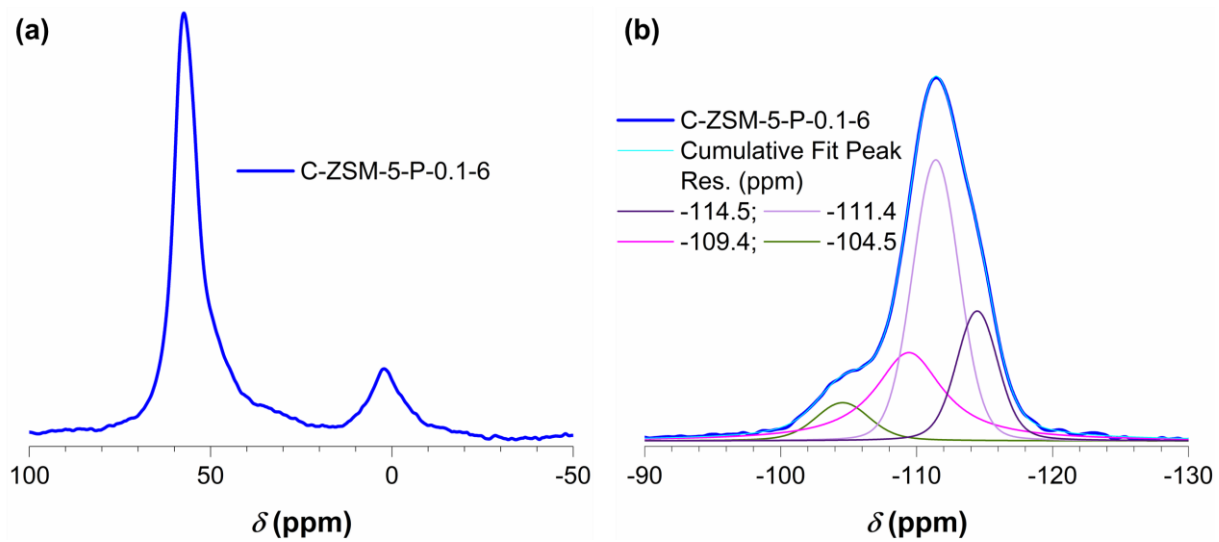**Figure S5.11**. XRD patterns of C-ZSM-5 and C-ZSM-5-P-0.1-6 zeolites.

Figure S5.12. (a) ^{27}Al MAS NMR spectrum and (b) ^{29}Si MAS NMR spectra of the C-ZSM-5-P-0.1-6 zeolite.
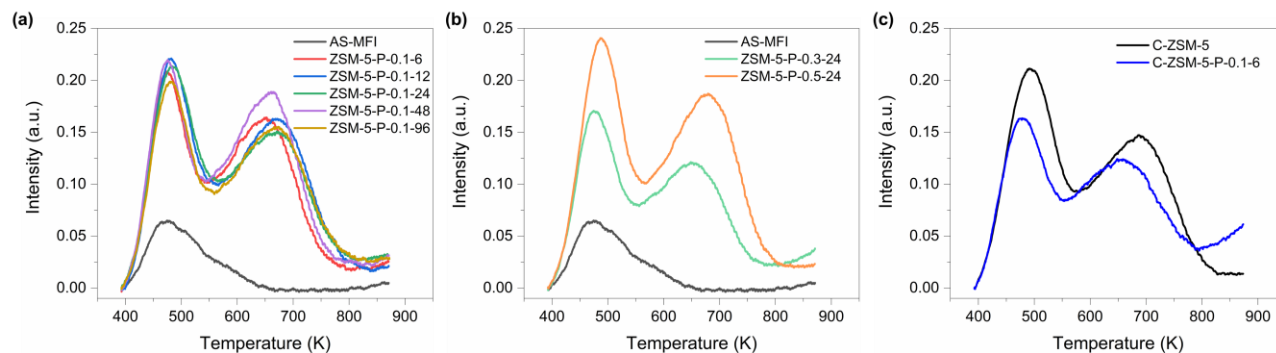
Figure S5.13. Comparative NH_3-TPD curves of (a) AS-MFI and mesoporous ZSM-5 nanoboxes (*i.e.* ZSM-5-P zeolites), (b) AS-MFI, ZSM-5-P-0.3-24 and ZSM-5-P-0.5-24 zeolites, and (c) C-ZSM-5 and C-ZSM-5-P-0.1-6 zeolites.
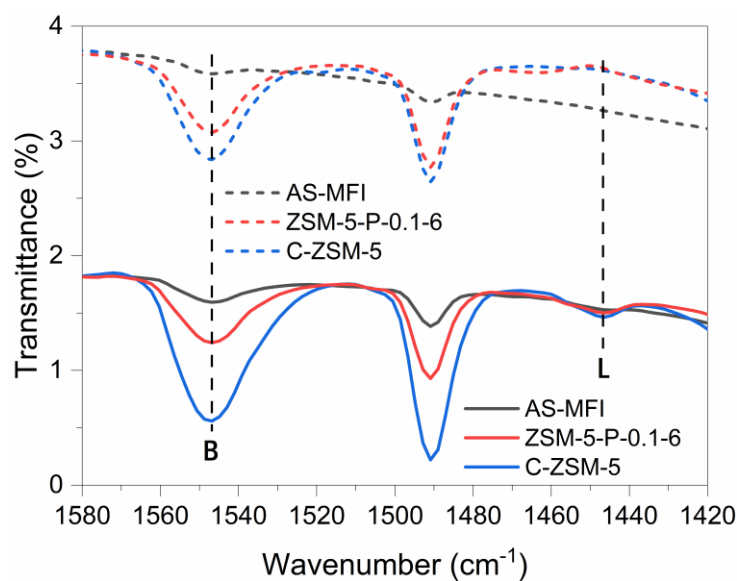

Figure S5.14. IR spectra, in the region characteristic of adsorbed pyridine vibrations, of the relevant zeolite catalysts after pyridine sorption and evacuation at 200 °C (solid lines) and 350 °C (dash lines).

Table S5.3. Acidic properties of the zeolite catalysts under investigation by NH_3-TPD.

| Sample	Temperature at maximum [K]		Weak acidity [μmol g^{-1}]	Strong acidity [μmol g^{-1}]
	First peak	Second peak		
AS-MFI	473	569	107.6	24.1
ZSM-5-P-0.1-6	471	645	249.6	403.1
ZSM-5-P-0.1-12	478	666	292.9	425.4
ZSM-5-P-0.1-24	480	662	293.3	364.7
ZSM-5-P-0.1-48	472	652	248.7	448.7
ZSM-5-P-0.1-96	477	661	248.2	382.6
ZSM-5-P-0.3-24	474	648	208.9	286.6
ZSM-5-P-0.5-24	485	675	303.1	469.2
C-ZSM-5	488	682	321.6	393.6
C-ZSM-5-P-0.1-6	474	651	215.1	282.3
C-HO-ZSM-5	468	640	131.1	214.4
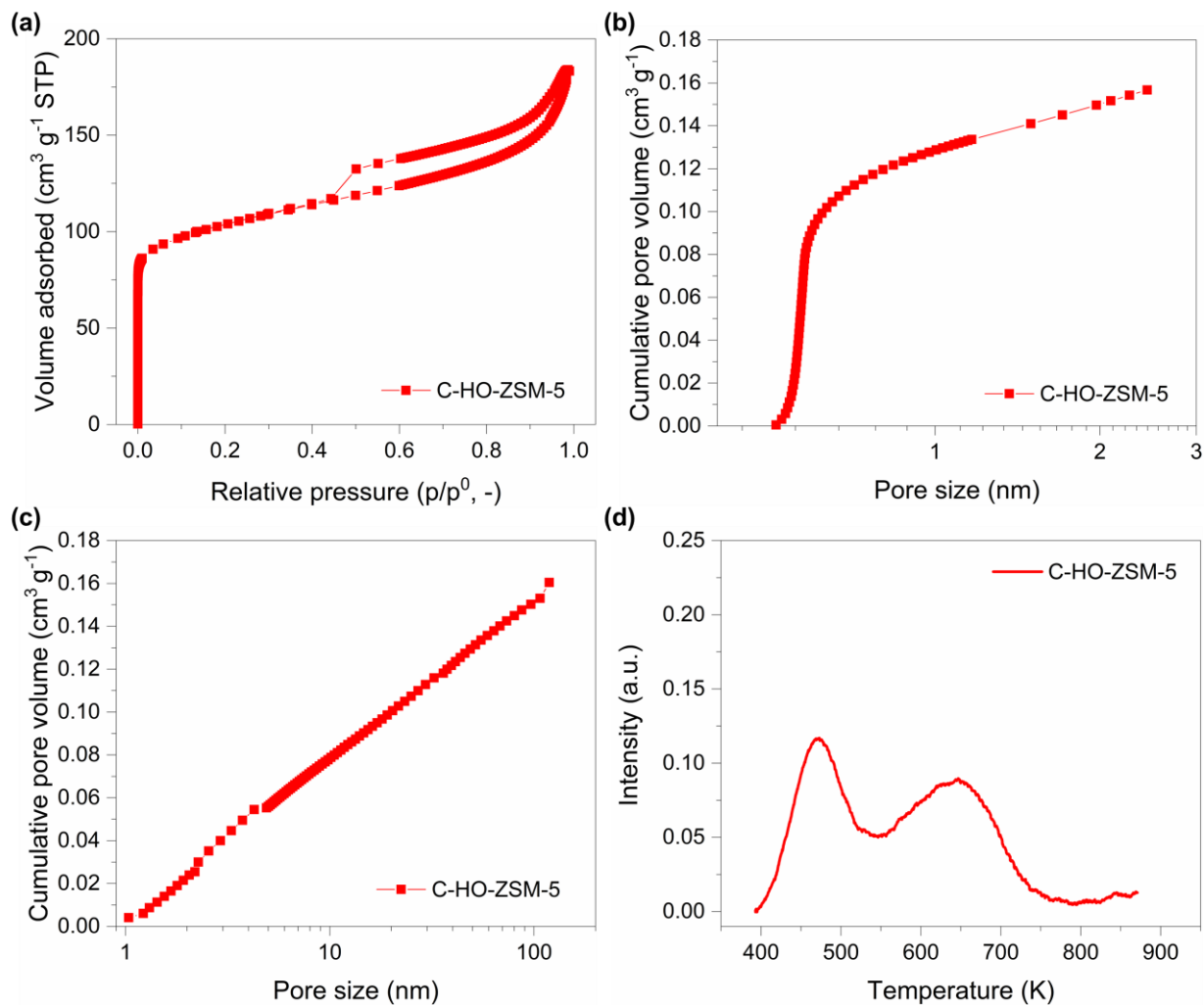
Figure S5.15. (a) N_2 adsorption-desorption (open symbols) isotherms, (b) micropore cumulative pore volume, (c) mesopore cumulative pore volume, and (d) NH_3-TPD curves of C-HO-ZSM-5 (SAR = ~45).
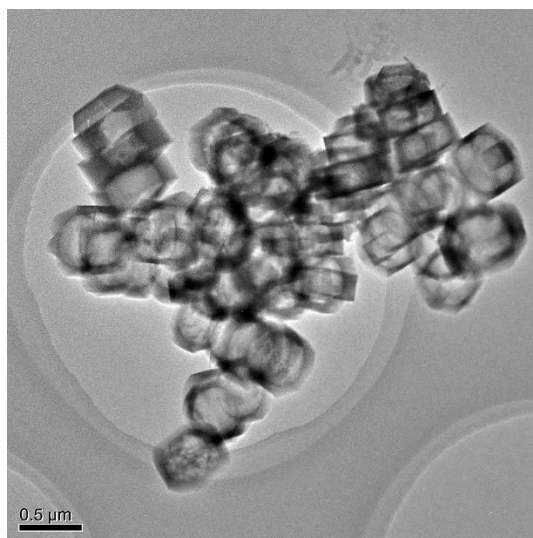
Figure S5.16. TEM micrographs of C-HO-ZSM-5 (SAR = ~45).

Table S5.4. Key Physical and chemical properties of the zeolite catalysts used for cracking reactions.

Catalysts	S_{BET} [m^2 g^{-1}]	S_{micro} [m^2 g^{-1}]	$S_{ext.}$ [m^2 g^{-1}]	V_{micro} [cm^3 g^{-1}]	V_{total} [cm^3 g^{-1}]	SAR[a] [-]	Acidity[b] [μmol g^{-1}]
AS-MFI	375	275	100	0.12	0.22	12.3	24.1
ZSM-5-P-0.1-6	521	372	149	0.15	0.41	15.6	403.1
C-ZSM-5	341	285	56	0.14	0.21	13.4	393.6
C-HO-ZSM-5	379	234	145	0.10	0.28	44.9	214.4

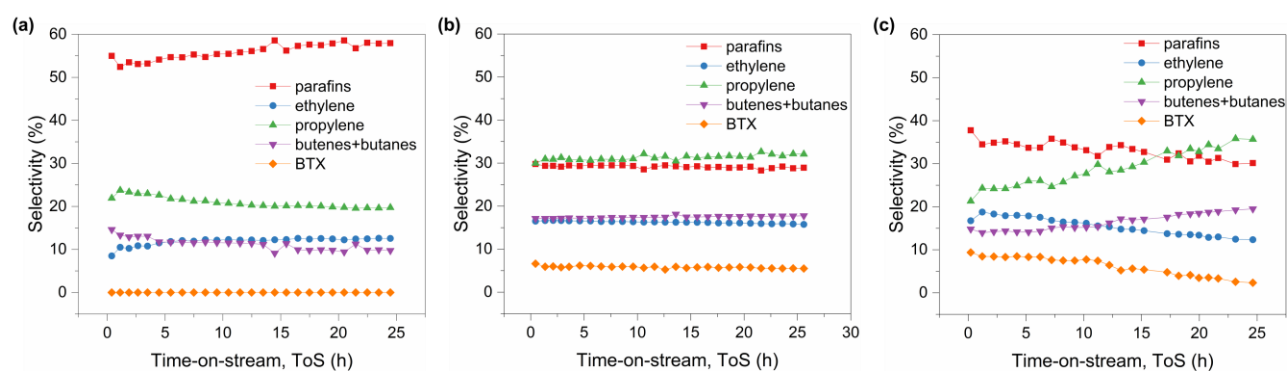[a] Molar SAR values by ICP; [b] Strong acidity by NH$_3$-TPD.

Figure S5.17. Selectivity of *n*-octane cracking as a function of time-on-stream over (a) AS-MFI, (b) ZSM-5-P-0.1-6 and (c) C-ZSM-5 zeolites.

139

Table S5.5. Conversions and selectivity of *n*-octane cracking reactions (at 540 °C) over the zeolite catalysts under study.[a]

Zeolite	Conversion[b] [%]	Selectivity [%]					P/E[c] [-]
		parafins	ethylene	propylene	butenes+butanes	BTX	
AS-MFI	3.2	53.9	10.2	22.7	13.3	0.00	2.2
ZSM-5-P-0.1-6	72.7	29.3	16.6	30.7	17.2	6.2	1.8
ZSM-5-P-0.1-6 (regenerated)	72.8	29.8	16.8	30.0	17.3	6.1	1.8
ZSM-5-P-0.1-24	75.2	30.7	16.9	27.1	16.2	9.0	1.6
ZSM-5-P-0.1-48	82.3	31.8	17.6	25.9	16.2	8.5	1.5
ZSM-5-P-0.1-96	88.5	33.4	17.7	22.3	14.2	12.3	1.3
C-ZSM-5	90.0	35.8	17.9	23.2	14.3	8.8	1.3
C-HO-ZSM-5	31.0	29.3	9.0	38.1	23.5	0.0	4.2

[a] All data are the averaged values of the first three hours on stream with the margin of errors of *ca.* 7% for C-ZSM-5 and <1.5% for the rest; [b] carbon mass balances >95.0%; [c] the propylene/ethylene (P/E) ratio.

Table S5.6. Conversion and selectivity of cumene cracking reactions (at 320 °C) over the zeolite catalysts under study.[a]

Catalyst	Conversion[a] [%]	Selectivity [%]				
		parafins	ethylene	propylene	butenes+butanes	BTX
ZSM-5-P-0.1-6	94.0	7.0	0.7	7.3	11.3	73.8
C-ZSM-5	66.1	6.06	0.7	7.7	10.1	75.3
C-HO-ZSM-5	83.4	5.0	0.4	11.7	11.1	71.8

[a] All data are the averaged values of the first three hours on stream with the margin of errors of *ca.* 21% for C-ZSM-5, *ca.* 5% for C-HO-ZSM-5 and 0.3% for ZSM-5-P-0.1-6; [b] carbon mass balances >95.0%.
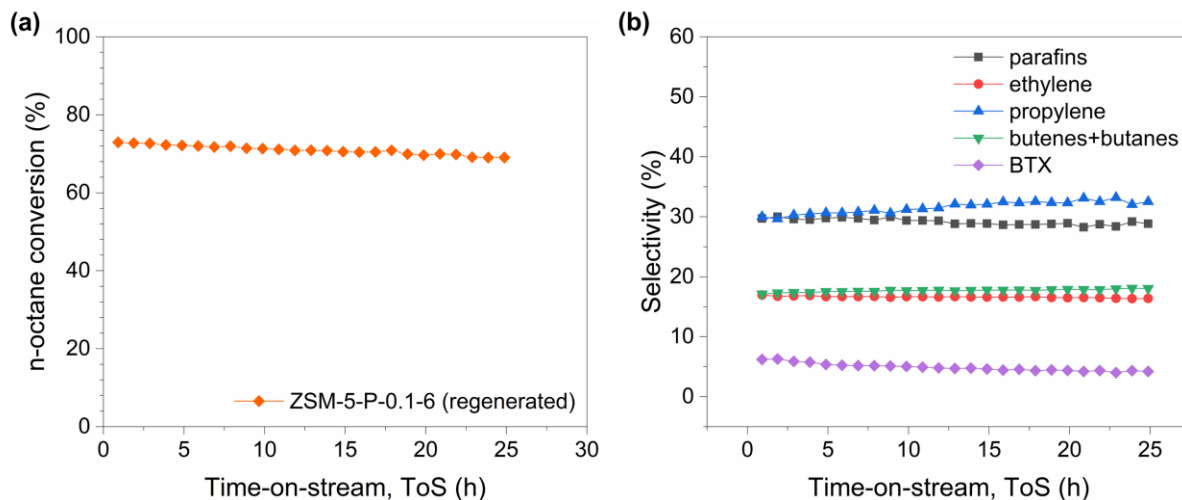
Figure S5.18. (a) conversion and (b) selectivity of *n*-octane cracking over the regenerated ZSM-5-P-0.1-6-U zeolite catalyst.
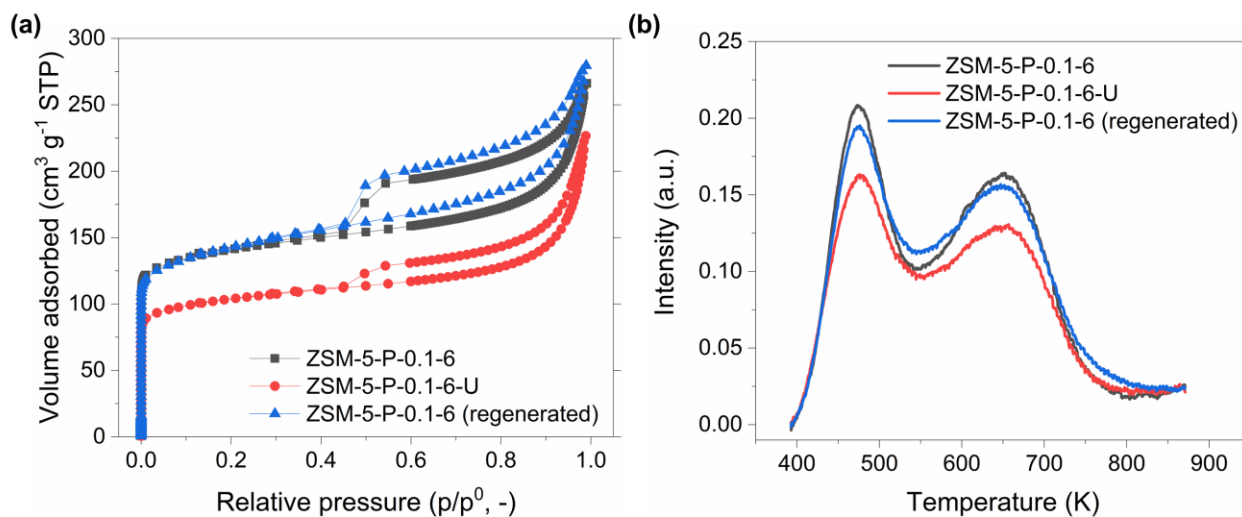

Figure S5.19. (a) N_2 adsorption/desorption isotherms and (b) NH_3-TPD curves of the ZSM-5-P-0.1-6, ZSM-5-P-0.1-6-U and regenerated ZSM-5-P-0.1-6 zeolite catalysts.
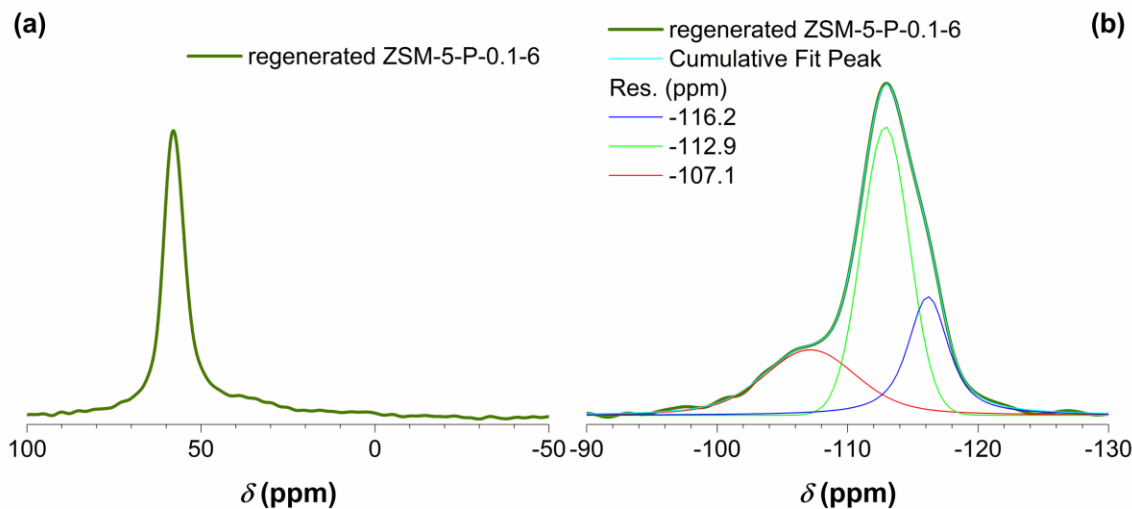
Figure S5.20. (a) ^{27}Al MAS NMR and (b) ^{29}Si MAS NMR spectra of the regenerated ZSM-5-P-0.1-6 zeolite.

Table S5.7. Comparative textural properties of the fresh, used and regenerated ZSM-5-P-0.1-6 zeolite catalyst by N_2 physisorption.

Sample	S_{BET} $[m^2\,g^{-1}]$	S_{micro} $[m^2\,g^{-1}]$	$S_{ext.}$ $[m^2\,g^{-1}]$	V_{micro} $[cm^3\,g^{-1}]$	V_{total} $[cm^3\,g^{-1}]$
ZSM-5-P-0.1-6	521	372	149	0.15	0.41
ZSM-5-P-0.1-6-U	382	265	117	0.11	0.35
Regenerated ZSM-5-P-0.1-6	522	369	153	0.15	0.43

Table S5.8. Comparative acidic properties of the fresh, used and regenerated ZSM-5-P-0.1-6 zeolite catalyst by NH_3-TPD.

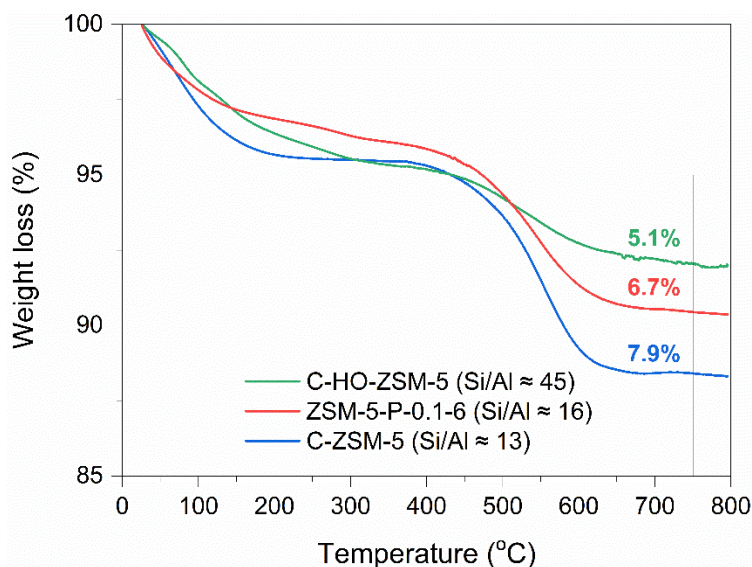| Sample	Temperature at maximum [K]		Weak acidity $[\mu mol\,g^{-1}]$	Strong acidity $[\mu mol\,g^{-1}]$
	First peak	Second peak		
ZSM-5-P-0.1-6	471	645	249.6	403.1
ZSM-5-P-0.1-6-U	471	645	221.7	313.2
Regenerated ZSM-5-P-0.1-6	471	642	250.6	397.1

Figure S5.21. Weight loss of the used zeolite catalysts (by TGA) from the cumene cracking reactions.

Table S5.9. Comparative textural properties of the fresh and used ZSM-5-P-0.1-6 (SAR = ~16), C-HO-ZSM-5 (SAR = ~45) and C-ZSM-5 (SAR = ~13) from the catalytic cracking reactions by N_2 physisorption.

Sample	S_{BET} $[m^2 g^{-1}]$	S_{micro} $[m^2 g^{-1}]$	$S_{ext.}$ $[m^2 g^{-1}]$	V_{micro} $[cm^3 g^{-1}]$	V_{total} $[cm^3 g^{-1}]$
ZSM-5-P-0.1-6	521	372	149	0.15	0.41
ZSM-5-P-0.1-6-U[a]	382	265	117	0.11	0.35
ZSM-5-P-0.1-6-U[b]	249	188	61	0.08	0.31
C-HO-ZSM-5	379	234	145	0.10	0.28
C-HO-ZSM-5-U[a]	304	193	111	0.10	0.20
C-HO-ZSM-5-U[b]	213	178	35	0.08	0.20
C-ZSM-5	341	285	56	0.14	0.21
C-ZSM-5-U[a]	92	75	17	0.03	0.05
C-ZSM-5-U[b]	20	16	4	0.01	0.02

[a] The used zeolite from *n*-octane cracking; [b] the used zeolite from cumene cracking.

Table S5.10. Comparative acidic properties of the fresh and used zeolite catalysts (from cracking reactions) by NH$_3$-TPD.

Sample	Temperature at maximum [K]		Weak acidity[a] [μmol g^{-1}]	Strong acidity[b] [μmol g^{-1}]
	First peak	Second peak		
ZSM-5-P-0.1-6	471	645	249.6	403.1
ZSM-5-P-0.1-6U[a]	471	645	221.7	313.2
ZSM-5-P-0.1-6U[b]	475	640	192.8	228.3
C-HO-ZSM-5	468	640	131.1	214.4
C-HO-ZSM-5-U[a]	478	666	102.9	168.4
C-HO-ZSM-5-U[b]	465	605	74.5	100.6
C-ZSM-5	488	682	321.6	393.6
C-ZSM-5-U[a]	472	637	146.6	172.0
C-ZSM-5-U[b]	480	669	117.6	104.9

[a] The used zeolite from *n*-octane cracking; [b] the used zeolite from cumene cracking.
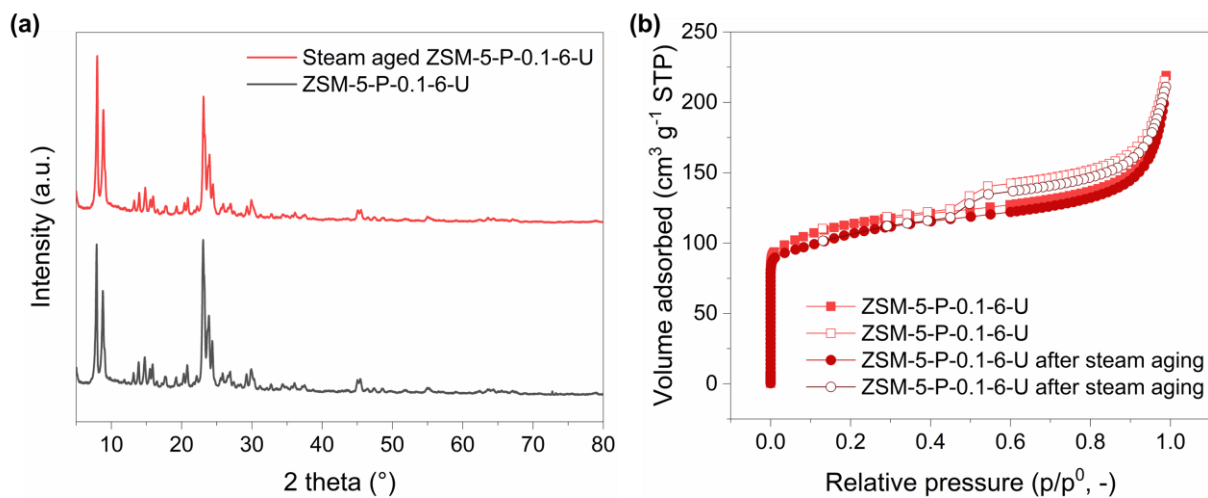

Figure S5.22. (a) XRD patterns and (b) N$_2$ adsorption/desorption isotherms of ZSM-5-P-0.1-6-U before and after the steam aging.

Table S5.11. Textural properties ZSM-5-P-0.1-6-U (from the catalytic *n*-octane cracking) and its counterpart after steam aging treatment.

Sample	S_{BET} [m^2 g^{-1}]	S_{micro} [m^2 g^{-1}]	$S_{ext.}$ [m^2 g^{-1}]	V_{micro} [cm^3 g^{-1}]	V_{total} [cm^3 g^{-1}]
ZSM-5-P-0.1-6-U	415	262	153	0.11	0.34
Steam aged ZSM-5-P-0.1-6-U	391	244	147	0.10	0.33

Table S5.12. Information of the parent MFI zeolites and the resulting zeolites prepared using the conventional post-synthetic alkaline treatment methods.

Parent zeolites			Post-treatment conditions	Resulting mesoporous zeolites		Ref.
zeolite	SAR	Crystal size		Textural property	SAR	
ZSM-5	40	µm aggregates	0.2 M NaOH at 80 °C (5 h)	Mesoporous	n/a	1
ZSM-5	37	n.a.	0.05 M NaOH at 50 or 70 °C (0.5–30 h)	Mesoporous	374–2133	2
ZSM-5	37	µm aggregates	0.2 M NaOH at 65 °C (0.5 h)	Mesoporous	24	3
ZSM-5	37	µm aggregates	0.2 M NaOH at 35–85 °C (15–120 min)	Mesoporous	24–37	4
ZSM-5	17	n.a.	0.2 M NaOH at 65 °C (30 min)	Limited mesoporosity	15	5
	19			Limited mesoporosity	18	
	26			Mesoporous	18	
	37			Mesoporous	24	
	42			Mesoporous	29	
	176			Mesoporous	133	
	1038			Limited mesoporosity	560	
ZSM-5	26	400–700 nm	0.2 M NaOH at 65 °C (15 or 30 min)	Mesoporous and hollow	18–19	6
	41	20–30 µm		Mesoporous and hollow	32	
ZSM-5	72	200–300 nm	0.6 M Na$_2$CO$_3$ at 80°C for 36 h.	Hollow structure	49	7
ZSM-5	50	<100 nm	0.1 M NaOH at 80°C (2–5 min, 1–10 h)	Hollow structure	27–41	8
	14	µm aggregates	0.1 M NaOH at 80°C for one week	Limited mesoporosity	n/a	

Table S5.13. Information of the parent MFI zeolites and the resulting zeolites prepared using the conventional post-synthetic methods using TPAOH solutions.

Parent zeolites			Post-treatment conditions	Resulting mesoporous zeolites		Ref.
zeolite	SAR	Crystal size		Textural property	SAR	
silicalite-1	-	<200 nm	0.56 M TPAOH with additional Al sources (Al(NO$_3$)$_3$) at 170 °C (0.75–24 h)	Hollow structure	50–100	9
silicalite-1	-	0.5–1 μm	0.56 M TPAOH with Al(NO$_3$)$_3$ at 170 °C (24 h)	Heterogeneous mesoporosity	125	
silicalite-1	-	μm		Mesoporous	33–402	10
ZSM-5	100	<300 nm	1 M TPAOH at 170 °C (24 h)	Hollow structure	101–105	11
ZSM-5	40–79	<200 nm	TPAOH (0.05–0.5 M) at 170 °C (72 h)	Hollow structure	47–70	12
ZSM-5	50	300–500 nm	TPAOH (0.15 or 0.3 M) at 170 °C (72 h)	Hollow structure	n/a	13
ZSM-5	37	n.a.	TPAOH (0.3 M) at 170 °C (72 h)	Hollow structure	33	14
silicalite-1	-	200–900 nm	0.3 M TPAOH with NaAlO$_2$ at 170 °C (72 h) with different liquid-to-solid ratios	Hollow structure	41–63	15
silicalite-1	-	<100 nm	TPAOH with NaAlO$_2$ at 170 °C (72 h) with different synthesis times	Hollow structure	31–51	16

References

1.   O. Masaru, S. Shin-ya, T. Junko, N. Yasuto, K. Eiichi, M. Masahiko, *Chem. Lett.* **2000**, *29*, 882–883.

2.   T. Suzuki, T. Okuhara, *Microporous Mesoporous Mater.* **2001**, *43*, 83–89.

3.   J. C. Groen, L. A. A. Peffer, J. A. Moulijn, J. Pérez-Ramírez, *Microporous Mesoporous Mater.* **2004**, *69*, 29–34.

4.   J. C. Groen, L. A. A. Peffer, J. A. Moulijn, J. Pérez-Ramírez, *Colloids Surfaces A* **2004**, *241*, 53–58.

5.   J. C. Groen, J. C. Jansen, J. A. Moulijn, J. Pérez-Ramírez, *J. Phys. Chem. B* **2004**, *108*, 13062–13065.

6.   J. C. Groen, T. Bach, U. Ziese, A. M. Paulaime-van Donk, K. P. de Jong, J. A. Moulijn, J. Pérez-Ramírez, *J. Am. Chem. Soc.* **2005**, *127*, 10792–10793.

7.   C. Mei, Z. Liu, P. Wen, Z. Xie, W. Hua, Z. Gao, *J. Mater. Chem.* **2008**, *18*, 3496–3500.

8.   D. Fodor, F. Krumeich, R. Hauert, J. A. van Bokhoven, *Chem. Eur. J.* **2015**, *21*, 6272–6277.

9.   Y. Wang, A. Tuel, *Microporous Mesoporous Mater.* **2008**, *113*, 286–295.

10.   D. Verboekend, J. Pérez-Ramírez, *Chem. Eur. J.* **2011**, *17*, 1137–1147.

11.   S. Li, A. Tuel, D. Laprune, F. Meunier, D. Farrusseng, *Chem. Mater.* **2015**, *27*, 276–282.

12.   C. Dai, A. Zhang, M. Liu, X. Guo, C. Song, *Adv. Func. Mater.* **2015**, *25*, 7479–7487.

13.   Z. Hong, Z. Wang, D. Chen, Q. Sun, X. Li, *Appl. Surf. Sci.* **2018**, *440*, 1037–1046.

14.   J. Li, M. Liu, X. Guo, S. Zeng, S. Xu, Y. Wei, Z. Liu, C. Song, *Ind. Eng. Chem. Res.* **2018**, *57*, 15375–15384.

15.   Z. Ma, T. Fu, Y. Wang, J. Shao, Q. Ma, C. Zhang, L. Cui, Z. Li, *Ind. Eng. Chem. Res.* **2019**, *58*, 2146–2158.

16.   J. Shao, T. Fu, Z. Ma, C. Zhang, H. Li, L. Cui, Z. Li, *Catal. Sci. Technol.* **2019**, *9*, 6647–6658.

Chapter 6: The design and optimisation of a heterogeneous tin and gallium doped zeolite Y catalytic system for the green isomerisation of hexose sugars using low-field NMR relaxation measurements

The content of this chapter will be published as a full research article. Author contributions are as follows; Luke Forster designed and performed the NMR measurements. Philippa James and Dedi Sutarma prepared the catalysts and carried out the catalytic tests. Luke Forster, Carmine D'Agostino and Marco Conte prepared the manuscript.

Abstract

Novel tin and gallium doped zeolite Y catalysts were prepared via wet impregnation and tested for the catalytic isomerisation of glucose to produce fructose and mannose. When methanol was used as the reaction solvent the pure zeolite Y was found to convert 39 % of glucose to the isomerisation products whilst the tin and gallium doped zeolites converted 55 % and 51 % of glucose respectively. No isomerisation occurred when water was used as the reaction solvent and intermediate conversion were seen in ethanol.

2D NMR relaxation time measurements found that the reaction solvents studied interact with the catalyst surfaces with interaction strengths in the order; water > ethanol > methanol for both the non-doped and metal doped zeolites in agreement with the catalytic data obtained, where the highest activity was in methanol and the lower was in water. NMR relaxation time measurements imply that the reduced catalytic activity in water and ethanol compared to methanol are due to relatively strong adsorption of the reaction solvent to the zeolite surfaces thereby blocking reactants from the catalytically active sites situated on the zeolite surface hence suppressing the isomerisation reaction.

2D NMR displacement experiments showed that water readily displaces both methanol and ethanol from the zeolite pores. Methanol is displaced at a faster rate than ethanol due to its' weaker interaction with the zeolite surface. The displacement of the alcohols from the zeolite pores by water was found to occur at the same rate regardless of whether the zeolite was doped or not. This was explained by considering the ratio of the water adsorption strength to that of the alcohols which demonstrated that impregnation using tin or gallium metal does not significantly influence the relative strengths of adsorption of the water and alcohols thereby the displacement rate is unaffected by the presence of metal centres.

6.1. Introduction

In recent times, the development of chemical systems with minimal environmental impact has become of paramount importance to academic and industrial researchers alike. This is due to rapidly increasing levels of pollution and the subsequent environmental concerns that arise. [1] As such, green and sustainable chemistry has become one of the most important concepts to combat climate change; thereby reducing environmental damage. Green chemistry is a broad and far reaching concept defined by twelve key principles; one of which is catalysis. [2]

The role of catalysis in green chemistry lies in its' ability to increase the efficiency of chemical manufacturing systems by reducing the production of waste products [3-5] or potentially allowing new, sustainable feedstocks or fuels to be used in chemical processes that were previously not viable. [6-8]

As crude oil stocks are rapidly depleting, it is vital that new sustainable alternatives are discovered. One promising alternative route to renewable biofuels is through the valorisation of biomass. [9, 10] Biomass is generally comprised of carbohydrates, proteins, lipids and fatty acids and it is through the breakdown of these molecules, generally carbohydrates, that high value platform chemicals can be produced to be used as versatile building blocks to form useful products, such as fuels and chemical monomers. [11-14] 5-hydroxymethlfurfural (HMF) is one such industrially desirable platform chemical that can be derived from carbohydrates and used for the production of a wide range of important building block chemicals such as 2,5-furandicarboxylic acid [15-17] and 2,5-dimethylfuran [18-20] or even levulinic acid, which has been previously recognised as one the top twelve building blocks that can be derived from biomass feedstock. [21]

The usefulness of biomass as a feedstock to produce platform chemicals is critically dependent on the efficient conversion of cellulosic matter. Pentose (C5) sugars, such as xylose, have been suggested as appropriate molecules for this process due to a high atom efficiency when converting to levulinic acid [22, 23] but the formation of insoluble, undesired side products such as humins can lead to catalyst poisoning [24, 25] thereby decreasing the viability of the overall process. The hexose (C6) sugar, glucose, has also been considered as it is efficiently produced by the hydrolysis of cellulose [26, 27] and is therefore cheap and highly abundant. However, glucose is a relatively inert molecule due to its stable 6 membered ring structure, and the subsequent dehydration of glucose to HMF is a relatively inefficient process. [28] As such, fructose has been suggested as an alternative

as its 5-membered ring structure is more reactive and more prone efficient dehydration step via enolization of the open chain saccharide. [29, 30] Fructose is, however, much less abundant than its isomer glucose and finds much use in the food and drink industry as a sweetener [31, 32] resulting in a higher relative cost. Therefore, it is vital to find efficient processes for the conversion of glucose to fructose.

Currently, the most promising catalyst reported for the glucose to fructose isomerisation reaction is a Sn doped beta zeolite converting 50 wt% of glucose with a selectivity of 84 wt% to fructose and 16 % to mannose within the temperature range of 343 to 413 K. [33] The Sn beta zeolite possesses two separate types of active sites; the "closed" form and "open" form corresponding to non-hydrolysed, fully coordinate Sn sites and partially hydrolysed Sn sites respectively [34] with the open site being the most catalytically active. [35] However, the reaction is shown to occur more readily in methanol than in water as the Sn beta possess hydrophobic micropores thereby allowing a greater uptake of methanol solvent as opposed to water [36, 37] giving rise to a partial solvation of the sugar-catalyst complex during reaction thereby increasing activity. [28]

Such solvent effects are widespread in the field of heterogeneous catalysis, but relatively little work has been carried out so far to characterise such catalysts and reaction mixtures/reactive species as well as to quantify and rationalise the impact of such effects upon catalytic activity. NMR relaxation measurements represent a valuable tool to provide vital information on such phenomena. Indeed, it has been shown that NMR relaxation time measurements can be used to characterise the adsorption strengths of reactants with the catalyst surface. [38] By comparison of these adsorption strengths for both the reactant and solvents, the solvent effects seen in the liquid phase oxidations of both 1,4-butanediol [39, 40] and various 1,3-propanediols [41] have been explained using NMR relaxation measurements and therefore the optimal solvent in which to carry out these reactions can be identified. Recently, NMR relaxation measurements have also shown that oxygenated heterocyclic compounds form Lewis acid-base pairs with sites on the surface of TiO_2 and therefore inhibit catalyst activity [42] showing that non oxygenated solvents such as cyclohexane are preferable for reactions using this support.

In this work, novel tin and gallium doped zeolite Y catalysts are synthesised and shown to effectively isomerise glucose to produce relatively high yields of fructose and mannose. The effect of the reaction solvent upon the overall catalytic activity of the system is evaluated using NMR relaxation measurements to aid optimisation of the catalytic system.

6.2. Experimental

6.2.1. Materials

Materials were used as delivered, without any additional purification, unless otherwise specified: Gallium (III) nitrate hydrate (Ga(NO$_3$)$_3$·H$_2$O, Acros, 99.9998%), Tin (IV) chloride pentahydrate (SnCl$_4$·5H$_2$O, Fisher, Pure), Zeolite Y (Zeolyst), Glucose (D-(+)-Glucose, Alfa Aesar, anhydrous, 99%), Fructose (Fisher, >99%), Mannose (D-(+)-Mannose, Alfa Aesar, 99%), Methanol (Fisher, HPLC Grade, >99.9%), Ethanol (Sigma, Anhydrous, ≤0.005% water). Deionised water was obtained from a laboratory water purification system.

6.2.2. Catalyst preparation

The desired amount of metal precursor (Ga(NO$_3$)$_3$·H$_2$O, 78.5 mg; or SnCl$_4$·5H$_2$O, 59.1 mg) to produce a 1 wt. % gallium or tin catalyst was dissolved in deionised water (25 mL) and the support (zeolite Y, 1.98 g) was added under vigorous stirring. The resultant slurry was heated to 80 °C under stirring and the solvent evaporated to dryness. The slurry was then dried at 120 °C overnight for 16 h in a fan-assisted oven and calcined at 550 °C for an additional 4 h in a static-air muffle furnace (temperature ramp 20 °C min^{-1}).

6.2.3. Catalytic testing

Glucose (125 mg), catalyst (Table 6.1) and water (4 mL) or methanol (4 mL) were added to an ACE pressure vessel equipped with a magnetic stirrer bar. The tube was then immersed into a preheated aluminium block and heated at 120 °C for 2 h. On completion, the reaction mixture was quenched in an ice bath, centrifuged to remove the catalyst and refrigerated until analysed.

Table 6.1. The mass of catalyst used for testing the isomerisation of glucose reaction. The mass of catalyst was adjusted in such a way to preserve a constant molar metal to substrate (M:S) ratio between the active metal and the substrate.

Catalyst	Mass used for testing (mg)
Ga/Y	48.4
Sn/Y	82.4
Zeolite Y only	75.0

6.2.4. Analysis of reaction mixtures

Reaction mixtures were analysed using high-performance liquid chromatography (HPLC) using a Shimadzu UPLC XR equipped with an Evaporative Light Scattering Detector- Low Temperature (ELSD-LT). The method development was completed by adapting a current method previously established within the research group, which used a Phenomenex Rezex ROA- Organic Acid H$^+$ (8%), 250 by 4.6 mm column and was known to separate glucose and fructose.

Glucose, fructose and mannose were dissolved in water at various concentrations between 150 and 2000 mg/L, and eluted over 25 minutes and injection volume of 10 µL.

The obtained chromatograms were then analysed to calculate the conversion and selectivity as defined in (1) and (2):

$$Conversion\ (\%) = \frac{\sum(Product\ Peak\ Areas)}{\sum(Product\ and\ Reagent\ Peak\ Areas)} \tag{6.1}$$

$$Selectivity\ to\ Product\ X\ (\%) = \frac{\sum(Peak\ Area\ of\ X)}{\sum(Product\ Peak\ Areas)} \tag{6.2}$$

6.2.5. NMR relaxation 2D T_1-T_2 correlation analysis

Large grains of non-doped and Ga or Sn doped zeolite Y were soaked in *n*-octane, deionised water, methanol or ethanol (~2 mL) for 2 days prior to analysis. The zeolites were removed from the

respective liquids and gently dried on a pre-soaked filter paper to remove excess liquid from the outer surface whilst avoiding removal of liquid from the internal pore structure.

Following drying, the zeolites were transferred to 5 mm NMR tubes and tested using a T_1-T_2 NMR pulse sequence (Figure 6.1) to determine spin-lattice and spin-spin relaxation times. The typical error for all T_1-T_2 measurements was approximately 3 %.
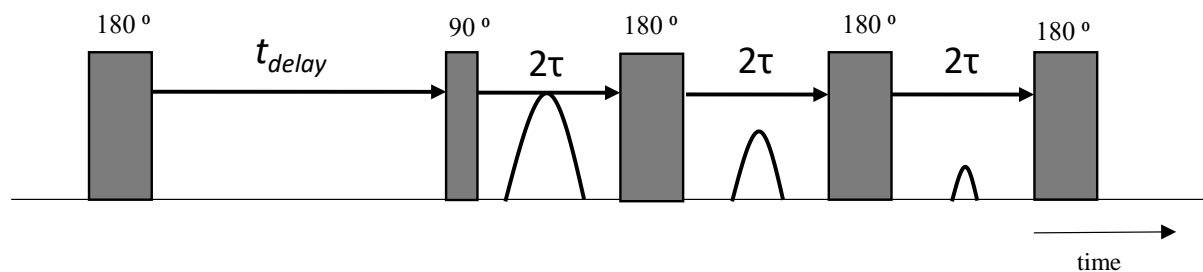

Figure 6.1. T_1-T_2 NMR pulse sequence. The thin and thick vertical bars represent 90° and 180° radiofrequency (RF) pulses, respectively. T_1 relaxation is encoded in the variable time t_{delay}. T_2 relaxation is encoded in the train of n 180 ° pulses. A single data point is acquired at the centre of each echo time, τ.

Sixteen recovery delays were used, from 1 ms to 500 ms. The echo train of the CPMG sequence was composed of 1200 or 1600 echoes dependent upon the sample acquired in a single shot with an echo spacing of $2\tau = 1$ ms. Each data set was acquired with 4 scans in approximately 2 min.

The 2D data was processed using an algorithm kindly provided by Prof. Michael Johns of the University of Western Australia, Perth based on the presented by Venkataramanan et al. [43]

6.2.6. NMR relaxation 2D T_1-T_2 correlation displacement experiments

Relatively large grains (approximately 125 mm^3 in volume) of non-doped and Ga or Sn doped zeolite Y were soaked in methanol or ethanol (~ 2 mL) for 2 days prior to analysis. The large grains were removed from the liquid before being dried, prepared and analysis using the same process detailed previously.

The large zeolite grains were then removed from the NMR tube and left in an excess of the displacing liquid, water (~ 2 mL), for the amount of time specified, hereon referred to as the displacement time. The excess liquid was again removed prior to acqusition of the NMR data using the process detailed previously to obtain a 2D T_1-T_2 correlation plot for varying values of the displacement time.

6.3. Results and discussion

6.3.1. Catalytic testing

Both the metal doped and non-doped zeolites were tested for the conversion of glucose to its' isomerisation products, glucose and mannose. As the reaction solvent has been shown to play a significant role in heterogeneous catalytic reactions previously; by influencing factors such as the adsorption of reactive species, [40-42] the solubility of reagents [44] and directly influencing the catalytic cycle through interactions with species involved in the catalytic cycle. [45] To investigate potential solvent effects the reactions using each catalyst were carried out using water, methanol or ethanol as reaction solvent. For the reactions using water as the reaction solvent, 0% conversion of glucose was observed. Previous work has demonstrated that the use of water with zeolites possessing hydrophilic pores and high Lewis acidity can result in a significant decrease in catalytic activity; [30] due to the coordination of water to Lewis acidic sites via electron-rich oxygen atoms thereby hindering coordination of reactive species hence suppressing catalytic activity. [29]

The use of alcohol solvents, namely, methanol and ethanol resulted in conversion of glucose to its isomerisation products and the results of these tests are shown in Table 6.2 and represented graphically in Figure 6.2.

Table 6.2. Conversion and selectivity to fructose and mannose values for the catalysed glucose isomerisation reaction using zeolite Y only, Ga/Y or Sn/Y as catalyst and methanol or ethanol as the reaction solvent.

Catalyst		Solvent	
		MeOH	EtOH
Zeolite Y only	Conversion (%)	39 ± 2	12 ± 2
	Fructose Selectivity (%)	31 ± 2	30 ± 2
	Mannose Selectivity (%)	69 ± 2	70 ± 2
Ga/Y	Conversion (%)	51 ± 2	12 ± 2
	Fructose Selectivity (%)	37 ± 2	35 ± 2
	Mannose Selectivity (%)	63 ± 2	65 ± 2
Sn/Y	Conversion (%)	55 ± 2	11 ± 2
	Fructose Selectivity (%)	31 ± 2	32 ± 2
	Mannose Selectivity (%)	69 ± 2	68 ± 2
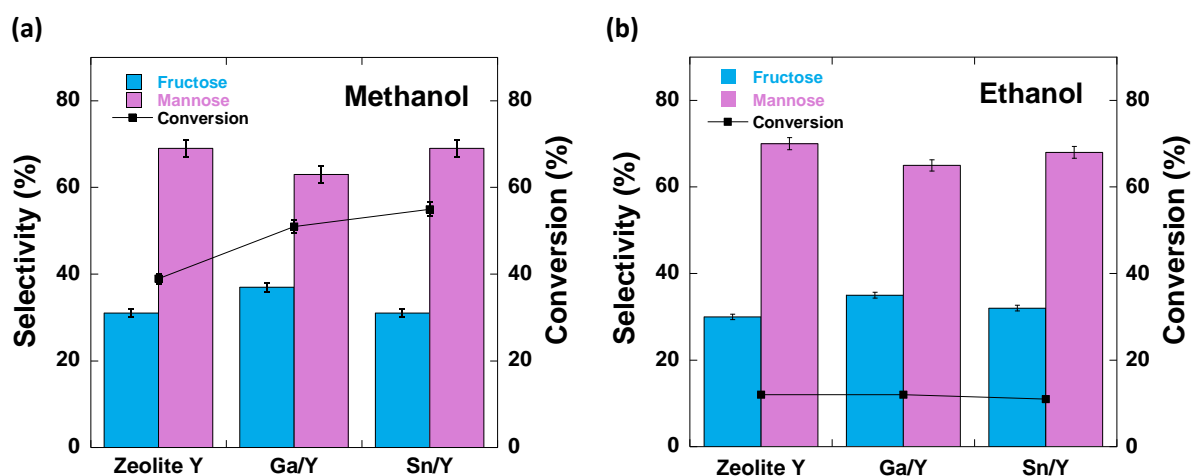
Figure 6.2. Product selectivity and overall conversion values of the glucose isomerisation reaction using the catalysts zeolite Y, Ga/Y and Sn/Y in (a) methanol and (b) ethanol solvent. The blue and pink columns represent the fructose and mannose selectivities respectively and the black line indicates the conversion values.

Using non-doped zeolite Y as catalyst for this reaction showed glucose conversions of approximately 39 % to the isomerisation products, matching the current optimal conversion of 40 % reported in the literature for the same reaction using zeolite Y as catalyst [46] indicating that appropriate reaction conditions were used in this study. Impregnation of zeolite Y with tin and gallium metals showed a marked improvement in the conversion values to 55 % and 51 % respectively. This increase in conversion indicates both that zeolite Y can facilitate the isomerisation and epimerisation of the sugars within its pore structure and that tin and gallium are active catalytic species for this reaction. As discussed previously, when the Sn/zeolite beta catalyst was used, a similar solvent effect was also seen for the glucose isomerisation in that the catalytic activity is enhanced when methanol solvent is used as opposed to water. [36, 37] This occurs due to an increased uptake of methanol into the relatively hydrophobic zeolite pores (or alternatively less hydrophilic than the external surface of the zeolite crystals) when compared to that of water leading to an increased solvation and therefore stabilisation of the sugar-catalyst complex intermediate. [28]

In ethanol, the conversion although higher than in water, was significantly lower than in methanol (ca 10-12%) although this did not lead to a substantial difference in selectivity between mannose and fructose.

6.3.2. 2D T_1-T_2 NMR relaxation

To investigate the solvent effect occurring in the catalytic isomerisation of glucose, T_1-T_2 measurements were performed to assess the relative adsorption strengths of the reaction solvents used; water, methanol and ethanol, with the surface of the various catalysts.

In brief, if a fluid is confined in a porous medium, the measured relaxation times (T_1, T_2) are given by: [47, 48]

$$\frac{1}{T_{1,\text{pore}}} = \frac{1}{T_{1,\text{bulk}}} + \rho_1 \frac{S}{V} \tag{6.3}$$

$$\frac{1}{T_{2,\text{pore}}} = \frac{1}{T_{2,\text{bulk}}} + \rho_2 \frac{S}{V} + D \tag{6.4}$$

The first terms of these equations represent the relaxation time, T_x, of the bulk solvent; in the second term, attributed to water close to or in contact with the surface, ρ_x is the surface relaxivity,

which depends on the intrinsic surface chemistry of the material and is effectively a measure of how strongly the guest molecule interacts with the surface. D represents an additional term dependent upon the diffusivity of the molecule under study and $\frac{S}{V}$ is the surface-to-volume ratio.

Generally, for high $\frac{S}{V}$ materials, the bulk liquid term is negligible as the T_x of a bulk liquid is usually much greater than that of the same liquid confined inside pore structure (for example, for bulk liquid water $T_1 \approx 2.9$ s), hence one can write: [49]

$$\frac{1}{T_{x,\text{pore}}} \approx \rho_x \frac{S}{V} \tag{6.5}$$

A change of T_x in pores relative to bulk can therefore be due to either a variation of adsorbate/adsorbent surface interaction, reflected in ρ_x, or in a change in internal surface area and pore dimension, reflected in $\frac{S}{V}$.

It follows that when T_1 and T_2 are determined for the same guest molecule within the same porous media, then the surface-area-to-volume ratio term is constant and the dependence of the relaxation times upon the pore structures can be removed by taking the ratio T_1/T_2. This ratio is therefore a measurement of only the surface interactions occurring between the guest molecule and the pore walls/surface and is defined as:

$$\frac{T_1}{T_2} \approx \frac{\rho_2}{\rho_1} \tag{6.6}$$

Indeed, it has been shown that this ratio is related to the molecular mobility (tumbling) of molecules. BPP theory of relaxation, [50] states that the correlation time, τ_c, the average time taken for a molecule to rotate 1 radian from its original starting position, is dependent upon the T_1 and T_2 values as shown in Figure 2.8.

This can be interpreted as molecules that interact more strongly with the surface of a porous medium will be more restricted in their motion and therefore T_1 will be much larger than T_2. That is, the T_1/T_2 ratio will be large whereas in bulk liquids which have unrestricted movement the ratio will be approximately equal to 1. Previous work has shown that this ratio is related to surface adsorption and can be directly correlated to adsorption energies determined using temperature programmed desorption (TPD). [3] As such, the T_1/T_2 ratio can find great use in the field of catalysis

and surface science to quantify the strength of surface interactions taking place and explain phenomena such as solvent effects. [39-41]

The 2D T_1-T_2 correlation maps obtained can be seen in Figure 6.4 and T_1/T_2 values were determined from the peak maximum for all plots.
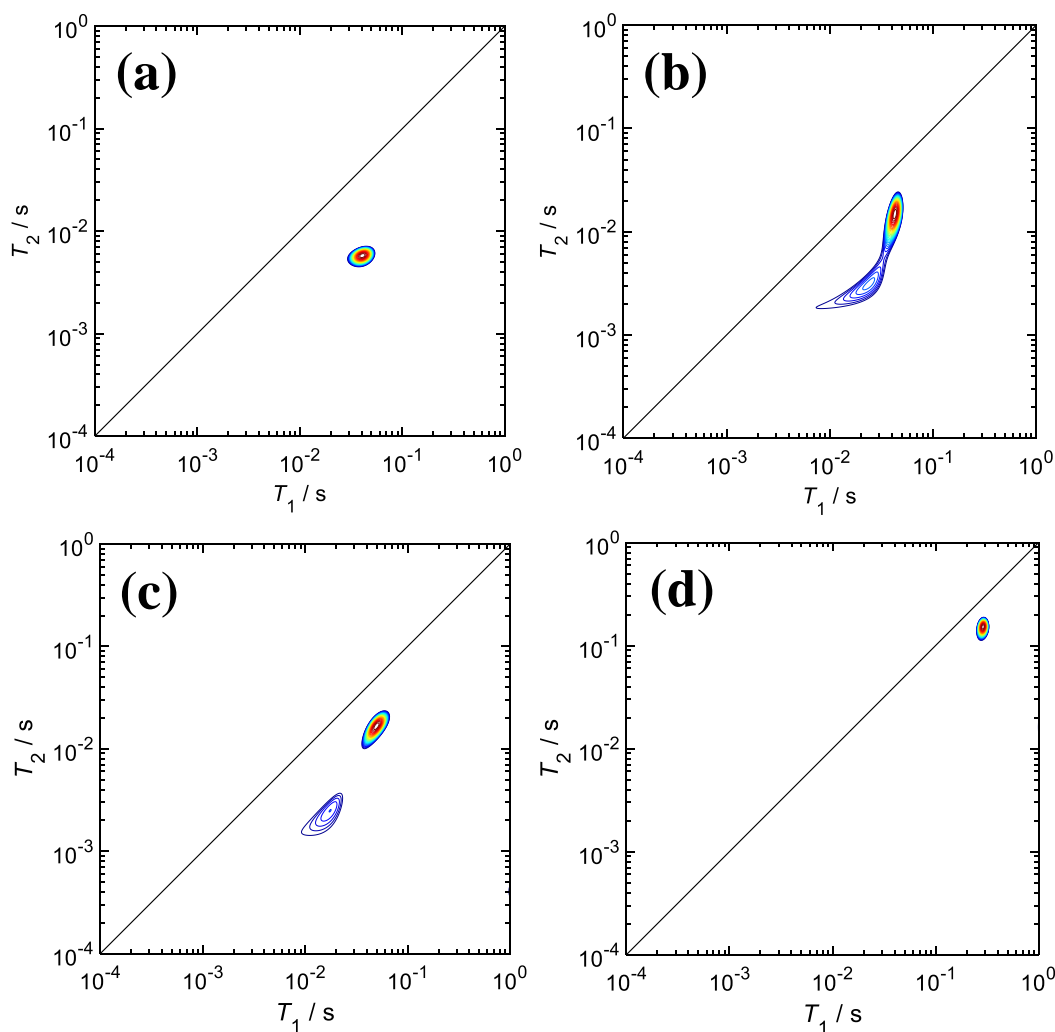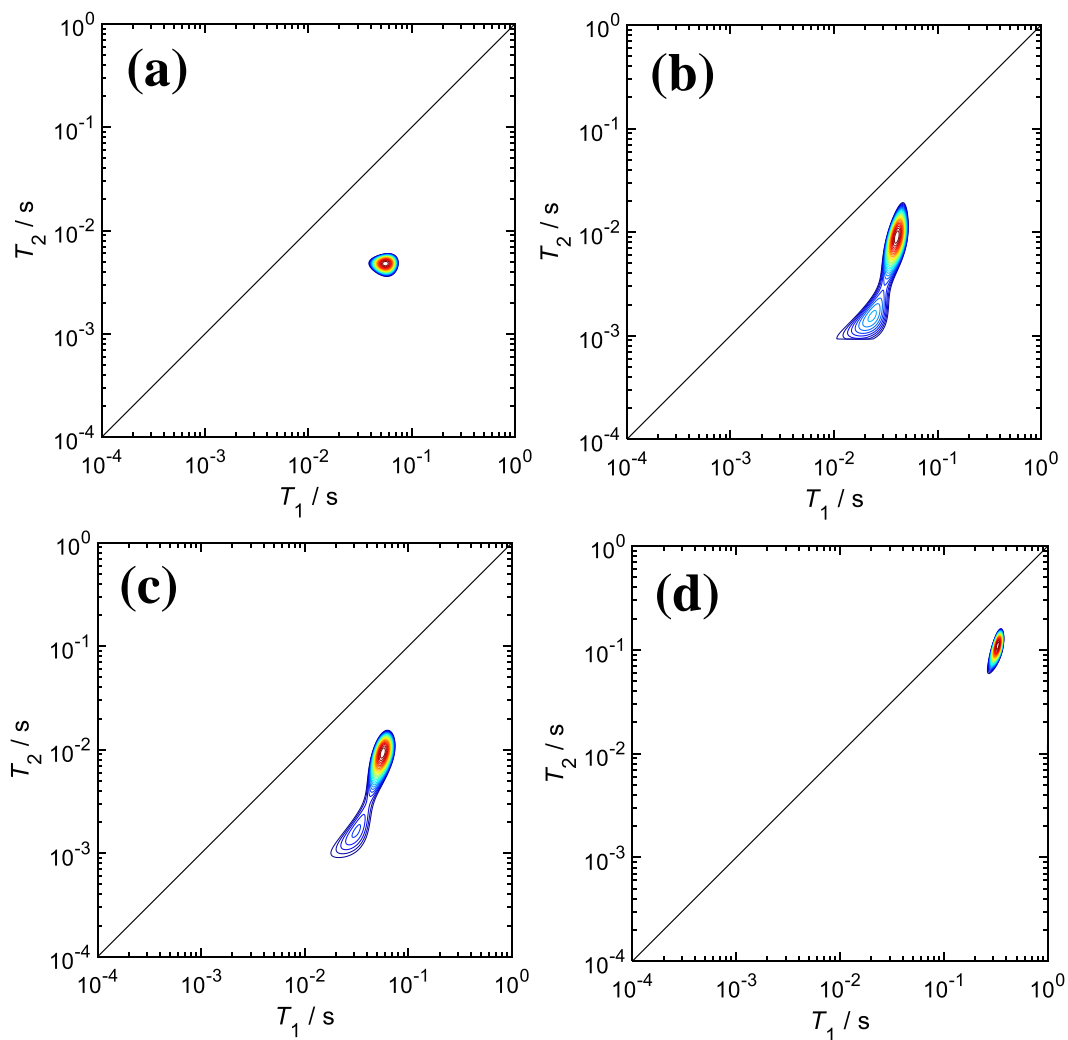

Figure 6.4. T_1-T_2 relaxation correlation plots for (a) water, (b) methanol, (c) ethanol and (d) octane imbibed within the pores of zeolite Y. The solid black line indicates $T_1 = T_2$.

From the T_1/T_2 ratios, as previously discussed, it is possible to determine the relative strengths of surface interactions for the solvent imbibed within zeolite Y. Water has $T_1/T_2 \approx 7.1$ indicating that this is the most strongly adsorbed of the solvents tested and this relatively strong adsorption could be responsible for the solvent effect observed in the isomerisation of glucose. This can be expected, as water molecules can strongly interact with any OH groups present on the zeolite surface. The

zeolite surface shows a slight preference for ethanol as opposed to methanol as seen by the respective T_1/T_2 values of 3.1 and 2.8. This implies that the zeolite surface adsorbs ethanol more strongly than methanol and further supports the catalytic data which shows the catalyst is active in methanol but not ethanol. n-octane was used as a reference probe molecule. Due to its lack of chemical functionality, surface interactions with the zeolite will be limited and thereby the motion of the molecule will be relatively fast when compared to the reaction solvents. This is confirmed as n-octane shows the lowest T_1/T_2 of 1.9. It should be noted that the correlation plots obtained using methanol and ethanol show a second, less intense peak at approximately $T_1/T_2 \approx 7.1$, of a similar value to that of the peak obtained in the water plot. Anhydrous alcohol solvents were used to obtain these plots therefore this peak is attributed to the presence of strongly adsorbed water already present on the zeolite surface prior to the analysis.

The experiments conducted for the solvents imbibed within the parent zeolite were repeated for the Ga and Sn doped zeolites and the resultant plots can be seen in Figures 6.5 and 6.6.

Figure 6.5. T_1-T_2 relaxation correlation plots for (a) water, (b) methanol, (c) ethanol and (d) octane imbibed within the pores of zeolite Ga/Y. The solid black line indicates $T_1 = T_2$.
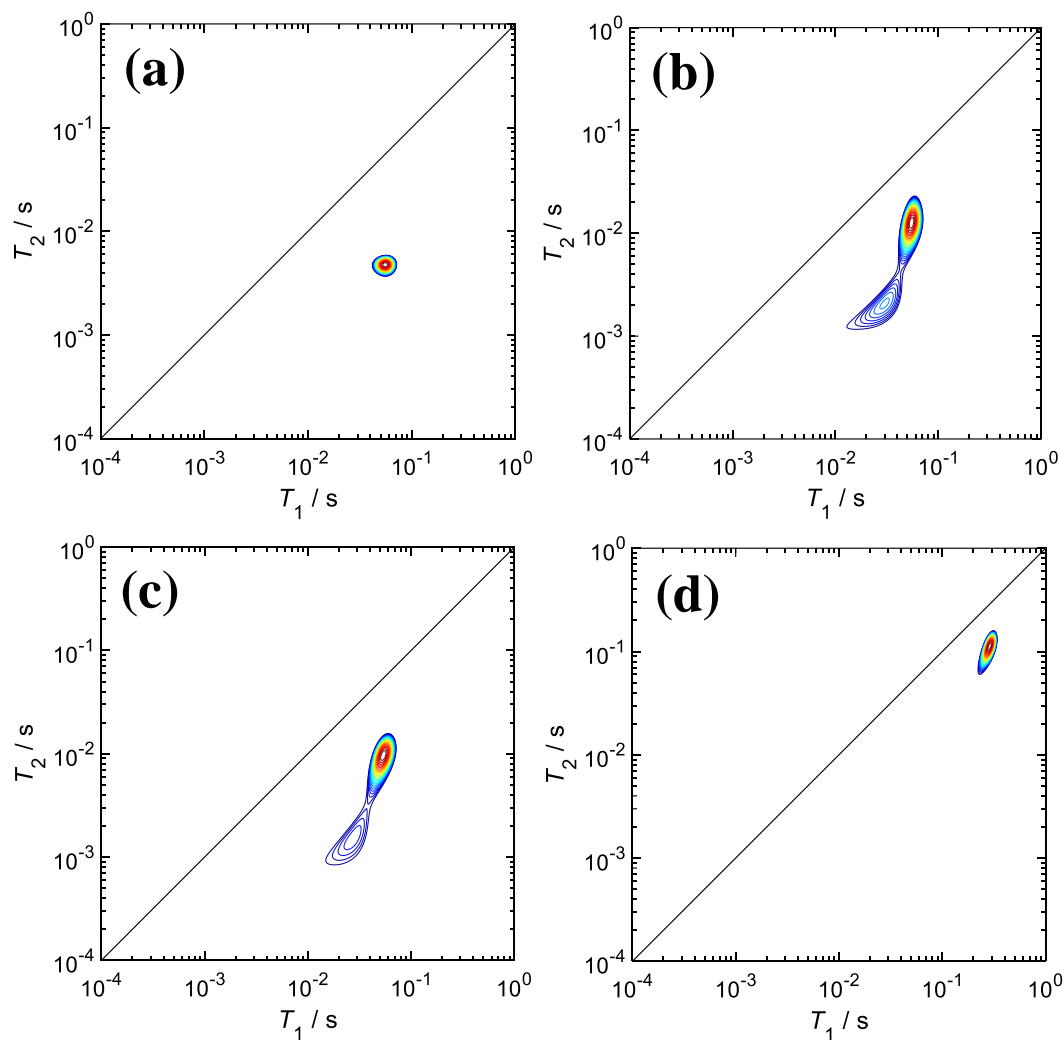
Figure 6.6. T_1-T_2 relaxation correlation plots for (a) water, (b) methanol, (c) ethanol and (d) octane imbibed within the pores of zeolite Sn/Y. The solid black line indicates $T_1 = T_2$.

The trend in relative adsorption strengths can be seen to be the same for both the metal doped zeolites and the parent zeolite. The results of all tests are summarised in Table 6.3 and a clearer, graphical representation can be seen in Figure 6.7.

Table 6.3. The T_1/T_2 ratios determined for the reaction solvents water, methanol and ethanol imbibed within zeolite Y and doped zeolites Ga/Y and Sn/Y. The error on all measurements is 3 %. The peak error arises from the inherent error in the width of the peak in each respective direction.

Sample	$(T_1/T_2)_{H2O}$	$(T_1/T_2)_{MeOH}$	$(T_1/T_2)_{EtOH}$	$(T_1/T_2)_{Oct}$
Zeolite Y	7.1 ± 0.2	2.7 ± 0.1	3.1 ± 0.1	1.9 ± 0.1
Ga/Y	11.2 ± 0.3	4.4 ± 0.1	5.9 ± 0.2	3.1 ± 0.1
Sn/Y	11.2 ± 0.3	4.4 ± 0.1	5.9 ± 0.2	2.5 ± 0.1
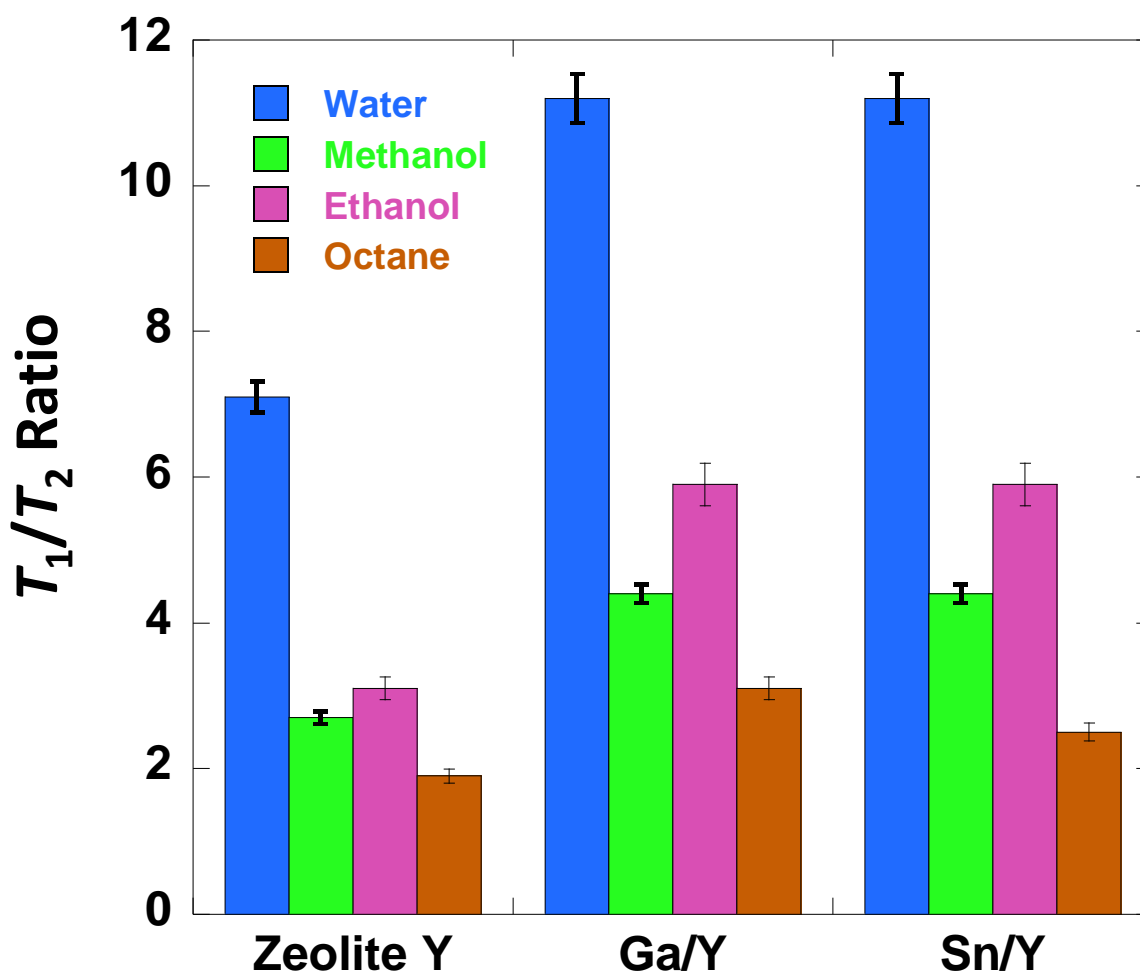
Figure 6.7. T_1-T_2 ratios of water, methanol, ethanol and *n*-octane imbibed within the pores of the parent zeolite Y and metal doped derivatives Ga/Y and Sn/Y.

The T_1/T_2 ratio of water is shown to be the greatest across all samples indicating that, when imbibed within the pores of the zeolites, water exhibits the most reduced mobility, hence highest surface affinity. This can be attributed to the interaction of water with the zeolite surfaces (for example,

through hydrogen bonding with surface hydroxyl groups). The relatively strong interaction of water with the catalyst surface will limit the accessibility of any reactants (in this case glucose) to active sites located on the catalyst surface thereby resulting in a decreased catalytic activity. Whilst the metal doped zeolites show higher T_1/T_2 ratios when compared to that of the parent zeolite, it should be noted that the T_1/T_2 ratio can be affected by many other factors such as the presence of internal magnetic field gradients. Indeed, it has even been shown that T_2 values can differ significantly even for the same adsorbate in similar porous materials, [51] therefore this must be considered when comparing values across the different zeolite samples.

It is also important to note the effect of the different solvents upon the stabilisation of the ring-opened species when converting from glucose to fructose. In actuality, the sugars may exist in many different conformations in solution each with their own varying stabilities and reactivities. The stability of the ring opened sugar conformations and any related reaction intermediates and transition states will also have a significant impact on the conversion and selectivity. [52,] Study of this effect is beyond the scope of this work but it is important to consider that this effect will influence the results obtained.

In the doped zeolites, Ga/Y and Sn/Y, ethanol shows a higher T_1/T_2 ratio when compared to that of methanol indicating that ethanol has a stronger interaction with the zeolite surface as opposed to methanol, and the reactivity by using this solvent is intermediate in between methanol and water. Clearly, the reaction using methanol shows the highest catalytic activity as it interacts relatively weakly with the zeolite surface and therefore allows reactants to access catalytically active sites on the zeolite surface resulting in an increased activity. This effect is not seen in the non-metal doped parent zeolite Y as ethanol and methanol show effectively the same T_1/T_2 within this zeolite (Figure 6.7) indicating that they interact with the surface equally, so the introduction of the metal appears to affect the adsorption of the solvents significantly.

T_1/T_2 ratios obtained using n-octane confirm that the difference in T_1/T_2 ratios are due to differences in the surface interactions taking place between the reaction solvents and catalyst surfaces. Alkanes contain no functional groups and as such will have little or no interaction with the catalyst surface and this is confirmed as for all the zeolite samples, n-octane shows the lowest value of T_1/T_2. As n-octane will not interact with the surface of the catalyst its mobility will be affected only by the structure and size of the catalyst pores. If no or weak interactions were taking place between the

other solvents and the zeolite surfaces, all T_1/T_2 values obtained would be equivalent to that of n-octane. As this is clearly not the case, it can be concluded that the trend in T_1/T_2 seen is due to adsorption of the solvent molecules to the zeolite surface.

6.3.3. 2D T_1-T_2 NMR solvent displacement

The results of the solvent displacement experiments can be seen below. Figure 6.8a-6.8c shows the displacement of methanol by water and Figure 6.9a-6.9c shows the displacement of ethanol by water. There is a visible peak at $T_1/T_2 = 7.05$ for zeolite Y (Figures 6.8a and 6.9a) and at $T_1/T_2 = 11.23$ for the doped zeolites Ga/Y and Sn/Y (Figures 6.8b, 6.8c, 6.9b and 6.9c respectively) attributed to strongly adsorbed water present on the zeolite surfaces.

At 0 s, methanol/ethanol is present within the pores of the zeolite and the respective peaks can be clearly seen on the spectra. With increasing displacement time, the alcohol peaks decrease in intensity and the water peak increases in intensity as water displaces the alcohol from the pores. After 600 s, methanol is completely displaced from the pores of the zeolites studied (Figures 6.8a–6.8c) whereas a weak ethanol peak can still be seen (Figures 6.9a–6.9c). This supports the previous NMR relaxation studies as ethanol was determined to adsorb more strongly to the zeolite surface than methanol (evidenced by the respective T_1/T_2 ratio values) which, in turn, supports the catalytic data as the glucose isomerisation reaction occurs readily in methanol and with low conversion in ethanol or water.
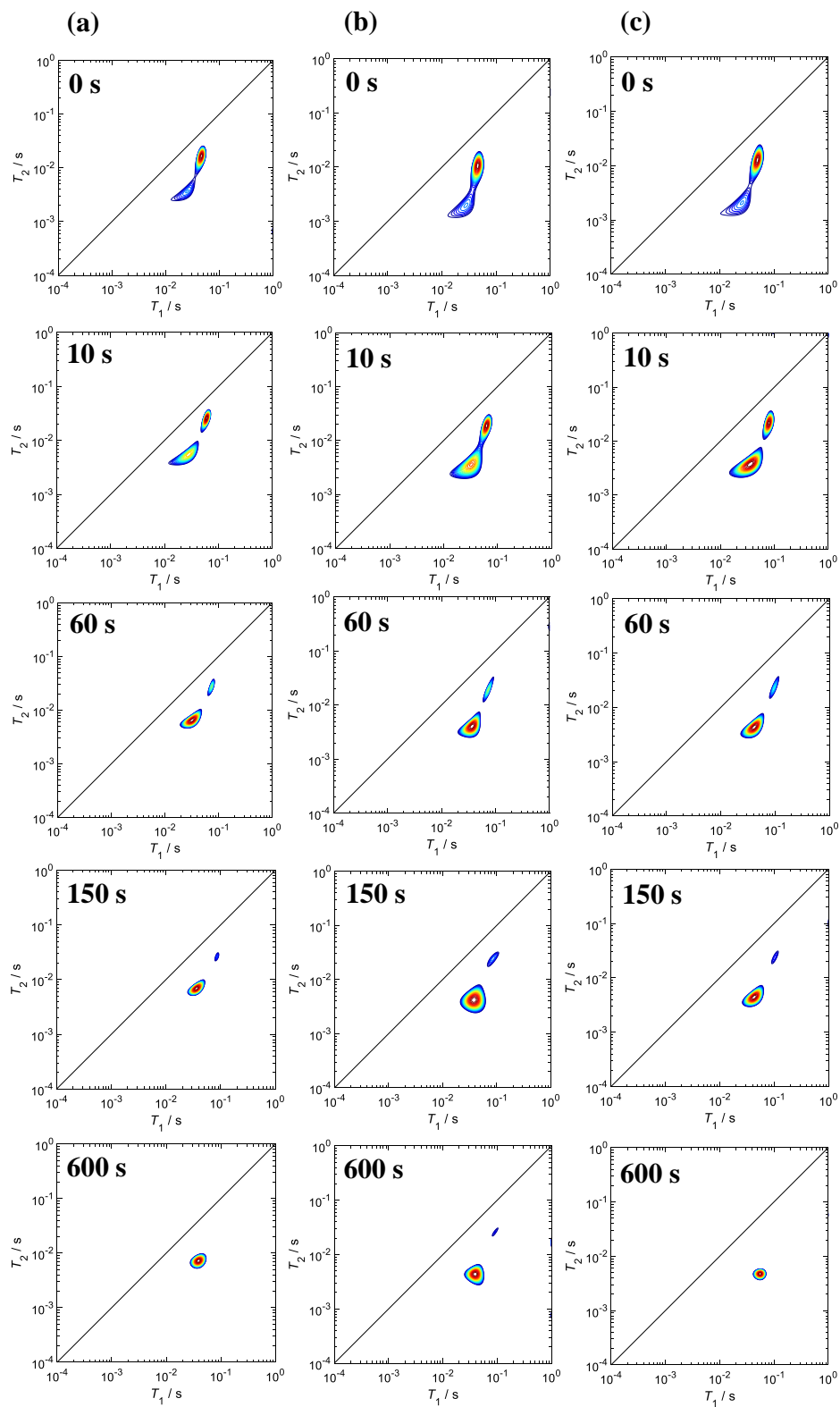
Figure 6.8. T_1-T_2 relaxation correlation plots for methanol being displaced by water within the pores of (a) zeolite Y, (b) Ga/Y and (c) Sn/Y at the displacement time intervals of 0 s, 10 s, 60 s, 150 s and 600 s.
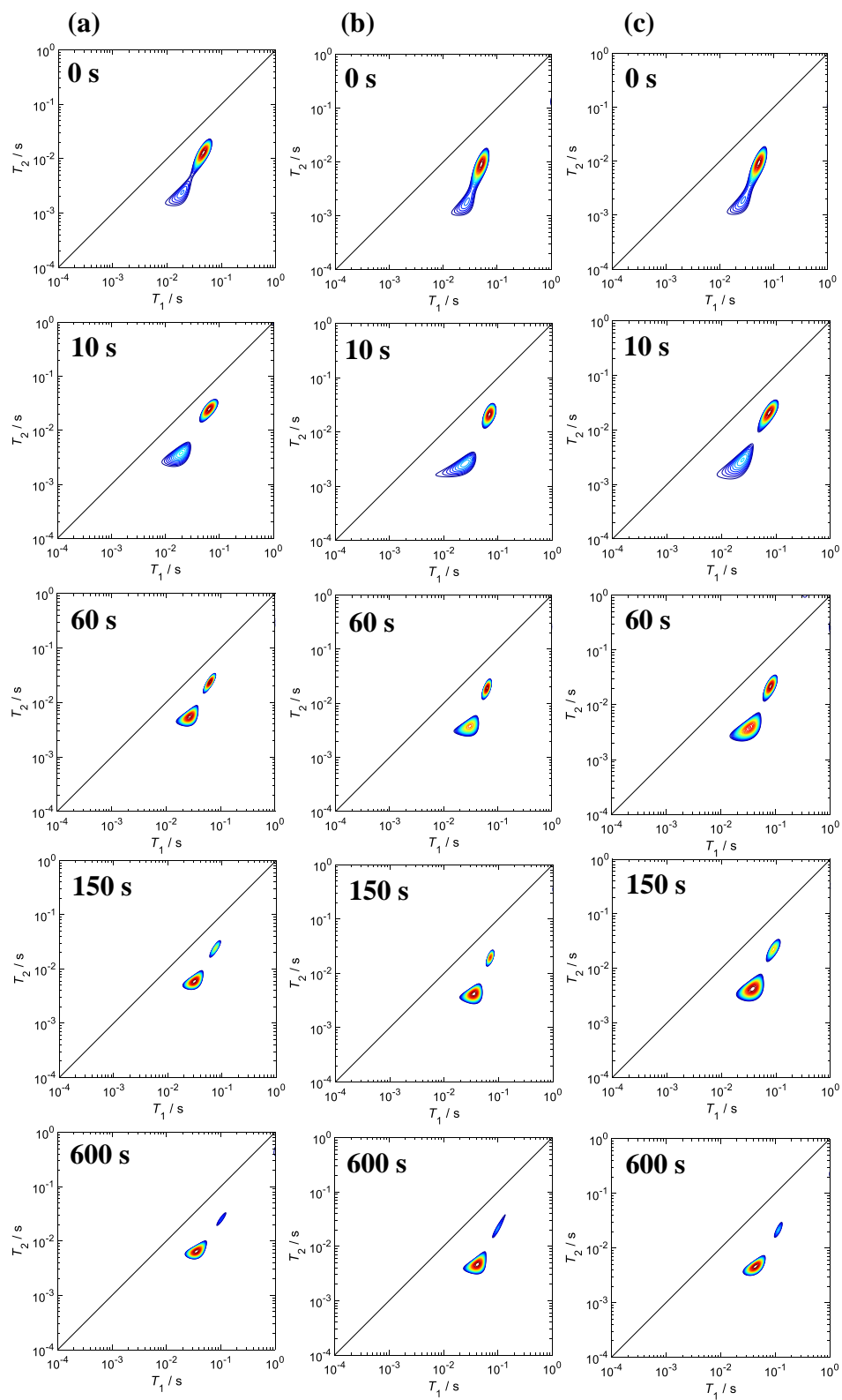
Figure 6.9. T_1-T_2 relaxation correlation plots for ethanol being displaced by water within the pores of (a) zeolite Y, (b) Ga/Y and (c) Sn/Y at the displacement time intervals of 0 s, 10 s, 60 s, 150 s and 600 s.

To allow quantification of the solvent displacement experiments, the volume fractions of both water and the respective alcohol at each displacement time were determined. This analysis was performed by integration of both solvent peaks at each point and the volume fraction of each alcohol was determined by the following equation:

$$V_{Alc} = \frac{I_{Alc}}{I_{tot}} = \frac{I_{Alc}}{I_{Alc} + I_W} \tag{6.7}$$

Where I_{Alc} is the integral of the alcohol peak and I_W is the integral of the water peak. To account for the water already strongly adsorbed to the zeolite surface (found to account for approximately 30% of the total integral), (7) must be altered as follows:

$$V_{Alc} = \frac{I_{Alc}}{I_{Alc} + I_W - I_{W,0}} \tag{6.8}$$

Where $I_{w,0}$ is the integral of the water peak at 0 s. The variation in volume fraction of the alcohols imbibed within the pore of the zeolite samples with displacement time can be seen in Figure 10.
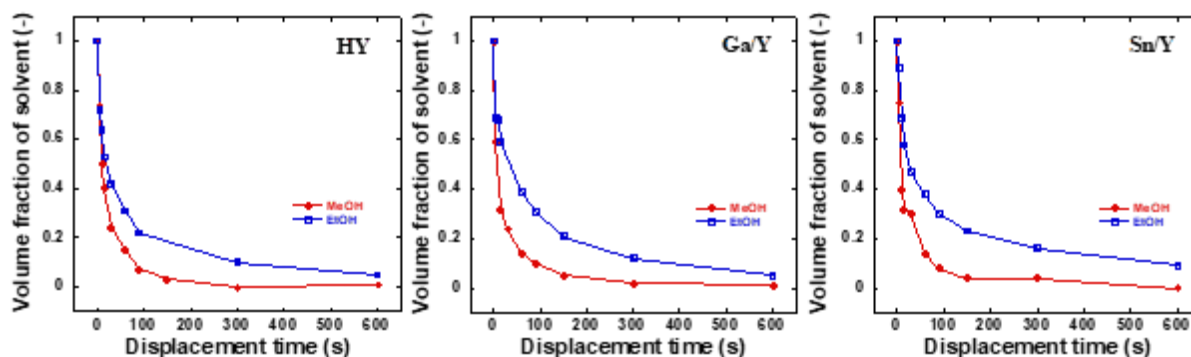
Figure 6.10. The volume fraction of methanol/ethanol remaining within the pores of the zeolite Y, Ga/Y and Sn/Y during the displacement by water as a function of displacement time. The connecting lines are a guide to the eye.

With increasing displacement time both alcohols are displaced from the zeolite pores by water as is expected, however, methanol is clearly displaced much more rapidly than ethanol for the zeolites. Indeed, methanol is fully displaced from all the zeolites by water after only 300 s, whereas ethanol remains in the pores (between 4 – 7 % of the total volume) after 600 s. This can again be attributed to ethanol's increased affinity for the zeolite surface as previously determined from the T_1/T_2 ratio values making the displacement of ethanol molecules from the zeolite surface a slower process.

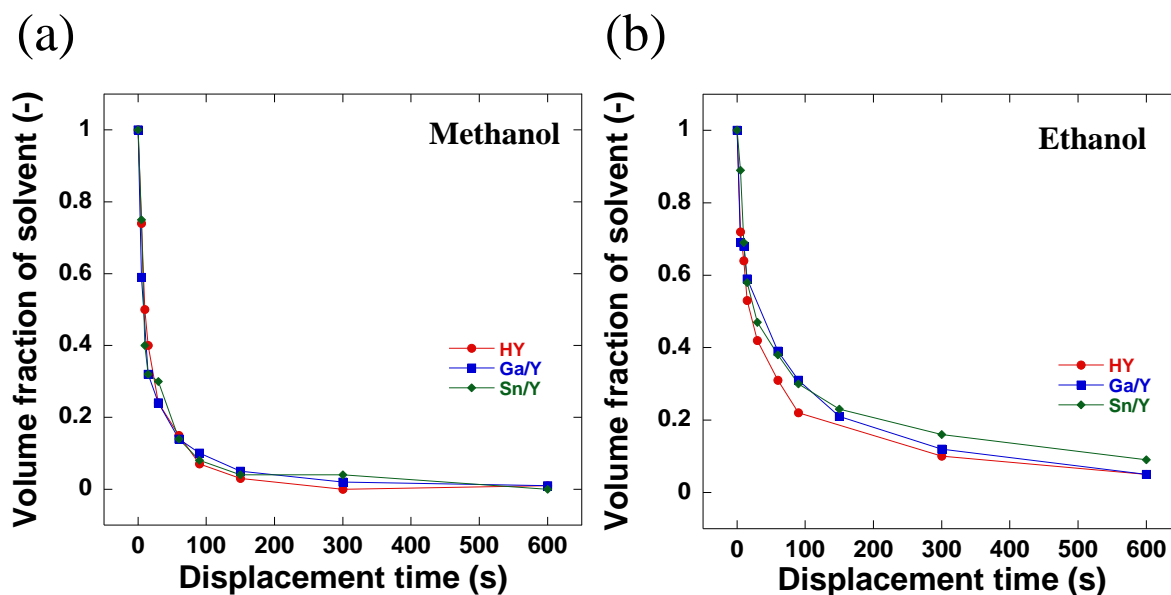The effect of impregnating the zeolite Y with Ga and Sn can be seen in Figure 6.11.

Figure 6.11. The volume fraction of (a) methanol and (b) ethanol remaining within the pores of the zeolite Y, Ga/Y and Sn/Y during the displacement by water as a function of displacement time. The connecting lines are a guide to the eye.

Despite the differences in T_1/T_2 ratio values (Table 6.3) previously seen when the zeolite was doped with the metals, the displacement process is seen to be unaffected by the presence of the metal centres. This can be explained by considering the following ratio:

$$\alpha_x = \frac{\left(\frac{T_1}{T_2}\right)_{H2O}}{\left(\frac{T_1}{T_2}\right)_X} \tag{6.9}$$

Calculated α_{MeOH} and α_{EtOH} values can be found in Table 6.4. Values of α_{MeOH} and α_{EtOH} are statistically the same regardless of whether the metal is present or not. This indicates that regardless of the presence of metal, the relative interaction strengths of water and alcohol is the same which causes the displacement of alcohol by water to proceed at the same rate regardless of the metal centre.

Table 6.4. The T_1/T_2 ratios determined for the reaction solvents water, methanol and ethanol imbibed within the parent zeolite sample Y and doped zeolites Ga/Y and Sn/Y. The error on all measurements is 3 – 5 %.

Sample	$(T_1/T_2)_{H2O}$	$(T_1/T_2)_{MeOH}$	$(T_1/T_2)_{EtOH}$	α_{MeOH}	α_{EtOH}
Zeolite Y	7.1 ± 0.2	2.7 ± 0.1	3.1 ± 0.1	2.62 ± 0.2	2.3 ± 0.1
Ga/Y	11.2 ± 0.3	4.4 ± 0.1	5.9 ± 0.2	2.54 ± 0.3	1.9 ± 0.4
Sn/Y	11.2 ± 0.3	4.4 ± 0.1	5.9 ± 0.2	2.54 ± 0.3	1.9 ± 0.4

6.4. Conclusions

In this paper, zeolite Y both non-doped and doped with gallium and tin metal were tested as catalysts for the isomerisation of glucose to fructose and mannose using 3 different solvents: water, methanol and ethanol. For each catalyst, catalytic activity was found to be highest in methanol but inactive in water. Intermediate activity was seen when ethanol was used as the reaction solvent. Zeolite Y was shown to be catalytically active for this reaction under the reaction conditions used achieving conversions comparable to similar systems used in the literature for the same reaction. Catalytic activity increased significantly upon impregnation of zeolite Y with tin and gallium species.

To investigate the solvent effect seen in this reaction, 2D NMR relaxation correlation measurements were performed. T_1/T_2 ratio values obtained from the resultant correlation plots confirmed that methanol adsorbs the weakest to the zeolite surfaces and water adsorbs the strongest. This supported the catalytic data suggesting that the solvent effect is due to a blockage of active sites on the zeolite surface by the strong adsorption of water molecules. *n*-octane correlation plots confirmed that the difference in T_1/T_2 ratios is due to differences in the strength of interactions between the solvent molecules and the catalyst surfaces evidenced by the low T_1/T_2 obtained, which is to be expected for an alkane due to their distinct lack of chemical functionality with which they can interact with the catalyst surface.

2D NMR displacement studies support the relaxation data as methanol is displaced from the zeolite pores by water more readily than ethanol. This is due to the stronger interactions between ethanol and the zeolite surface making ethanol more difficult to displace from the zeolite pores than methanol which interacts with the zeolite surface more weakly. The displacement of the alcohols from the zeolite pores by water was found to occur at the same rate regardless of whether the metal

was doped or not. This was explained by considering the value α_x, which is the ratio of the water T_1/T_2 value and the respective alcohol T_1/T_2 value. When these values were calculated it was found that α_{MeOH} and α_{EtOH} were the same across all of the zeolite samples studied showing that impregnation using tin or gallium metal does not significantly influence the relative strengths of adsorption of the water and alcohols thereby the displacement rate is unaffected by the presence of metal centres.

To summarise, the study reported here highlight the development and optimisation of a moderately active, novel catalytic system to produce industrially valuable sugar compounds. The influence of the reaction solvent upon the overall catalytic activity was investigated using a low-field, benchtop NMR instrument, which is currently finding increasing use in the academic and industrial sectors as a relatively cheap and easy way of performing studies such as the work described in this paper. Therefore, it is apparent that this work is of value not only to those working in the area of catalytic sugar isomerisation but also to those investigating solvent effects in heterogeneous catalytic reactions and designing and optimising heterogeneous catalytic processes.

References

1.   P. T. Anastas and J. C. Warner, *Green Chemistry: Theory and Practice*, Oxford University Press, Oxford, 1998.

2.   P. T. Anastas, M. M. Kirchhoff and T. C. Williamson, *Appl. Catal. A Gen.*, 2001, **221**, 3-13.

3.   R. A. Sheldon, I. Arends and U. Hanefeld, *Green Chemistry and Catalysis*, Wiley-VCH, Weinheim, 2007.

4.   R. A. Sheldon, *ChemComm*, 2008, 3352-3365.

5.   P. T. Anastas, L. B. Bartlett, M. M. Kirchhoff and T. C. Williamson, *Catal. Today*, 2000, **55(1-2)**, 11-22.

6.   D. M. Alonso, J. Q. Bond and J. A. Dumesic, *Green Chem.*, 2010, **12**, 1493-1513.

7.   G. Baskar and R. Aiswarya, *Renew. Sustain. Energy Rev.,* 2016, **57**, 496-504.

8.   B. H. Shanks, *Ind. Eng. Chem. Res.,* 2010, **49**, 10212-10217.

9.   H. Li, Z. Fang, R. L. Smith Jr and S. Yang, *Prog. Energy Combust. Sci.*, 2016, **55**, 98-194.

10.   R. A. Sheldon, *J. Mol. Catal. A Chem.*, 2016, **422**, 3-12.

11.   C. M. Liu and S. Y. Wu, *Renew. Energy*, 2016, **96**, 1056-1062.

12.   L. E. Manzer, *Appl Catal A Gen*, 2004, **272(1-2)**, 249-256.

13.   W. Won and C. T. Maravelias, *Renew. Energy*, 2017, **114**, 357-366.

14.   H. C. Ong, W. H. Chen, A. Farooq, Y. Y. Gan, K. T. Lee and V. Ashokkumar, *Renew. Sustain. Energy Rev*, 2019, **113**, 109266.

15.   M. Sajid, X. Zhao and D. Liu, *Green Chem.*, 2018, **20**, 5427-5453.

16.   G. Yi, S. P. Teong and Y. Zhang, *Green Chem.*, 2016, **18**, 979-983.

17.   X. Han, C. Li, X. Liu, Q. Xia and Y. Wang, *Green Chem.*, 2017, **19**, 996-1004.

18.   J. Shi, Y. Wang, X. Yu, W. Du and Z. Hou, *Fuel*, 2016, **163,** 74-79.

19.   Y. Zu, P. Yang, J. Wang, X. Liu, J. Ren, G. Lu and Y. Wang, *Appl Cat B Env*, 2014, **146,** 244-248.

20.   P. Yang, Q. Xia, X. Liu and Y. Wang, *Fuel*, 2017, **187**, 159-166.

21.   S. Chen, T. Maneerung, D. C. W. Tang, Y. S. Ok and C. H. Wang, *Chem. Eng. J.*, 2017, **328**, 246-273.

22.   B. Chamnankid, C. Ratanatawanate and K. Faungnawakij, *Chem. Eng. J.*, 2014, **258**, 341-347.

23. Y. Shao, K. Sun, L. Zhang, Q. Xu, Z. Zhang, Q. Li, S. Zhang, Y. Wang, Q. Liu and X. Hu, *Green Chem.*, 2019, **21**, 6634-6645.

24. X. Hu, C. Lievens, C. A. Larcher and C. Z. Li, *Bioresource Technol.*, 2011, **102(21)**, 10104-10113.

25. M. A. Mellmer, J. M. R Gallo, D. M. Alonso and J. A. Dumesic, *ACS Catal.*, 2015, **5**, 3354-3359.

26. A. Onda, T. Ochi and K. Yanagisawa, *Green Chem.*, 2008, **10**, 1033-1037.

27. S.G. Aspromonte, A. Romero, A. V. Boix and E. Alonso, *Cellulose*, 2019, **26**, 2471-2485.

28. J. R. Christianson, S. Caratzoulas and D. G. Vlachos, *ACS Catal.*, 2015, **5**, 5256-5263.

29. T. Ennaert, J. Van Aelst, J. Dijkmans, R. De Clercq, W. Schutyser, M. Dusselier, D. Verboekend and B. F. Sels*, Chem. Soc. Rev.*, 2016, **45**, 584-611.

30. J. Faria, M. P. Ruiz and D. E. Resasco, *ACS Catal.*, 2015, **5**, 4761-4771.

31. Y. P. Li, M. Head-Gordon and A. T. Bell, *ACS Catal.*, 2014, **4**, 1537-1545.

32. Q. Yang, M. Sherbahn and T. Runge, *ACS Sustain. Chem. Eng..*, 2016, **4**, 3526- 3534.

33. M. Moliner, Y. Román-Leshkov and M. E. Davis, *Proc. Natl. Acad. Sci. USA*, 2010, **107**, 6164.

34. A. Corma, *Chem. Rev.*, 1995, **95(3)**, 559-614.

35. R. Bermejo-Deval, M. Orazov, R. Gounder, S. J. Hwang, and M. E. Davis, *ACS Catal.*, 2014, **4(7)**, 2288-2297.

36. R. Gounder and M. E. Davis, *J. Catal.*, 2013, **308**, 176−188.

37. R. Gounder and M. E. Davis, *AIChE J.*, 2013, **59(9)**, 3349-3358.

38. C. D'Agostino, J. Mitchell, M. D. Mantle and L. F. Gladden, *Chem. Eur. J.*, 2014, **20(40)**, 13009-13015.

39. C. D'Agostino, G. L. Brett, P. J. Miedziak, D. W. Knight, G. J. Hutchings, L. F. Gladden and M. D. Mantle, *Chem. Eur. J.*, 2012, **18(45)**, 14426-14433.

40. C. D'Agostino, M. R. Feaviour, G. L. Brett, J. Mitchell, A. P. E. York, G. J. Hutchings, M. D. Mantle and L. F. Gladden, *Catal. Sci. Technol.*, 2016, **6**, 7896-7901.

41. C. D'Agostino, T. Kotionova, J. Mitchell, P. J. Miedziak, D. W. Knight, S. H. Taylor, G. J. Hutchings, L. F. Gladden and M. D. Mantle, *Chem. Eur. J.*, 2013, **19(35)**, 11725-11732.

42. C. D'Agostino, M. D. Mantle and L. F. Gladden, *Microporous Mesoporous Mater.*, 2018, **269**, 88-92.

43. Y. Q. Song, L. Venkataramanan, M. D. Hürlimann, M. Flaum, P. Frulla and C. Straley, *J. Magn. Reson.*, 2002, **154**, 261–268.

44. G. Bellussi, A. Carati and R. Millini, in *Zeolites and Catalysis: Synthesis, Reactions and Applications*, ed. J. Čejka, A. Corma and S. Zones, Wiley-VCH Verlag GmbH, Weinheim, 2010, ch. 16, pp. 449-485.

45. M. G. Clerici, *Top. Catal.*, 2001, **15(2-4)**, 257-263.

46. V. Sebastián, C. Casado and J. Coronas, in *Zeolites and Catalysis: Synthesis, Reactions and Applications*, ed. J. Čejka, A. Corma and S. Zones, Wiley-VCH Verlag GmbH, Weinheim, 2010, ch. 14, pp. 389-410.

47. K. R. Brownstein and C. E. Tarr, *J. Magn. Reson.*, 1977, **26**, 17-24.

48. J. H. Strange, J. Mitchell and J. B. W. Webber, *Magn. Reson. Imaging*, 2003, **21**, 221-226.

49. N. Robinson, C. D'Agostino and L. F. Gladden, *Faraday Discuss.*, 2017, **204**, 439-452.

50. N. Bloembergen, E. Purcell and R. Pound, *Phys. Rev.*, 1948, **73**, 679-712.

51. J. Mitchell, S. Stark and J. H. J. Strange, *J. Phys. D,* 2005, **38**, 1950-1958.

52. Y. Kim, A. Mittal, D. J. Robichaud, H. M. Pilath, B. D. Etz, P. C. St John, D. K. Johnson and S. Kim, *ACS Catal*, 2020, **10(24)**, 14707-14721.

Chapter 7: Light-driven, heterogeneous organocatalysts for novel C-C bond formation towards valuable perfluoroalkylated intermediates

This chapter has been published as a full research article in the journal *Science Advances*. [1] [Light-driven, heterogeneous organocatalysts for C–C bond formation toward valuable perfluoroalkylated intermediates | Science Advances (sciencemag.org)](#)

Michele Melchionna, Paolo Fornasiero, and Maurizio Prato conceived the main idea and directed the work. Giacomo Filippini designed and performed the catalytic experiments. Francesco Longobardo prepared and characterized the carbon nitrides. Lucia Nasi performed the HRTEM experiments. Luke Forster conceived part of the idea related to surface analysis through NMR, designed and performed the NMR experiments, did the data processing and analysis and wrote the manuscript section on NMR. Alejandro Criado performed and discussed the XPS experiments. Michele Melchionna prepared the manuscript.

Abstract

The favorable exploitation of carbon nitride (CN) materials in photocatalysis for organic synthesis requires the appropriate fine-tuning of the CN structure. Here we present a deep investigation of the structure/activity relationship of CN in the photocatalytic perfluoroalkylation of organic compounds. Four types of CN bearing subtle structural differences were studied via conventional characterization techniques and innovative NMR experiments, correlating the different structures with the fundamental mechanistic nexus, especially highlighting the importance of the halogen bond strength between the reagent and the catalyst surface. The optimum catalyst exhibited an excellent performance, with a very wide reaction scope, and could prominently trigger the model reaction using natural sun. The work lays a platform for establishing a new approach in the development of heterogeneous photocatalysts for organic synthesis related to medical, agro- and material chemistry.

7.1. Introduction

There is increasing pressure on industry for a rapid switch to new sustainable synthetic schemes to access chemicals of widespread use. In this context, heterogeneous photocatalysis by readily available, metal-free catalysts has a formidable appeal. In contrast with homogeneous systems, heterogeneous catalysts can be easily recycled; moreover, the metal-free nature avoids some typical drawbacks of metal-based catalysis such as: i) high cost of the metal; ii) poor compatibility with particular reaction environments; iii) decrease of activity over time due to nanoparticle aggregation. Graphitic carbon nitride (*g*-CN) is an ideal semiconductor nanomaterial candidate, with a relatively narrow band-gap, extensively used in photocatalytic applications related to energy, such as H_2 production, water oxidation and CO_2 reduction. [2-4] It is a stable material, that can be prepared by simple and scalable procedures, and properties and reactivity can be fine-tuned by carrying out structural modifications. [5] For instance, protonation and doping with heteroatoms other than N can adjust the electronic band edges and increase exposed surface area [6-8] while intercalation of metal ions can improve charge carriers mobility, decrease the band gap and provide the material with additional catalytic sites. [9, 10] In recent years, use of *g*-CN has been extended to photocatalytic organic synthesis for preparing industry-relevant compounds. While mainly employed in photo-catalytic oxidation of small molecules, [11, 12] there are also notable examples of C-C and C-heteroatom bond formation reactions, [13-16] including the functionalization of arenes and heteroarenes with fluoroalkylated groups, [17] that are important compounds in medicinal chemistry, agrochemistry and material science. [18-20] The use of *g*-CN circumvents that of catalysts such as Ru/Ir/Cu metal complexes, [21-23] that are associated with high cost, toxicity and non-recyclability, or that of organic dye-based catalysts, that require very high catalyst loadings. [24-26] Hence, the development of stable and cost-effective visible-light photocatalysts for C-C bond formation towards fluoroalkylated compounds is highly demanded. An in-depth analysis of the mechanistic features of the reaction, and the consequent structure/activity relationship, will establish the platform for the rational design of new and more effective material-based catalysts, for a range of different reactions. Here, diversely modified CN catalysts were prepared and investigated in the visible-light photocatalytic perfluoroalkylation of electron-rich organic substrates (**1**) by using simple perfluoroalkyl iodides (**2**) as the radical sources under mild operative conditions. The choice of **2** as model substrates lies in their high tendency to form reactive fluorinated radicals upon photo-induced single electron transfer processes. [27] The post-synthetic modifications

afforded materials with fine-tuned properties, and a robust correlation between the structural features and the catalytic behaviour was for the first time established by the combination of detailed characterization, advanced nuclear magnetic resonance (NMR) spectroscopy, and production rates. Moreover, the catalysis could be extended to many substrates, covering a wide reaction scope, including arenes as well as unsaturated aliphatic molecules. New insights were acquired into the specific and most relevant interactions between the CN materials and the employed fluorinated substrates (**2**), which modulate kinetics and thermodynamics of the photocatalytic reaction. Finally, the best performing photo-catalyst, with a very low loading, was successfully tested under Sun exposure at ambient temperature, demonstrating the excellent catalytic competence under real operative conditions.

7.2. Experimental

7.2.1. Materials

Commercial reagents and solvents were purchased from Sigma-Aldrich, Fluka, Alfa Aesar, Fluorochem, VWR and used as received, without further purification, unless otherwise stated. 1,3,5-trimethoxybenzene (**1a**), 2,6-diisopropylaniline (**1b**), methyl 5-acetylsalicylate (**1c**), caffeine (**1d**), 1-hexene (**1e**), 1-decen (**1f**), 5-hexen-1-ol (**1i**), 6-bromo-1-hexene (**1k**), 6-chloro-1-hexene (**1l**), 1-hexyne (**1n**), nonafluoro-1-iodobutane (**2a**), perfluorohexyl iodide (**2b**), heptadecafluoro-1-iodooctane (**2c**), 2,6-lutidine, melamine and potassium carbonate are all commercially available. The preparation of olefins **1g**, **1h**, **1j** and **1m** is detailed in the Supporting information (SI).

7.2.2. Synthesis of nanomaterials

All nanomaterials were prepared using commercial reagents and solvents purchased Sigma-Aldrich and used as received, without further purifications. For the *g*-CN, the furnace used was a cubic muffle operating under static air atmosphere; the samples were positioned in the middle. For the *am*-CN and *red*-CN, the furnace used was tubular, with the cylindrical quartz reactor inserted horizontally. The gas stream was inlet from one side of the reactor and exit to the other, with high-vacuum glass connectors. The gas mixture and flux was set used calibrated mass flow controllers.

g-CN: 10 g of melamine were transferred in a covered alumina crucible and heated in muffle furnace at 550°C for 300 minutes with a ramping time of 5 °C/min. The final product was milled in order to have a uniform powder.

red-CN: 0.75 g of g-CN were transferred in an alumina boat-shaped crucible and thermally heated in a tubular furnace at 520°C for 120 minutes with a ramping time of 2 °C/min in a mixture of argon (200 mL/min) and hydrogen (30 mL/min) flow.

am-CN: 0.75 g of g-CN were transferred in an alumina boat-shaped crucible and thermally heated in a tubular furnace at 620°C for 120 minutes with a ramping time of 2 °C/min in argon flow.

ox-CN: preparation: 0.75 g of g-CN were transferred in a 600 mL distillation flask, dispersed in 300 mL of a solution 4 M nitric acid and sonicated for 5 h. The product was collected by filtration and washed with 250 mL of MilliQ and 250 mL of methanol.

7.2.3. Catalytic testing

All reactions were set up under an argon atmosphere in Schlenk tubes, unless otherwise stated. Synthesis grade and anhydrous solvents were used as purchased. The catalysts were all grinded in a mortar for a period of 15 minutes prior to photocatalytic experiments, after which time thinly powdery samples are obtained. Chromatographic purification of products was accomplished using flash chromatography on silica gel (35-70 mesh). For thin layer chromatography (TLC) analysis throughout this work, Merck pre-coated TLC plates (silica gel 60 GF254, 0.25 mm) were employed, using UV light as the visualizing agent (254 nm), basic aqueous potassium permanganate ($KMnO_4$) stain solution or iodine, and heat as developing agents. Organic solutions were concentrated under reduced pressure on a Büchi rotatory evaporator.

7.2.4. Characterisation of materials

7.2.4.1. Thermogravimetric analysis (TGA)

TGA was performed on a TGA Q500 (TA Instruments) in air. The samples were equilibrated at 100 °C for 20 min, following a ramp of 10 °C/min up to 830 °C. Raman spectra were acquired using an Invia Renishaw spectrometer equipped with a diode laser at 785 nm.

7.2.4.2. Ultraviolet visible (UV-vis) spectroscopy

Diffuse reflectance UV-vis spectroscopy was performed with a Thermo Scientific Evolution 600 spectrophotometer, equipped with a diffuse reflectance accessory Praying–Mantis sampling kit (Harrick Scientific Products, USA).

UV-vis spectra for starting materials were performed with Shimadzu UV-2450.

7.2.4.3. X-Ray photoelectron microscopy (XPS)

XPS for the all nanomaterials was performed with a SPECS Sage HR 100 spectrometer with a non-monochromatic X ray source of Magnesium with a Kα line of 1253.6 eV energy and 250 W. XPS data was fitted using CasaXPS software. Standard transmission electron microscopy

7.2.4.4. Transmission electron microscopy (TEM)

TEM images were carried out on TEM Philips EM208, using an acceleration voltage of 100 kV. HR-TEM characterization was performed using a JEOL 2200FS microscope operating at 200 kV, equipped with an Energy Dispersive Spectrometer (EDX) and a high-angle annular dark-field (HAADF) detector. To minimize the radiation damage from the electron beam, the HRTEM images were acquired using a very low beam current and low exposure time.

7.2.4.5. X-Ray diffraction (XRD)

X-ray diffraction (XRD) was performed on a Philips X'Pert diffractometer using a monochromatized Cu Kα (λ= 0.154 nm) X-ray source in the range 20° < 2θ < 100.

7.2.4.6. Nitrogen (N_2) adsorption-desorption

N_2 physisorption was performed with a Micrometrics ASAP 2020 analyzer at liquid nitrogen temperature. All the nanomaterials were degassed at 150°C for 12h at 10 µmHg. The Specific Surface Area was calculated applying the BET method equation. Pore size distributions were determined to the adsorption branch of the isotherms with BJH method equation.

7.2.4.7. ^1H and ^{19}F NMR relaxation measurements

NMR experiments were performed on a $^1H/^{19}F$ Magritek SpinSolve 43 MHz benchtop NMR spectrometer. For ^{19}F NMR measurements a pulse length of 130.4 µs was used, with a pulse amplitude of -6 dB for the 90 ° pulse and 0 dB for the 180 ° pulse, a receiver gain of 52 and acquiring 8192 points in the time domain with a dwell time of 50 µs. For ^1H NMR measurements

a pulse length of 18 μs was used, whilst the other acquisition parameters were the same as those used for the ^{19}F NMR experiments.

T_1 was measured using the inversion recovery pulse sequence, [28] (Figure 2.5) with a repetition time of $5 \times T_1$, acquiring 16 time delay steps logarithmically spaced and a number of scans varying between 8 – 16 for ^{1}H NMR experiments and between 32 – 64 for ^{19}F NMR experiments, depending on the signal-to-noise ratio (SNR) of the sample.

T_2 was measured using the Carr-Purcell-Meiboom-Gill (CPMG) pulse sequence [28] (Figure 2.7b) using an echo time of 1 ms with 16 steps, using two echoes per step and 16 – 32 scans for ^{1}H NMR experiments and 128 – 1024 scans for ^{19}F NMR experiments.

To prepare solid samples for the NMR experiments, the photocatalyst solid particles were soaked in the liquid under investigation (~2 mL) for 24 h to ensure full saturation of the solid. The saturated solid samples were then transferred to 5 mm NMR tubes. To minimise errors due to evaporation of the liquid, a small amount of pure liquid was dropped onto a filter paper, which was placed under the cap of the NMR tube. The NMR tube was then placed into the magnet and left for approximately 20 min to achieve thermal equilibrium before measurements started.

7.3. Results and discussion

Three structural and chemical variations were introduced into the pristine *g*-CN, adopting a reduction protocol (*red*-CN), a mild oxidation protocol (*ox*-CN) and a thermal amorphization protocol (*am*-CN) (Figure 7.1). The chosen modifications introduce a specific feature in each material that was expected to reflect in a diverse interaction with the substrate, as described in detail below.
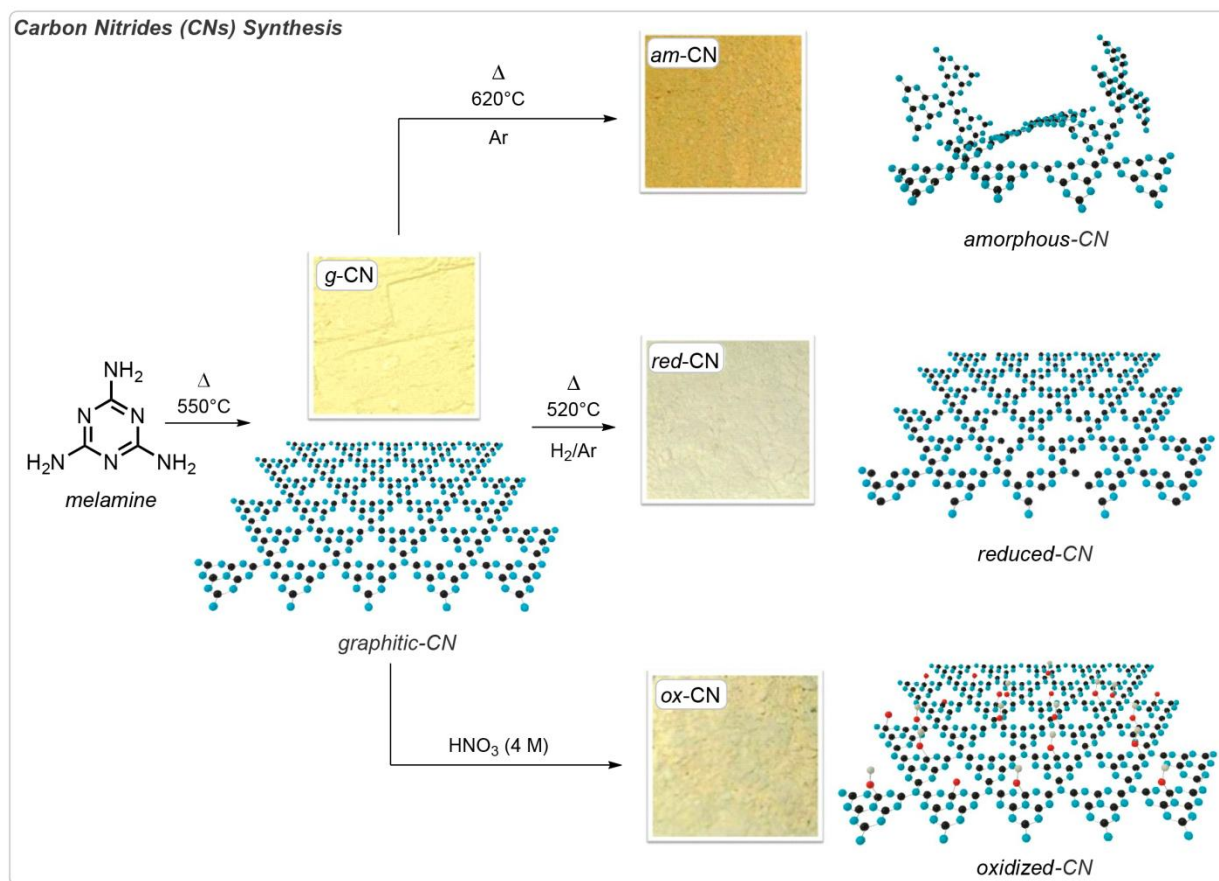
Figure 7.1. Sketch of synthesis and structure of the different CN materials. Graphical sketch of the synthesis of the various CN structures, with the associated photograph of the as-obtained powdery material. Standard thermal conditions applied to melamine lead to synthesis of graphitic carbon nitride (*g*-CN), where the morphology is typically described by melem units connected in-plane; oxidative treatment presumably introduce small amounts of oxygenated functional groups on the surface (*ox*-CN), while reductive treatment partly remove N atoms creating planar vacancies (*red*-CN; higher temperature thermal treatment under inert atmosphere generates partially amorphous structure by misalignment of CN planar domains (*am*-CN). Note: the graphic rendering of the structure is only an idealized depiction used for the benefit of discussion. Real CN structures are much more complex. Photo credit: Francesco Longobardo, University of Trieste, Italy.

Microscopic analysis through TEM revealed that the three modifications result in slight morphological alterations, with the smooth sheet-like geometry of *g*-CN being partially scrambled (Figure S7.1). A visual inspection of the materials reveals a change in the colour depending on the specific treatment, consequent to the structural change and in turn a change in the electronic properties of each CN (Figure 7.1). In particular, H_2/Ar high temperature treatment (*red*-CN) has been reported to lead to defective structure introducing superficial nitrogen vacancies, [29] confirmed here by X-ray photoelectron spectroscopy (XPS, *vide infra*). The absence of N atoms not only creates additional defects in the structure, but also decreases the overall polarization of the C atoms on the surface of the catalyst. In contrast, the oxidation protocol (*ox*-CN) introduces additional amounts of oxygen atoms, as confirmed by X-Ray photoelectron spectroscopy (XPS), presumably through formation of oxygenated functional groups on the surface, similarly to oxidation of other carbon nanostructures. [30, 31] In principle the presence of such functional groups can be non-innocent, contributing to direct interaction with the substrate; alternatively, O atoms inserted onto the CN surface can behave as dopants and tune the electronic properties. [32] Higher temperature treatment under inert atmosphere (*am*-CN) is able to disrupt hydrogen bonding of the NH/NH_2 groups causing misalignment between strands of polymeric melon units with consequent partial amorphization and particle size reduction (*am*-CN). [33] High-resolution TEM (HRTEM) shows differences in the thermally treated materials (*am*-CN and *red*-CN) as compared with the conventional *g*-CN. In particular, the crystalline domains in the latter are more clearly identified and present in high density, with the lattice fringes being confirmed by Fast Fourier Transform (FFT) from which an interplanar spacing of 0.32 nm is seen in agreement with literature (Figure 7.2c). [34] In contrast, for *am*-CN the crystal fringes are not easily detected, with the observed dominant FFT pattern being associated to an amorphous material (Figure 7.2a). Moreover, the FFT of *g*-CN reveals the order of the in-plane geometry, namely the intra-layer spacing of 0.68 nm is appreciated as observed in other reports (Figure 7.2d). [34, 35] Such feature is not found in *am*-CN, presumably as the order is partly broken. For *red*-CN that was treated under milder conditions than am-CN we could observe some crystalline domains although much less densely distributed in comparison with *g*-CN (Figure 7.2b). Finally, the most interesting feature for *ox*-CN, where the qualitative crystalline domains distribution looks intermediate between *am*-CN and *red*-CN based on HRTEM inspection (Figure 7.2e), is gained by Energy-dispersive X-ray spectroscopy (EDX) elemental mapping, that shows that this is the only sample where oxygen is present in significant

percentage throughout the material (Figure 7.2f). Two very sensitive techniques to confirm the disruption of the long-range order ("amorphization") are X-Ray Powder Diffraction (XRD) and Raman spectroscopy as also reported by Kang et al. previously. [33]
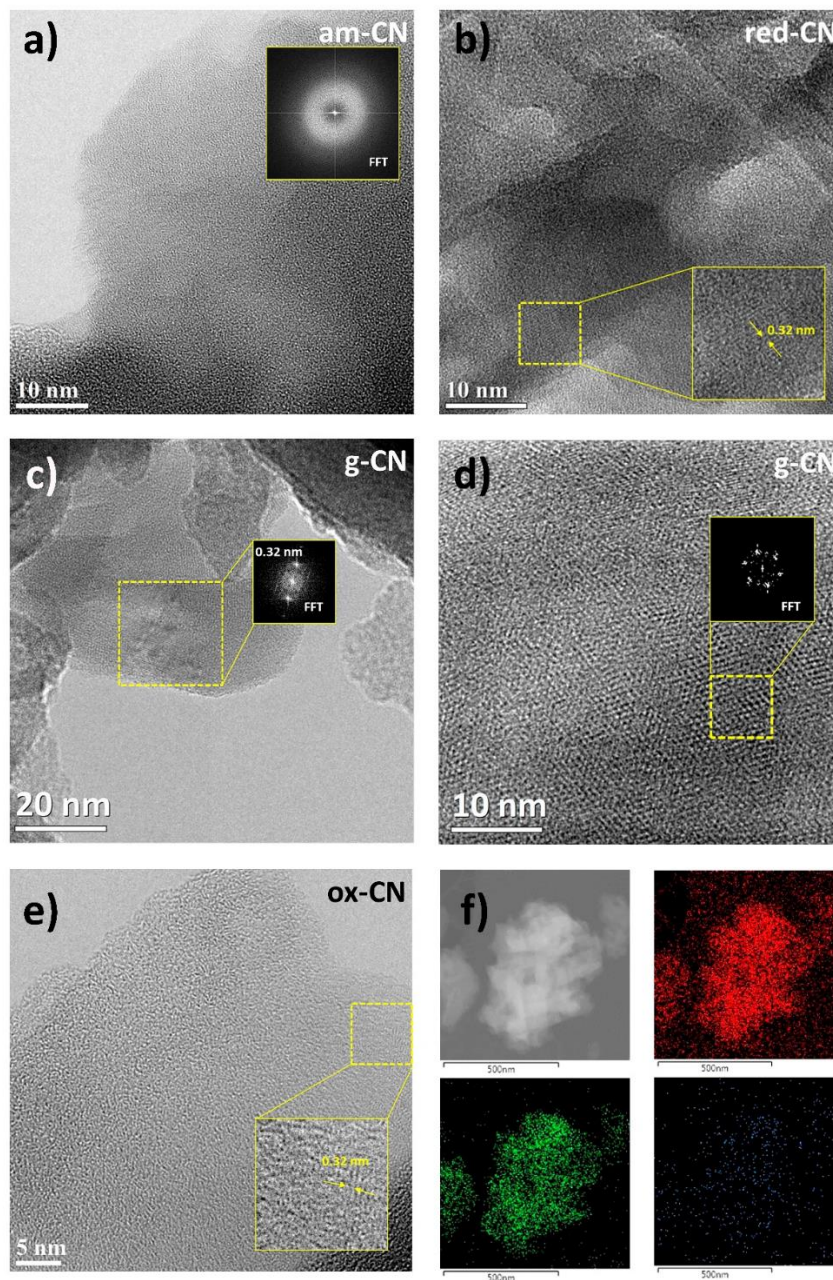
Figure 7.2. High-resolution microscopy of the four samples. a) representative HRTEM image of *am*-CN; inset: FFT of a selected area showing the pattern of a typical amorphous material; b) representative HRTEM image of *red*-CN; inset: high magnification of a selected area, showing the crystal lattice fringe, where a 0.32 nm interlayer spacing is measured; c) representative HRTEM of *g*-CN with the FFT (inset) showing the lattice fringe with the expected 0.32 nm interlayer spacing and d) high magnification of a selected area of c) with the FFT showing the intra-layer XRD pattern with a 0.68 nm spacing ; e) representative HRTEM image of *ox*-CN with the inset showing the lattice fringe with the 0.32 nm inter-layer spacing and f) EDX elemental mapping of *ox*-CN: Carbon (red), nitrogen (green) and oxygen (blue).

In particular, it can be observed for *am*-CN that the strong 27.2° peak ascribed to the (002) plane of the interlayer stacking of the conjugated aromatic system, [35] associated to the crystallinity of the material, is broader and less intense as compared to the other three samples, in agreement with an increased amorphous nature (Figure 7.3b). The calculated crystallite size (inset Table Figure 7.3b) is therefore smaller (5.4 nm), implying a reduction of the number of layers in *am*-CN. Consistently, the intensity of the (100) reflection at 12.7°, which is associated to the intra-layer spacing (also observed in the HRTEM), decreases from *g*-CN to *am*-CN, further corroborating the hypothesis of the partial rupture of the strands of heptazines. In agreement with this hypothesis, Raman spectroscopy reveals the different profiles for the four materials. It is known that Raman spectroscopy of CN materials under visible excitation is problematic due to the strong fluorescence in such wavelength range. [36] However, use of Near-Infrared (NIR) excitation provides an informative Raman pattern. NIR-Raman spectra of the four samples show the characteristic peaks at ~ 705 cm^{-1}, and 990 cm^{-1}, due to breathing modes of the rings, and ~ 1200 cm^{-1} due to the A1 vibration of the melem units (Figure 7.3a). [37, 38] The lower peak intensity pattern in *am*-CN, as compared to the other three materials, is in line with the increased amorphous character as observed also in the XRD. Further evidence is finally provided by the thermogravimetric analysis (TGA), where the combustion temperature is decreased by about 50 °C in all treated CN with respect to that of the pristine material (Figure S7.2), implying a lesser crystallinity.
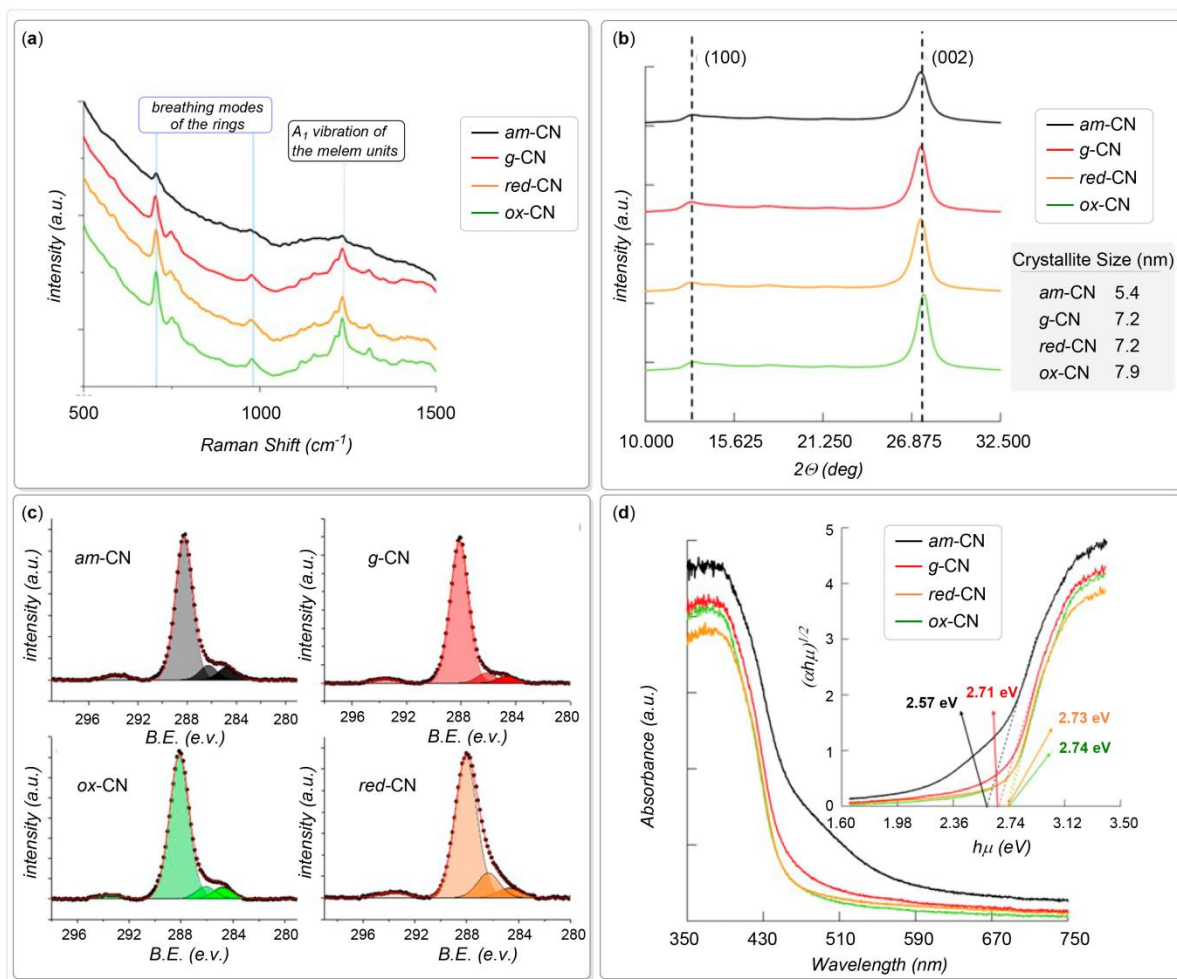
Figure 7.3. Physical characterization. NIR Raman spectra (a) and XRD diffractogram (b) of the four materials; crystallite size reported in the table of fig (b) were calculated by applying the Scherrer equation to the (002) reflection; (c) High-resolution XPS spectra in the C1s binding energy (B.E.) range; (d) DRS spectra and the corresponding band gap (inset).

X-Ray Photoelectron Spectroscopy (XPS) shows that for all materials the two main components C and N are in similar atomic ratios (see Table S7.1), with *red*-CN bearing a lower content of N, as expected for a H_2-treated CN material. [29] In addition, the increment of C-N component (286.2 eV) of *red*-CN as compared to the other samples reflects the reduction process. All C1s spectra could be deconvoluted in four components, 284.8, 286.2, 288.2 and 293.5 eV, assigned to C-C, C–N, C=N–C and π-π* species. [39] Amorphization by higher temperature treatment is reflected into the lower contribution of the aromatic component (288.2 eV) with respect to the other species, as compared to *g*-CN (Figure 7.3c). The anticipated increase in oxygen content is finally confirmed

in *ox*-CN, where O at% reaches 5.3%. For all materials, high-resolution spectrum of the N1s core level could be deconvoluted into three different peaks, including the most intense component at 398.8 eV assigned to C=N-C nitrogen atoms in the sp^2-hybridized nitrogen, a component N-(C)$_3$ originating from the three-coordinated nitrogen atoms at 400.7 eV, and a minor contribution at around 404.5 eV, whose attribution is controversial, and in some cases has been related to a N-N bonding (Figure S7.3). [39] Importantly, XPS analysis also confirm absence of metal species in detectable amounts. This is an important aspect in relation to the recent debate on the true "metal-free" nature of carbon nanostructures that may contain metal impurities. [40] While XPS provides information on the superficial element composition, the metal-free nature of the bulk catalysts was further proved by inductively coupled plasma optical emission spectrometry (ICP-OES) where metals were below the limit of detection. The materials were also characterized by elemental analysis to evaluate the differences in the bulk (Table S7.2). As expected, the composition of all samples remains very similar to each other, and in agreement with values reported for graphitic carbon nitride prepared from melamine precursor, where the C:N atomic ratio is ~ 0.66 due to residual uncondensed melamine. [34, 41, 42] This confirms that the structural modifications are mainly involving the surface of the materials, which are those relevant for the catalysis as it is where adsorption of reagents occurs.

The band gap results affected by the post-modification of each sample, as observed by UV-Vis diffuse reflectance spectroscopy (DRS) analysis, which shows a different absorbance profile of *am*-CN, whose band gap is reduced to 2.57 eV as compared to *g*-CN (2.71 eV). The oxidative and reductive treatments, in contrast, cause smaller variations suggesting a lower disruption of the long-range order (2.73 eV for *red*-CN and 2.74 eV for *ox*-CN). It is also observed that the absorption profile for *am*-CN also present a broad peak at lower energy (larger wavelength) which could be associated to the presence of intra-gap states, as also previously suggested (Figure 7.3d). [43] The valence band (VB) edge for the four materials was calculated by the analysis of the XPS profile in the low binding energy range (Figure S7.4), with values in the range expected from previous literature. [44] Compared to the *g*-CN (VB = 1.83 eV), the thermal treatment carried out for preparing *am*-CN and *red*-CN decreases the energy of the VB, while the oxidative treatment increases it (Figure S7.5). As a result, the calculated conduction bands (CB) edges for *am*-CN and *red*-CN are localized at more negative energies (-0.92 eV and -1.28 eV, Figure S7.5), thus being more efficient for reduction of the substrates, based on the reported redox potential ranges of the

perfluoroalkyl iodides (~ -0.76 V vs RHE).(*20*) In any case, the CB of all samples are adequate for performing the reduction step on the fluorinated compounds while it is insufficient for other non-fluorinated substrates that were tested (see below), whose redox potentials lie at significantly more negative energies, thus requiring future development of the CN catalysts, with *ad hoc* engineering of the band structure by alternative synthetic methodologies.

Structural distortions are accompanied by relatively small changes in surface area, with the Brunauer-Emmett-Teller (BET) surface area remaining in the range between 7 and 19 m^2 g^{-1}, namely relatively low as expected for CN materials. [45] (Figure S7.6). However, despite in all cases the isotherms and the t-plot analysis indicating the presence of meso/macro-pores, the pore size distribution is affected, with the average pore diameter increasing in the order *g*-CN (maximum of distribution: 65 nm) < *red*-CN (maximum of distribution: 73 nm) < *ox*-CN (maximum of distribution: 78 nm) < *am*-CN (maximum of distribution: 122 nm) (Figure S7.7). Larger pores in *am*-CN presumably minimize mass diffusion restrictions, contributing to increase the activity of this catalyst.

As a primary goal of the investigation, the relationship between the structure of the material and its photocatalytic activity was thoroughly investigated on a model reaction, in order to reveal the key parameters influencing activity. For this reason, 1,3,5-trimethoxy-benzene (**1a**) as the model electron-rich organic molecule, and perfluorobutyl iodide (**2a**) as the fluorinated precursor were chosen (Table 7.1).

Table 7.1. Catalytic tests on the model reaction. Optimization studies and control experiments. Reactions were performed on 0.1 mmol scale. [a] Yield determined by ^{1}H-NMR spectroscopy using 1,1,2-trichloroethene as the internal standard. [b] Isolated yield. Photo credit: Giacomo Filippini, University of Trieste, Italy.

Optimization of conditions was carried out with the pristine photocatalyst (*g*-CN), under 450 nm blue monochromatic irradiation at ambient temperature. Under the standard conditions (Entry 1, Table 7.1), the studied transformation proceeds quantitatively to afford **3a** (yield > 99%) after 24 hours and with complete product selectivity. In contrast, deviations from standard conditions severely affects the reaction. In particular, absence of catalyst (Entry 2, Table 7.1), absence of light (Entry 3, Table 7.1), presence of oxygen (Entry 4, Table 7.1), and presence of (2,2,6,6-Tetramethylpiperidin-1-yl)oxyl (TEMPO; Entry 5, Table 7.1) prevent the transformation, confirming both the photocatalytic and radical nature of the process. Other deviations from standard conditions such as the change of irradiation wavelength as well as changes of base, reaction **stoichiometry**, and solvent, are also detrimental (Entries 6-11, Table 7.1). The photocatalytic activity of the four different prepared materials was then screened. Reducing the amount of *g*-CN to half (0.35 %w/v) results in a significant drop of yield (Entry 12, Table 7.1).

188

Disappointingly, the use of *ox*-CN leads to the formation of product **3a** in very poor chemical yield (Entry 13, Table 7.1). On the other hand, both *red*-CN and *am*-CN provide very high yield, respectively 90% and 99% (Entries 14-15, Table 7.1). The best reaction conditions were thus found as shown in Entry 16, Table 1. Notably, the amorphous catalyst is highly performant even at lower loadings, reaching a 89% yield at 0.125% w/v, which is a very low loading as compared to typical reported conditions (Entry 17, Table 7.1). [17]

The rates of product formation were calculated for product **3a** with the four catalysts. Following very recent proposed guidelines for reporting the activity of photocatalysts, [46] the rates were also calculated per surface area of the four catalytic materials (Table S7.3), in order to evaluate the contribution of the geometric effect. It can be seen that over the 24 h reaction time, if normalized by the surface area, the *red*-CN catalyst is apparently more efficient, hinting that intrinsically such a catalyst is more active. However, it must be noted that *red*-CN after 24 h is unable to convert totally the reagent, while *am*-CN does. If normalized per mass of catalyst, *am*-CN is the most efficient.

A plausible mechanism that drives the catalytic reaction by the *am*-CN is proposed based on previous findings and supported by NMR studies (*see below*).
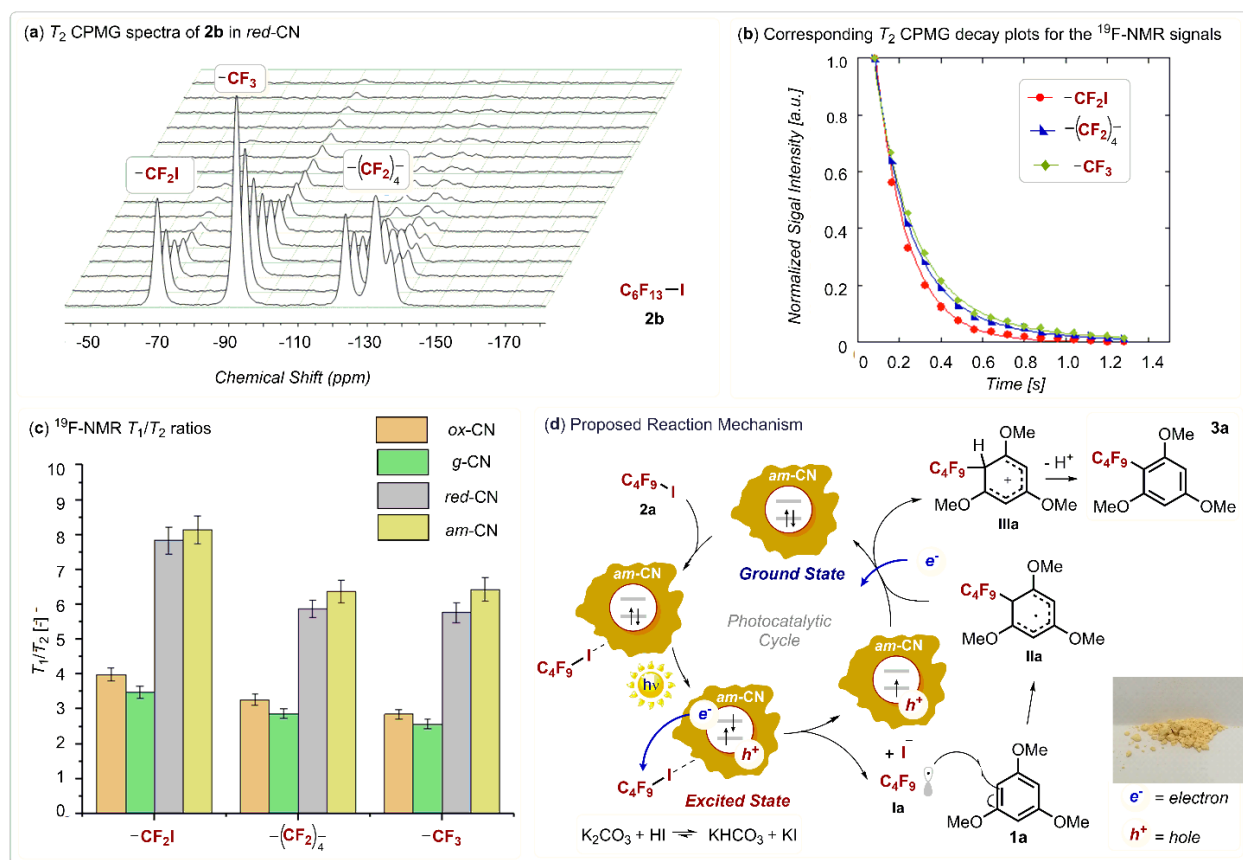
Figure 7.4. NMR investigation and proposed mechanism. (a) T_2 CPMG spectra of perfluorohexyl iodide in *red*-CN. The CF$_2$I resonance is at approximately -69 ppm, that of the CF$_3$ at approximately -92 ppm, and the (CF$_2$)$_4$ peaks in the range -120 – -145 ppm; (b) Corresponding T_2 CPMG decay plots for the NMR signals of CF$_2$I, (CF$_2$)$_4$ and CF$_3$ fitted using a single CPMG exponential decay; (c) ^{19}F NMR T_1/T_2 ratio of the different moieties of perfluorohexyl iodide in the various CN-based photocatalytic materials used in this work; (d) Proposed reaction mechanism which drives the photocatalytic perfluorobutylation of **1a**. The perfluorinated substrate binds the catalyst surface via iodine halogen bond. After photoexcitation and charge separation in the semiconducting catalyst, excited electrons are injected from the catalyst to the substrate, forming the radical **Ia**. The radical then attacks the aromatic molecule leading to the cascade reaction generating the final product. Photo credit: Francesco Longobardo, University of Trieste, Italy.

Figure 7.4d shows the catalytic cycle, where prior to photo-induced charge separation in the semiconductor, the binding of **2a** occurs presumably *via* halogen bonding with the *N* atoms of the photocatalyst. [47] This step is of high importance, as it dramatically affects the rate of the injection of the photo-excited electron into the C$_4$F$_9$I reagent and thus also the formation of the ·C$_4$F$_9$ radical (**Ia**). Finally, the as-formed open-shell species **Ia** attacks the aromatic ring of the trimethoxy-benzene (**2a**) and the catalysis eventually evolves to the final desired product (**3a**). We also

evaluated the apparent quantum yield (AQY) of reaction producing **3a** by *am*-CN, in order to gain insights into the possibility of a chain-propagating mechanism, for which the quantum yield is expected to be > 1, as discussed in recent reports on photocatalysis mechanisms. [48] As the AQY is of 0.016 mmol(**3a**)/mmol photons, therefore < 1, the reaction does not presumably occur via a chain-propagation process, although this cannot be totally ruled out as the AQY < 1 may also derive from a highly inefficient initiation step. [48]

Assessment of the iodine halogen bond strength and its effect on reactivity was investigated by ^{19}F NMR T_1/T_2 relaxation measurements using perfluorohexyl iodide (**2b**) as our probe molecule (we chose a longer-alkyl chain substrate due to the lower volatility than **2a**). The T_1/T_2 ratio has been shown to be a robust indicator of strength of surface interactions of liquids confined in porous catalysts. [49] It has previously been demonstrated that such measurements allow the quantification of the strength of hydrogen bonding of liquids confined in porous catalysts, [50] as reported by some of us who studied the behavior of alcohols inside porous silica, using ^{1}H NMR T_1/T_2 relaxation. [51] Prompted by such results, in this work we have extended the methodology in order to probe the strength of surface interactions of the perfluoroalkyl iodide reagent over the different catalysts screened for the reactions and exploiting ^{19}F NMR. T_1 was measured using the inversion recovery pulse sequence, whilst T_2 was measured using the Carr-Purcell-Meiboom-Gill (CPMG) pulse sequence. Figure 7.4a contains a typical data set, which shows the T_2 CPMG decay of the perfluoroalkyl iodide compound inside the *red*-CN sample. Figure 7.4b shows the T_2 CPMG decay of CF_2I, $(CF_2)_4$ and CF_3, from which it can be seen that within the same molecule the various groups have different T_2 CPMG decay rates, with the resonance of the CF_2I having a significantly faster decay compared to the $(CF_2)_4$ and CF_3.

Two important observations can be drawn from the data in Table S7.4 and Figure 7.4c. Firstly, in all cases the T_1/T_2 of the CF_2I moiety of perfluorohexyl iodide is higher compared to those of the $(CF_2)_4$ and CF_3 within the same molecule. In particular, the following trend, consistent across all materials, can be observed:

$$T_1/T_2 \text{ [CF}_2\text{I]} > T_1/T_2 \text{ [(CF}_2\text{)}_4] \simeq T_1/T_2 \text{ [CF}_3]$$

This indicates that the strength of surface interaction of the CF_2I is greater compared to the rest of the molecule and groups further away from this moiety exhibit a weaker interaction. The presence of van der Waals dipole-dipole interactions with the surface of CN does not explain this trend as

such forces are present for all moieties and should be even stronger for fluorine-richer moieties, such as $(CF_2)_4$ and CF_3. This suggests that it is the iodine atom which differentiates the CF_2I moiety, especially if it is considered that the strength of halogen bonding is the highest for iodine as compared with the other halogens. [52] Hence, the current results and the previously published work [51] strongly support the hypothesis that the ^{19}F T_1/T_2 trend observed in this work can be ascribed to the ability of the CF_2I to form halogen bonding with the solid surface of the catalyst, giving exclusive new insights into adsorbate/adsorbent interactions in these materials. Further insights into the relaxation behaviour can be drawn by calculation of surface relaxivities (see SI for details), that provide more evidence on the catalytic trend.

Secondly, by looking at the T_1/T_2 of the CF_2I group of perfluorohexyl iodide in different catalysts, the following trend can be identified:

$$T_1/T_2 \ [\textit{am-}\text{CN}] > T_1/T_2 \ [\textit{red-}\text{CN}] > T_1/T_2 \ [\textit{ox-}\text{CN}] \simeq T_1/T_2 \ [\textit{g-}\text{CN}]$$

The trend exactly parallels with the reactivity trend in Table 7.1, indicating that materials with a higher surface affinity for the fluorinated substrate are also those with the highest activity. This strongly suggests that the ability of the perfluoroalkyl iodide to form halogen bonding with the solid material is a critical factor determining reactivity and support the reaction mechanisms proposed in Figure 7.4c, highlighting the importance of the binding of the perfluoroalkyl iodide to the catalyst surface.

Further insights into the relaxation behaviour can be drawn by calculation of surface relaxivities. In order to do this, we consider the biphasic fast-exchange model. According to this model, fluids in contact with solid surfaces exhibit NMR relaxation times that can be very different from those of the same liquid as bulk, which can be described according to:

$$\frac{1}{T_{1,2}} = \frac{1}{T_{1,2,bulk}} + \rho_{1,2}\frac{S}{V} \tag{7.1}$$

The first term is the contribution of the bulk, the second term is the contribution of the surface, whereby $\rho_{1,2}$ are the relaxivities associated to $T_{1,2}$, and $\frac{S}{V}$ is the surface-to-volume ratio. Surface relaxivities characterise the ability of the surface to facilitate relaxation and are related to the adsorbate/adsorbent affinity. Assuming cylindrical pores, the expression can be written in terms of pore diameter as:

$$\frac{1}{T_{1,2}} = \frac{1}{T_{1,2,bulk}} + \rho_{1,2}\frac{4}{d} \tag{7.2}$$

Usually the bulk term is much larger than the surface term, hence the approximation:

$$\frac{1}{T_{1,2}} \approx \rho_{1,2}\frac{4}{d} \tag{7.3}$$

Hence, by knowing the typical value of pore diameter d of the solid material it is possible to calculate ρ_1 and ρ_2. The ratio $\rho_1/\rho_2 \approx T_1/T_2$. Values of ρ_1 and ρ_2 are reported in Table 7.1, together with single values of T_1 and T_2.

Table 7.1. Values of ^{19}F NMR T_1, T_2, T_1/T_2 and surface relaxivities, ρ_1 and ρ_2, of different moieties of perfluorohexyl iodide within different photocatalysts.

Sample	NMR peak	T_1 [ms]	T_2 [ms]	T_1/T_2 [-]	ρ_1 [nm/s]	ρ_2 [nm/s]
g-CN	CF$_2$I	1124 ± 33	323 ± 9	3.48 ± 0.17	9.35 ± 0.28	32.55 ± 0.98
	(CF$_2$)$_4$	1190 ± 35	417 ± 12	2.86 ± 0.14	8.82 ± 0.26	25.20 ± 0.75
	CF$_3$	1163 ± 34	455 ± 12	2.56 ± 0.13	9.01 ± 0.27	23.10 ± 0.69
ox-CN	CF$_2$I	1136 ± 33	286 ± 8	3.98 ± 0.18	15.84 ± 0.47	63.00 ± 1.89
	(CF$_2$)$_4$	1250 ± 37	385 ± 11	3.25 ± 0.16	14.40 ± 0.43	46.80 ± 1.40
	CF$_3$	1235± 36	435 ± 13	2.84 ± 0.14	14.58 ± 0.44	41.40 ± 1.24
red-CN	CF$_2$I	1149 ± 34	147 ± 4	7.82 ± 0.39	16.10 ± 0.48	124.10 ± 3.72
	(CF$_2$)$_4$	1149 ± 34	196 ± 5	5.86 ± 0.25	15.88 ± 0.47	93.08 ± 2.79
	CF$_3$	1176 ± 35	204 ± 5	5.76 ± 0.29	15.51 ± 0.46	89.43 ± 2.68
am-CN	CF$_2$I	1042 ± 30	128 ± 3	8.13 ± 0.40	28.32 ± 0.85	230.10 ± 6.90
	(CF$_2$)$_4$	1010 ± 29	159 ± 4	6.36 ± 0.32	29.21 ± 0.87	185.85 ± 5.55
	CF$_3$	1053 ± 31	164 ± 4	6.42 ± 0.33	28.03 ± 0.84	179.95 ± 5.93

It can be observed that *am*-CN has by far the highest ρ_1 and ρ_2 values among all materials. Differences in ρ_2 across all samples are much more evident compared to ρ_1. In particular, it can be seen that the most active samples, *am*-CN and *red*-CN, have values of ρ_2 which exceeds by far

the least active samples, *ox*-CN and *g*-CN. At this point it is worth noting that whilst T_1 is more representative of the overall pore structure, T_2 is more affected by the local surface chemistry. The results strongly suggest then that the different preparation conditions of the solids affect significantly the local surface chemistry of the final CN photocatalyst.

^{1}H NMR T_1/T_2 relaxation measurements using the reaction solvent, dimethylformamide (DMF) were carried out to evaluate the contribution of the solvent affinity to the reaction (Figure 7.5 and 7.6).
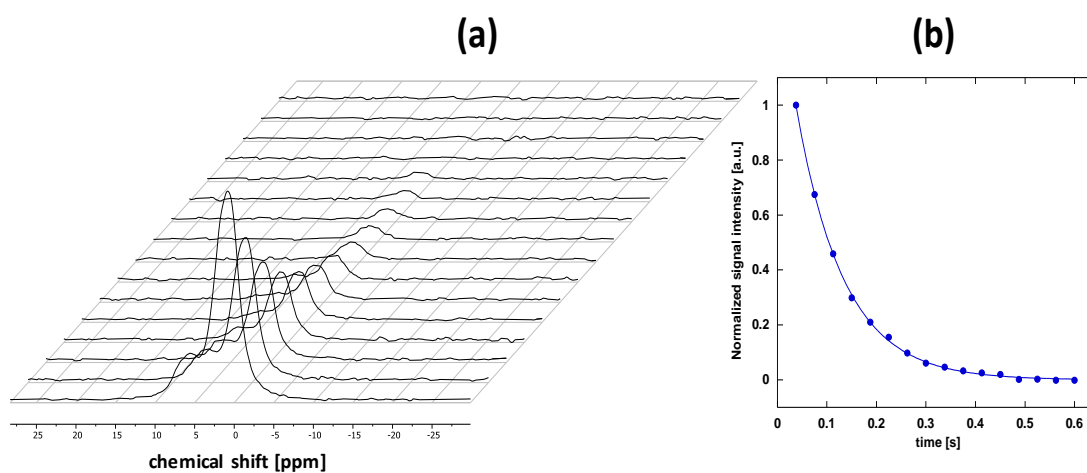
Figure 7.5. (a) T_2 CPMG spectra of DMF in *ox*-CN and (b) the corresponding T_2 CPMG decay plot for the whole spectrum.
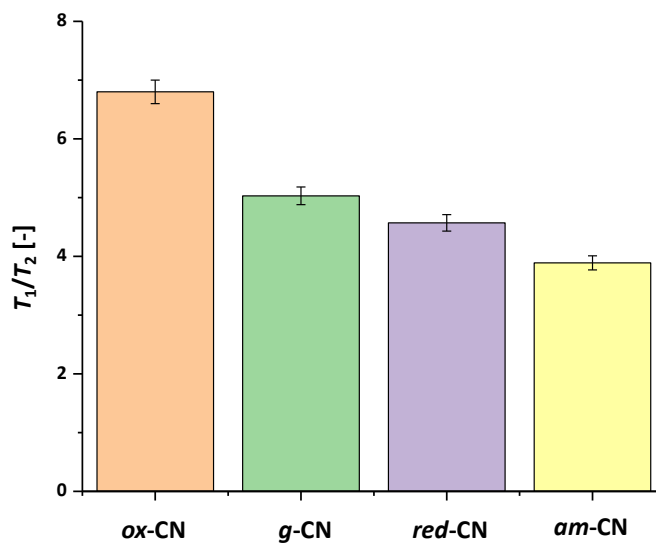
Figure 7.6. T_1/T_2 ratio of DMF imbibed within the various CN-based photocatalytic materials used in this work.

From this data, it is possible to identify a clear trend in T_1/T_2 ratio value for DMF imbibed within the pores of the various photocatalysts:

$$T_1/T_2 \; [ox\text{-}CN] > T_1/T_2 \; [g\text{-}CN] > T_1/T_2 \; [red\text{-}CN] > T_1/T_2 \; [am\text{-}CN]$$

As noted, the trend is inverse to that of activity, which suggests that when the DMF solvent has a lower surface interaction with the catalyst surface it can be easily displaced by the reagent, hence preventing the blocking of catalytically active sites (Figure 7.6 and Table 7.2).

Table 7.2. Values of ^{1}H NMR T_1, T_2 and T_1/T_2 of the DMF solvent within different photocatalysts. * Relative errors are in the range 3-5%; for bulk DMF $T_1 = T_2 = 3501$ ms.

Sample	T_1 [ms]	T_2 [ms]	T_1/T_2 [-]
g-C$_3$N$_4$	2133 ± 64	424 ± 13	5.03 ± 0.15
ox-C$_3$N$_4$	653 ± 20	96 ± 3	6.80 ± 0.20
red-C$_3$N$_4$	1722 ± 52	377 ± 11	4.57 ± 0.14
am-C$_3$N$_4$	1929 ± 58	496 ± 15	3.89 ± 0.12

The advanced NMR studies therefore shed important new light on the structure/activity relationship in CN materials, as connected with the microstructure of the specific sample. In particular, the NMR results indicate that the stronger surface affinity of the perfluoroalkyl iodide for the catalyst relative to that of the solvent is critical for controlling the access to the active sites of the substrate. This has been previously observed for liquid-phase oxidation over heterogeneous catalysts. [53]

As mentioned above, other parameters are however important for defining the overall catalytic performance. In particular, the reduced band gap of am-CN resulting in its better absorption at 450 nm could contribute significantly. Discerning quantitatively the contribution of the different parameters is extremely complicated. However, in order to confirm that optical properties are not the unique cause of the higher performance of am-CN, catalytic experiments were carried out on the four materials with a higher energy LED (395 nm corresponding to 3.14 eV) on the model reaction (Table S7.4). Instead of a flattening of the activity among the four photocatalysts following saturation of the electron/hole separation process with such a higher energy light source,

we still observed a clear and significant difference in the activity trend, which remains almost unaltered. This rules out a sole effect on the performance due to CB population differences, but strongly suggests that other factors are involved, although the reduced bandgap in *am*-CN does play a role.

The scope of the reaction was then investigated using *am*-CN (0.27% w/v) as photocatalyst under the optimized operative conditions (Scheme 7.1), and functionalization of a variety of aromatic, heteroaromatic and unsaturated aliphatic substrates (**1a**-**n**), even bearing reaction-sensitive functional groups, was successfully achieved, confirming the high tolerance of the photocatalyst (products **3a**-**p**, isolated yield up to 97%). Notably, catalytic tests using natural sunlight (product **3g**) also proved successful, and remarkably the reaction was completed within 4 hours in analogy with the artificial illumination test on the same alkene substrate (**1e**). This is an essential aspect for future real applications of *am*-CN as photocatalyst in organic synthesis. The stability of the *am*-CN photocatalyst was evaluated by recycling the catalyst three times at the end of the reaction for product **3g** and we did not observe any significant decrease of activity, the small differences being due to the physical loss of the *am*-CN material during separation from the reaction environment (Figure S7.8).
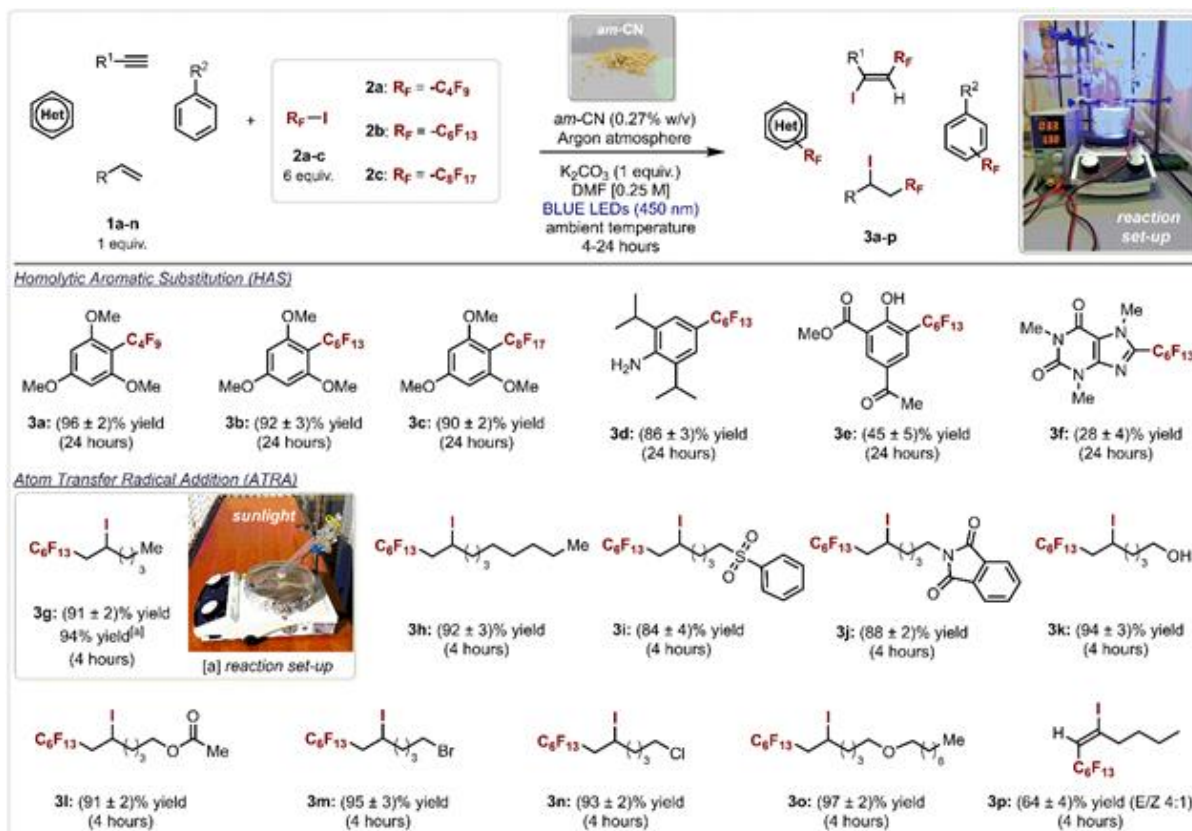
Scheme 7.1. Evaluation of the scope of the photochemical reaction. Survey of the organic compounds and perfluoroalkyl iodides which can participate in the photocatalytic process. Conditions: reactions conducted in Schlenk tubes in DMF (0.25 M) on 0.1 mmol scale of **1**, 0.6 mmol of perfluoroalkyl iodide **2**, 0,1 mmol of K_2CO_3 and 0.27 % w/v of *am*-CN, degassed by four freeze-pump-thaw cycles and irradiated for 4-24 hours by a blue LEDs strip (450 nm). [a] Outdoor experiment and the used set-up (from 9:00 to 13:00 of the 5th of August 2019, in Trieste, see Figure S7.9). Photo credit: Giacomo Filippini, University of Trieste, Italy.

To the best of our knowledge, the investigated reactions have been exclusively performed with homogeneous photocatalysts, so that our example is the first with a heterogeneous catalyst. Nevertheless, we compared the performance versus homogeneous systems (Table S7.5). Given the large scope of reaction investigated herein, we selected product **3k** as a representative case study, given that it is the most represented in literature. It can be seen from the rate of production of **3k** that despite the intrinsically general higher activity of homogeneous catalysts, *am*-CN performs better than most of the reported catalysts. This result, combined with the metal-free nature of *am*-CN and with the advantages of heterogeneous catalysis highlights the great appeal of the present material and especially the synthetic approach for fine-tuning activity, which can be subject to future developments.

Finally, we explored the generality of the catalytic behavior using a less electron-rich substrate, anisole, and observed a dramatic decrease of activity (overall yield 25%) and selectivity (NMR shows presence of a complex mixture of adducts, presumably associated with different regio-isomers or bifunctionalization) (Table S7.6). The poor regio-selectivity is not surprising as it is typically associated with reactions proceeding with HAS mechanism. [54] Other simple molecules such as benzene or naphthalene did not exhibit any reactivity, as also expected based on the absence of strongly electron-donating groups on the substrate (Table S7.6). Moreover, non-terminal alkenes such as cyclohexene displayed a drop of yield (19%) presumably to steric effects, together with a low diastereoselectivity (2:1 *trans*:*cis* isomers were formed, Table S7.6). Equally, the reaction with non-perfluorinated hydrocarbons fails to proceed (Table S7.7), as expected from considerations on the band structure of the semiconductor photo-catalysts, located at energies suitable to convert reagents with a redox potential within the band gap. The absence of the fluorine groups implies a significant shift of the redox potential towards much more negative values, out of the reduction ability of the described photocatalysts.

7.4. Conclusions

In conclusion, we present an in depth experimental analysis of the photocatalytic activity for the perfluoroalkylation of electron-rich organic substrates by carbon nitride materials in relation to their different microstructure. A discrimination of the critical parameters that define activity is carried out through a combined set of investigations based on different characterization techniques. In particular, for the first time, advanced ^{19}F NMR provides key quantitative insights into the importance of reagent affinity towards the solid catalyst through formation of halogen bonding, which in turn depends on the local structure. This NMR approach could therefore be extended to other types of heterogeneous catalytic reactions involving halogen bonding. Our proof of concept study is finally condensed into a practical exploitation of the best catalyst by using natural solar light for achieving high activity synthesis of a perfluorinated alkyl iodide. While focusing on pefluoroalkyl compounds, the work has the potential to inspire future rational design of CN-based photocatalysts for other organic reactions, provided the CN catalyst is tailored with the suitable structural and electronic properties.

References

1.   G. Filippini, F. Longobardo, L. Forster, A. Criado, G. Di Carmine, L. Nasi, C. D'Agostino, M. Melchionna, P. Fornasiero and M. Prato, *Sci. Adv.*, 2020, **6**, eabc9923.

2.   S. Cao, J. Low, J. Yu and M. Jaroniec, *Adv. Mater.*, 2015, **27**, 2150-2176.

3.   J. Liu, H. Wang and M. Antonietti, *Chem. Soc. Rev.*, 2016, **45**, 2308-2326.

4.   J. Zhang, Y. Chen and X. Wang, *Energy. Environ. Sci.*, 2015, **8**, 3092-3108.

5.   Y. Wang, X. Wang and M. Antonietti, *Angew. Chem. Int. Ed.*, 2012, **51**, 68-89.

6.   Y. Zhang, A. Thomas, M. Antonietti and X. Wang, *J. Am. Chem. Soc.*, 2009, **131**, 50-51.

7.   G. Liu, P. Niu, C. Sun, S. C. Smith, Z. Chen, G. Lu and H. Cheng, 2010, *J. Am. Chem. Soc.*, **132**, 11642-11648.

8.   Y. Wang, Y. Di, M. Antonietti, H. R. Li, X. Chen and X. C. Wang, *Chem. Mater.*, 2010, **22**, 5119-5121.

9.   H. Pan, Y. Zhang, V. B. Shenoy and H. Gao, *ACS Catal.*, 2011, **1**, 99-104.

10.   X. Wang, X. Chen, A. Thomas, X. Fu and M. Antonietti, *Adv. Mater.*, 2009, **21**, 1609-1612.

11.   X. Ye, Y. Cui, X. Qiu and X. Wang, *Appl. Catal. B*, 2014, **152-153**, 383-389.

12.   X. Chen, J. Zhang, X. Fu, M. Antonietti and X. Wang, *J. Am. Chem. Soc.*, 2009, **131**, 11658-11659.

13.   L. Möhlmann, M. Baar, J. Riess, M. Antonietti, X. Wang and S. Blechert, *Adv. Synth. Catal.*, 2012, **354**, 1909-1913.

14.   C. Cavedon, A. Madani, P. H. Seeberger and B. Pieber, *Org. Lett.*, 2019, **21**, 5331-5334.

15.   B. Pieber, J. A. Malik, C. Cavedon, S. Gisbertz, A. Savateev, D. Cruz, T. Heil, G. Zhang and P. H. Seeberger, *Angew. Chem. Int. Ed.*, 2019, **58**, 9575-9580.

16.   B. Pieber, M. Shalom, M. Antonietti, P. H. Seeberger and K. Gilmore, *Angew. Chem. Int. Ed.¸* 2018, **57**, 9976-9979.

17.   I. Ghosh, J. Khamrai, A. Savateev, N. Shlapakov, M. Antionetti and B. König, *Science*, 2019, **365**, 360-366.

18.   K. Müller, C. Faeh and F. Diederich, *Science*, 2007, **317**, 1881-1886.

19.   Y. Zhou, J. Wang, Z. Gu, S. Wang, W. Zhu, J. Aceña, V. A. Soloshonok, K. Izawa and H. Liu, *Chem. Rev.*, 2016, **116**, 422-518.

20.   R. Berger, G. Resnati, P. Metrangolo, E. Weber and J. Hulliger, *Chem. Soc. Rev.*, 2011, **40**, 3496-3508.

21.   C.-J. Wallentin, J. D. Nguyen, P. Finkbeiner and C. R. J. Stephenson, *J. Am. Chem. Soc.*, 2012, **134**, 8875-8884.

22.   S. Barata-Vallejo, M. V. Cooke and A. Postigo, *ACS Catal.*, 2018, **8**, 7287-7307.

23.   D. A. Nagib and D. W. C. MacMillan, *Nature¸* 2011, **480**, 224-228.

24.   G. Magagnano, A. Gualandi, M. Marchini, L. Mengozzi, P. Ceroni and P. F. Cozzi, *Chem. Commun.*, 2017, **53**, 1591-1594.

25.   E. Arceo, E. Montroni and P. Melchiorre, *Angew. Chem. Int. Ed.¸* 2014, **53**, 12064-12068.

26.   T. Yajima and M. Ikegami, *Eur. J. Org. Chem.*, 2017, **2017**, 2126-2129.

27.   W. R. Dolbier, *Chem. Rev.*, 1996, **96**, 1557-1584.

28.   E. Fukushima and S. W. Roeder, *Experimental pulse NMR: A Nuts and Bolts Approach¸* Addison-Wesley, Boston, U.S.A., 1981.

29.   P. Niu, L. Yin, Y. Yang, G. Liu and H. Cheng, *Adv. Mater.*, 2014, **26**, 8046-8052.

30.   M. Melchionna and M. Prato, *ECS J. Solid State Sci. Technol.¸* 2013, **2**, M3040-M3045.

31.   Z. Lu, G. Chen, S. Siahrostami, Z. Chen, K. Liu, J. Xie, L. Liao, T. Wu, D. Lin, Y. Liu, T. F. Jamarillo, J. K. Nørskov and Y. Cui, *Nat. Catal.*, 2018, **1**, 156-162.

32.   M. Melchionna, P. Fornasiero and M. Prato, *Adv. Mater.*, 2019, **31** 1802920.

33.   Y. Kang, Y. Yang, L. Yin, X. Kang, G. Liu and H. Cheng, *Adv. Mater.*, 2015, **27 (31)**, 4572-4577.

34.   T. Sano, S. Tsutsui, K. Koike, T. Hirakawa, Y. Teramoto, N. Negishi and K. Takeuchi, *J. Mater. Chem. A*, 2013, **1 (21)**, 6489-6496.

35.   F. Fina, S. K. Callear, G. M. Carins and J. T. S. Irvine, *Chem. Mater.*, 2015, **27**, 2612-2618.

36.   P. F. McMillan, V. Lees, E. Quirico, G. Montagnac, A. Sella, B. Reynard, P. Simon, E. Bailey, M. Deifallah and F. Corà, *J. Solid State Chem.*, 2009, **182**, 2670-2677.

37.   P. V. Zinin, L. Ming, S. K. Sharma, V. N. Khabeshesku, X. Liu, S. Hong, S. Endo and T. Acosta, *Chem. Phys. Lett.*, 2009, **472 (1-3)**, 69-73.

38.   B. Jürgens, E. Irran, J. Senker, P. Kroll, H. Müller and W. Schnick, *J. Am. Chem. Soc.*, 2003, **125 (34)**, 10288-10300.

39.   J. Fang, H. Fan, M. Li and C. Long, *J. Mater. Chem. A*, 2015, **3**, 13819-13826.

40.   L. Wang, A. Ambrosi and M. Pumera, *Angew. Chem. Int, Ed.*, 2013, **52**, 13818-13821.

41. Y. Liao, S. Zhu, Z. Chen, X. Lou and D. Zhang, *Phys. Chem. Chem. Phys.*, 2015, **17**, 27826-27832.

42. H. Yan, Y. Chen and S. Xu, *Int. J. Hydrog. Energy*, 2012, **37**, 125-133.

43. K. Schwinghammer, B. Tuffy, M. B. Mesch, E. Wirnhier, C. Martineau, F. Taulelle, W. Schnick, J. Senker and B. V. Lotsch, *Angew. Chem. Int. Ed.*, 2013, **52**, 2435-2439.

44. A. Savateev, I. Ghosh, B. König and M. Antonietti, *Angew. Chem. Int. Ed.*, 2018, **57**, 15936-15947.

45. H. Yan, *Chem. Commun.*, 2012, **48**, 3430-3432.

46. M. Melchionna and P. Fornasiero, *ACS Catal.*, 2020, **10**, 5493-5501.

47. C. Rosso, G. Filippini and M. Prato, *Chem. Eur. J.*, 2019, **25**, 16032-16036.

48. L. Buzzetti, G. E. M. Crisenza and P. Melchiorre, *Angew. Chem. Int. Ed.*, 2019, **58**, 3730-3747.

49. C. D'Agostino, J. Mitchell, M. D. Mantle and L. F. Gladden, *Chem. Eur. J.*, 2014, **20**, 13009-13015.

50. N. Robinson, C. Robertson, L. F. Gladden, S. J. Jenkins and C. D'Agostino, *ChemPhysChem*, 2018, **19**, 2472-2479.

51. N. Robinson, L. F. Gladden, C. D'Agostino, *Faraday Discuss.*, 2017, **204**, 439-452.

52. P. Politzer, P. Lane, M. C. Concha, Y. Ma and J. S. Murray, *J. Mod. Model.*, 2007, **13**, 305-311.

53. C. D'Agostino, M. R. Feaviour, G. L. Brett, J. Mitchell, A. P. E. York, G. J. Hutchings, M. D. Mantle and L. F. Gladden, *Catal, Sci. Technol.*, 2016, **6**, 7896-7901.

54. W. R. Bowman and J. M. D. Storey, *Chem. Soc. Rev.*, 2007, **36**, 1803-1822.

## Supporting information

Synthesis of alkenes 1g, 1h, 1j and 1m

(Hex-5-en-1-ylsulfonyl)benzene (1g).
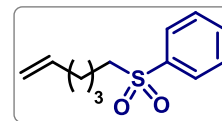
Prepared according to the literature procedure. [1] In a two neck round-bottomed flask, purged under argon, a mixture of 6-bromo-1-hexene **1k** (260 µL, 2 mmol, 1 equiv.), sodium benzenesulfinate (391 mg, 2.4 mmol, 1.2 equiv.) tetrabutylammonium iodide (74 mg, 0.2 mmol, 0.1 equiv.) in dry DMF (2 mL) was heated up to 60°C and stirred over 5 hours. The reaction was quenched by the addition of brine (5 mL) and then extracted with ethyl acetate (3 x 5 mL). The organic phases were combined and washed with brine (5 mL) and then dried over sodium sulfate. The solvent was removed under reduced pressure and the residue was purified by flash column chromatography (*n*-hexane/ethyl acetate 9:1) to give the corresponding alkene **1g** as a colorless oil (372 mg, 83% yield). The characterization of the compound matches with the data reported in the literature.(*54*) ^{1}H-NMR (400 MHz, CDCl$_3$) δ 7.99 – 7.85 (m, 2H), 7.73 – 7.61 (m, 1H), 7.62 – 7.53 (m, 2H), 5.82 – 5.60 (m, 1H), 5.04 – 4.89 (m, 2H), 3.17 – 3.01 (m, 2H), 2.10 – 1.96 (m, 2H), 1.81 – 1.66 (m, 2H), 1.55 – 1.36 (m, 2H); HRMS calculated for C$_{12}$H$_{16}$O$_2$S (M-Na): 247.0769, found: 247.0766.

2-(hex-5-en-1-yl)isoindoline-1,3-dione (1h).
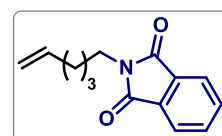

Prepared according to the literature procedure. [1] In a two neck round-bottomed flask, purged under argon, a mixture of 6-chloro-1-hexene **1l** (400 µL, 3 mmol, 1 equiv.), potassium phthalimide (610 mg, 3.3 mmol, 1.1 equiv.) and potassium iodide (50 mg, 0.3 mmol, 0.1 equiv.) in dry DMF (5 mL) was heated up to 90°C and stirred overnight. The reaction was quenched by the addition of water (10 mL) and then extracted with dichloromethane (3 x 10 mL). The organic phases were combined and washed with KOH 0.2 M (10 mL), brine (10 mL) and then dried over sodium sulfate. The solvent was removed under reduced pressure and the residue was purified by flash column chromatography (n-hexane/ethyl

acetate 9:1) to give the corresponding alkene **1h** as a pale yellow oil (506 mg, 74% yield). The characterization of the compound matches with the data reported in the literature.(*54*) ^{1}H-NMR (400 MHz, CDCl$_3$) δ 7.84 (dd, *J* = 5.5, 3.0 Hz, 2H), 7.70 (dd, *J* = 5.4, 3.1 Hz, 2H), 5.78 (ddt, *J* = 16.9, 10.2, 6.7 Hz, 1H), 5.04 – 4.91 (m, 2H), 3.69 (t, *J* = 7.3 Hz, 2H), 2.10 (dd, *J* = 14.3, 7.2 Hz, 2H), 1.75 – 1.65 (m, 2H), 1.44 (dt, *J* = 15.2, 7.5 Hz, 2H); HRMS calculated for C$_{14}$H$_{15}$NO$_2$ (M-Na): 252.1000, found: 252.0992.

Hex-5-en-1-yl acetate (1j).
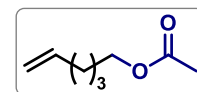
Prepared according to the literature procedure. [1] In a two neck round-bottomed

flask, purged under argon, a solution of 5-hexen-1-ol **1i** (420 μL, 3.5 mmol, 1 equiv.) and 2,6-lutidine (408 μL, 3.5 mmol, 1 equiv.) in dry THF (10 mL) was stirred at 0°C for 10 minutes. Acetyl bromide (260 μL, 3.5 mmol, 1 equiv.) was added dropwise and the solution was stirred at room temperature over 3 hours. The reaction was quenched by the addition of water (10 mL) and then extracted with diethyl ether (3 x 10 mL). The organic phases were combined and washed with brine (10 mL) and then dried over sodium sulfate. The solvent was removed under reduced pressure to give the corresponding alkene **1j** as a pale yellow oil (141 mg, 28% yield). The characterization of the compound matches with the data reported in the literature.(*54*) ^{1}H-NMR (400 MHz, CDCl$_3$) δ 5.80 (ddt, *J* = 16.9, 10.2, 6.7 Hz, 1H), 5.08 – 4.87 (m, 2H), 4.06 (t, *J* = 6.7 Hz, 2H), 2.19 – 1.99 (m, 5H), 1.73 – 1.56 (m, 2H), 1.54 – 1.37 (m, 2H); HRMS calculated for C$_8$H$_{14}$O$_2$ (M-Na): 165.0892, found: 165.0885.

1-(hex-5-en-1-yloxy)octane (1m).
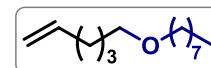
Prepared according to the literature procedure. [1] In a two neck round-

bottomed flask, purged under argon, a solution of 5-hexen-1-ol **1i** (420 μL, 3.5 mmol, 1 equiv.) and 1-bromooctane (610 μL, 3.5 mmol, 1 equiv.) in dry THF (14 mL) was stirred at 0°C for 10 minutes. Sodium hydride (170 mg, 4.2 mmol, 1.2 equiv.) was added portionwise and the solution was heated up to reflux and stirred overnight. The reaction was quenched by the

addition of ammonium chloride (10 mL) and then extracted with ethyl acetate (3 x 10 mL).

The organic phases were combined and washed with brine (10 mL) and then dried over sodium

sulfate. The solvent was removed under reduced pressure and the residue was purified by flash

column chromatography (*n*-hexane/ethyl acetate 95:5) to give the corresponding alkene **1m** as

a pale yellow oil (494 mg, 67% yield). The characterization of the compound matches with the

data reported in the literature.(*54*) ^{1}H-NMR (400 MHz, CDCl$_3$) δ 5.79 (ddt, *J* = 16.9, 10.2, 6.7

Hz, 1H), 5.06–4.89 (m, 2H), 3.38 (td, *J* = 6.6, 4.9 Hz, 4H), 2.12–2.01 (m, 2H), 1.56 (dp, *J* =

9.6, 6.8 Hz, 4H), 1.49–1.38 (m, 2H), 1.38–1.22 (m, 10H); HRMS calculated for $C_{14}H_{28}O$ (M-

Na): 235.2038, found: 235.2032.

General procedures for the photocatalytic fluoroalkylation of organic compounds and characterization data
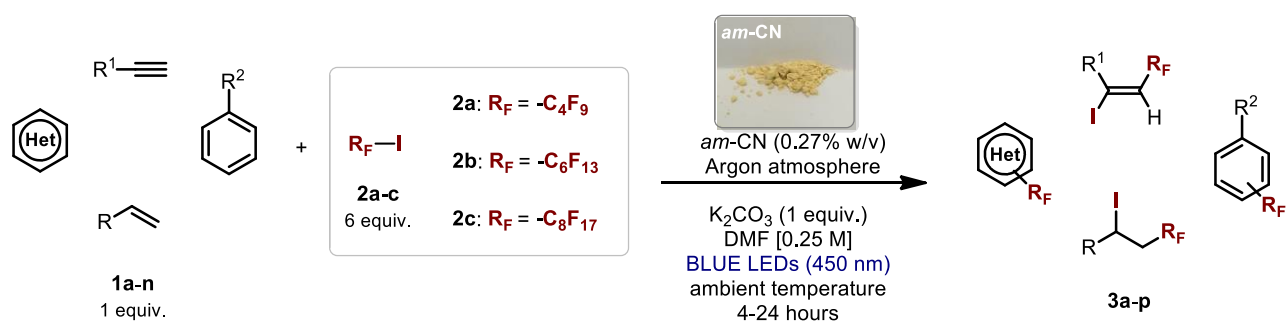
Scheme S7.1. General scheme for the fluoroalkylation of organic compounds. Photo credit: Francesco Longobardo, University of Trieste (Italy)

A 10 mL Schlenk tube was charged with the appropriate electron-rich organic compound **1** (0.1

mmol, 1 equiv.), perfluoroalkyl iodide **2** (0.6 mmol, 6 equiv.), potassium carbonate (0.1 mmol,

1 equiv.) and *am*-CN (0.27 w/v, 1.4 mg). To this suspension was then added *N,N*-

dimethylformamide (0.4 mL, [**1**]$_0$ = 0.25 M). The reaction mixture was thoroughly degassed

via freeze-pump-thaw cycles (x 3) and the schlenk tube was filled with argon and placed in the

centre of 8 blue LEDs system at 450 nm (3.5 V and 700 mA controlled by an external power

supply). The LEDs were produced and purchased by AddicoreTM (for more details, see: https://www.addicore.com/3W-Royal-Blue-LED-on-Star-Board-Heatsink-p/ad425.htm).

Stirring (400 rpm) was maintained for 24 hours (4 hours for compounds **3g-p**) and then the irradiation was stopped. The reaction crude was diluted with a 5% lithium chloride solution and extracted with ethyl acetate (three times). The organic phase was filtered through sodium sulfate. The solvent was removed under reduced pressure and the residue was purified by column chromatography (eluent: *n*-hexane/ethyl acetate) to give the corresponding fluoroalkyl compound **3**.

Calculation of yields

The production yields listed in Table 7.1 and referred to product 3a were determined by ^{1}H-NMR spectroscopy in CDCl$_3$ using 1,1,2-trichloroethylene (0.10 mmol, 9 μL) as the internal standard (I.S.). The following formula has been used:

$$Production\ Yield(\%) = \frac{Integration\ of\ the\ NMR\ signal\ of\ 3a\ [\delta\ 6.2\ ppm\ (s, 2H)]\ x\ 50}{Integration\ of\ the\ NMR\ signal\ of\ the\ I.\,S.\ [\delta\ 6.5\ ppm\ (s, 1H)]}$$

The isolated yields of products 3a-3p listed in Scheme 7.1 have been calculated using the following formula:

$$Isolated\ Yield(\%) = \frac{Actual\ Yield\ x\ 100}{Theretical\ Yield}$$

For the calculation of the Apparent Quantum yield (AQY) the following equation was used:

$$AQY = \frac{number\ of\ moles\ of\ product\ formed}{number\ of\ moles\ of\ incident\ photons}$$

The moles of product and emitted photons were calculated after 5 hours of a photocatalytic experiment under typical conditions.

Characterization data of the reaction products

**1,3,5-trimethoxy-2-(perfluorobutyl)benzene (3a)**.
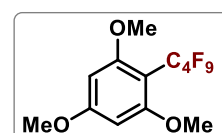
Prepared according to the general procedure using 1,3,5-trimethoxybenzene **1a** (0.1 mmol, 17 mg) and nonafluoro-1-iodobutane **2a** (0.6 mmol, 103 μL). The product **3a** was obtained as white solid (37 mg, 96% yield). The characterization of the compound matches

with the data reported in the literature. [2] ^{1}H-NMR (400 MHz, CDCl$_3$) δ 6.15 (s, 2H), 3.84 (s, 3H), 3.80 (s, 6H); ^{19}F-NMR (376 MHz, CDCl$_3$) δ -80.97 (m, 3F), -102.86 (m, 2F), -123.00 (m, 2F), -126.44 (m, 2F); HRMS calculated for C$_{13}$H$_{11}$F$_9$O$_3$ (M-Na): 409.0462, found: 409.0463.

1,3,5-trimethoxy-2-(perfluorohexyl)benzene (3b).
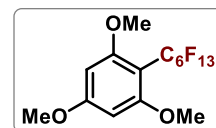
Prepared according to the general procedure using 1,3,5-trimethoxybenzene **1a** (0.1 mmol, 17 mg) and perfluorohexyl iodide **2b** (0.6 mmol, 130 μL). The product **3a** was obtained as white solid (45 mg, 92% yield). The characterization of the compound matches with the data reported in the literature. [3] ^{1}H-NMR (400 MHz, CDCl$_3$) δ 6.13 (s, 2H), 3.85 (s, 3H), 3.81 (s, 6H); ^{19}F-NMR (376 MHz, CDCl$_3$) δ -80.83 (m, 3F), -102.67 (m, 2F), -122.14 (m, 4F), -122.69 (m, 2F), -126.17 (m, 2F); HRMS calculated for C$_{15}$H$_{11}$F$_{13}$O$_3$ (M-Na): 509.0398, found: 509.0390.

1,3,5-trimethoxy-2-(perfluorooctyl)benzene (3c).
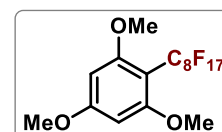
Prepared according to the general procedure using 1,3,5-trimethoxybenzene **1a** (0.1 mmol, 17 mg) and heptadecafluoro-1-iodooctane **2c** (0.6 mmol, 158 μL). The product **3c** was obtained as white solid (52 mg, 90% yield). The characterization of the compound matches with the data reported in the literature. [3] ^{1}H-NMR (400 MHz, CDCl$_3$) δ 6.15 (s, 2H), 3.84 (s, 3H), 3.80 (s, 6H); ^{19}F-NMR (376 MHz, CDCl$_3$) δ -80.84 (t, J = 10.0 Hz, 3F), -102.66 (m, 2F), -121.75 (m, 2F), -122.05 (m, 6F), -122.79 (m, 2F), -126.15 (m, 2F); HRMS calculated for C$_{17}$H$_{11}$F$_{17}$O$_3$ (M-Na): 609.0334, found: 609.0335.

2,6-diisopropyl-4-(perfluorohexyl)aniline (3d).
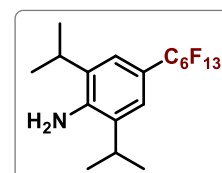
Prepared according to the general procedure using 2,6-diisopropylaniline **1b** (0.1 mmol, 19 μL) and perfluorohexyl iodide **2b** (0.6 mmol, 130 μL). The product **3d** was obtained as white solid (42 mg, 86% yield). The characterization of the compound matches with the data reported in the literature. [4] ^{1}H NMR (400 MHz, CDCl$_3$) δ

7.19 (s, 2H), 4.05 (s, 2H), 2.91 (hept, J = 6.8 Hz, 2H), 1.29 (d, J = 6.8 Hz, 12H) ; ^{19}F NMR (376 MHz, CDCl$_3$) δ -80.85 (m, 3F), -109.41 (m, 2F), -121.57 (m, 2F), -121.89 (m, 2F), -122.85 (m, 2F), -126.17 (m, 2F) ; HRMS calculated for C$_{18}$H$_{18}$F$_{13}$N (M-H): 496.1309, found: 496.1306.
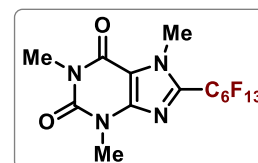
Methyl 5-acetyl-2-hydroxy-3-(perfluorohexyl)benzoate (3e).
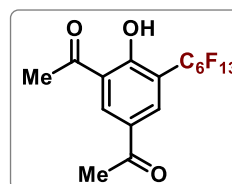
Prepared according to the general procedure using methyl 5-acetylsalicylate **1c** (0.1 mmol, 19 mg) and perfluorohexyl iodide **2b** (0.6 mmol, 130 μL). The product **3e** was obtained as white solid (23 mg, 45% yield). The characterization of the compound matches with the data reported in the literature. [5] ^{1}H NMR (400 MHz, CDCl$_3$) δ 8.68 (s, 1H), 8.31 (s, 1H), 4.04 (s, 3H), 2.61 (s, 3H); ^{19}F NMR (376 MHz, CDCl$_3$) δ -80.95 (t, J = 10.0 Hz, 3F), -108.97 (t, J = 14.3 Hz, 2F), -121.18 (m, 2F), -121.90 (m, 2F), -122.85 (m, 2F), -126.22 (m, 2F); HRMS calculated for C$_{16}$H$_8$F$_{13}$O$_4$ (M-H): 511.0220, found: 511.0218.

1,3,7-trimethyl-8-(perfluorohexyl)-3,7-dihydro-1H-purine-2,6-dione (3f).

Prepared according to the general procedure using caffeine **1d** (0.1 mmol, 19 mg) and perfluorohexyl iodide **2b** (0.6 mmol, 130 μL) over 48 hours of irradiation. The product **3f** was obtained as white solid (14 mg, 40% yield). The characterization of the compound matches with the data reported in the literature. [6] ^{1}H NMR (400 MHz, CDCl$_3$) δ 4.19 (s, 3H), 3.60 (s, 3H), 3.42 (s, 3H); ^{19}F NMR (376 MHz, CDCl$_3$) δ -80.74 (m, 3F), -108.96 (m, 2F), -121.01 (m, 2F), -121.39 (m, 2F), -122.71 (m, 2F), -126.06 (m, 2F); HRMS calculated for C$_{14}$H$_{11}$F$_{13}$N$_4$O$_2$ (M-K): 553.0311, found: 553.0526.

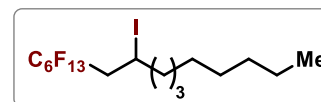**1,1,1,2,2,3,3,4,4,5,5,6,6-tridecafluoro-8-iodododecane (3g)**.
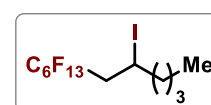
Prepared according to the general procedure using 1-hexene **1e** (0.1 mmol, 13 μL) and perfluorohexyl iodide **2b** (0.6 mmol, 130 μL). The product **3g** was obtained as

colorless oil (48 mg, 91% yield). The characterization of the compound matches with the data reported in the literature.(*54*) ^{1}H NMR (400 MHz, CDCl$_3$) δ 4.43 – 4.26 (m, 1H), 3.04 – 2.66 (m, 2H), 1.94 – 1.72 (m, 2H), 1.58 – 1.22 (m, 4H), 0.93 (t, *J* = 7.2 Hz, 3H); ^{19}F NMR (376 MHz, CDCl$_3$) δ -80.86 (m, 3F), -111.92 (m, 1F), -114.69 (m, 1F), -121.84 (m, 2F), -122.91 (m, 2F), -123.69 (m, 2F), -126.19 (m, 2F) ; It was not possible to measure the HRMS (ESI-MS) of compound **3g** due to its poor tendency to ionize.

1,1,1,2,2,3,3,4,4,5,5,6,6-tridecafluoro-8-iodohexadecane **(3h)**.

Prepared according to the general procedure using 1-decen **1f** (0.1 mmol, 19 µL) and perfluorohexyl iodide **2b** (0.6 mmol, 130 µL). The product **3h** was obtained as colorless oil (54 mg, 83% yield). The characterization of the compound matches with the data reported in the literature.(*54*) ^{1}H-NMR (400 MHz, CDCl$_3$) δ 4.40 – 4.27 (m, 1H), 3.06 – 2.63 (m, 2H), 1.90 – 1.69 (m, 2H), 1.43 – 1.18 (m, 12H), 0.89 (t, *J* = 6.9 Hz, 3H); ^{19}F NMR (376 MHz, CDCl$_3$) δ -80.85 (m, 3F), -111.80 (m, 1F), -114.70 (m, 1F), -121.82 (m, 2F), -122.90 (m, 2F), -123.71 (m, 2F), -126.18 (m, 2F) ; It was not possible to measure the HRMS (ESI-MS) of compound **3h** due to its poor tendency to ionize.

((7,7,8,8,9,9,10,10,11,11,12,12,12-tridecafluoro-5-iodododecyl)sulfonyl)benzene (3i).
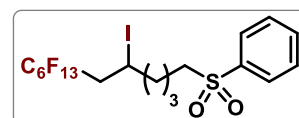
Prepared according to the general procedure using (hex-5-en-1-ylsulfonyl)benzene **1g** (0.1 mmol, 22 mg) and perfluorohexyl iodide **2b** (0.6 mmol, 130 µL). The product **3i** was obtained as colorless oil (57 mg, 84% yield). The characterization of the compound matches with the data reported in the literature.(*54*) ^{1}H-NMR (400 MHz, CDCl$_3$) δ 7.95–7.88 (m, 2H), 7.71–7.64 (m, 1H), 7.58 (t, *J* = 7.6 Hz, 2H), 4.26 (ddd, *J* = 13.3, 8.5, 5.2 Hz, 1H), 3.15–3.08 (m, 2H), 2.99–2.62 (m, 2H), 1.87–1.70 (m, 4H), 1.71–1.60 (m, 1H), 1.56–1.45 (m, 1H); ^{19}F-NMR (376 MHz, CDCl$_3$) δ -80.80 (m, 3F), -111.52 (m, 1F), -114.69 (m, 1F), -121.80 (m, 2F), -122.85 (m,

2F), -123.61 (m, 2F), -126.09 (m, 2F); HRMS calculated for $C_{18}H_{16}F_{13}IO_2S$ (M-Na): 692.9606, found: 692.9600.

2-(7,7,8,8,9,9,10,10,11,11,12,12,12-tridecafluoro-5-iododdecyl)isoindoline-1,3-dione (3j).
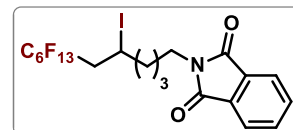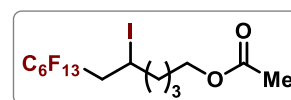
Prepared according to the general procedure using 2-(hex-5-en-1-yl)isoindoline-1,3-dione **1h** (0.1 mmol, 23 mg) and perfluorohexyl iodide **2b** (0.6 mmol, 130 μL). The product **3j** was obtained as colorless oil (60 mg, 88% yield). The characterization of the compound matches with the data reported in the literature.(*54*) ^{1}H-NMR (400 MHz, CDCl$_3$) δ 7.84 (dd, *J* = 5.5, 3.0 Hz, 2H), 7.71 (dd, *J* = 5.4, 3.1 Hz, 2H), 4.30 (ddd, *J* = 16.8, 8.3, 5.3 Hz, 1H), 3.71 (t, *J* = 7.2 Hz, 2H), 3.00–2.68 (m, 2H), 1.95–1.39 (m, 6H); ^{19}F-NMR (376 MHz, CDCl$_3$) δ -80.87 (tt, *J* = 10.0, 2.2 Hz, 3F), -111.77 (m, 1F), -114.63 (m, 1F), -121.83 (m, 2F), -122.93 (m, 2F), -123.69 (m, 2F), -126.20 (m, 2F); HRMS calculated for $C_{20}H_{15}F_{13}INO_2$ (M-Na): 697.9837, found: 697.9832.

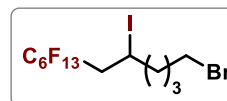## 7,7,8,8,9,9,10,10,11,11,12,12,12-tridecafluoro-5-iododdecan-1-ol (3k).
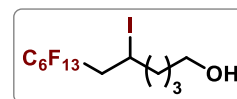
Prepared according to the general procedure using 5-hexen-1-ol **1i** (0.1 mmol, 12 μL) and perfluorohexyl iodide **2b** (0.6 mmol, 130 μL). The product **3k** was obtained as colorless oil (52 mg, 94% yield). The characterization of the compound matches with the data reported in the literature.(*54*) ^{1}H-NMR (400 MHz, CDCl$_3$) δ 4.34 (ddd, *J* = 13.4, 8.4, 5.3 Hz, 1H), 3.68 (t, *J* = 6.1 Hz, 2H), 3.03 – 2.68 (m, 2H), 1.93 – 1.75 (m, 2H), 1.71 – 1.44 (m, 4H); 19F-NMR (376 MHz, CDCl3) δ -80.83 (m, 3F), -111.76 (m, 1F), -114.67 (m, 1F), -121.80 (m, 2F), -122.86 (m, 2F), -123.65 (m, 2F), -125.57 – -126.96 (m, 2F); ; HRMS calculated for $C_{12}H_{12}F_{13}IO$ (M-Na): 568.9623, found: 568.9612.

7,7,8,8,9,9,10,10,11,11,12,12,12-tridecafluoro-5-iododdecyl acetate (3l).

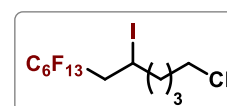Prepared according to the general procedure using hex-5-en-1-yl acetate **1j** (0.1 mmol, 14 mg) and perfluorohexyl iodide **2b** (0.6 mmol, 130 µL). The product **3l** was obtained as colorless oil (53 mg, 91% yield). The characterization of the compound matches with the data reported in the literature.(*54*) ^{1}H-NMR (400 MHz, CDCl$_3$) δ 4.32 (ddd, J = 13.4, 8.5, 5.1 Hz, 1H), 4.08 (t, J = 6.3 Hz, 2H), 3.02–2.68 (m, 2H), 2.05 (s, 3H), 1.91–1.43 (m, 6H); ^{19}F-NMR (376 MHz, CDCl$_3$) δ -80.85 (m, 3F), -111.63 (m, 1F), -114.68 (m, 1F), -121.83 (m, 2F), -122.89 (m, 2F), -123.66 (m, 2F), -126.17 (m, 2F); HRMS calculated for C$_{14}$H$_{14}$F$_{13}$IO$_2$ (M-Na): 610.9728, found: 610.9723.

12-bromo-1,1,1,2,2,3,3,4,4,5,5,6,6-tridecafluoro-8-iodododecane (3m).

Prepared according to the general procedure using 6-bromo-1-hexene **1k** (0.1 mmol, 14 µL) and perfluorohexyl iodide **2b** (0.6 mmol, 130 µL). The product **3m** was obtained as colorless oil (58 mg, 95% yield). The characterization of the compound matches with the data reported in the literature.(*54*) ^{1}H-NMR (400 MHz, CDCl$_3$) δ 4.40–4.25 (m, 1H), 3.43 (t, J = 6.7 Hz, 1H), 3.27–3.15 (m, 1H), 3.05–2.67 (m, 2H), 2.05–1.59 (m, 6H); ^{19}F-NMR (376 MHz, CDCl$_3$) δ -80.85 (m, 3F), -111.62 (m, 1F), -114.65 (m, 1F), -121.81 (s, 2F), -122.89 (m, 2F), -123.65 (m, 2F), -126.18 (m, 2F); It was not possible to measure the HRMS (ESI-MS) of compound **3m** due to its poor tendency to ionize.

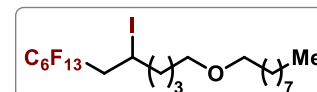**12-chloro-1,1,1,2,2,3,3,4,4,5,5,6,6-tridecafluoro-8-iodododecane** (**3n**).
Prepared according to the general procedure using 6-chloro-1-hexene **1l** (0.1 mmol, 13 µL) and perfluorohexyl iodide **2b** (0.6 mmol, 130 µL). The product **3n** was obtained as colorless oil (53 mg, 93% yield). The characterization of the compound matches with the data reported in the literature.(*54*) ^{1}H-NMR (400 MHz, CDCl$_3$) δ 4.33 (ddd, J = 13.5, 8.4, 5.2 Hz, 1H), 3.56 (t, J = 6.5 Hz, 2H), 3.05–2.65 (m, 2H), 1.92–1.52 (m, 6H); ^{19}F-NMR (376 MHz, CDCl$_3$) δ -80.85 (m, 3F), -111.68 (m, 1F), -114.67 (m, 1F), -121.84 (m, 2F), -122.92 (m, 2F),

-123.65 (m, 2F), -126.18 (m, 2F); It was not possible to measure the HRMS (ESI-MS) of compound **3n** due to its poor tendency to ionize.

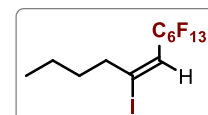**1,1,1,2,2,3,3,4,4,5,5,6,6-tridecafluoro-8-iodo-12-(octyloxy)dodecane (3o).**

Prepared according to the general procedure using 1-(hex-5-en-1-yloxy)octane **1m** (0.1 mmol, 21 mg) and perfluorohexyl iodide **2b** (0.6 mmol, 130 μL). The product **3o** was obtained as colorless oil (64 mg, 97% yield). The characterization of the compound matches with the data reported in the literature.(*54*) ^{1}H-NMR (400 MHz, CDCl$_3$) δ 4.45–4.24 (m, 1H), 3.51–3.34 (m, 4H), 3.04–2.68 (m, 2H), 1.95–1.74 (m, 2H), 1.71–1.44 (m, 6H), 1.40–1.20 (m, 10H), 0.88 (t, J = 6.9 Hz, 3H); ^{19}F-NMR (376 MHz, CDCl$_3$) δ -80.82 (tt, J = 9.9, 2.2 Hz, 3F), -111.82 (m, 1F), -114.61 (m, 1F), -121.81 (m, 2F), -122.88 (m, 2F), -123.66 (m, 2F), -126.17 (m, 2F); HRMS calculated for C$_{20}$H$_{28}$F$_{13}$IO (M-Na): 681.0875, found: 681.0870.

(*E*)-7,7,8,8,9,9,10,10,11,11,12,12,12-tridecafluoro-5-iodododec-5-ene (3p).

Prepared according to the general procedure using 1-hexyne **1n** (0.1 mmol, 12 μL) and perfluorohexyl iodide **2b** (0.6 mmol, 130 μL). The product **3p** was obtained as colorless oil (34 mg, 64% yield, 4:1 *E*/*Z*). The characterization of the compound matches with the data reported in the literature.(*54*) (*E*)-isomer: ^{1}H-NMR (400 MHz, CDCl$_3$) δ 6.35 (t, J = 14.4 Hz, 1H), 2.66 (t, J = 7.6 Hz, 2H), 1.59 (m, 2H), 1.38 (m, 2H), 0.97 (t, J = 7.3 Hz, 3H). The (*Z*)-isomer appears at 6.16 ppm; . (*E*)-isomer: ^{19}F-NMR (376 MHz, CDCl$_3$) δ -80.82 (t, J = 10.4 Hz, 3F), -105.46 (t, J = 13 Hz, 2F), -121.70 (m, 2F), -122.86 (m, 2F), -123.30 (m, 2F), -126.17 (m, 2F). The (*Z*)-isomer appears at – 108.50 ppm; It was not possible to measure the HRMS (ESI-MS) of compound **3p** due to its poor tendency to ionize.

Uv-vis spectra of starting materials

Photocatalyst, namely *am*-CN, is the only species that can absorb light at 450 nm. We did not

observe any ground-state association between **1a** and the radical source **2a**, because their combination does not lead to relevant change of the absorption spectra (Figure S7.10, black line overlays the red line).
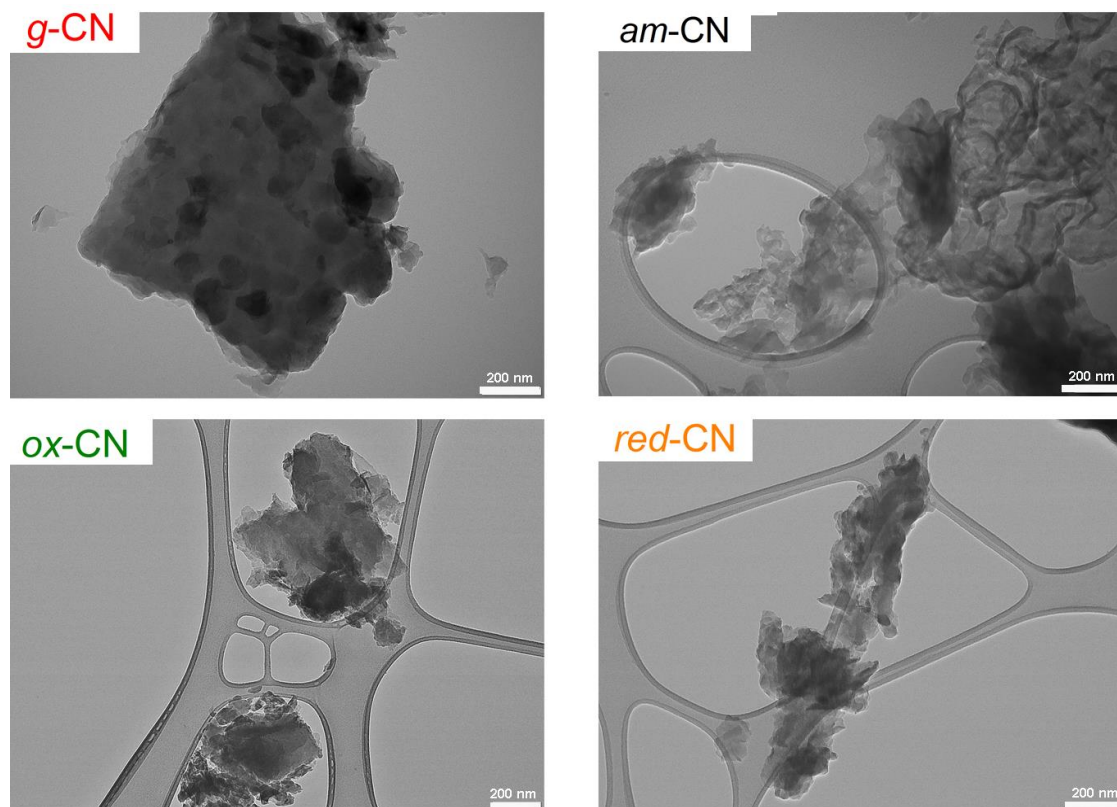
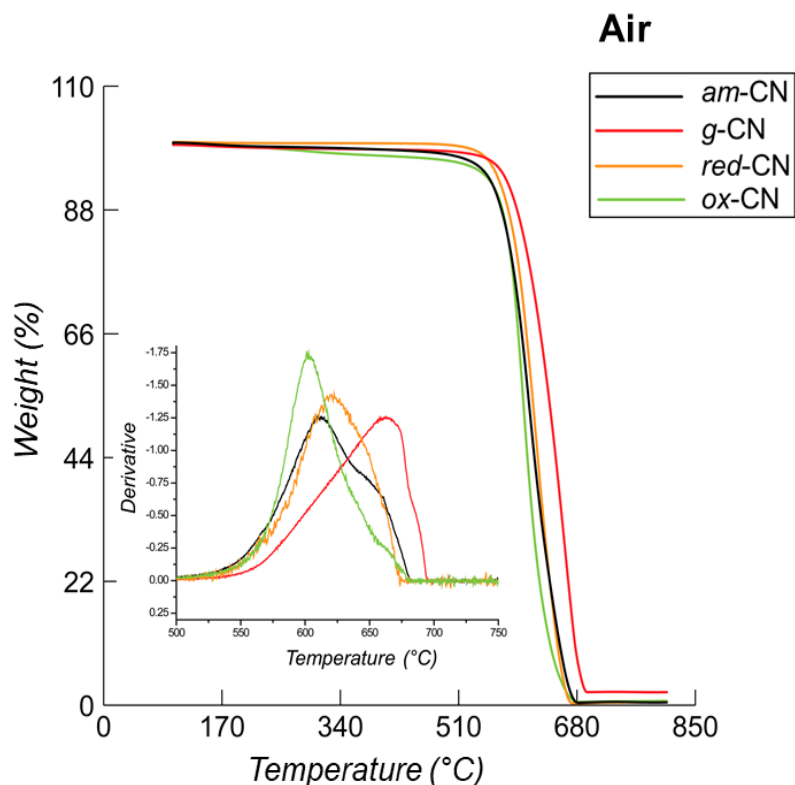**Figure S7.1:** Representative TEM images of the CN samples.

Figure S7.2: TGA analysis of the four materials under air. The combustion temperature onset of all the modified CN is reduced by ~50 °C as compared to the *g*-CN, as better observed in the figure inset, where the weight derivative is shown.
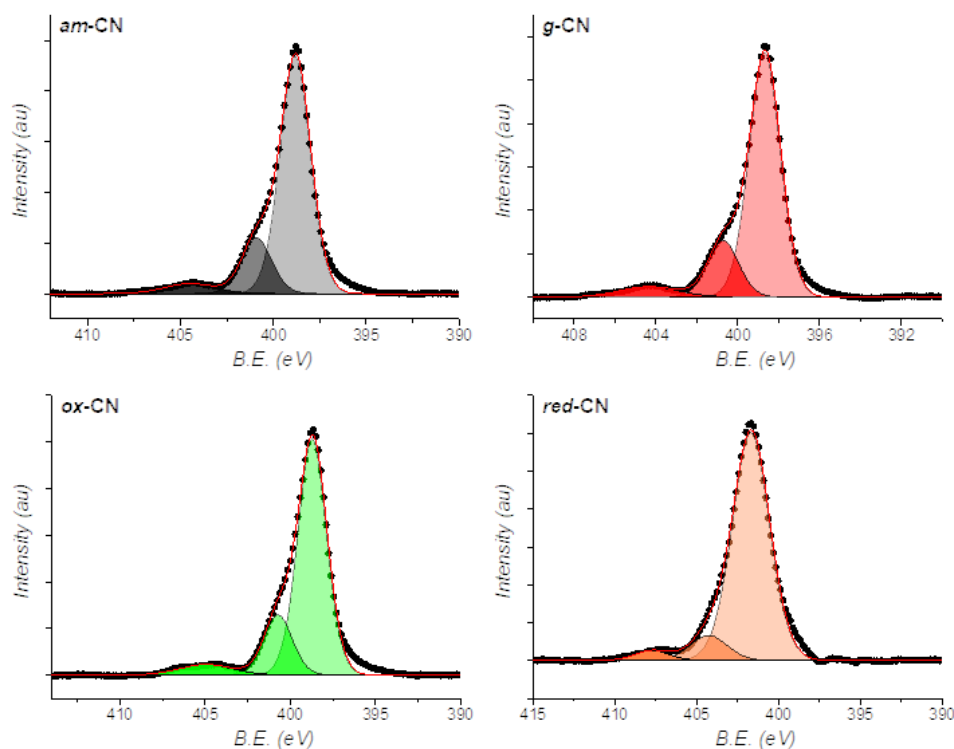

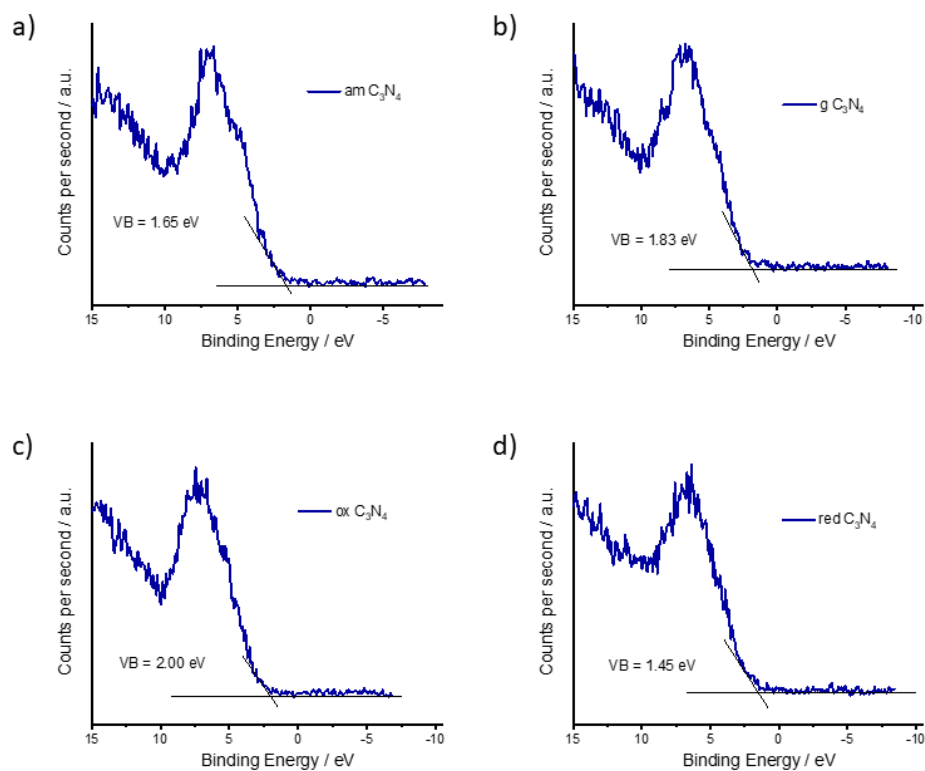**Figure S7.3.** XPS showing the deconvoluted N1s core level spectra.

Figure S7.4. XPS of the four samples in the low binding energy range. The VB is calculated from the intercept of the onset of the first peak with the baseline.
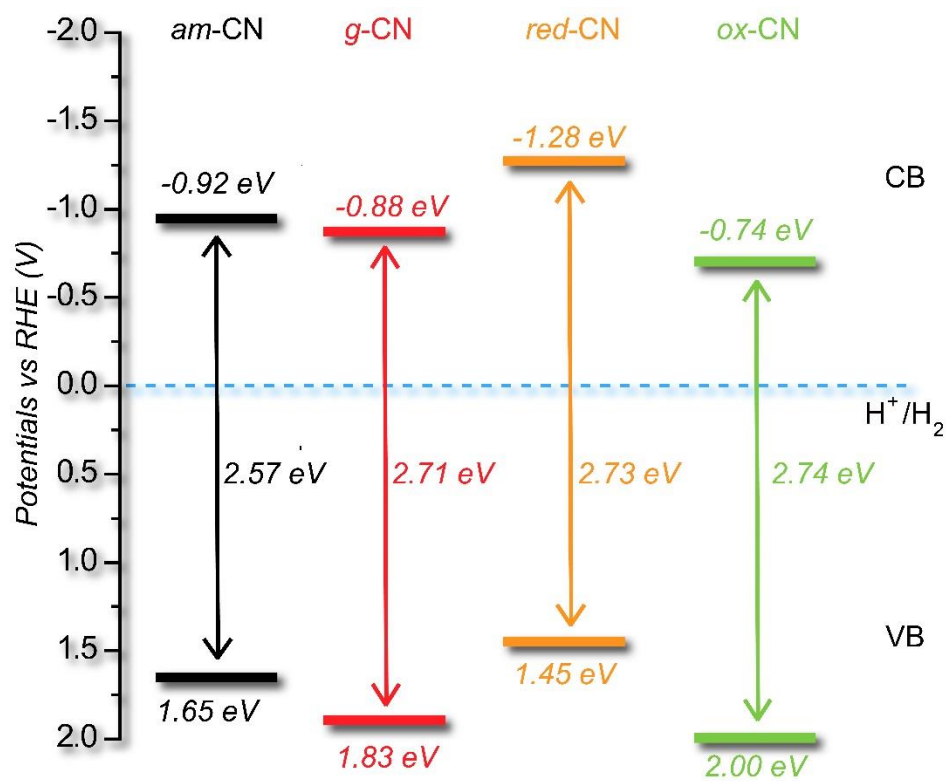
Figure S7.5. Schematic representation of the VB and CB positions for the four materials with energy values in eV. RHE stands for Reversible Hydrogen Electrode.
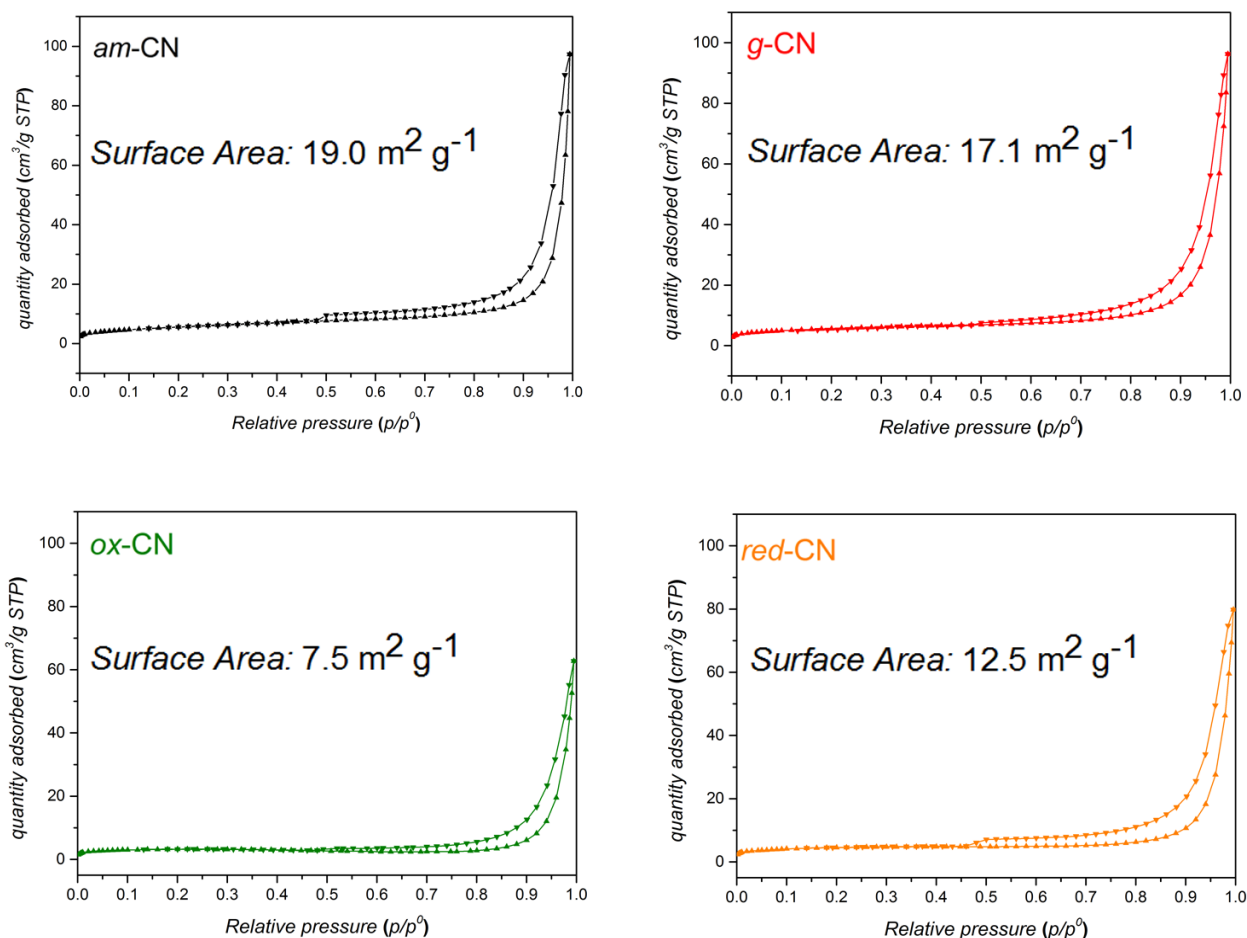
Figure S7.6. N_2 physisorption isotherms of the four materials, with report of their specific surface area.

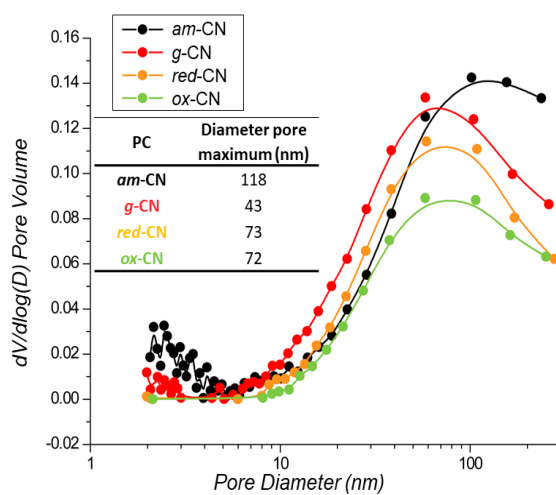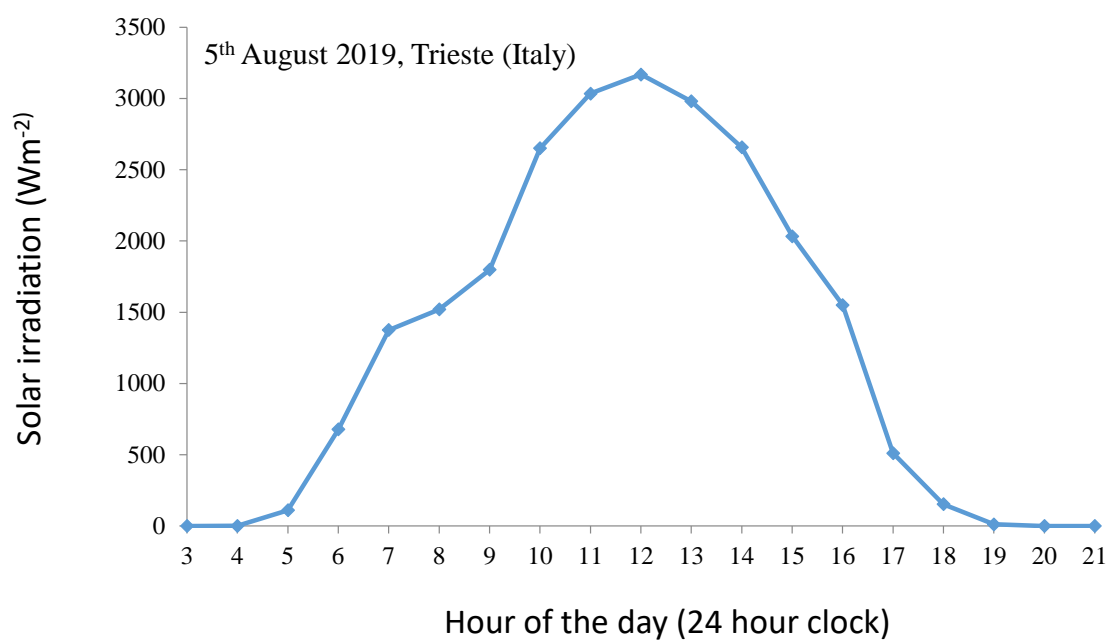**Figure S7.7.** Pore size distribution (inset reporting the maximum of the curve).

Figure S7.8. Outdoor experiment: solar irradiation over time the 5th of August 2019, in Trieste.
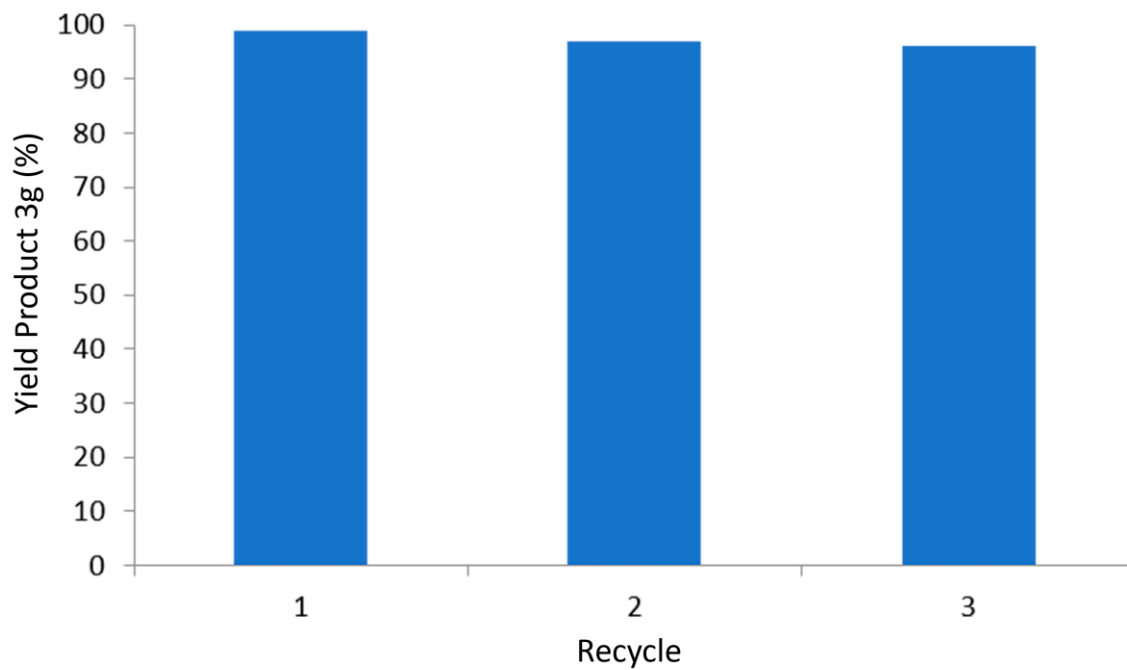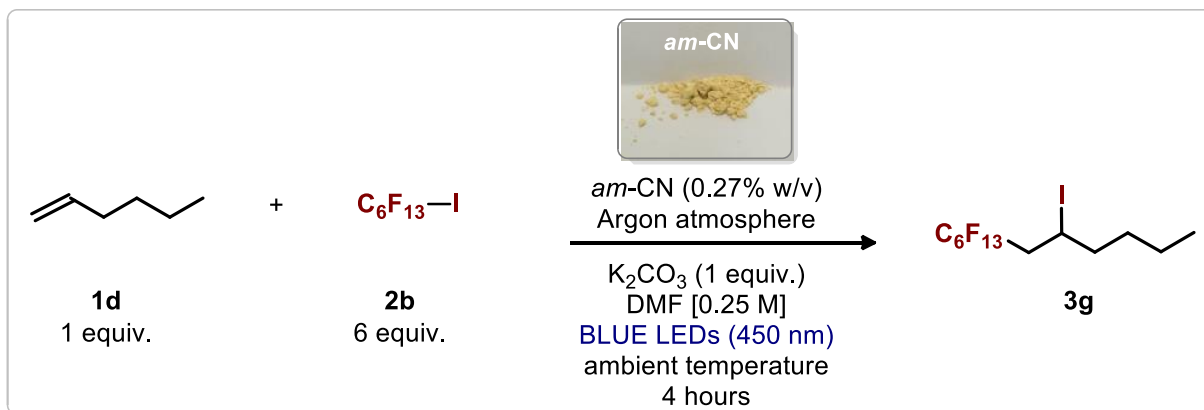
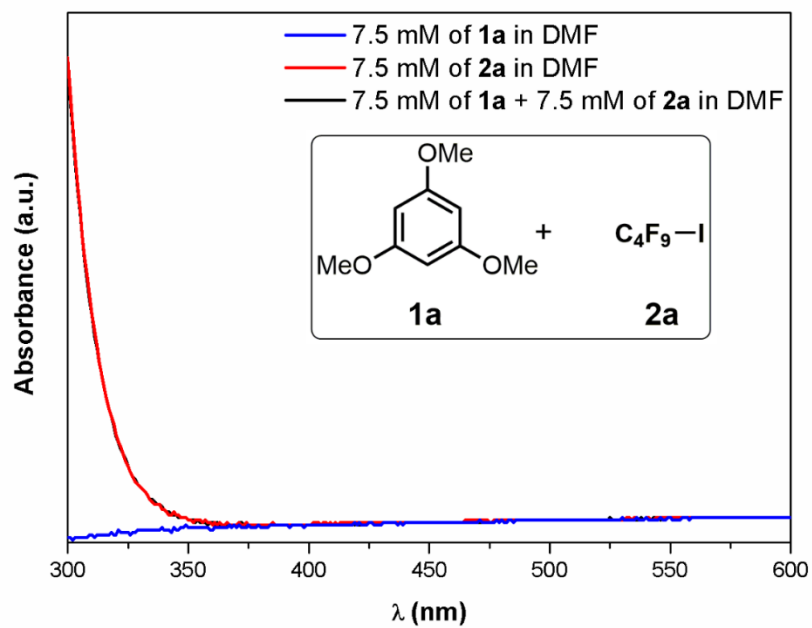**Figure S7.9.** Recycling tests for reaction producing **3g** with *am*-CN.

Figure S7.10. Uv-vis spectra of trimethoxybenzene (**1a**), perfluorobutyl iodide (**2a**) and their combination (optical length 1 cm).

Table S7.1. XPS analysis.

Sample	C / at%	N / at%	O / at%
am-CN	43.13	56.87	-
g-CN	42.33	57.67	-
ox-CN	41.94	52.71	5.35
red-CN	45.00	55.00	-

Components derived from fitting analysis.

Sample	Core level	Component	Binding Energy / eV	Area / %
am-CN	*C1S*	C-C	284.80	7.20
		C-N	286.22	8.29
		C=N-C	288.23	80.80
		pi-pi*	293.69	3.70
	N1S	C=N-C	398.80	76.50
		N-(C)3	400.87	18.05
		N-N[b]	404.49	5.45
g-CN	*C1S*	C-C	284.80	4.16
		C-N	286.11	6.20
		C=N-C	288.11	86.11
		pi-pi*	293.59	3.53
	N1S	C=N-C	398.65	75.98
		N-(C)3	400.69	17.60
		N-N[b]	404.32	6.43
ox-CN	*C1S*	C-C	284.80	6.78
		C-N	286.04	7.26
		C=N-C	288.12	82.70
		pi-pi*	293.50	3.27
	N1S	C=N-C	398.67	74.6
		N-(C)3	400.68	19.06
		N-N[b]	404.93	6.34
red-CN	*C1S*	C-C	284.80	5.28
		C-N	286.36	13.52
		C=N-C	288.14	76.89
		pi-pi*	293.79	4.31
	N1S	C=N-C	398.59	86.76
		N-(C)3	401.18	9.59
		N-N	404.66	3.65

Table S7.2. Elemental analysis of the four CN materials.

Sample	C (%)	N (%)	H (%)
am-CN	34.52	59.85	1.640
g-CN	34.67	61.36	1.720
red-CN	34.42	60.66	1.740
ox-CN	33.96	59.87	1.780

Table S7.3. Rates of production (per gram of catalyst and per square meter of catalyst) for reaction generating product **3a**.

Entry	Photocatalyst	Yield **3a**	Rate of Production $(\text{mmol}_{3a}\ \text{g}^{-1}\ \text{h}^{-1})$	$(\text{mmol}_{3a}\ \text{m}^{-2}\ \text{h}^{-1})$
1	*g*-CN	20%	0.46	0.027
2	*ox*-CN	10%	0.23	0.030
3	*red*-CN	90%	2.08	0.166
4	*am*-CN	>99%	2.32	0.122

Table S7.4. Comparison of the photocatalytic activity with different LED wavelengths for the production of **3a** with the four catalysts.

Entry	Photocatalyst	LEDs (nm)	Yield
1	*g*-CN	450	20%
2	*g*-CN	395	17%
3	*ox*-CN	450	10%
4	*ox*-CN	395	13%
5	*red*-CN	450	90%
6	*red*-CN	395	87%
7	*am*-CN	450	>99%
8	*am*-CN	395	98%

Table S7.5. Comparison between the activity of photocatalyst *am*-CN with other reported photocatalysts for production of compound **3k**.
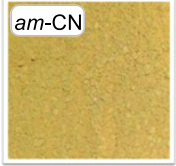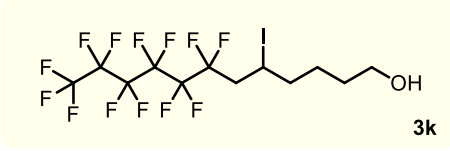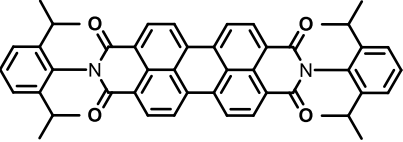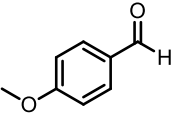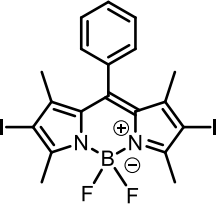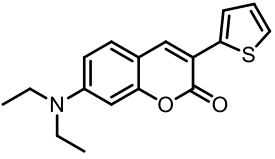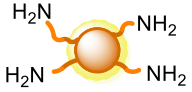
Rate of Production [mmol h^{-1} g^{-1}] = $\dfrac{\text{Yield of Product } \mathbf{3k} \text{ [mmol]}}{\text{Reaction Time [hours] x Weight of Photocatalyst [g]}}$

am-CN

16.79 mmol h^{-1} g^{-1}

3k

Selected Photocatalysts

693 mmol h^{-1} g^{-1}

ChemPhotoChem **2019**, *3*, 193-197

Ru[(bpy)$_3$]Cl$_2$

260 mmol h^{-1} g^{-1}

J. Am. Chem. Soc. **2012**, *134*, 8875-8884

1.45 mmol h^{-1} g^{-1}

Angew. Chem. Int. Ed. **2014**, *53*, 12064-12068

2.92 mmol h^{-1} g^{-1}

Chem. Commun. **2017**, *53*, 1591-1594

1.70 mmol h^{-1} g^{-1}

Chem. Commun. **2018**, *54*, 10044-10047

amine-rich N-doped carbon nanodots (NCNDs)

0.97 mmol h^{-1} g^{-1}

Chem. Eur. J. **2019**, *25*, 16032-16036

Table S7.6. Limitation of the reported photochemical transformation using catalyst *am*-CN.
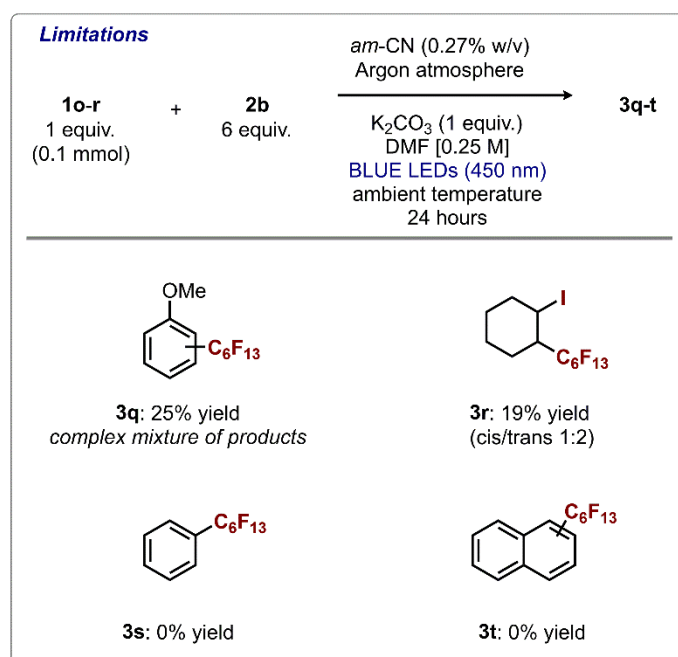
Table S7.7. Photocatalytic tests with different radical precursors with higher redox potential.
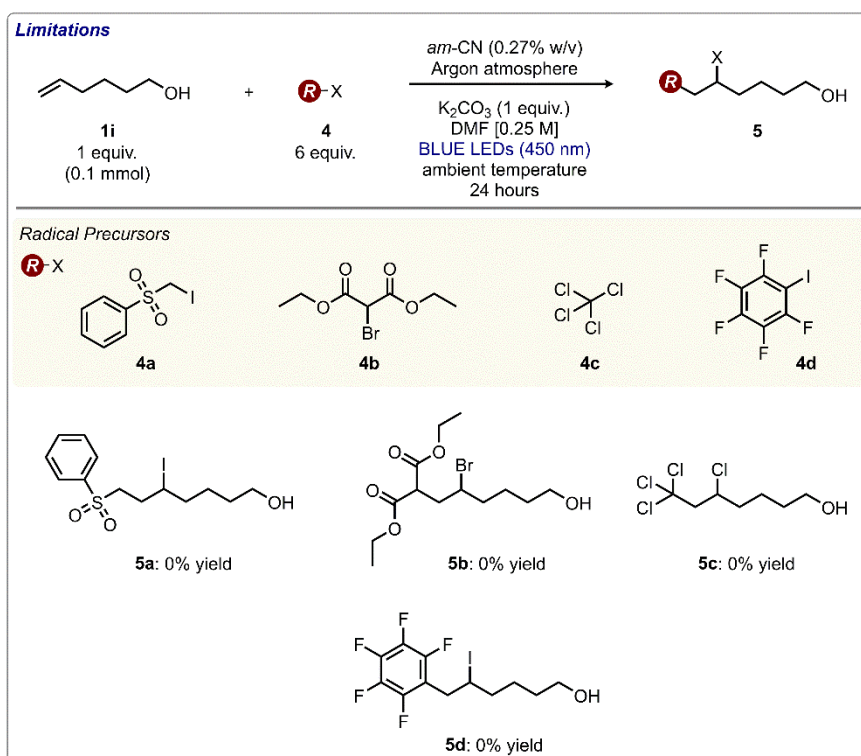
References

1.   C. Rosso, G. Filippini, P. G. Cozzi, A. Gualandi and M. Prato, *ChemPhotoChem*, 2019, **3**, 193-197.

2.   Y. Wang, J. Wang, G. Li, G. He and G. Chen, *Org. Lett.*, 2017, **19**, 1442-1445.

3.   L. Cui, Y. Matusaki, N. Tada, T. Miura, B. Uno and A. Itoh, *Adv. Synth. Catal.*, 2013, **355**, 2203-2207.

4.   C. He, J. Gu and X. Zhang, *Tetrahedron Lett.*, 2017, **58**, 3939-3941.

5.   G. Filippini, M. Nappi and P. Melchiorre, *Tetrahedron¸* 2015, **71**, 4535-4542.

6.   K. Aikawa, Y. Nakamura, Y. Yokota, W. Toya and K. Mikami, *Chem. Eur. J.*, 2015, **21**, 96-100.

Chapter 8: Tailoring pore structure and surface chemistry of microporous Alumina-Carbon Molecular Sieve Membranes (Al-CMSMs) by altering carbonization temperature for optimal gas separation performance: An investigation using low-field NMR relaxation measurements

This chapter has been published as a full article in the journal *Chemical Engineering Journal*.
[1] Tailoring pore structure and surface chemistry of microporous Alumina-Carbon Molecular Sieve Membranes (Al-CMSMs) by altering carbonization temperature for optimal gas separation performance: An investigation using low-field NMR relaxation measurements - ScienceDirect

Author contributions are as follows; Luke Forster conceived the main idea of the work, performed the NMR measurements, data processing and analysis and wrote the whole manuscript. Margot Anabell Llosa-Tanco and David Alfredo Pacheco Tanaka prepared the carbon molecular sieve membranes. Camilla Brencio performed the permeation experiments. Matthew Lindley and Sarah J. Haigh performed the TEM experiments. Carmine D'Agostino provided support in writing and revising the article as well as managing the research work. Vincenzo Spallina revised the article.

Abstract

In this work, we applied low field, NMR spin-lattice measurements to evaluate for the first time the effect of carbonization temperature (range 600-1000 °C) on the preparation of Alumina-Carbon Molecular Sieve Membranes (Al-CMSMs), providing new insights into intra-pore fluid interactions. The results show that the average Al-CMSM pore size generally increases with carbonization temperature whilst the hydrophilicity of the pore surface, and the amount of strongly adsorbed H_2O, decreases with an increasing carbonization temperature. As such, lower carbonization temperatures produce more hydrophilic membranes, with further evidence provided by FTIR measurements demonstrating the presence of polar functional groups on the surface, with water interacting more strongly with the membrane surface, as evidenced by NMR.

It was found that the Al-CMSM carbonization temperature significantly affected permeance and H_2O/CH_4 permselectivity by altering the membrane pore size distribution and pore

hydrophilicity. H_2O permeance values are seen to be up to 100 times larger than respective CH_4 permeance values. The greater permeance of H_2O is attributed to the larger kinetic diameter of CH_4 relative to H_2O and the adsorption of water in the hydrophilic pores enhancing the adsorption-diffusion transport mechanism. Optimal water permeation temperatures are thus higher for the more hydrophilic membranes, obtained at lower carbonization temperatures, as more energy is required to remove strongly adsorbed water blocking the pores. At higher carbonization temperatures, the Knudsen diffusion mechanism of permeance dominates over the adsorption-diffusion mechanism thereby reducing permeance as diffusion slows due to collisions between gas molecules and the pore walls. CH_4 permeation always occurs *via* Knudsen diffusion with CH_4 permeance increasing with permeation temperature due to the increased rate of CH_4 diffusion.

8.1. Introduction

The separation of gases is relevant to a vast array of industrial and chemical engineering sectors including the petrochemical and pharmaceutical industries. As such, the separation of different gases from gaseous mixtures is an industrial process of much importance and the development of cheap and efficient methods and materials capable of selective gas separation is of great interest. Amongst the most promising processes currently available for gas separation and purification is membrane separation owing to its relatively low consumption of energy, ease of use, low relative construction costs and possible use for continuous operation. [2]

Several classes of gas separation membranes are currently in use and can be classified into: polymeric, inorganic and mixed-matrix membranes; the main advantages of inorganic membranes are a high stability at high temperatures, and that they do not suffer plasticization. Nevertheless, in dense inorganic membranes the main mechanism of permeation is solution diffusion which is a slow process.

For porous defect free membranes, the mechanism of permeation depends on both the size of the pore and the interaction between the pore surface and the permeating gas molecules. In micropores (0.5- 2 nm) where the mechanism of permeation is by adsorption-diffusion, whereby the more adsorbable gas permeates preferentially through the membrane, simultaneously blocking the passage of the smaller gases. In ultra-microporous membranes (0.25 – 0.5 nm), separation can occur by molecular sieving where only the gas molecules smaller than the membrane pores will pass through the membrane or microporous Knudsen type diffusion, which occurs mainly at high temperatures where adsorption effects are attenuated and the gas molecules collide with the pores increasing the diffusion path length. [3]

The adsorption-diffusion mechanism of membrane separation can be effectively improved by functionalization of the porous membranes. It has been reported how different gas separation membranes can be functionalized using amine groups to drastically improve selectivity and activity [4-6] whilst functionalization of certain graphene oxide membranes with carboxyl groups has been shown to increase membrane hydrophilicity and therefore improve performance for water separation. [7] The functionalization of membranes with nitro groups, [8] hydroxyl groups, [9] ethers [10] and metal nanoparticles [11] has been shown to significantly affect separation activity in various ways.

A relatively new class of promising materials for separation technologies are carbon molecular sieve membranes (CMSMs). CMSMs are prepared by carbonization of an appropriate

polymeric precursor under an inert atmosphere or vacuum. [12, 13] The CMSM morphology consists of small graphene layers that are packed imperfectly, forming a structure commonly referred to as turbostratic carbon. The nanosized openings within/between layers are considered slit-like micro and ultra-micropores. [14] There is no long range structural order, and therefore not a single pore size but instead a broad pore size distribution. The mechanism of gas transport in CMSM is a combination of molecular sieving and adsorption-diffusion. [3]

The pore size distribution and the surface properties of the pores in CMSMs can be tuned by changing the polymer precursor, time and temperature of carbonization, and by applying pre/post synthesis treatment of the precursor or product, respectively. [15-17] It has been shown that the functional groups present within the pores of separation membranes (i.e., changing the wettability of the membrane pores) can influence the permeance of molecules passing through the porous structure due to favourable molecular interactions (adsorption-diffusion). [18]

Varying the carbonization temperature during the CMSM preparation process is a common method of altering the physical and chemical properties and therefore permeation properties of CMSM and their performance for gas separation. Indeed, it has been shown that an increase in carbonization temperature can reduce the size of micropores present in the membrane. [19] Many reports have also shown that at higher carbonization temperatures, the pore size tends to shrink increasing the permselectivity of a specific membrane whilst decreasing the permeability. [20-25] Shrinkage of the pores favours the molecular sieving mechanism of permeation in CMSMs; hence, CMSMs prepared at higher carbonization temperatures selectively allow molecules to pass through with the separation performance determined by pore size and the molecular dimensions of the gas. [26] Therefore, it is clear that the optimum carbonization temperature must be investigated to find the right balance between the permselectivity and permeability.

It has been reported that when CMSMs prepared from P84 polyimide films carbonized from 600 to 900 °C are used for various gas separations, the best performance for CO_2/CH_4 and CO_2/N_2 separations were obtained using a carbonization temperature of 800 °C. [18, 27] For a CMSM derived from Matrimid polyimide, the best temperature of carbonization for O_2/N_2 and CO_2/CH_4 and C_3H_6/C_3H8 gas separations was 550 °C. [28] Fuertes et al. [29] reported that CMSMs prepared from novolak phenolic resin using a carbonization temperature of 700 °C were highly effective for the recovery of hydrocarbons from hydrocarbon-N_2 mixtures, whilst those prepared using a carbonization temperature of 800 °C were most effective for O_2/N_2, CO_2/CH_4

separation. Finally, those prepared at a carbonization temperature of 900-1000 °C had the best performance for separating mixtures of gases with molecular sizes smaller than 0.4 nm. [29]

Self-supported CMSMs are brittle and hence in order to improve the mechanical strength, thermal stability and permeation properties, thin, supported CMSMs are required. Pacheco and Llosa reported for the first time the preparation of supported composite alumina CMSM (Al-CMSM) from phenolic resins (resol [30-32] and novolac [12, 33]) in a one dip coating carbonization process.

For Al-CMSMs prepared from novolac and boehmite precursors; the average pore size and pore size distribution vary with the carbonization temperature within the temperature range of 450 – 1000 °C. [34] The membranes carbonized at low temperature possess hydrophilic groups able to adsorb water thereby blocking the pores and reducing the pore size of the microporous domain. This water can be removed by heating; therefore, the size of the pore (amount of water adsorbed) will change with the temperature; in a reversible process. [34] It was found that by saturating the pores of the membrane with water before gas separation, the permeation properties are improved by covering all the hydrophilic sites with water reducing the pore size and increasing the selectivity. [35, 36] When the water adsorption effect on Al-CMSM carbonized at 550 and 600 °C was studied for the separation of H_2 from a H_2-CH_4 mixture; it was concluded that water adsorption is an essential parameter to improve the separation properties; indeed, a H_2 purity of 98.95 % from 10 % H_2-90 % CH_4 was obtained. [36] The improvement was found to be more remarkable when working at high temperatures, therefore, interaction of water with the pores of the membrane should be studied. [36]

Power-to-X processes have unlocked the possibility to convert renewable H_2 and CO_2 from the atmosphere into valuable chemicals such as methane, methanol and dimethyl-ether that can be later used as fuels or bulk chemicals. [37] These processes are currently carried out at relatively high temperatures (200 - 300 °C) and pressures (up to 40 bar) and generally produce large quantities of H_2O. This is detrimental for both the equilibrium conversion and catalyst stability and therefore the *in-situ* removal of H_2O from the reactors used will result in a significant conversion enhancement and thus process intensification. [37, 38]

Composite Alumina Carbon Molecular Sieve Membranes (Al-CMSMs) are a promising material system for the required separation of H_2O from the reactors. For membrane water-gas permeation by the adsorption-diffusion mechanism, water molecules must be adsorbed on to

the surface of the pores. The extent to which this can occur will depend on: a) hydrophilicity and pore size distribution of the membrane and b) the temperature and pressure of permeation.

In this work, Al-CMSMs were prepared at various temperatures of carbonization and tested for their performance in H_2O and CH_4 permeance at relatively high temperatures. The surface properties of the pores play an important role in determining the performances of these materials, yet measuring surfaces within the pore space of such membranes has proven to be very challenging and little is known about how carbonization affects surface chemistry. Here NMR relaxation was used for the first time for this class of materials to probe the interactions and molecular dynamics of molecules confined within such carbon membranes in order to investigate how a change in carbonization temperature affects the structural and surface properties of CMSMs and how this can alter their performances for practical applications.

8.2. Experimental

8.2.1. Chemicals

Deionized water was obtained from a laboratory water purification system; n-hexane (≥99 %) was obtained from Sigma Aldrich and used as supplied.

8.2.2. Al-CMSMs preparation

The tubular supported Al-CMSMs were prepared by the one dip-dry-carbonization step method previously reported. [12, 32] The supports are porous α-alumina tubes (10 mm and 7 mm outer and inner diameter respectively) 15 cm long from Inopor. Both ends were connected to dense alumina tubes using a glass seal. [33] One end was closed and the other open to allow the permeating gases to flow. The porous supports were introduced into a dipping solution containing novolac resin (13 wt%), formaldehyde (2.4 wt%), ethylenediamine (0.4 wt%), boehmite (as a precursor of alumina, 0.8 wt%) in N-methyl-2-pyrrolidone (NMP) using a vacuum pump. The remaining precursor solution was placed in a Teflon dish to make unsupported Al-CMSM films and used for membrane characterization. Both supported and unsupported membranes were dried in an oven at 100 °C overnight. The tubular supported membranes were dried under continuous rotation inside an oven to guarantee a uniform thickness. The Al-CMSMs were carbonized at temperatures from 600 °C to 1000 °C for two hours under a continuous flow of nitrogen. Figure 8.1 shows a 15 cm long supported Al-CMSM where both ends were supported in a dense alumina tube. One side was closed (left side in Figure 8.1) and the other left open to allow the permeating gas to flow.
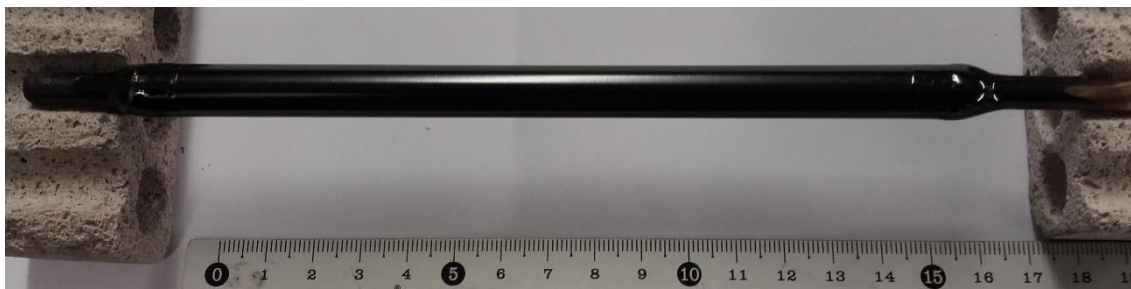
Figure 8.1. Al-CMSM supported on porous alumina tube connected to dense alumina tubes.

8.2.3. H_2O and CH_4 gas permeation studies

A schematic representation of the experimental facility designed to perform vapor permeation experiments is depicted in Figure 8.2. The setup consists of four main sections: (i) the feed section; (ii) the pressure vessel containing the membrane; (iii) the cooling section and the (iv) retentate/permeate analysis section. A series of mass flow controllers, from Brooks Instrument, are provided in order to set the desired amount of gas to feed inside the system in (mL min^{-1}). Demineralized water is contained in a tank and the desired amount to be fed inside the system is set through the mass flow controller (g h^{-1}); H_2O is provided above atmospheric pressure to overcome the pressure drop along the feeding line and output separation. H_2O is then evaporated at a temperature of 120 °C in a controller evaporator mixer (CEM) in which a minimum amount of N_2 (≥ 0.15 mL min^{-1}) is used as the carrier gas.

Several temperature controllers are used to maintain the temperature of the lines in which the gas mixture flows at temperatures above 150 °C, in order to ensure that the water does not condense inside the system. The permeator section consists of a stainless steel vessel, where the membrane is connected to the main body from the flange on the top. The vessel is placed inside an electrical oven in order to maintain isothermal conditions in the membrane.

Both retentate and permeate gases leave the membrane at the separation temperature and go through the cooling section. This consists of two coolers, for the permeate side and the retentate side, respectively, which condense the unseparated steam contained in the mixture.

Finally, liquid water is collected inside containers placed at the outlet of the condensers, while the other gases will reach the analysis section, in which it is possible to measure the amount of gas permeated through the film flow meters (HoribaStec). A µ-GC analyser is also included in the analysis section, in order to analyse the composition of the permeate feed.

Several Al-CMSMs were carbonized at temperatures between 600 and 1000 °C. Each carbon membrane was tested at temperatures ranging from 150 to 300 °C, while the pressure difference between the feed and the permeate was maintained at 3 bar, keeping the permeate side at atmospheric conditions. Pressure at the membrane inlet and permeate side was controlled by back-pressure regulators from Bronkhorst and temperature inside the membrane was controlled by two thermocouples, placed at the feed/retentate and permeate side respectively.

The permeation tests with pure water were performed with a stream mixture of 92.5 % H_2O and 7.5 % N_2 due to the presence of the CEM. The membranes were exposed to a flux of water for a fixed time interval, at the end of which the amount of water permeated was collected and the H_2O permeability was derived accordingly.
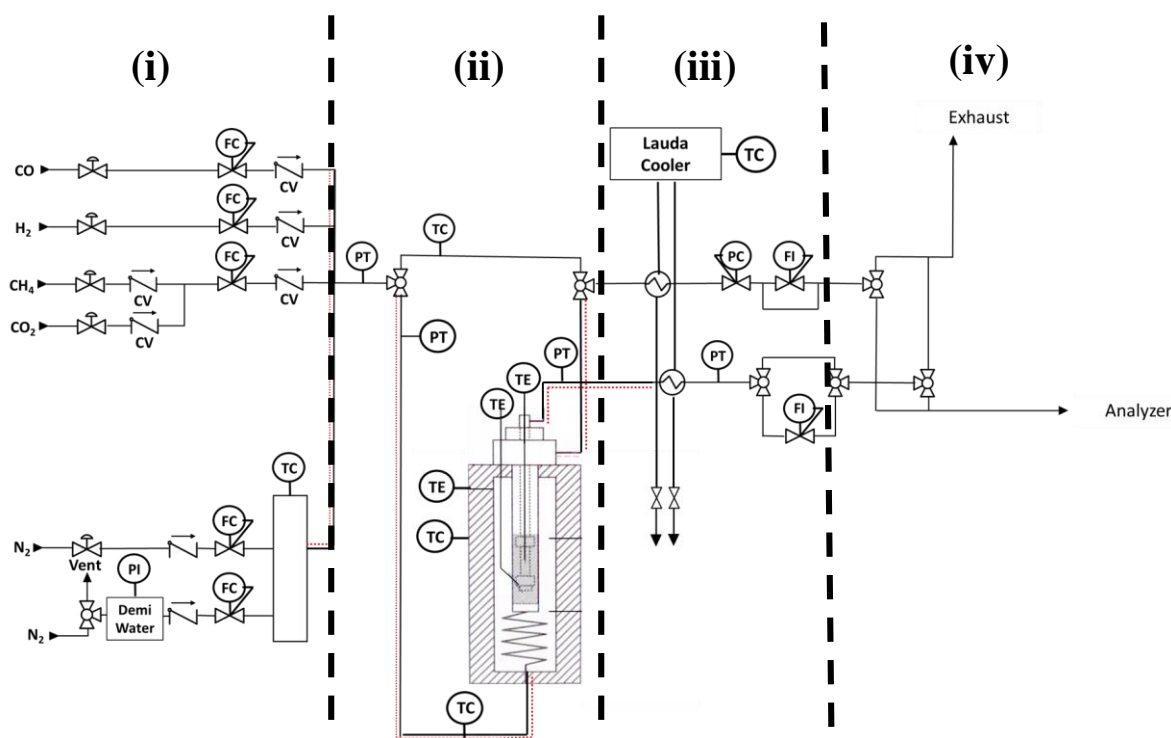
Figure 8.2. Schematic representation of the experimental facility designed to perform vapor permeation experiments. The four main sections: (i) the feed section; (ii) the pressure vessel containing the membrane; (iii) the cooling section; and the (iv) retentate/permeate analysis section are labelled.

8.2.4. Thermogravimetric analysis (TGA)

TGA data was acquired on a Netzsch TGA 760, in the temperature range from 20 – 900 °C, heating rate at 5 °C min^{-1} under nitrogen. The analysed samples were self-supported precursor films before carbonization, and the amount of sample used was ~ 5 mg.

8.2.5. FTIR analysis

The IR spectra were obtained using an Agilent Cary 630 FTIR with a ZnSe diffuse module for powder sample analysis. The samples were first ground and then diluted with KBr powder, obtaining a final mixture with 5 % (w/w) of carbon membrane material. Micro lab PC Software was used to extract the absorbance data. The final plots were obtained by subtracting the KBr spectrum from that of one of the diluted samples, normalizing the signal intensity for all plots with respect to the absorbance of pure KBr and, finally, by converting the absorbance into transmittance (T %).

8.2.6. NMR measurements

Samples were prepared for the NMR measurements by soaking in water or *n*-hexane for at least 48 hours to allow the membranes to equilibrate. The Al-CMSMs were then dried on a pre-soaked filter paper to remove any excess liquid on the external surface and finally transferred to 5 mm NMR tubes. To ensure a saturated atmosphere in the NMR tube, hence minimizing errors due to evaporation of volatile liquids, a small amount of pure liquid was placed onto absorbed filter paper, which was then placed under the cap of the NMR tube. The tube sample was finally placed into the magnet and left for approximately 15 minutes before starting the measurements, in order to achieve thermal equilibrium.

NMR experiments were performed in a Magritek SpinSolve benchtop NMR spectrometer operating at a ^{1}H frequency of 43 MHz. The NMR spin lattice relaxation time was measured using the inversion recovery technique (Figure 8.3). The typical error of all T_1 measurements was approximately 3 %.

The spin-lattice relaxation time constant is determined by plotting the acquired signal intensities as a function of the time delay, $t = \tau$ in accordance with the following equation:

$$\frac{M_z(t)}{M_0} = 1 - 2\,e^{-\frac{t}{T_1}} \tag{8.1}$$

where $M_z(t)$ is the signal intensity at the respective time delay, τ, and M_0 is the signal intensity at equilibrium.

Inversion recovery experiments were performed using a 16-step inversion recovery pulse sequence and a maximum inversion delay ranging from 1–5 s for experiments using water and between 1–3 s for experiments using *n*-hexane. 16 scans were used for each time delay.

8.2.7. High resolution transmission electron microscopy (HRTEM)

Transmission electron microscopy (TEM) was performed on an FEI Talos F200X operated at 200 kV with images captured using a Ceta-M 4k CMOS camera.

8.3. Results and discussion

The TGA analysis of the non-supported membrane carried out under N_2 is shown in Figure 8.3b; the unsupported membrane precursor contains the partially condensed polymer, remains of the solvent (NMP) and boehmite. During the carbonization, NMP and volatile reaction products such as H_2O, CO, CO_2, H_2 are released; [39] the peak observed in differential thermal gradient (DTG) around 200 °C is that of the solvent and volatiles; significant weight loss occurs until 550 °C. From 550 to 900 °C, the TGA data can be divided in to two regions (550 - 650 and 650 - 900 °C). Water and gas evolution of a resol phenol formaldehyde resin during carbonization was studied by Marinkovic; [39] the water evolution was significant between 100 and 600 °C and completed by 700 °C; H_2 started to evolve at 400 °C having a peak at 650 °C. From 800 °C, only H_2 was released. In addition, Funabiki et al. [40] studied the carbonization of a phenolic resin and reported that as the temperature of carbonization increases, the content of oxygen groups decreases. The results in Figure 8.3b shows for our Al-CMSM precursors at 700 °C almost all the oxygen groups were removed. At higher temperatures, the cross-link groups in the phenolic resin are destroyed, which leads to clustering of the aromatic units and subsequent rearrangement of the restacked graphite planes, reducing the pore size of the membranes. [41] During carbonization, unstable carbon groups are formed in the membrane. After cooling, these groups can react with water from the environment (water chemisorption) making the membrane hydrophilic. Figure 8.3a shows the C-O stretching frequency (1240 cm^{-1}) intensity as a function of the carbonization temperature used to produce the Al-CMSM membranes. A sharp decrease in intensity is observed in the 550 - 650 °C temperature range suggesting that above this temperature most of the oxygen containing groups were removed.
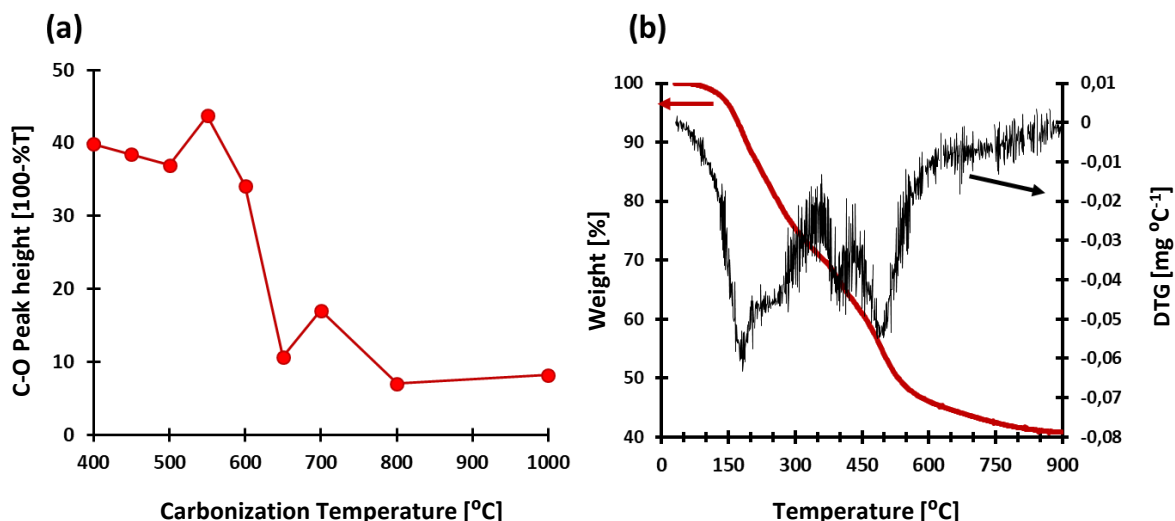
Figure 8.3. (a) FTIR C-O peak height of unsupported Al-CMSM precursor where T % is the percentage of transmittance and 100 – T % is related to the amount of C-O functional groups on the Al-CMSM surface and (b) TGA/DTG analysis.

The release of gas during heating of the precursor leads to the formation of pores and shrinkage of the membrane. The effect of the carbonization temperature on Al-CMSM (prepared with the same conditions as in this paper) on pore size distribution was reported by Mendes et al. from the CO_2 adsorption isotherm at 0 °C; the equilibrium values were obtained using a gravimetric method and the data was processed using the Dubinin-Astakhov equation (Figure 8.4). [33] The micropore distribution can be divided in to two regions: 0.25 - 0.5 nm and 0.5 - 0.9 nm representative of the pore sizes relevant to molecular sieving (MS) and adsorption-diffusion (AD) mechanisms of transport respectively. Most of the pores on the membrane carbonized at 550 °C are within the AD region with a maximum pore size of around 0.65 nm. When the carbonization temperature is increased to 650 °C, an important change in the pore size distribution occurs, that is, the number of pores in the MS region increases considerably. In the AD region, the peak maximum is shifted to the left at around 0.55 nm. At a higher carbonization temperature of 750 °C the number of pores in the MS region decreases, the number of pores in the AD region increases, and the peak maximum returns to 0.65 nm.
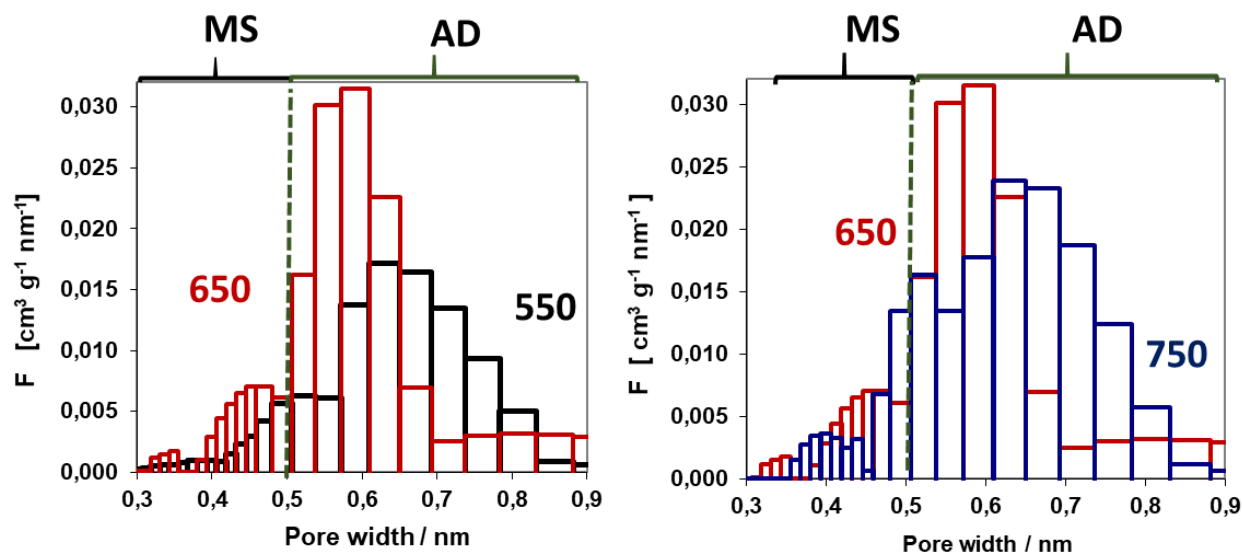
Figure 8.4. Micropore size distribution of Al-CMSMs carbonized at 550, 650 and 750 °C showing the molecular sieving and adsorption-diffusion regions (adapted from Tanco et al. [33] with permission of Elsevier).

The porous nature of the membranes was examined by TEM analysis (Figure S8.1). However, due to the very small dimensions of the pores, (of the order of molecular dimensions) and the disordered nature of the material it was not possible to use high resolution TEM imaging to visualise differences in the porosity for different carbonisation temperatures. All Al-CMSMs showed nanostructured carbon membranes implanted with nanosized alumina. This highlights the importance of NMR relaxation measurements to characterise differences in porosity, which is subsequently discussed.

8.3.1. NMR relaxation measurements

The effect of the carbonization temperature used during sample preparation upon the surface chemistry of the Al-CMSMs was assessed by using water and n-hexane to probe hydrophilic and hydrophobic interactions of the Al-CMSMs surface, respectively. Low-field NMR experiments, [42, 43] in particular low field NMR relaxation measurements [44-48] have previously been successfully used to understand the role of water and other solvent interactions in porous catalysts and here the same idea is extended to membranes.

Spin-lattice relaxation time (T_1) NMR results are shown in Figure 8.5a and b for water and n-hexane, respectively. The experimental data were fitted using single exponential functions and the quality of data and fitting is excellent ($R^2 > 0.99$). The extracted T_1 values are shown for different carbonization temperatures in Figure 8.6, with absolute values tabulated in Table S8.1.

(a)

(b)
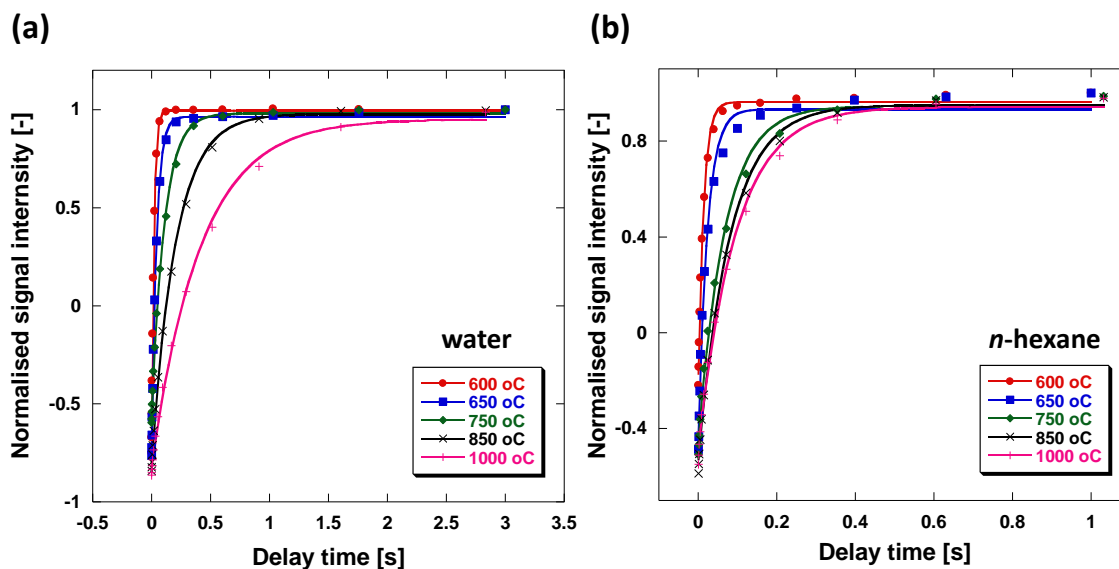
Figure 8.5. T_1 inversion recovery plots of (a) H_2O and (b) CH_4 confined within Al-CMSMs prepared using various carbonization temperatures. Solid lines represent fitting to a single inversion recovery exponential. Due to extremely fast relaxation of *n*-hexane molecules within the CMSM pores, spins have already relaxed to some degree even at the lowest delay times used, therefore the normalised signal intensity does not reach -1. This is not thought to significantly impact the results obtained and is merely a peculiarity of the system studied.

An increase in carbonization temperature is seen to increase the time that the confined liquid takes to fully relax within the micropores for both guest molecules across all samples studied. This effect is significant for the tests using water; however, when using *n*-hexane, the difference in the time taken for the signal to fully recover is seen to increase only slightly in CMSMs carbonized between 600 – 800 ⁰C before becoming almost constant for CMSMs carbonized at above 800 ⁰C.
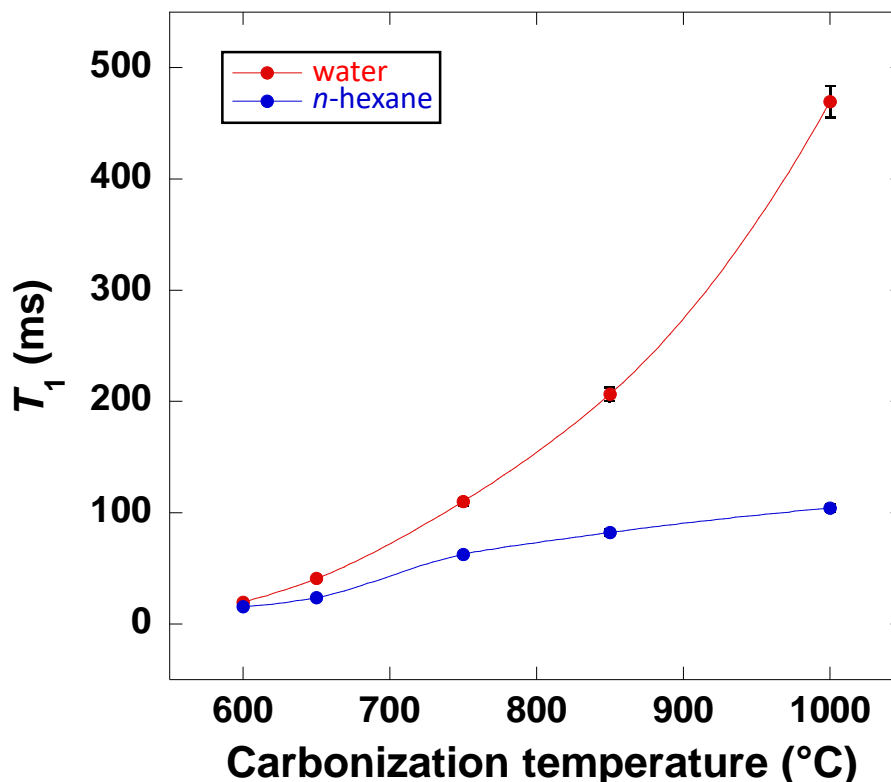
Figure 8.6. T_1 values of *n*-hexane and water confined within the micropores of Al-CMSMs as a function of Al-CMSM carbonization temperature. The approximate error for T_1 values is 3 %. Solid lines are a guide to the eye.

According to Bloembergen-Purcell-Pound (BPP) theory (Chapter 2.1.6.), T_1 values of fluids are related to the molecular tumbling motion of the molecule being analysed. Generally, for fast tumbling fluids, such as water and *n*-hexane, T_1 is large when tumbling is unrestricted and therefore molecular motion is very fast; this then decreases to a minimum as molecular motion becomes slower/the molecule becomes more restricted. [49]

The T_1 values of confined liquids, $T_{1,obs}$, compared to the bulk $T_{1,bulk}$, depend on multiple factors, which can be summarized by the following equation: [50]

$$\frac{1}{T_{1,obs}} = \frac{1}{T_{1,bulk}} + \frac{2\alpha\rho_i}{d_{pore}} + \frac{8\alpha D_o}{d_{pore}^2} \tag{8.2}$$

where α is a pore shape factor, ρ_i is the surface relaxivity, d_{pore} is the pore size and D_o is the self-diffusivity of the liquid under confinement. This equation allows for the determination of two limiting cases upon the spin-lattice relaxation times of confined liquids, namely the slow diffusion limit (when bulk diffusion dominates i.e., when surface relaxivity or the pore size is very large) or the fast diffusion limit (when surface processes dominate i.e., when surface relaxivity is weak or pore size is very small). [51] In the case of liquids confined within porous

materials, the bulk term is negligible and two new equations can be written for the fast and slow diffusion limits respectively;

$$\frac{1}{T_{1,obs}} = \frac{2\alpha\rho_i}{d_{pore}} \tag{8.3}$$

$$\frac{1}{T_{1,obs}} = \frac{8\alpha D_o}{d_{pore}^2} \tag{8.4}$$

The small micropores of the order of approximately 1.50–1.80 nm are sufficiently large to allow access of both *n*-hexane and water (kinetic diameters of 0.27 and 0.43 nm respectively) [36, 52] however, it is apparent that these molecules will be under a significant degree of confinement which will greatly affect their mobility within the porous structure of the Al-CMSMs. As the liquids are highly confined within the micropores of the Al-CMSMs, they are defined by the fast diffusion limit. The fast diffusion limit can be rewritten as:

$$T_1 \approx \frac{d_{pore}}{\rho_1} \tag{8.5}$$

Using this equation, it can be inferred that the general increase in T_1 across all samples for both guest molecules is down to the general increase in the average pore size with increasing carbonization temperature. Figure 8.4 showed that the volume and number of smaller micropores increases with the carbonization temperature up to 650 ⁰C whereas at higher carbonization temperatures the pore size distribution indicates that a wider range of larger micropores are formed. [33] As the micropores become larger with increasing carbonization temperature, the guest molecules will become less confined and therefore more mobile so T_1 will increase.

However, as the trend for *n*-hexane and water is different (Figure 8.6), clearly the surface relaxivity has a significant effect on the T_1 values, besides that of the pore size. Indeed, the T_1 relaxation time can be used as a tool to study surface effects on the configuration of water and hydrocarbons, which has been extensively applied to study wettability in rocks and minerals. [53-55] In the case of the membranes used in this work, the difference in mobility between *n*-hexane and water can be effectively related to the relative surface affinities of each respective guest molecule for the surface of the Al-CMSMs. By taking the ratio of the respective T_1 values, the pore size dependence can be removed to give an effective measure of wettability, denoted as *H*, where a higher value indicates a greater degree of hydrophilicity.

$$H = \frac{T_{1,HEX}}{T_{1,H_2O}} = \frac{\rho_{H_2O}}{\rho_{HEX}} \tag{8.6}$$

By plotting the effective hydrophilicity parameter, H, as a function of the carbonization temperature as seen in Figure 8.7 and Table S8.1, it can be seen that Al-CMSMs generally become increasingly, less hydrophilic, and hence more hydrophobic, with increasing carbonization temperature.
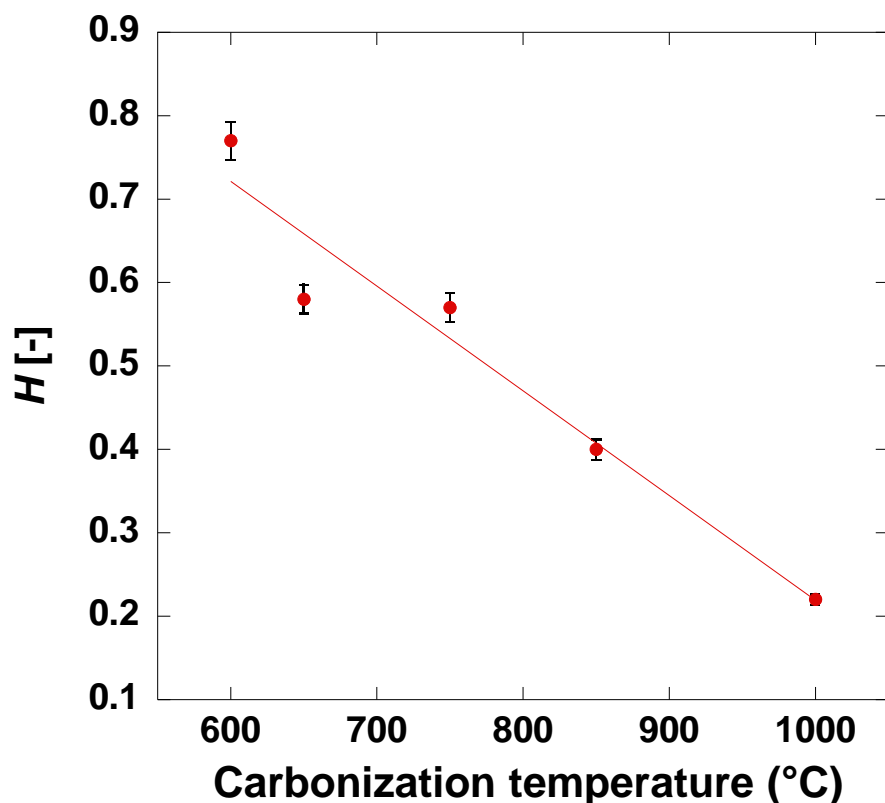
Figure 8.7. A plot of the effective hydrophilicity parameter H as a function of Al-CMSM carbonization temperature. Error is approximately 3 % for each value of H.

All values for H are less than 1 indicating that n-hexane interacts more strongly with the Al-CMSM surface regardless of carbonization temperature. This is due to the inherent hydrophobicity of carbon materials; however, the wettability of the surfaces clearly changes significantly with carbonization temperature. This change in wettability can be attributed to the physical and chemical adsorption of water within the Al-CMSM pores after carbonization as previously discussed. Clearly, the carbonization temperature influences the extent to which water adsorbs to the pore surface and hence the overall permeation performance of the Al-CMSMs. As the carbonization temperature increases, more hydrophilic groups are being removed from the surface, making the membrane more hydrophobic. [56]

242

8.3.2. H₂O and CH₄ permeation studies.

In this work CH_4 was selected due to its hydrophobicity and larger kinetic diameter (0.39 nm) when compared with water (0.27 nm). [36, 52] Previous work has shown that when Al-CMSM are synthesized and then exposed to air the gas permeance decreases. [33] Decomposition of the polymer during synthesis creates pores with reactive carbons lining the pore surface and these reactive carbons can then react with water from the atmosphere producing hydrophilic oxygen containing functional groups on the Al-CMSM surface. These groups cause water to strongly adsorb to the hydrophilic pore surface, leading to an overall decrease in effective pore size [33, 57] thereby reducing permeability of the Al-CMSM. Upon heating during the separation process, these adsorbed water molecules desorb from the Al-CMSM pore surface, increasing the effective pore size and allowing greater permeance of gas molecules of an appropriate size. [34] Therefore, the permeance of a given Al-CMSM towards a certain molecule will be dependent on not just the pore size but also the strength of the interaction between the pore surface and the adsorbed water layer, hence hydrophilicity, which will in turn influence the effective pore size.

The H_2O and CH_4 gas permeation properties were measured at 150 °C, 200 °C, 250 °C and 300 °C with a pressure difference of 3 bar between the retentate and permeate sides (Tables S2 and S3). The results are plotted as a function of the different carbonization temperatures used to prepare each membrane in Figure 8.8.
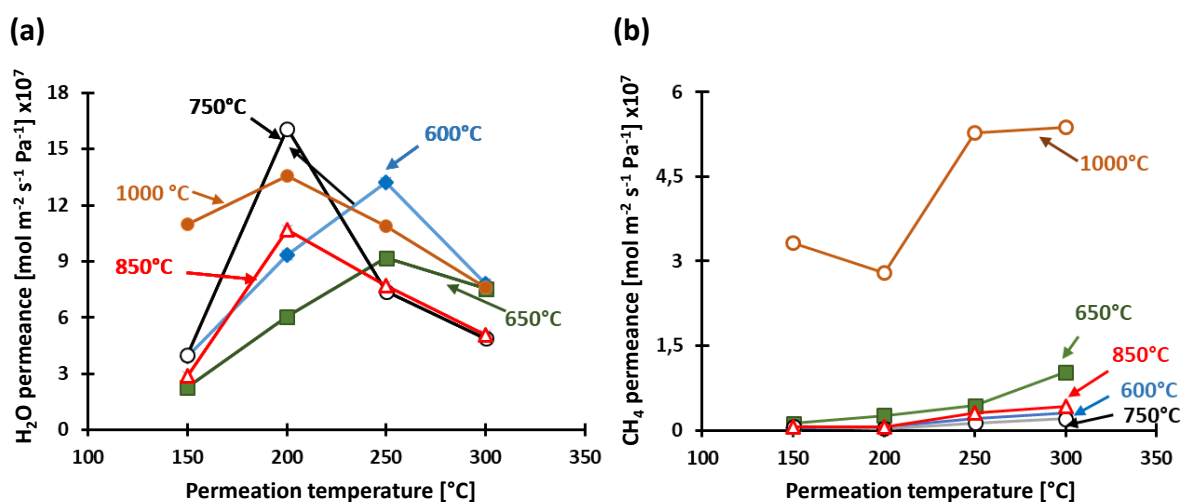

Figure 8.8. (a) H_2O and (b) CH_4 permeance of Al-CMSMs prepared using various temperatures of carbonization as a function of permeation temperature (pressure 3 bar). Note the axis scaling $\times 10^{-7}$ mol m⁻²s⁻¹Pa⁻¹. The accuracy of the equipment is approximately 3 % so the instrumental error bars are mostly too small to be visible on the graphs.

H_2O permeance values are found to range between orders of $10^{-7} – 10^{-6}$ mol s^{-1} m^{-2} Pa^{-1} (Figure 8.8a, Figure S8.2a, Table S8.2), whilst the CH_4 permeance values range between $10^{-8} – 10^{-7}$ mol s^{-1} m^{-2} Pa^{-1} (Figure 8.8b, Figure S8.2b, Table S8.3). This difference in permeance is attributed to the much larger kinetic diameter of CH_4 when compared to H_2O (0.39 nm [52] as opposed to 0.27 nm, [35] respectively) and the adsorption of water on the hydrophilic pores enhancing the adsorption-diffusion transport.

It can be seen that H_2O and CH_4 permeances are both dependant on the Al-CMSM carbonization temperature and the permeation temperature. CH_4 permeance values (Figure 8.8b, Figure S8.2b, Table S8.3) are generally shown to increase with the permeation temperature, showing maximum values of CH_4 permeance at 300 °C, which is attributed to the increased rate of diffusion of CH_4 molecules. As for the effect of carbonization temperature on CH_4 permeance, for CH_4 permeation tests with membranes carbonized in the range of 600-850 °C, the maximum permeance is produced at 650 °C, which is related to the changes in the pore size distribution and porosity at this temperature compared to 550 and 750 °C (see Figure 8.4), that is, at 650 °C the number of pores in the MS region is higher compared to membranes carbonized at 600 °C and 750°C. Finally, when the carbonization temperature is 1000 °C, the CH_4 permeance is very high, which can be attributed to the presence of structural defects in the membrane. The supported Al-CMSM is thin ($\approx$3 µm) hence during heat at such high temperature treatment the three dimensional shrinkage of the membrane will produce through hole defects.

For H_2O permeance (Figure 8.8a, Figure S8.2a, Table S8.2), the main observation is that as the carbonization temperature of the membrane increases, the maximum water permeation is shifted to lower temperature. This can be explained in light of the NMR measurements, which indicate that higher carbonization temperatures lead to less hydrophilic membranes (see Figure 8.7), due to the loss of polar functional groups on the membrane pore surface (see Figure 8.3). This decrease in hydrophilicity, hence decrease in water interactions with the membrane surface, leads to lower temperature requirements for water removal. Conversely, at lower carbonization temperature, more polar groups are present on the surface, hence more hydrophilicity and stronger interactions with water, which requires higher temperatures to be removed. At 150 °C permeations are generally the lowest due to condensation of water in the pores at this temperature (we note here that the operating pressure is 3 bar hence water at 150 °C is close to its condensation point); . In particular, for the more hydrophilic membranes

(carbonized at 600 and 650 °C), the maximum permeances are at approximately 250 °C and for the less hydrophilic membranes (750, 850 and 1000 °C) the maximum permeances are at approximately 200 °C; as mentioned above, for more hydrophilic membranes water interacts more strongly with polar groups over the surface and is therefore removed at higher temperatures. At further higher temperatures the permeance drops and this is because as the temperature is further increased, the adsorption-diffusion mechanism of permeation becomes less relevant due to the loss of polar groups from the pore surface preventing the required interaction between water and the pore surface. Consequently, Knudsen-type diffusion becomes the dominant mechanism of permeation; hence, diffusing water molecules will collide with the pore walls thereby increasing the diffusion path length and decreasing the permeance. CH_4 permeation will always occur via Knudsen diffusion, as CH_4 cannot strongly adsorb to the hydrophilic surface due to its lack of polar functional groups. Therefore, CH_4 diffusion will always increase with the permeation temperature due to the increased rate of diffusion of CH_4 molecules. The respective changes in H_2O and CH_4 permeance are reflected in the H_2O/CH_4 permselectivity at the differing temperatures of permeations (Table S8.4, Figure S8.3).

We note that when the carbonization temperature is increased from 650 to 750 °C, the number of pores in the AD region increases considerably (see Figure 8.4) and the maximum is shifted from ≈ 0.55 nm to ≈ 0.65 nm, which is reflected in the increase of H_2O permeation observed.

Additionally, the NMR relaxation measurements (Figure 8.7) show that the membranes prepared at 650 °C and 750 °C have effectively the same degree of hydrophilicity. Therefore, any change in the permeance must be solely due to the changes in the porosity and pore size. We also note that for a permeation temperature of 150 °C, the permeance of water measured for the membrane carbonized at 1000 °C is much higher compared to that recorded at lower carbonization temperatures. This can be attributed to the presence of defects, due to sintering effects and differences in expansion coefficients of the different materials composing the membrane, as well as to larger pores in the AD region. In addition, the lack of functional groups due to the low hydrophilicity of the membrane carbonized at 1000 °C may play a key role in preventing condensation at 150 °C, hence increasing permeance. The increase in pore size and general decrease in pore hydrophobicity with increasing carbonization temperature are supported by the findings of the low field NMR relaxation measurements (Figures 8.6 & 8.7) as discussed in the previous section.

8.4. Conclusions

The permeance and permselectivity of an Al-CMSM to H_2O and CH_4 gases changes with the temperature of carbonization used to prepare the membrane and the temperature of permeation used during gas separation. TGA analysis in N_2 atmosphere shows that up to a carbonization temperature of 650 °C, weight loss is due to the removal of water. FTIR analysis of the C-O stretching frequency of the unsupported membranes indicates that between 550-650 °C, there is a sharp decrease in the oxygen content and in the 650-700 °C range, a small increase of C-O groups present on the pore surface is observed followed by a decrease in C-O groups to a constant C-O group content at higher carbonization temperatures in the range 800-1000 °C. The pore size and pore size distribution changes considerably with the carbonization temperature. By increasing the carbonization temperature from 550-650 °C the porosity of the membrane increases in the MS region and in the AD region below 0.65 nm, while from 650 - 750 °C, the number of pores below 0.65 nm decreases and the number of pores above 0.65 nm increases.

NMR relaxation measurements have shown that an increase in carbonization temperature during the preparation of Al-CMSMs causes larger micropores to form thereby increasing the average membrane pore size. T_1 measurements confirm this as both hydrophilic and hydrophobic substrates (water and *n*-hexane respectively) show a higher T_1 when confined within the membrane micropores, which indicates increased guest molecule tumbling/mobility with increasing carbonization temperature. That is, confinement of both molecules decreases with increased carbonization temperature. NMR relaxation measurements also show that CMSMs prepared at higher carbonization temperatures generally have a more hydrophobic surface than those prepared at lower temperatures as evidenced by the reduced mobility of *n*-hexane within the pore space relative to the mobility of water within the same pore space. The increased hydrophilicity of CMSMs carbonized at lower temperatures is attributed to the presence of oxygen containing groups within the pores, which interact with water and reduce the mobility of water relative to *n*-hexane. All pores were found to be hydrophobic overall due to the inherent hydrophobicity of carbon.

The permeance of H_2O and CH_4 was studied for the Al-CMSMs as a function of permeation temperatures. For the more hydrophilic membranes (carbonized at 600 and 650 °C), the maximum permeances for H_2O are at 250 °C and for the less hydrophilic membranes (750, 850 and 1000 °C) they are at 200 °C. This is explained as water interacts more strongly with polar

groups in the more hydrophilic membranes and they require higher temperatures to be removed. Therefore, at higher temperatures, the water adsorbed on the pores diminishes and consequently the adsorption-diffusion mechanism of permeation becomes less favourable. As such, Knudsen type diffusion becomes the predominant mechanism of permeation and the molecules of water collide with the pores thereby increasing the diffusion path length and decreasing the permeance. When the carbonization temperature is increased from 650 to 750 °C, the number of pores in the AD region increases considerably and the maximum is shifted from ≈ 0.55 nm to ≈ 0.65 nm which is reflected by an almost doubling of the permeation.

For membranes produced at the highest carbonization temperature (1000 °C), the permeance of both CH_4 and H_2O are relatively high due to the presence of structural defects in the membranes, creating larger holes and allowing access of larger molecules. This is well explained by the drop of the ideal perm-selectivity down to very low values (approximately 1.4). The lowest H_2O permeances were detected in the tests at the operating temperature of 150 °C, due to water condensation in the pores blocking access to gas molecules. In all cases, the permeance of H_2O is higher than CH_4, due to the smaller kinetic diameter of H_2O allowing for easier diffusion.

CH_4 permeance generally increases with the permeation temperature reaching a maximum at 300 ºC due to the increased rate of diffusion of CH_4 molecules at higher temperatures. CMSMs carbonized in the temperature range 600 - 850 ºC show a maximum CH_4 permeance at a carbonization temperature of 650 ºC. CH_4 permeance varies with carbonization temperature as the porosity and pore size distribution of the membrane changes with the carbonization temperature. When CMSMs are prepared using a carbonization temperature of 1000 ºC, CH_4 permeance is at its greatest due to structural defects within the CMSM allowing CH_4 molecules to permeate freely.

Overall, this work shows that Al-CMSMs are promising membranes for membrane reactors where *in-situ* removal of water is required in order to shift the equilibrium, such in the production of fuels from H_2 and CO_2, owing to the high water permeance in the temperature range 200 - 250 °C.

References

1. L. Forster, C. D'Agostino, M. A. Llosa-Tanco, V. Spallina, C. Brencio, F. Gallucci, M. Lindley, S. J. Haigh and D. A. Pacheco-Tanaka, *Chem. Eng. J.*, 2021, 129313.

2. R. W. Spillman, *Chem. Eng. Prog.*, 1989, **85 (1)**, 41-62.

3. J. Gilron and A. Soffer, *J. Membr. Sci.*, 2002, **209 (2)**, 339-352.

4. J. Shen, G. Liu, K. Huang, Q. Li., K. Guan, Y. Li and W. Jin, *J. Membr. Sci.*, 2016, **513**, 155-165.

5. N. Wang, A. Mundstock, Y. Liu, A. Huang and J. Caro, *Chem. Eng. Sci.*, 2015, **124**, 27-36.

6. M. Jia, Y. Feng, S. Liu, J. Qiu and J. Yao, *J. Membr. Sci.*, 2017, **539**, 172-177.

7. Y. Yuan, X. Gao, Y. Wei, X. Wang, J. Wang, Y. Zhang and C. Gao, *Desalination*, 2017, **405**, 29-39.

8. Y. Kinoshita, K. Wakimoto, A. H. Gibbons, A. P. Ifashani, H. Kusuda, E. Sivaniah and B. Ghalei, *J. Membr. Sci.*, 2017, **539**, 178-186.

9. R. Swaidan, B. Ghanem, E. Litwiller and I. Pinnau, *J. Membr. Sci.*, 2015, **475**, 571-581.

10. J. Deng, L. Bai, S. Zeng, X. Zhang, Y. Nie, L. Deng and S. Zhang, *RSC Adv.*, 2016, **6**, 45184-45192.

11. S.S. Hosseini, Y. Li, T. Chung and Y. Liu, *J. Membr. Sci.*, 2007, **302 (1-2)**, 201-217.

12. M. A. Llosa Tanco, D. A. Pacheco Tanaka, S. C. Rodrigues, M. Texeira and A. Mendes, *Int. J. Hydrog. Energy*, 2015, **40**, 5653-5663.

13. S. Saufi and A. F. Ismail, *Carbon*, 2004, **42 (2)**, 241-259.

14. R. Singh and W. J. Koros, *J. Membr. Sci.*, 2013, **427**, 472-478.

15. A. F. Ismail and L. I. B. David, *J. Membr. Sci.*, 2001, **193 (1)**, 1-18.

16. V. C. Geiszler and W. J. Koros, *Industrial & Engineering Chemistry Research,* 1996, **35**, 2999-3003.

17. P. S. Tin, T-S. Chung, S. Kawi and M. D. Guiver, *Microporous and Mesoporous Materials,* 2004, **73 (3)**, 151-160.

18. P.S. Tin, T-S. Chung, Y. Liu and R. Wang, *Carbon*, 2004, **42 (15)**, 3123-3131.

19. P. S. Tin, T-S. Chung and A. J. Hill, *Industrial & Engineering Chemistry Research*, 2004, **43**, 6476-6483.

20. H. Lee, M. Monji, D. Parsley, M. Sahimi, P. Liu, F. Egolfpoulos and T. Tsotsis, *Ind. Eng. Chem. Res.*, 2013, **52**, 1122-1132.

21. H. Hatori, H. Takagi and Y. Yamada, *Carbon*, 2004, **42 (5-6)**, 1169-1173.

22. J. Koresh and A. Soffer, *Carbon*, 1984, **22 (2)**, 225.

23. Y. Xiao, Y. Dai, T-S. Chung and M. D. Guiver, *Macromolecules*, 2005, **38 (24)**, 10042-10049.

24. J. Barsema, J. Balster, V. Jordan, N. F. van der Vegt and M. Wessling, *J. Membr. Sci.*, 2003, **219 (1-2)**, 47-57.

25. S. Fu, G. B. Wenz, E. S. Sanders, S. S. Kulkarni, W. Qiu, C. Ma and W. J. Koros, *J. Membr. Sci.*, 2016, **520**, 699-711.

26. H. Kita, M. Yoshino, K. Tanaka and K. Okamoto, *ChemComm*, 1997, **11**, 1051-1052.

27. N. H. Ismail, W. N. W. Salleh, N. Sazali, A. F. Ismail, N. Yusof and F. Aziz, *Sep. Purif. Technol.*, 2018, **195**, 295-304.

28. K. M. Steel and W. J. Koros, *Carbon*, 2003, **41 (2)**, 253-266.

29. T. A. Centeno, J. L. Vilas and A. B. Fuertes, *J. Membr. Sci.*, **228 (1)**, 45-54.

30. M. Teixeira, M. C. Campo, D. A. Pacheco Tanaka, M. A. Llosa Tanco, C. Magen and A. Mendes, *Carbon*, 2011, **49**, 4348-4358.

31. M. Teixeira, S. Rodrigues, M. Campo, D. A. Pacheco Tanaka, M. A. Llosa Tanco, L. Madeira, J. Sousa and A. Mendes, *Chem. Eng. Res. Des.*, 2014, **92**, 2668-2680.

32. M. Teixeira, M. Campo, D. A. Pacheco Tanaka, M. A. Llosa Tanco, C. Magen and A. Mendes, *Chem. Eng. Res. Des.*, 2012, **90**, 2338-2345.

33. M. A. Llosa Tanco, D. A. Pacheco Tanaka and A. Mendes, *Int. J. Hydrog. Energy*, 2014, **40**, 3485-3496.

34. J. A. Medrano, M. A. Llosa-Tanco, D. A. Pacheco-Tanaka and F. Gallucci, *Chem. Eng. J.*, 2020, **394**, 124957.

35. EPO, 19383095.7-1104, 2020.

36. M. L. V. Nordio, J. A. Medrano, M. S. Annaland, D. A. Pacheco Tanaka, M. Llosa-Tanco and F. Gallucci, *Energies*, 2020, **13**, 3577; doi:10.3390/en13143577.

37. N. Diban, A. T. Aguayo, J. Bilbao, A. Urtiaga and I. Ortiz, *Ind. Eng. Chem. Res.*, 2013, **52**, 10342-10354.

38. J. van Kampen, J. Boon, F. van Berkel, J. Vente and M. van Sint Annaland, *Chem. Eng. J.*, 2019, **374**, 1286-1303.

39. K. Funabiki, M. Nakamura and M. Tsuriya, Japan Thermosetting Plastics Industry Association, 1981, **2 (4)**, 220-235.

40. T. A. Centeno, J. L. Vilas and A. B. Fuertes, J. Membr. Sci., 2004, **228**, 45-54.

41.   M. J. Lasahki, M. Fayaz, S. Niknaddaf and Z. Hashisho, *J. Hazard. Mater.*, 2012, **212-242**, 154-163.

42.   L. Forster, M. Lutecki, H. Fordsmand, L. Yu and C. D'Agostino, *Mol. Syst. Des. Eng.*, 2020, **5**, 1193-1204.

43.   G. Campos-Villalobos, F. R. Siperstein, C. D'Agostino, L. Forster and A. Patti , *Appl. Surf. Sci.*, 2020, **516**, 146089.

44.   G. Di Carmine, D. Ragno, A. Massi and C. D'Agostino, *Org. Lett.*, 2020, **22 (13)**, 4927-4931.

45.   C. D'Agostino, M. R. Feaviour, G. L. Brett, J. Mitchell, A. P. E. York, G. J. Hutchings, M. D. Mantle and L. F. Gladden, *Catal. Sci. Technol.*, 2016, **6 (21)**, 7896-7901.

46.   C. D'Agostino, G. Brett, G. Divitini, C. Ducati, G. J. Hutchings, M. D. Mantle and L. F. Gladden, *ACS Catal.*, 2017, **7 (7)**, 4235-4241.

47.   C. D'Agostino, R. D. Armstrong, G. J. Hutchings and L. F. Gladden, *ACS Catal.*, 2018, **8 (8)**, 7334-7339.

48.   G. Filippini, F. Longobardo, L. Forster, A. Criado, G. Di Carmine, L. Nasi, C. D'Agostino, M. Melchionna, P. Fornasiero and M. Prato, *Sci. Adv.*, 2020, **6(46)**, eabc9923.

49.   N. Bloembergen, E. Purcell and R. Pound, *Phys. Rev.*, 1948, **73**, 679-712.

50.   J-P. Korb, *Prog. Nucl. Magn. Reson. Spectrosc.*, 2018, **104**, 12-55.

51.   J-P. Korb, *Chapter 10: Diffusive Dynamics in Porous Materials as Probed by NMR Relaxation-based Techniques* in *Diffusion NMR of Confined Systems: Fluid Transport in Porous Solids and Heterogeneous Materials*, The Royal Society of Chemistry, Cambridge, 2016.

52.   T. Borjigin, F. Sun, J. Zhang, K. Cai, H. Ren and G. Zhu, *ChemComm*, 2012, **48**, 7613-7615.

53.   H. Guan, D. Brougham, K. S. Sorbie and K. J. Packer, *J. Pet. Sci. Eng.*, 2002, **34 (1-4)**, 35-54.

54.   V. Bortolotti, P. Macini, E. Mesini, F. Srisuriyachai, P. Fantazzini and M. Gombia, *Combined Spatially Resolved and Non-resolved ^{1}H NMR Relaxation to Assess and Monitor Wettability Reversal in Carbonate Rocks*, European Association of Geoscientists & Engineers, 2009, https://doi.org/10.3997/2214-4609-pdb.151.iptc13443.

55.   J-P. Korb, B. Nicot, A. Louis-Joseph, S. Bubici and G. Ferrante, *J. Phys. Chem. C*, 2015, **118 (40)**, 23212-23218.

56.   A. Yan, B. W. Lau, B. S. Weissman, I. Külaots, N. Y. C. Yang, A. B. Kane and R. H. Hurt, *Adv. Mater.*, 2006, **18**, 2373-2378.

57.   Z. Laušević and S. Marinković, Carbon, 1986, **24 (5)**, 575-580.

Supporting information
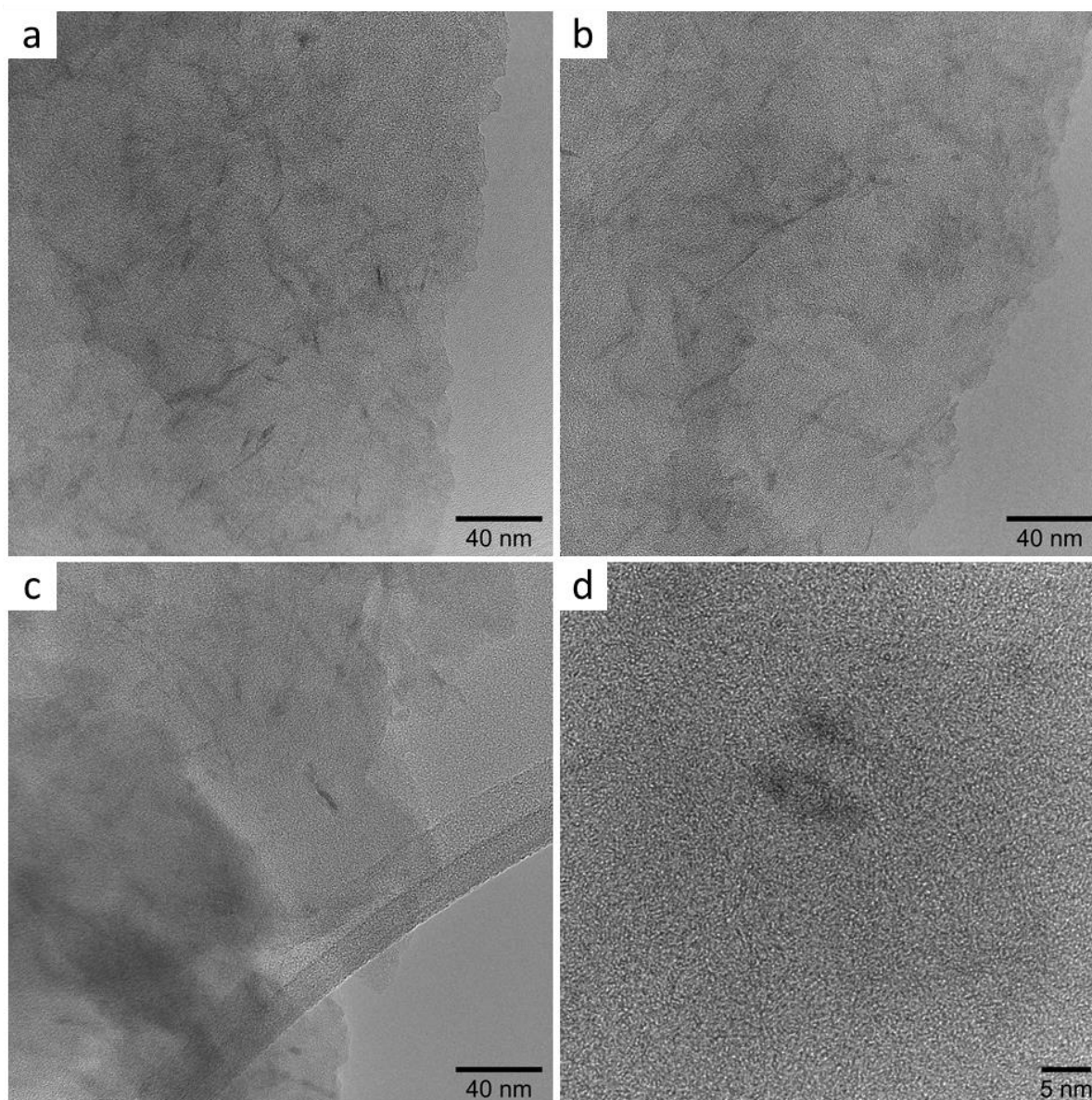
Figure S8.1. HRTEM images of the Al-CMSM membranes carbonized at (a) 600°C, (b) 650°C and (c) 750°C showing little morphological variation at this scale. (d) Porosity in the 600°C membrane remained indistinguishable at the highest magnifications, which was similarly the case for those carbonized at 650°C and 750°C. Needle-like crystalline particles (~10 nm long by ~3 nm thick) are the impregnated alumina and showed a random distribution in all the observed samples.

Table S8.1. T_1 and calculated hydrophilicity parameter, H, values of hexane and water confined within the micropores of CMSMs prepared using varying carbonization temperatures. The approximate error for T_1 values is 3 %.

Carbonization temperature (ºC)	$T_{1,Hexane}$ (ms)	$T_{1,Water}$ (ms)	H (-)
600	14 ± 0.4	19 ± 0.6	0.74 ± 0.03
650	23 ± 0.7	41 ± 1.2	0.56 ± 0.03
750	68 ± 2.0	107 ± 3.2	0.64 ± 0.03
850	81 ± 2.4	205 ± 6.2	0.40 ± 0.02
1000	95 ± 2.9	415 ± 12.5	0.23 ± 0.02

Table S8.2. H_2O permeance obtained using CMSMs prepared using differing carbonization temperatures and tested at varying permeation temperatures and 3 bar pressure difference between feed and permeate maintaining the permeate side at atmospheric conditions. The accuracy of the experimental equipment is approximately 3 %.

Carbonization temperature (ºC)	H_2O permeance at given temperatures of permeation (mol m^{-2} s^{-1} Pa^{-1} · 10^{-7})			
	150 ºC	200 ºC	250 ºC	300 ºC
600	3.93 ± 0.12	9.35 ± 0.28	13.24 ± 0.40	7.79 ± 0.23
650	2.27 ± 0.07	6.04 ± 0.18	9.17 ± 0.28	7.54 ± 0.23
750	4.02 ± 0.12	16.10 ± 0.48	7.40 ± 0.22	4.88 ± 0.15
850	$2.89 \pm 0.0.9$	10.71 ± 0.32	7.70 ± 0.23	5.05 ± 0.15
1000	10.99 ± 0.33	13.58 ± 0.41	10.87 ± 0.33	7.60 ± 0.23

Table S8.3. CH_4 permeance obtained using CMSMs prepared using differing carbonization temperatures and tested at varying permeation temperatures and 3 bar pressure difference between feed and permeate maintaining the permeate side at atmospheric conditions. The accuracy of the experimental equipment is approximately 3 %.

Carbonization temperature (ºC)	CH_4 permeance at given temperatures of permeation (mol m^{-2} s^{-1} Pa^{-1} · 10^{-8})			
	150 ºC	200 ºC	250 ºC	300 ºC
600	0.34 ± 0.01	0.56 ± 0.02	2.09 ± 0.60	3.14 ± 0.10
650	1.24 ± 0.04	2.60 ± 0.08	4.31 ± 0.13	10.29 ± 0.31
750	0.71 ± 0.02	0.33 ± 0.01	1.29 ± 0.04	2.04 ± 0.06
850	0.63 ± 0.02	0.58 ± 0.02	3.08 ± 0.09	4.26 ± 0.13
1000	33.27 ± 1.00	27.89 ± 0.84	52.74 ± 1.58	53.70 ± 1.61
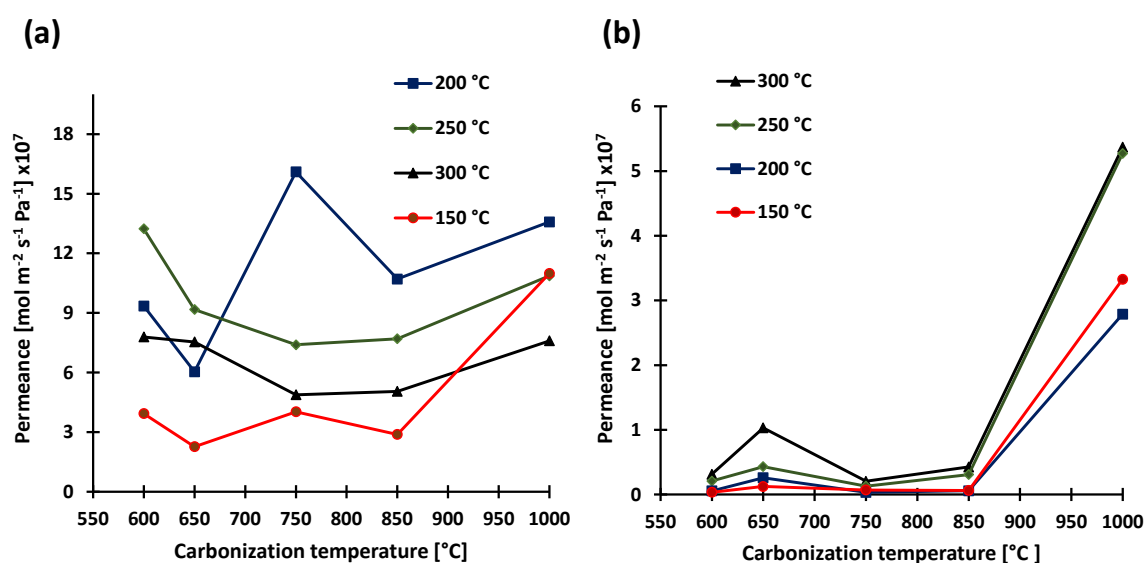
Figure S8.2. (a) H_2O and (b) CH_4 permeance (×10^{-7} mol m^{-2} s^{-1} Pa^{-1} x10^{-7}) of Al-CMSMs prepared using various temperatures of carbonization as a function of permeation temperature (pressure difference between feed and permeate 3 bar). The accuracy of the experimental equipment is approximately 3 %.

Table S8.4. H_2O/CH_4 permselectivity obtained using CMSMs prepared using differing carbonization temperatures and tested at varying permeation temperatures and 3 bar pressure difference between feed and permeate maintaining the permeate side at atmospheric conditions. The accuracy of the experimental equipment is approximately 3 %.

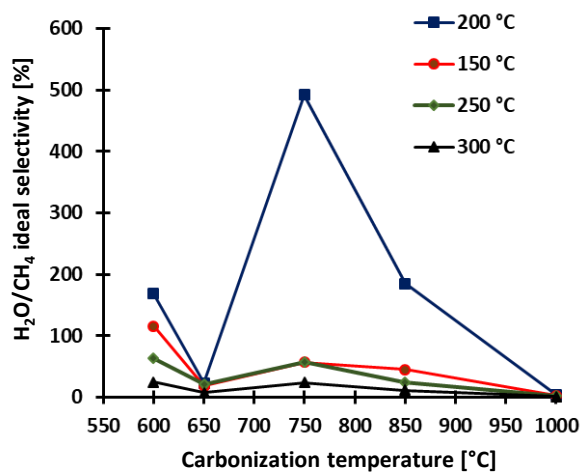| Carbonization temperature (^{o}C)	H_2O/CH_4 permselectivity at given temperatures of permeation (-)			
	150 ^{o}C	200 ^{o}C	250 ^{o}C	300 ^{o}C
600	116 ± 3	168 ± 5	63 ± 2	25 ± 1
650	18 ± 1	23 ± 1	21 ± 1	7 ± 1
750	57 ± 2	492 ± 15	57 ± 2	24 ± 1
850	46 ± 1	185 ± 6	25 ± 1	12 ± 1
1000	3 ± 1	5 ± 1	2 ± 1	1 ± 1

Figure S8.3. H_2O/CH_4 permselectivity values at varying temperatures of permeation as a function of CMSM carbonization temperature (pressure 3 bar). The accuracy of the equipment is approximately 3 %.

Chapter 9: Conclusions

The conclusions and main achievements of the work presented in this thesis are summarised below for each chapter.

Chapter 4

The textural properties of Al_2O_3 catalyst supports, namely the pore size and macropore content, were systematically altered by changing the calcination temperature used during the carrier preparation. An increased preparation calcination temperature was found to instigate Al_2O_3 phase transitions resulting in Al_2O_3 carriers with greater pore sizes and increased macropore content. PFG-NMR was used to investigate the effect of altering textural properties upon the mass transport properties of the Al_2O_3 carriers. It was found that mass transport occurs more readily in carriers with greater pore size and macropore content, in particular, up to a pore size of 17.0 nm diffusion increases very rapidly with pore size. In carriers with larger pore sizes, the increase in diffusivity is less marked. The effect of pore surface chemistry on the mass transport of functional molecules was also evaluated showing that surface interactions affect mass transport far more in small pore size carriers.

Chapter 5

A simple, novel strategy for the preparation of hierarchical ZSM-5 zeolites with a low silicon-to-alumina ratio was proposed and their effectiveness in fluid catalytic cracking reactions was investigated. PFG-NMR measurements using molecules of differing kinetic diameters were performed to investigate mass transfer properties and molecule accessibility across the meso-micro porous intra-crystalline pore network. PFG-NMR measurements confirmed that the high catalytic cracking activity of the hierarchical ZSM-5 zeolites was due to the increased accessibility of reactant molecules to the catalytic active sites in addition to the low silicon-to-alumina ratio.

Chapter 6

Zeolite Y supported gallium and tin catalysts were prepared via wet impregnation and tested for the catalytic isomerisation of glucose in different solvents. 2D NMR relaxation measurements confirmed that catalytic activity is affected significantly by adsorption of solvent molecules to the zeolite surface. 2D NMR relaxation solvent displacement measurements supported this finding as the rate of displacement of each solvent was proportional to their respective adsorption strengths as determined by 2D NMR relaxation measurements.

Chapter 7

Carbon nitride photocatalysts were subjected to one of four pre-treatments to alter the carbon nitride structure and surface chemistry. The treated photocatalysts were tested for their performance in photocatalytic C-C bond formation reactions using fluorinated substrates for a wide range of different substrates and using many differing sets of reaction conditions. ^{19}F NMR relaxation measurements using a model fluorinated species imbibed within each pre-treated catalyst showed the relative adsorption strengths of the fluorinated molecules were proportional to their catalytic activity whilst ^{1}H NMR relaxation measurements using the reaction solvent, DMF, were inversely proportional to the catalytic activity implying that the solvent can act to block the catalytically active sites. Both of these interactions depend on the surface chemistry of the catalyst as determined by the pre-treatment method used.

Chapter 8

Alumina-Carbon molecular sieve membranes (Al-CMSMs) were prepared using a range of carbonization temperatures to effectively alter the pore size, pore structure and pore wettability. Low field ^{1}H NMR relaxation measurements using hydrophobic n-hexane and water respectively showed that an increase in preparation carbonization temperature results in Al-CMSMs with larger, more hydrophobic, micropores. The performance of Al-CMSMs in the separation of gaseous H_2O/CH_4 mixtures was also seen to vary significantly with the carbonization temperature used for the membrane preparation. In smaller, more hydrophilic micropores, the adsorption-diffusion mechanism is dominant and H_2O permeance is favoured resulting in a high permselectivity. In larger, more hydrophobic micropores, Knudsen diffusion is more prevalent and CH_4 permeance increases thereby decreasing the H_2O/CH_4 permselectivity.

Chapter 10: Future Work

The findings detailed in this work can be expanded on as described below;

10.1 Diffusion in hierarchical systems

The findings in Chapters 4 and 5 prove the usefulness of low-field, benchtop NMR diffusion measurements to investigate both hierarchical macro-meso pore networks (Chapter 4) and meso-micro pore networks (Chapter 5). Clearly, low-field, benchtop NMR diffusion measurements are a valuable tool in aiding the design of catalytic materials and ensuring that mass transfer properties in such materials are optimised. As such, it would be interesting to apply the systematic studies used in this work to investigate other common classes of catalytic materials (i.e. TiO_2 or SiO_2 supports) to give a comprehensive overview of how to prepare these different classes of materials with specific pore sizes and porosities and specifically how this will impact the mass transport properties.

Building further on this, low-field, benchtop NMR diffusion measurements could be applied to investigate the impact of coking of hierarchical materials upon the mass transport properties. Coking is a common issue seen in catalytic processes resulting in a decreased lifetime for catalysts before they are required to be reactivated or disposed of. These measurements could be used to identify the locations of coke build up in the hierarchical porous networks and monitor the effect of coke build up in each region upon the overall mass transport properties of the reactions under study.

The use of these measurements to investigate more industrially relevant catalytic materials and aid their design and optimisation is a very interesting prospect that could yield very useful information.

10.2 Surface interactions of reactive species

The interaction of reactive species with a solid catalyst surface forms a large part of this thesis work (Chapters 4, 6, 7 and 8) and with good reason. The activity and selectivity of catalytic materials and processes is largely defined by adsorption and desorption processes. It is clear then, that the use of low-field, benchtop NMR relaxation measurements to determine relative strengths of adsorption of reactants and products alike has much to offer to the design of catalytic materials and processes.

The use of ^{19}F relaxation measurements (Chapter 7) to investigate halogen bonding strength is a useful tool to investigate many processes where halogen bonding is important. Halogen bonds are vital interactions in the field of crystal engineering and are also vitally important in the synthesis and structures of large biological molecules. As NMR measurements are non-destructive, relatively fast and easy to perform they could offer new insights into the halogen bonding interactions used to design such materials.

10.3 Characterisation of microporous materials

The findings in Chapter 8 demonstrate an effective new way to characterise both the relative pore sizes and relative wettabilities of a series of samples using the T_1 relaxation times for a relatively hydrophilic and hydrophobic guest molecule. This method of analysis allows for the determination of two important factors governing the mass transport properties of guest molecules through microporous species quickly and simply. As such, it would be interesting to see this methodology applied to other microporous materials, for example, other classes of microporous membranes such as; metallic (mostly Pd based) membranes, zeolite membranes and polymeric membranes in addition to other microporous materials.

10.4 ^{19}F NMR relaxation studies

The results in Chapter 7 also highlight the usefulness of ^{19}F NMR relaxometry for investigating complex reactions using fluorine containing molecules. The interactions of fluorine containing molecules with catalyst surfaces can be investigated as in Chapter 7 for a wide range of systems to give similar information. ^{19}F NMR has a similar chemical abundance to [1]H (100 %) but a much wider range of possible chemical shift values. This allows for different groups of fluorine containing molecules to be easily identified and investigated even on low field instruments as in Chapter 7.

Another interesting application of such NMR measurements would be to investigate the reaction kinetics of a reaction such as that in Chapter 7 using ^{19}F NMR. As only ^{19}F molecules can be detected during these measurements and the spectrometer is effectively blind to other nuclei, it would be possible to measure kinetic and adsorption data at various time points throughout the reaction to give information on the system in operando.